Wave Response Modelling and Innovative Cooling Technologies for Offshore Photovoltaics

ING. RYAN BUGEJA

Supervised by Prof. Luciano Mule' Stagno

Institute for Sustainable Energy

University of Malta

July 2023

A dissertation in fulfilment of the requirements for the degree of Doctor of Philosophy in Sustainable Energy

L-Università ta' Malta

INSTITUTE FOR SUSTAINABLE ENERGY

DECLARATION OF AUTHENTICITY FOR DOCTORAL STUDENTS

(a) Authenticity of Dissertation

I hereby declare that I am the legitimate author of this Thesis and that it is my original work.

No portion of this work has been submitted in support of an application for another degree or qualification of this or any other university or institution of higher education.

I hold the University of Malta harmless against any third-party claims with regard to copyright violation, breach of confidentiality, defamation and any other third party right infringement.

(b) Research Code of Practice and Ethics Review Procedures

I declare that I have abided by the University's Research Ethics Review Procedures.

□ As a Ph.D. student, as per Regulation 66 of the Doctor of Philosophy Regulations, I accept that my thesis be made publicly available on the University of Malta Institutional Repository.

To my son Mikele. May this instil in you courage, perseverance and determination

Acknowledgements

Immense gratitude goes towards my supervisor, and the Institute for Sustainable Energy's director, Prof. Luciano Mule' Stagno, for his academic and moral support throughout this journey. This research would not have been possible without the available resources and the flexibility he allowed.

The impact of this thesis would not have been possible without the funding and support of Malta Marittima, the Energy and Water Agency, TAKEOFF, and the University of Malta's Knowledge Transfer Office. I am also grateful to the Institute for Sustainable Energy's staff namely Mr. Terence Cilia and the late Mr. Malcolm Farrugia for their technical support and Mr. Aaron Grech for his administrative support. I would like to give a special acknowledgement to Prof. Ing. Charles Yousif for providing weather station data, which was essential for various parts of the research.

Gratitude goes towards my family for their continuous support. I am especially grateful to my wife, Davinia, for taking most of the load of a newborn and sacrificing her career for me to persevere in this journey. Last but not least, I would like to thank my son Mikele who has unknowingly been my source of happiness and courage for the past months.

Abstract

Solar energy is becoming increasingly popular, especially with countries racing to meet renewable energy share targets and achieve energy independence. However, inefficiencies in solar cells result in most absorbed energy being converted into heat, with only a small fraction being used to generate electrical energy.

While onshore solar installations have been predominant, offshore photovoltaics (PV) are emerging as a promising technology with vast untapped potential. Offshore photovoltaics refer to installing solar panels on floating structures or platforms in bodies of water, such as oceans, seas, and lakes. This approach offers several advantages over traditional onshore solar installations. Firstly, offshore photovoltaics can overcome the limitations posed by land availability, especially in densely populated areas or regions with limited suitable land for solar installations. Additionally, offshore photovoltaics can help to mitigate visual impacts and land-use conflicts associated with onshore installations, as they are located away from populated areas. Moreover, floating solar platforms open up possibilities for location sharing with other marine-based activities, such as aquaculture or water treatment, creating opportunities for integrated and sustainable use of marine resources. However, it is essential to address challenges related to technology development, installation logistics, environmental impacts, and cost-effectiveness to fully realise offshore photovoltaics' potential.

This thesis analyses the different parameters that could negatively affect the efficiency of offshore PV panels and focuses primarily on the incident solar radiation and the effect of temperature. A decrease in the insolation on PV panels directly results in a reduction in energy generation. Furthermore, an increase in solar cell temperatures results in a decreased conversion efficiency and, as a result, a decreased energy yield. Since no long-term offshore photovoltaic installation exists, various research and technology gaps still need to be addressed. For instance, floating structures will have some response to incoming waves. This response is highly dependent on the design of the floating structure and will have some effect on the insolation on offshore photovoltaic systems. However, there are currently no tools available that an offshore system designer can use to quantify this effect and optimise their design. This research presents a new simulation tool termed Offshore Solar Irradiance Calculator (OSIC) that can quantify this effect. The development of this tool is outlined in this thesis, and parametric analyses are presented, showing the impact of wave response motion on fixed and

tracking offshore PV installations. The findings of this research show that wave responses can affect incident radiation, ranging from a slight increase of 0.26% to a decrease of more than 12% for high amplitude wave responses. These findings could have significant impact on the design of offshore PV systems.

Moreover, this thesis also presents a patented Innovative Photovoltaic Cooling System (IPCoSy) that addresses limitations in existing PV cooling technologies. The cooling system involves the addition of a water chamber at the back of a conventional PV module, resulting in uniform cooling and a decreased pump switching frequency. The findings of this research showed that the positive effects of this cooling technology range from more than 10% increase in PV electrical energy yield, and thermal efficiencies of up to 56%. The development, testing and future recommendations of this technology are all presented in this research.

Therefore, this research contributes new knowledge toward optimising offshore photovoltaic installations through wave response modelling and innovative cooling technologies. Furthermore, this thesis contributes knowledge to improve the PV industry and presents technology that could also change the current concept of a PV module and revolutionise the integration of renewable energy in buildings and industry.

Keywords: Solar Energy, Offshore Photovoltaics, Solar Irradiance, Photovoltaic Temperature, Photovoltaic Cooling.

Contents

List of Figures

List of Tables

List of Abbreviations

Nomenclature

Maximum Power Point	P_{MPP}	Reference Efficiency	n_{Tref}
Area	A	Insolation on PV module	GPV
Cell Temperature	T_c	Reference Cell Temperature	$T_{c,ref}$
Temperature Coefficient	β_0	solar altitude angle	αs
solar azimuth angle	γ_s	Surface azimuth angle	γ
Zenith Angle	θz	Surface tilt angle	β
Beam angle of Incidence	θ	Transmittance Absorptance Coefficient	τα
Transmittance Absorptance Coefficient at a normal angle	$(\tau\alpha)_n$	Solar Declination Angle	δ
Hour Angle	ω	Bandgap energy	E_g
Reference Bandgap energy	$E_{g,ref}$	Eccentricity correction factor	ε_o
Open Circuit Voltage	V_{OC}	Electron charge	q
Maximum dark saturation current	$I_{o\,max}$	Short Circuit Current	I_{sc}
Diode ideality factor	n	Boltzmann constant	K
Nominal Operatic Cell Temperature	$T_{c,NOCT}$	Ambient Temperature at nominal conditions	$T_{a,NOCT}$
PV module temperature	T_m	Cell temperature at standard testing conditions	$T_{c,STC}$
Distance between the Sun and the Earth	r	Julian Day	N
Global irradiance on a surface tilted at an angle β and oriented at an angle γ	$G(\beta,\gamma)$	Ratio describing the dependence of a material's bandgap energy to temperature	C
Direct irradiance on a surface tilted at an angle β and oriented at an angle γ	$B(\beta,\gamma)$	Diffused irradiance on a surface tilted at an angle β and oriented at an angle γ	$D(\beta,\gamma)$
Ratio between beam radiation on a tilted surface and beam radiation on a horizontal surface	$R_{T\text{-}H}$	Latitude	∅

Albedo	ρ	Circumsolar and Horizon brightness coefficients	F1 & F2
Extra-terrestrial radiation incident on a plane normal to the radiation from the Sun	G_{on}	Solar constant (1367W/m^2)	Gsc
Clearness Factor	ε	Brightness factor	Δ
New tilt angle after wave movement	B_n	Azimuth angle between a raft and a solar panel	ψ
Young's Modulus	E	Poisson Coefficient	ν

1. Introduction

1.1 Background to the research work

Energy demands are predicted to increase globally by 33% between 2010 and 2030 [1]. Photovoltaic (PV) technology has become very popular and is recognised as one of the most reliable renewable energy sources. Most of the world is striving to increase its renewable energy output and achieve energy independence. The European Union is one of the leaders in this by setting a 2030 target of 42.5% renewable energy use, and even aiming at 45% [2]. Malta has a binding obligation to achieve a renewable energy share of 11.5% of its gross energy consumption by 2030 [3].

The Maltese Islands occupy a surface area of circa 316 km^2, with territorial waters covering approximately 3000 km^2. Furthermore, with a population of more than 500,000, Malta is one of the most densely populated countries in the world [4]. These factors lead to land being limited and very expensive. Land pricing significantly impacts large renewable energy installations since this will prolong the payback period and reduce economic viability. PV systems using crystalline silicon technology occupy about 7m^2 per Kilowatt Peak (kWp) [5]. Amorphous silicon modules require twice as much area. Thus, a 1 MWp solar farm will require between 7,000 m^2 and 15,000 m^2 of land.

Furthermore, Malta is geographically and economically limited in renewable energy options such as onshore and offshore wind, geothermal or hydroelectric. A study by Mott MacDonald on the feasibility of offshore wind farms showed that with wind speeds lower than Northern European installations and a limited space scenario, the Capex and Opex costs for wind farms would make it difficult for wind energy to be economically viable in Malta [5].

The Maltese Islands benefit from a very high annual global irradiance of approximately 1,933 kWh/m^2 [6]. For this reason, in a study on developing a European solar radiation database [7], Malta was rated as one of the countries with the highest potential for harvesting solar energy. Therefore, a combination of limitations, legal and environmental obligations and geographical advantages have led Malta to install a substantial amount of PV systems, especially on rooftops and integrate PV modules in buildings. Public, residential and commercial PV installations amounted to 221.15 MW_p by the end of 2022 [8]. However, not all rooftops are suitable for PV installations due to their orientation and shading from adjacent buildings. In addition, rooftops

are also used for other services, such as water storage, thus reducing the available space for PV installations. Hence, Malta requires other alternatives to keep increasing its renewable energy share.

Being an isolated island away from other landmasses, Malta is surrounded by a large sea area. Malta's Exclusive Fishing Management Zone, extending to 25 nautical miles from the shore, covers an area of 6,735 km^2 [9]. Hence, a logical way forward is to explore and study the feasibility of offshore photovoltaic farms.

Floating photovoltaics offer the potential for small countries like Malta, or other densely populated large coastal cities, to launch large solar farms that would otherwise not be possible on the limited available land. A Malta Council for Science and Technology (MCST) funded project, SolAqua–R&I-2012-041, has established the viability of offshore platforms and outlined the parameters under which they would be feasible [10]. Floating solar technology is gaining popularity, especially in countries with land space limitations [11]. China has already installed 40MW, 70MW, and 150MW floating photovoltaic farms [12]. Furthermore, recently the largest floating photovoltaic farm in the world has been commissioned, in Dezhou in China's Shandong province. This consists of 320MW floating photovoltaics combined with energy storage and onshore wind [13]. In addition, an Indonesian power company is planning a 200MW floating photovoltaic farm [14].

Floating PV installations have numerous advantages over land-based installations. Previous studies have shown that efficiency and yield improve due to the cooling effect of water and also the reduction in dust effects because of the cleaner environment [6][11][15][10]. Furthermore, a floating installation on freshwater bodies can benefit the surrounding environment by reducing water evaporation and improving water quality by inhibiting algae growth [16].

However, floating installations present various challenges, especially structural design and anchoring [11]. Furthermore, other issues, such as high moisture levels and the durability and survivability of the installation, need to be kept in mind when designing and installing floating photovoltaics [15]. Most existing floating photovoltaic installations were designed and installed on lakes, dams or reservoirs. Environmental and climatic issues in these areas are less severe than those found in marine environments [6], making the design of such systems less critical. Offshore installations need to cater for constant exposure to the corrosion effects of salt and the mechanical forces from a combination of wind, waves and tides [17].

A research gap exists in having software that can quantify the effect of movement, caused by a response to waves, on the incident solar irradiance on offshore photovoltaic installations. Furthermore, there is also a research gap on effectively utilising the available large body of water to keep the operating temperatures of offshore photovoltaic modules at optimum levels without affecting the absorption of solar radiation.

1.2 Aims and objectives of this research work

This research aims to find innovative solutions to optimise offshore photovoltaic installations, focusing on improving power output and increasing economic feasibility. Therefore, this study aims to address existing research gaps and provide new solutions to push forward photovoltaic technology. Furthermore, this study aims to create innovative products that, besides optimising offshore PV installations, can also be implemented for land installations and broaden their market suitability.

Hence, the objectives of this research to accomplish this aim are:

O.1 Perform state-of-the-art research on solutions to decrease the effect of various parameters that reduce PV power generation and economic feasibility.

O.2 Develop and validate a simulation tool that analyses the effect of wave response motion on the incident solar irradiance on offshore PV installations.

O.3 Analyse separately the effects of pitch, yaw and roll wave response movements on the incident solar radiation on offshore PV installations.

O.4 Analyse the effect of wave response motion on both fixed and tracking offshore PV installations.

O.5 Develop an innovative PV cooling system targeted towards offshore PV installations, that can also be applied to land installations.

O.6 Test different PV cooling system designs and propose the most feasible design and suggestions for future development.

1.3 Research questions

Given the above research background, aims, and objectives, the research questions that are to be answered by this study are as follows:

- How does wave response motion affect the incident solar irradiance on offshore fixed and tracking PV installations?
- What algorithms need to be applied to allow a user to input a wave characteristic equation and obtain the effect of that wave on the incident irradiance on a PV system?
- How can one use the offshore environment to effectively cool PV modules while addressing shortcomings of existing PV cooling technologies?
- Can a PV cooling technology be adequate for a broad market (offshore and land) to increase production scale and financial viability?

1.4 Organisation of this thesis

This thesis is organised as follows:

- Chapter 2 presents a background and literature review of the main factors that negatively affect PV power output, reduce the lifetime of PV modules, and, consequently, reduce the economic feasibility of a PV installation. Furthermore, this chapter presents state-of-the-art research on current technologies to address these derating factors. Finally, research gaps are identified, justifying the aims and objectives of this study.
- Chapter 3 analyses the effect of wave response motion on the insolation on fixed offshore photovoltaic installations. A simulation model is created and validated experimentally. This model accepts wave characteristic equations as input and calculates the effect of pitch, yaw and roll movements on the incident solar irradiance on a fixed PV system.
- Chapter 4 analyses the effect of wave response motion on the insolation on tracking offshore photovoltaic installations. The simulation model validated in Chapter 3 is further optimised and incorporated with a user-friendly graphical user interface (GUI).

The resultant simulation tool was termed Offshore Solar Irradiance Calculator (OSIC), and its features and results are presented in this chapter.

- Chapter 5 presents an innovative photovoltaic cooling system termed IPCoSy. The first part of this chapter explains the hypothesis of adding a water chamber at the back of a PV module to cool the solar cells. Furthermore, the added specific heat capacity would help reduce the cooling pump switching frequency since the solar cells would take longer to heat up when the cooling flow is switched off. Hence, this chapter presents the results of implementing the cooling system on small-scale solar panels. These results confirmed the initial hypothesis. The second part of this research investigates the implementation of the cooling system on large full-scale PV panels. Full-scale designs are presented, and their benefits and shortcomings are investigated. An experimental setup tested these prototypes, and the results were used to conduct a financial analysis of the product. Finally, the chapter ends with recommendations for future work to further develop this innovative cooling system.

- Chapter 6 presents the conclusions arising from this study. This chapter summarises and compares the work done throughout this research to the aims, objectives and research questions.

2. Background & literature review

2.1 Introduction

The maximum power, P_{MPP} (W), delivered by a photovoltaic module at a particular time interval is highly dependent on the solar radiation received by the module, G_{PV} (W/m^2), the solar cell temperature, T_c (°C) and the photoelectric conversion efficiency of the solar cell, n_{Tref}. Moreover, the solar cell temperature depends on the amount of solar radiation incident on the solar cells, the wind speed, the cells' efficiency and the ambient temperature, T_a (°C). Hence the maximum power output is calculated using equation (1) [18] where A is the surface area of the photovoltaic module (m^2), T_{ref} is a reference temperature (usually 25°C), and β_0 is the temperature coefficient describing the effect of temperature on the efficiency of solar cells. Therefore, this equation shows that to maximise the power output from a photovoltaic module, maximum solar radiation needs to reach the solar cells while keeping the solar cells' temperature as low as possible.

$$P_{MPP} = n_{Tref}\, A\, G_{PV}\, (1 - \beta_0 (T_c - T_{ref})) \quad (1)$$

2.2 Tilt and orientation

Photovoltaic modules should be installed in such a way as to maximise energy production. Two factors affecting energy harnessing from photovoltaics are the module's tilt and orientation. A photovoltaic module produces maximum power when placed perpendicular to incident Sun rays so that the power density on the absorbing surface is maximised. Therefore, by calculating the Sun's position with respect to a point on Earth, one can find the optimal tilt angle and orientation for a PV installation.

The Sun's location relative to a point on Earth is specified mainly using the solar altitude angle (αs) and azimuth angle (γs). The solar altitude angle is the angle between the horizon and the position of the Sun [19]. The solar azimuth angle is the angle on a plane parallel to the Earth's surface, measuring the Sun's position from the true geographic south. Other angles describing the tilt and orientation of a surface on Earth and the Sun's position can be seen in Figure 1 [19].

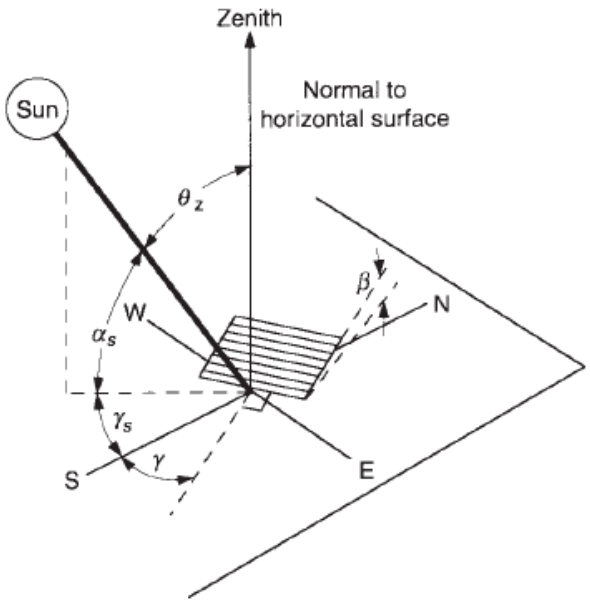

Figure 1: Angles describing the tilt and orientation of a surface on Earth and the position of the Sun [19].

Thus, optimum tilt angles for photovoltaic modules are highly dependent on the location of the installation. To calculate the optimum angle for photovoltaic installations, yearly solar radiation data for that particular location is required [20]. Generally, a surface with an inclination of 10-15° less than the latitude receives maximum global insolation in summer. In contrast, in winter, an inclination of 10-15° more than the latitude is required for maximum insolation [20]. Mondol et al. [20] studied the impact of array inclination and orientation on a PV system. A simulation using Transient System Simulation Tool (TRNSYS) showed the variation of total annual insolation with different azimuth and tilt angles, as shown in Figure 2 [20]. This study found that, for a latitude of 54°52'N and a longitude of 6°17'W, a surface oriented towards the south with a tilt angle of 30° gets maximum annual insolation. This study also shows that tilt has a much higher effect than orientation on the insolation received by a surface. A horizontal south-facing surface and a vertical south-facing surface receive 9.05% and 28.7% less insolation than a 30° south-facing surface. Furthermore, for a 30° tilted surface, a change in orientation of 30° from the south results in an annual reduction of 2% surface insolation [20]. Figure 3 [20] shows a normalised distribution of annual insolation on a surface as a function of the surface azimuth and tilt.

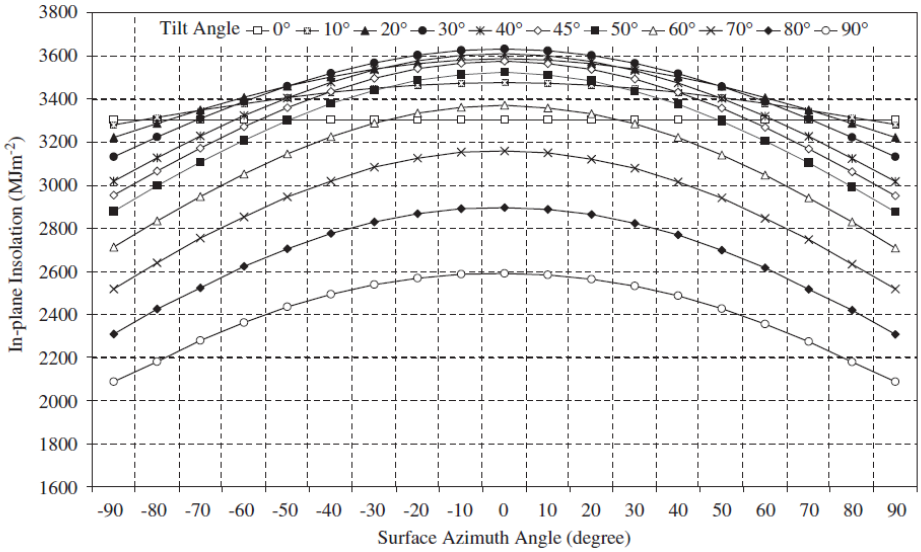

Figure 2: Variation of total annual insolation with varying azimuth and tilt angles [20].

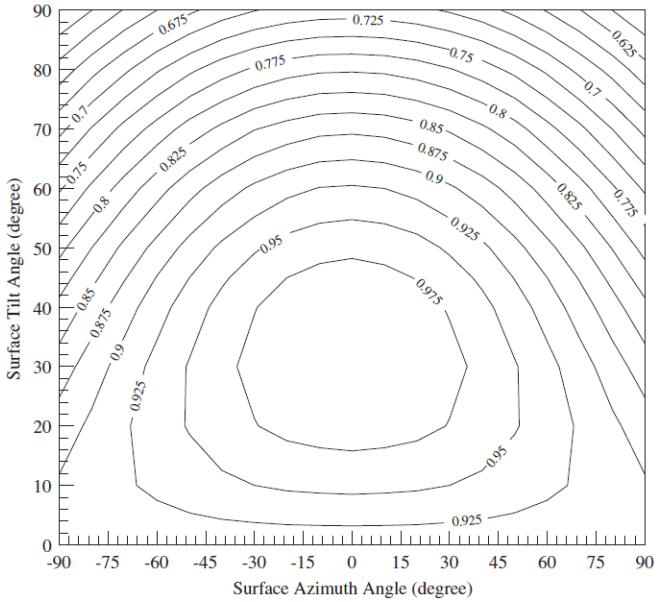

Figure 3: Normalised distribution of annual insolation on a surface as a function of the surface azimuth and tilt [20].

A study based in Malta by Rebé et al. [21] found that although a 30° tilt results in the maximum annual power generation, this might not always be the most economical setup. When having a larger space and a multi-row PV setup, a 15° tilt angle can house a larger number of panels due to lower separation between rows and thus result in a higher energy density and an improved rate of return. Another study in Hannover, Germany [22] claimed that tilt angle has little effect on PV power output. However, in these studies, a loss of 6% in summer and 10% in winter was still observed for non-optimal angles. A mathematical model [23] considering the variation of global irradiance, shows that an increase in power output is possible by varying a module's tilt

angle between cold and hot seasons. These improvements range from 3.5% to 26%, depending on the required hourly power uniformity. A. Bhaskara Rao and G. R. Padmanabhan [24] performed an experimental tilt angle study directly on a bare silicon solar cell under direct illumination from a laboratory light source. Therefore, this study eliminated the effects of anti-reflection coatings and glass covers to observe directly the behaviour of a p-n junction at different tilt angles. This study showed that an inclination of 60° results in a 60% drop in power compared to a horizontally placed solar cell.

As discussed above, the theoretical response of a silicon solar cell to tilt variations is calculated from basic geometry since an inclined surface receives less insolation than a horizontal one. However, A. Bhaskara Rao and G. R. Padmanabhan showed that the experimental results differ from theory. A big part of this deviation was due to reflection losses possibly caused by the cell's surface texture. However, these reflection losses were not quantified in this study. Furthermore, both the transmittance and absorptivity are dependent on the incident angle. The angle dependence of the ratio of the transmittance-absorptance coefficient at an angle ($\tau\alpha$) to the coefficient at a normal angle $(\tau\alpha)_n$ is shown in Figure 4 [19].

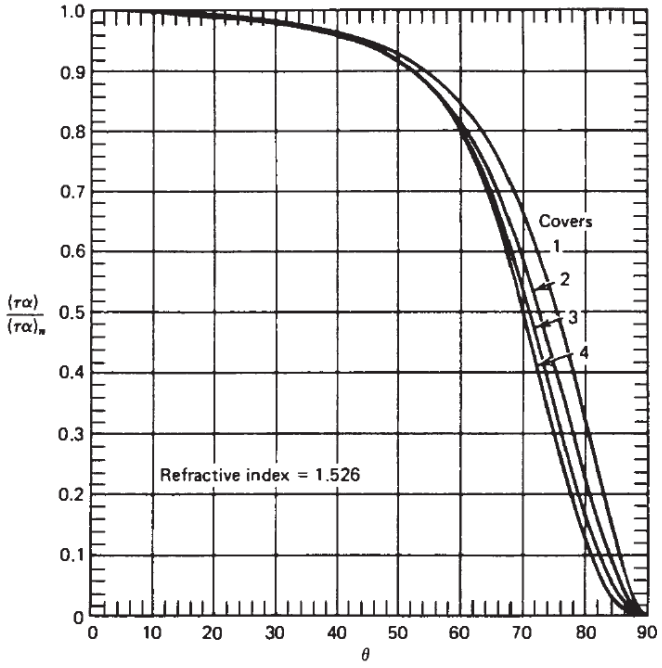

Figure 4: Typical $(\tau\alpha)/(\tau\alpha)_n$ curves for different incident angles [19].

The relationship of solar transmittance to the incident angle also depends on the material's surface texture. Typical values of solar transmittance, at different incident angles, for etched and unetched glass are shown in Table 1 [19].

Table 1: Solar transmittance for etched and unetched glass as a function of incidence angle [19].

	Transmittance by Incidence Angle						
Type of Glass	0°	20°	40°	50°	60°	70°	80°
Etched	0.941	0.947	0.945	0.938	0.916	0.808	0.562
Unetched	0.888	0.894	0.903	0.886	0.854	0.736	0.468

2.2.1 Tracking systems

A tracking system involves changing a PV system's tilt, orientation, or both, to maximise the incident solar radiation throughout the day. These movements can be done in various ways, categorised as passive or active trackers [25]. Passive trackers usually use a container filled with a low boiling point liquid. When heated by incident solar radiation, this liquid expands into a gas and pushes the remaining liquid to a shaded part of the container. This weight shift results in the solar panel's rotation until the fluid reaches thermal equilibrium, and hence the rotation stops [26][27]. Compared to fixed systems, passive trackers have been reported to achieve up to a 23.3% increase in power output [28] and even a 23% increase in efficiency [29]. Although passive tracking can be cheap to implement and maintain, it is sensitive to weather conditions such as low temperatures or radiation and high wind speeds [26].

Active tracking systems use geared motors, sensors and control algorithms to detect and follow the Sun's position during the day. Active photovoltaic trackers can give higher gains than passive trackers but usually come at a higher installation cost and may require more maintenance due to the increased number and complexity of components. These trackers have been classified into various categories; however, the most common are single-axis and dual-axis solar trackers [30]. Single-axis tracking can have either a horizontal axis parallel to the ground (Horizontal Single Axis Tracker - HSAT), a tilted axis with horizontal tracking (HTSAT), a vertical axis normal to the ground (Vertical Single Axis Tracker – VSAT) or a polar axis aligned with the polar star (PASAT) [31]. A study [32] found that HSATs are more suitable for low-latitude regions and can achieve an annual energy gain of 16% to 24% when the axis is oriented South-North. A similar study [33] concluded that VSATs are more suitable in regions with abundant solar resource where the effective incident solar radiation can be

increased by up to 28%. Another study [34] reported an energy yield gain of 15.4% when comparing an HSAT with a fixed installation.

Dual-axis trackers are the most complex to implement but can achieve the most significant increase in energy gain. These trackers have two axes, usually perpendicular to each other, with one axis adjusting the tilt of the solar panels while the other axis adjusts the azimuth. This tracking configuration can be controlled by either an open or closed-loop control system. In an open-loop control system, the control algorithm is programmed to make fixed daily movements based on weather data and irradiance models. The accuracy of this type of control is highly dependent on the quality of the data on which the programming is based.

In contrast, closed-loop tracking systems use sensors such as Light Dependent Resistors (LDRs) to get feedback of irradiance intensity. Based on this feedback, the tilt and azimuth of the solar panel are adjusted until a peak uniform intensity is reached. A closed-loop tracking system can accurately track the Sun's position and is mainly limited by the feedback sensor's accuracy. Sebastijan et al. [35] designed and tested an open-loop dual-axis solar tracker and achieved an increase in energy yield of 27% compared to fixed PV installations. Moreover, a closed-loop dual-axis solar tracking system was reported to increase daily energy yield by 39.43% [36]. Although these trackers can result in a considerable increase in efficiency, they require higher maintenance which make their use offshore less feasible. They are also susceptible to significant forces due to the weight of the panels and the effect of wind when the panels are at a high tilt angle [31].

2.2.2 Tilt and orientation of floating installations

Floating photovoltaic installations tend to adopt a different approach when choosing the tilt angles of the installed modules. In the case of such installations, one must consider a tilt angle adequate for the environment it will be installed in. The tilt angles for floating installations are determined by factors such as aesthetic impact, wind loading, and available space, in addition to optimal power generation. Researchers from the National Institute of Advanced Industrial Science and Technology installed floating photovoltaic modules in Aichi, Japan at a tilt of 1.3° facing south [37] [38]. Another system in Negret, Spain [39] was installed with a tilt of 10°. In comparison, the Solarolo project consisted of modules tilted at 8° to reduce the array's footprint and, thus, increase the output power density [38]. Lake Colignola's installation included horizontally mounted PVs with reflectors tilted at -60° and 60°, positioned at the modules' north and south [40][38].

Solar tracking is also being considered for floating photovoltaic installations. A passive floating solar tracking system was designed and implemented [41]. This system detects movement due to wave response and engages and disengages brakes for the solar panels to freely follow the wave motion until they face the Sun. Tina et al. [42] analysed the performance of tracking floating photovoltaic systems considering the cooling effect of the body of water underneath and the possible use of bifacial modules. They reported an energy gain of up to 47.4% for a floating dual-axis tracker, 16.9% for an E-W HSAT, 27.6% for a N-S HSAT and 31.3% for a VSAT. However, this study highlights that economic considerations were not taken into account. A floating tracking cooling system (FTCC) [40] developed and tested in Italy reports an efficiency gain of 25% when considering the effect of tracking alone. This system involves a combination of PVs and reflectors and uses two electric outboard motors to change the azimuth of the installation. A Liquid Solar Array (LSA) involves thin plastic concentrator lenses tracking on top of photovoltaic panels submerged in water to keep low temperatures [43]. When a prototype of this system was tested, an increase in production efficiency by 16% was observed [44]. Another innovative design involves a concentrated photovoltaic (CPV) floating tracker termed Sun-Spotter [43]. This design displaces water and air in a submerged cross enclosure. It takes advantage of the gravity and buoyancy effect to tilt the overlying CPV towards the Sun, as shown in Figure 5 [43].

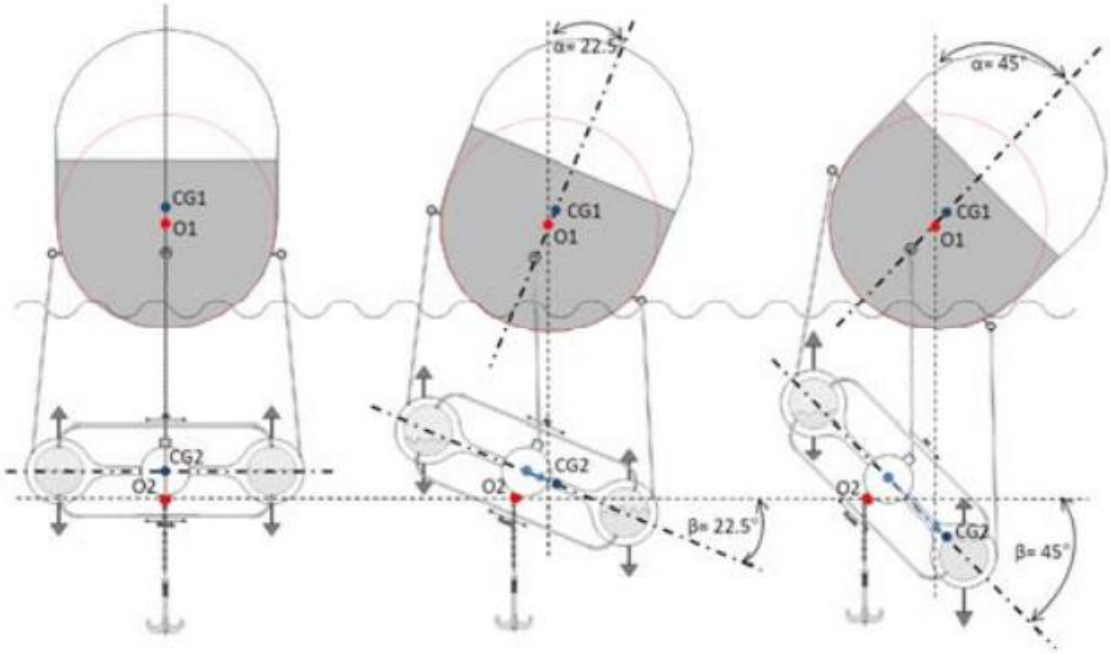

Figure 5: Sun-Spotter tracking mechanism [43].

A study [45] concluded that although floating tracking systems have a higher investment cost, the increased energy production compared to fixed floating PV systems accounts for a competitive levelised cost of energy (LCOE). Therefore, such systems should still be considered.

However, most of these systems are designed for relatively calm bodies of water. There is still a research gap in quantifying the effect of wave response motion on the performance of fixed and tracking offshore photovoltaic systems. This topic will be analysed in the following sections of this research.

2.3 Effect of temperature

Photovoltaic cells absorb approximately 80% of the incident light. However, conversion inefficiencies of solar cells result in only a portion of incident light energy being converted to electrical energy [46]. A photovoltaic module installed outside can have solar cells reaching a temperature up to 40°C above ambient temperature [47]. According to the law of conservation of energy, if a module's temperature rises, some of the solar energy is being converted to heat energy instead of electrical energy. This conversion inefficiency results from the fact that solar cells only use part of the solar spectrum to generate electricity. Typical conversion efficiencies for single junction solar cells range between 6% and 25% depending on the material technology [47]. An increase in solar cell temperature will result in a drop in the conversion efficiency of the module [48]. Therefore, the effect of temperature contributes towards solar modules operating at lower efficiencies. In a study by E. Radziemska [49] it was found that when a crystalline silicon cell's temperature is increased by 1 degree above 25℃, the module's conversion efficiency reduces in steps of 0.08%. Moreover, the output power is reduced by up to 0.65%. Furthermore, the fill factor also decreases at a rate of 0.2%/K. The fill factor is the ratio of the maximum power produced by the solar cells to the product of the open circuit voltage and short circuit current.

The dependence of the efficiency on temperature is given by equation (2) [50]. Here n_c and n_{Tref} are the solar cell conversion efficiencies at a particular cell temperature and at reference temperature, respectively. β_0 is the PV module temperature coefficient (example: 0.48%/K) and $T_c - T_{ref}$ shows the temperature difference between the cell temperature and the reference temperature [50].

$$n_c = n_{Tref}\left[1 - \beta_0\left(T_c - T_{ref}\right)\right] \quad (2)$$

An increase in temperature causes an increase in electron energy in the valence band. This further results in a decrease in the material's band gap since the energy gap between the conduction band and the valence band is narrowed. Furthermore, this leads to higher intrinsic carrier concentrations, which results in an increase in the dark saturation current of the p-n junction [50]. A higher intrinsic carrier concentration also results in a slight increase in the short circuit current. The relation between the bandgap energy and temperature is given by equation (3) [19].

$$\frac{E_g}{E_{g,ref}} = 1 - C\left(T_c - T_{c,ref}\right) \quad (3)$$

Here E_g is the bandgap energy of the material and $E_{g,ref}$ is the reference bandgap energy of the material, which is equal to 1.12eV for silicon. C is a ratio describing the dependence of a material's bandgap energy on temperature. For silicon, C is equal to 0.0002677. $T_{c,ref}$ is the reference temperature at standard test conditions, and Tc is the actual material temperature [19]. Also, the increase in dark saturation current decreases the open circuit voltage, as evidenced by equation (4) [51].

$$V_{OC} = \frac{E_g}{q} - \frac{nKT}{q}\left(ln\frac{I_{o\,max}}{I_{sc}}\right) \quad (4)$$

Here q is the electron charge, $I_{o\,max}$ is the maximum dark saturation current, K is the Boltzmann constant, and n is the diode ideality factor. Silicon at 300K exhibits a linear decrease of -2.3 mV/°C in open circuit voltage due to the increase in dark saturation current [47].

A study by Wen Cai et al. [51] showed that the temperature effect on the short circuit current of a solar cell differs for single crystalline and polycrystalline silicon. In single crystalline silicon, the short circuit current decreases with temperature due to an increase in thermal lattice vibrations, which hinders carrier mobility. Polycrystalline silicon solar cells exhibit a slight increase in short circuit current with an increase in temperature. This effect arises partly from the decreasing band gap, which results in additional lower energy photons being absorbed and converted to charge carriers. However, this effect can also be observed in single crystalline silicon and in both cases, it plays a minor role. The major temperature effect in polycrystalline silicon is contributed to the ratio of recombination area decreasing at a fast rate with increasing

temperature. Therefore, this leads to increased carrier mobility which translates to an increase in the short circuit current [51]. Although the short circuit current in polycrystalline silicon solar cells can increase by 0.1% per °C, the reduction in open-circuit voltage contributes to a net decrease in the maximum power that the PV cell can deliver [47].

In hot regions, PV modules can reach temperatures of up to 80°C, while in tropical environments, the temperature can rise beyond the operating range of the modules [1]. This not only results in a significant efficiency loss but also accelerates the module's degradation. Furthermore, Boussaid et al. [52] conducted a study showing that degradation due to temperature is of a higher magnitude in photovoltaic modules in open-circuit conditions. This effect is because, in open circuit conditions, charges only have the possibility of recombination through Shockley-Read-Hall (SRH) and Auger, both of which result in an increase in temperature in the cell material. This increase in temperature results in non-elastic expansion and contraction cycles of the crystal lattice, which in the long run, result in permanent cell degradation [52]. Therefore, cooling is one of the key solutions to consider when optimising a PV system design. Cooling not only improves the efficiency of the panel but also prolongs its life by dissipating excessive heat.

2.3.1 Temperature models.

Various mathematical models have been created to predict the PV cell or module temperatures. Tuza et al. [53] analysed and compared the Ross thermal model, the model used by Homer software and the model used by PVSYST software. The Ross thermal model is given by equation (5) and is only valid for free-standing solar modules. The temperature model used by Homer software is given by equation (6). It takes into account the Nominal Operating Cell Temperature ($T_{c,NOCT}$), the ambient temperature ($T_{a,NOCT}$), and Irradiance at nominal conditions ($G_{T,NOCT}$). Furthermore, this model also considers cell temperature at Standard Testing Conditions (STC) ($T_{c,STC}$). Equation (*7*) shows the temperature model used in PVSYST software. This model incorporates a constant heat transfer component (U_0), a convective heat transfer component (U_1) and is also dependent on wind speed (WS). Also, PVSYST recommends against using NOCT for predicting module temperature since this value does not contain any dependency on installation conditions. In Tuza's study, absorption coefficients were kept at 0.9 for all models and the conversion efficiency was set to 12%. Compared to an experimental setup, the Homer model performed best out of the three, followed by the Ross model and the PVSYST model having the largest percentage error. Equation (8) shows the

Sandia Laboratories PV module temperature (T_m) model where 'a' and 'b' are empirically-determined coefficients [54]. Furthermore, Sandia Laboratories use equation (9) to convert module temperature to cell temperature, where G_0 is a reference solar irradiance (1000W/m^2).

$$T_C = T_a + \frac{(T_{NOCT} - 20)}{800} + G_T \tag{5}$$

$$T_C = \frac{T_a + (T_{c,NOCT} - T_{a,NOCT})\left(\frac{G_T}{G_{T,NOCT}}\right)\left[1 - \frac{n_{mp,STC}(1 - \alpha_p T_{c,STC})}{\tau\alpha}\right]}{1 + (T_{c,NOCT} - T_{a,NOCT})\left(\frac{G_T}{G_{T,NOCT}}\right)\left(\frac{\alpha_p n_{mp,STC}}{\tau\alpha}\right)} \tag{6}$$

$$T_C = T_a + \frac{\alpha G_T(1 - n)}{U_0 + U_1 + WS} \tag{7}$$

$$T_m = G_T(e^{a+b.WS}) + T_a \tag{8}$$

$$T_c = T_m + \frac{G_T}{G_0}.\Delta T \tag{9}$$

The temperature increase of PV modules during the day has been modelled extensively in literature and the negative effects on the PV's efficiency were shown in many studies. This motivates the need for research on efficient cooling technologies for PV modules in order to regulate operating temperatures and optimise energy conversion efficiencies.

2.4 Cooling technologies:

Ongoing research resulted in various cooling technologies being implemented to cool photovoltaic modules. The heat from PV modules can be extracted either actively, for example, using water-cooling, forced air cooling, thermoelectric cooling and heat pipes, or passively using Phase Change Materials (PCMs), heat sinks and natural air cooling [47]. Figure 6 shows a range of thermal resistances for different cooling technologies [55][56]. The adequate cooling technology depends on the system's operating conditions, and capital and maintenance costs must be kept to a minimum to make such a system financially viable.

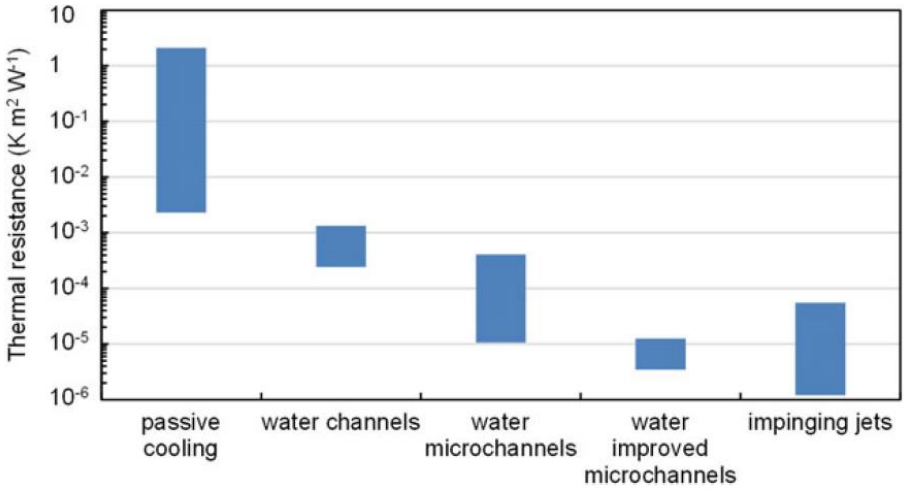

Figure 6: Range of thermal resistances for different cooling technologies [55].

2.4.1 Air cooling:

Air cooling is a cost-effective method to cool PV panels. However, the low density, thermal conductivity and volumetric heat capacity of air result in poor thermal performance making passive air cooling insufficient. Passive air cooling can be applied in double-skin façades or roofs, as shown in Figure 7 [55]. A double-skin façade/roof consists of PV modules as the outer skin and a building's façade/roof as the inner skin. The gap between the two layers allows air to flow passively (or actively if required), thus, cooling the PV modules in Summer and aiding in the building's central heating in winter [55].

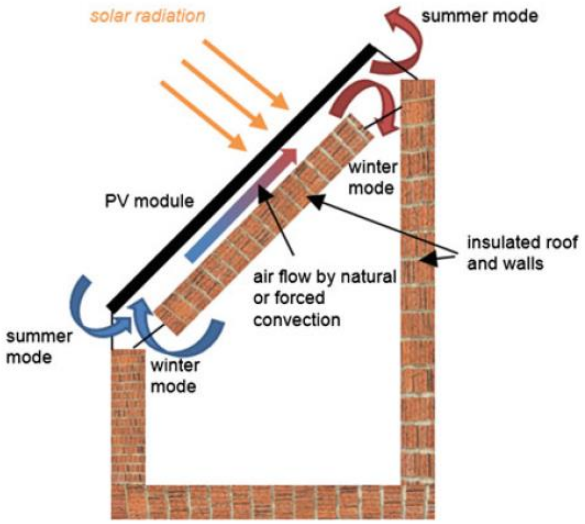

Figure 7: Illustration of a double-skin roof [55].

Forced (active) air cooling shows an improvement in thermal performance when compared to natural (passive) air cooling [47]. Teo et al. [57] designed an active PV air cooling system which increased solar cell operating efficiency by 3% to 6%. Three different heat exchangers

were studied with forced air circulation. This study showed that a honeycomb heat exchanger resulted in the best thermal performance due to higher surface area touching the back of the PV module and an even airflow due to the honeycomb structure. Natale Arcui et al. [58] concluded that a quasi-flat temperature profile between cooling air ducts could be achieved by using a metal sheet between the back of a PV module and air ducts. Furthermore, this back sheet reduces the number of cooling air ducts required. A study investigated and compared the effect of natural convection and active air cooling [59]. This study reported that the active cooling system performed much better than natural convection, with an increase in electrical power by up to 15% and a maximum decrease in PV panel temperature of 15°C.

In Kermanshah City, Iran, a panel was installed on top of a turbine roof ventilation system to use the ventilation system to cool the PV panel simultaneously [60]. It was reported that when the turbine was driven at maximum velocity, the PV-generated power increased by 29%. Another setup utilised 5W Direct Current (DC) fans, commonly found in cooling electronics like computers, installed at the back of a PV panel to extract heat from its back-side [61]. One module with four DC fans installed at the back experienced a temperature reduction of 22% when compared to a module with no cooling. It was also noted that modules with two and three fans had different back-side temperature distributions but only differed by 2% to 3% in terms of temperature values when compared to the module with four fans. Another study [62] compared different designs of a photovoltaic thermal (PVT) system using air as the cooling fluid. This study compared six different designs and concluded that a uniform temperature distribution was a critical factor in increasing the electrical and thermal efficiencies of the system. Figure 8 [62] shows a Computational Fluid Dynamics (CFD) analysis carried out in this study, indicating the variation in temperature distribution for different designs of the air PVT. Out of all the designs, the design labelled PVT-5 achieved the best overall average efficiency of 58.48% [62].

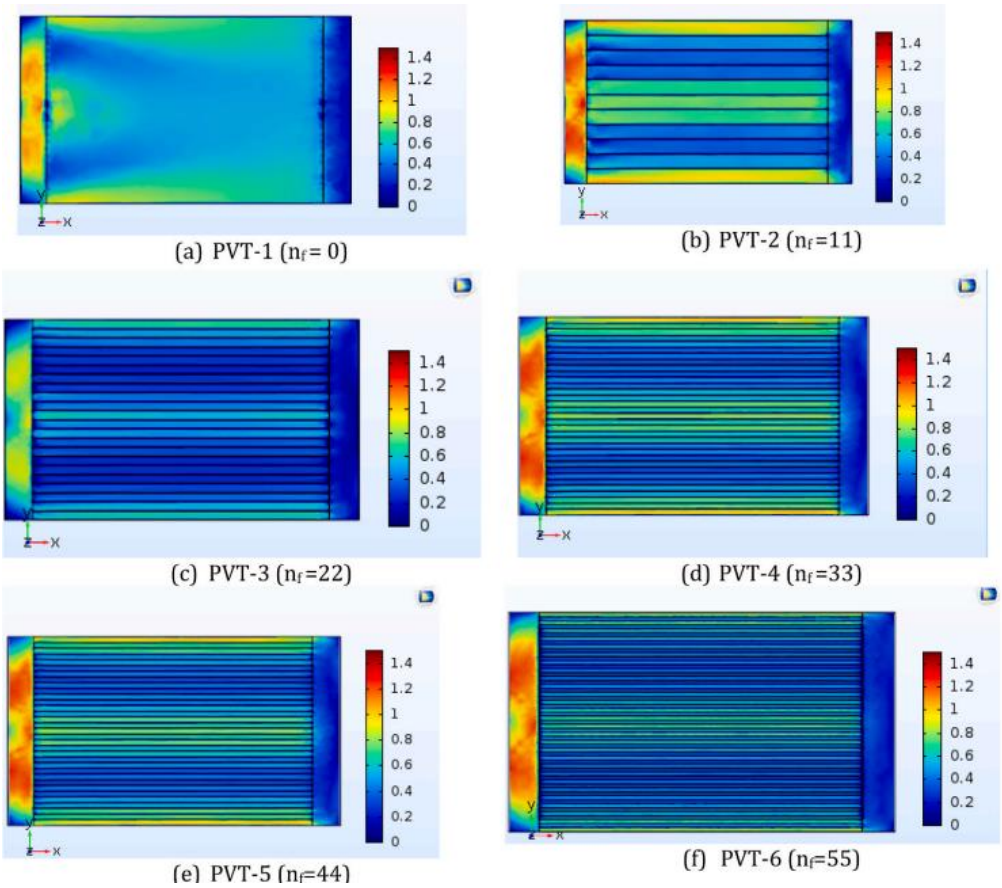

Figure 8: CFD analysis showing temperature distribution of different PVT designs [62].

2.4.2 Phase Change Material (PCM) cooling:

Phase Change Materials (PCMs) can change phase, for example, from solid to liquid, at specific temperatures. The distinguishing factor of phase change materials is their high latent heat effect resulting in heat absorption when the phase change occurs. PCMs are used for temperature control of electronics and are also being integrated with photovoltaics for passive heat storage, having the dual purpose of also passively cooling the PVs. A well-designed PV/PCM system enables the PVs to operate in near optimum temperatures while heating buildings at night by releasing the thermal energy stored in the PCM [63]. For a material to be adequate for use as a PCM, it must have a high thermal conductivity and a large latent heat [64].

Applications of PCM for solar energy can be classified into two main categories:

- Indirect contact latent heat storage and
- Thermal storage with direct contact heat exchangers.

For the indirect contact application, the PCM is encapsulated in a container, and a fluid is passed around this container, transferring heat without direct contact with the PCM itself. The

latter category involves direct contact between the heat source and the PCM. This application method eliminates the need for an expensive heat transfer surface which is usually the feasibility drawback for such systems [64].

In a study by Stropnik and Stritih [65], a PV module was modified with a phase change material RT28HC as shown in Figure 9 [65]. Results showed that at a certain point, there was a difference of 35.6°C surface temperature between modules with and without PCM. Furthermore, simulation results showed that, for a PV module installed in Ljubljana, the introduction of PCM led to an increase of 7.3% in yearly electricity production.

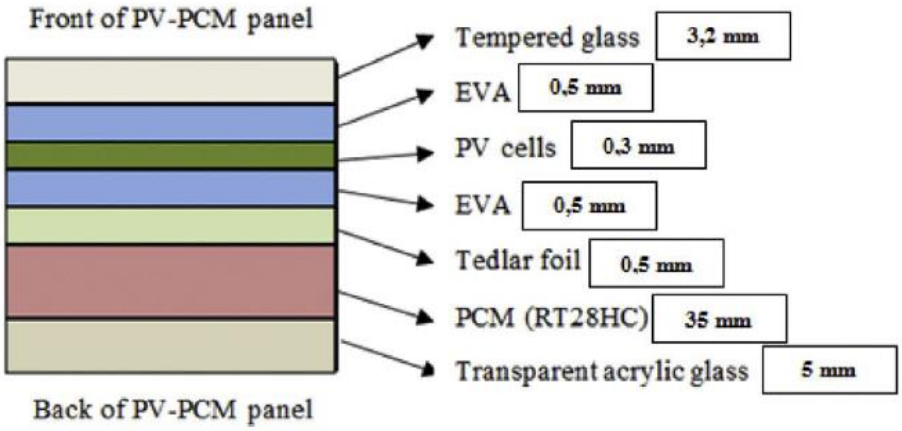

Figure 9: Schematic of PV/PCM module after modification [65].

The increase in annual energy output with the introduction of PCM with solar modules was investigated [66]. This study also identified the optimal PCM melting temperatures for different locations globally. It was found that PCM is viable mainly in places with very high insolation with little variability. Using PCM would thus increase the annual PV energy output by more than 6% in Mexico and eastern Africa, 2-5% in Europe and over 5% in most other locations [66]. In another study in Selangor, Malaysia a paraffin-PCM was mixed with Nano-SiC particles and nanofluid to increase the PV efficiency by increasing thermal conductivity. In these experiments the electrical efficiency was increased from 7.1% to 13.7% while a maximum thermal efficiency of 72% was achieved [67].

2.4.3 Heat sink and thermoelectric cooling:

Photovoltaic cooling technologies include the installation of heatsinks and thermoelectric modules (TEM) at the back of PV panels, similar to techniques used to cool electronics. A system combines PV panels, heatsinks and TEMs with the testing principle shown in Figure 10 [68][48]. This system uses thermoelectric modules to dissipate heat from the PV modules.

Furthermore, heatsinks are used to dissipate heat from the thermoelectric modules. This creates a temperature difference across the TEM, which results in the diffusion of charge carriers within the TEM materials. This results in the TEM producing power in addition to the increased PV module efficiency. This setup reported a maximum decrease in PV temperature of 8.29°C.

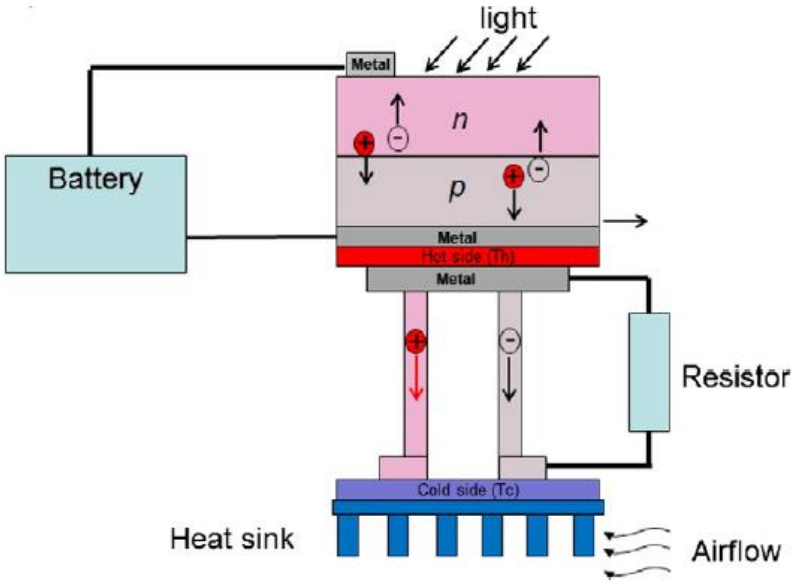

Figure 10: Testing principle of hybrid PV/TEM with integrated Heat Sink [68].

A hybrid PV/TEM system was tested at the Madinah site, where cell temperatures reached values of 83°C [69]. The tested system kept the PV temperature at 18°C lower than the PV panel without cooling. Furthermore, it was noted that adding TEM modules increased the capital cost of the PV panels by 6%. A. Kane et al. built a mathematical model in MATLAB to simulate heat sinking from a PV panel using TEM tiles [70]. The model shows a maximum increase in PV electrical efficiency of 18% and a maximum PV panel temperature reduction of 26%. It was also suggested that such hybrid PV/TEM systems would be more feasible if installed in locations with very hot climatic conditions. Another study investigated different cooling methodologies, including heatsinks and combined PCM with heatsinks [71]. While the heat sink method recorded a temperature difference of 3.6°C, it was noted that the setup combining PCM with heatsinks performed better, with a temperature difference of 13°C compared to a non-cooled PV panel. A combined PV/TEM setup was suggested to be integrated into buildings [72]. This setup involved a water channel underneath solar cells with a TEM attached to the back of this channel. This system produced a temperature difference of 16.2°C between the house's inside and ambient temperatures, making it capable of aiding in the house cooling system.

2.4.4 Water-cooling:

When adopting a forced convection PV cooling system, one must strike a balance between increased PV efficiency due to lower temperatures and power consumed by the pump, fan or any other device used to force convection. A study [73] presents steady state and transient models to optimise the pump switching frequency. This study adopted an electro-thermal analogy to construct the transient model. This analogy uses current and tension to represent temperature and heat flow. Furthermore, thermal elements are characterised by resistance and capacitance. Another study [74] determined that the ideal temperature to start cooling PVs is 45°C, and cooling should continue until the PV reaches a temperature of 35°C. These temperatures were determined to get the optimal balance between PV energy production and energy usage by the cooling system. The net energy output from a PV module equipped with a cooling system against the maximum allowable temperature is shown in Figure 11 [74].

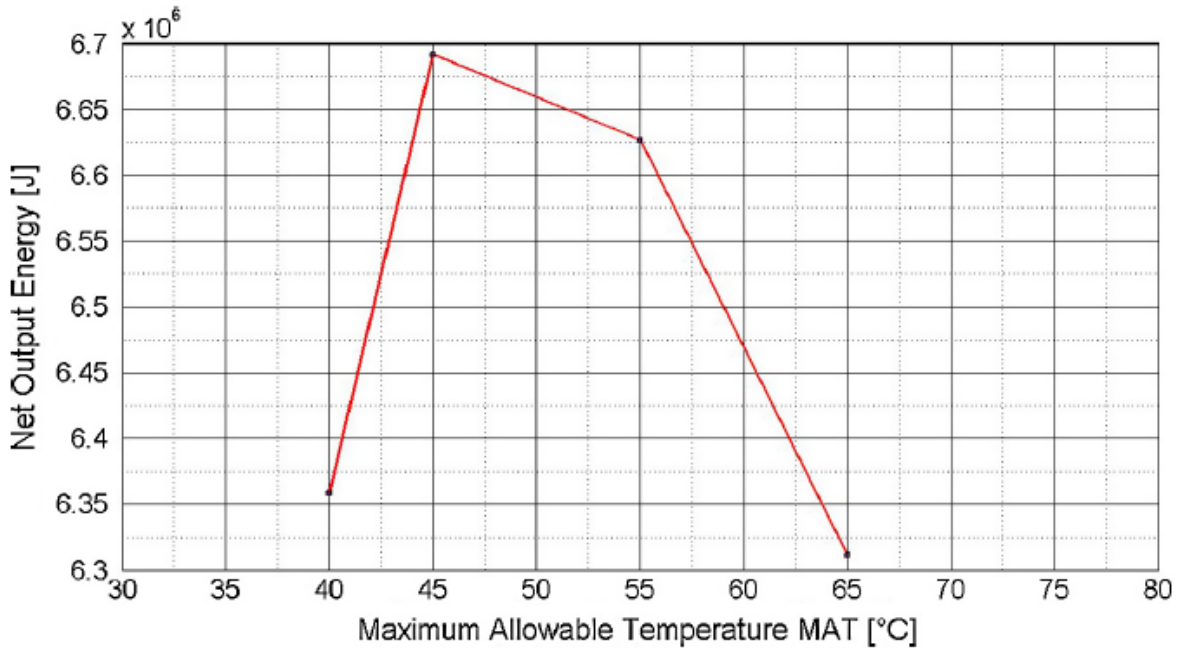

Figure 11: PV net output energy against maximum allowable temperature [74].

2.4.4.1 Front-Side Water-cooling

A water film on the front side of a PV module is sometimes used to create the desired cooling effect. Furthermore, the water film helps maintain a clean surface while also creating an anti-reflective coating, thus contributing further to the increase of solar cells' operating efficiency. However, when such cooling systems are employed, one must consider power consumption by the pump and water consumption due to evaporative losses [55].

S. Nižetić et al. presented a study [75] on cooling PVs using front and back water spraying in a Mediterranean climate. PV temperature was reduced from 52 °C to 24°C, with the lower temperature being limited by the temperature of the water. When considering electricity usage to pump water, a maximum of 7.7% effective increase in power output and 5.9% effective increase in efficiency were achieved. An essential improvement to this setup is eliminating the shading caused by the water sprinklers, as shown in Figure 12 [75]. Shading a PV module with a cooling setup may result in a power loss equal to or greater than the power gained by cooling. Furthermore, shading may cause mismatch issues on larger PV plants. Another study [76] examined the performance of a PV water pumping system with the PV module cooled by front water spraying. A maximum temperature reduction of 23°C was achieved due to water spray and evaporative cooling. This cooling methodology increased the mean PV cell efficiency by 3.26%, and an increase in the measured short circuit current implied an improved optical performance due to the water spray on the front surface. In this system, water was sprayed on the PV panels at a rate of 50 L/h, which resulted in the pumping system pumping an extra 165 L/h at a head of 16m due to the increased PV power output.

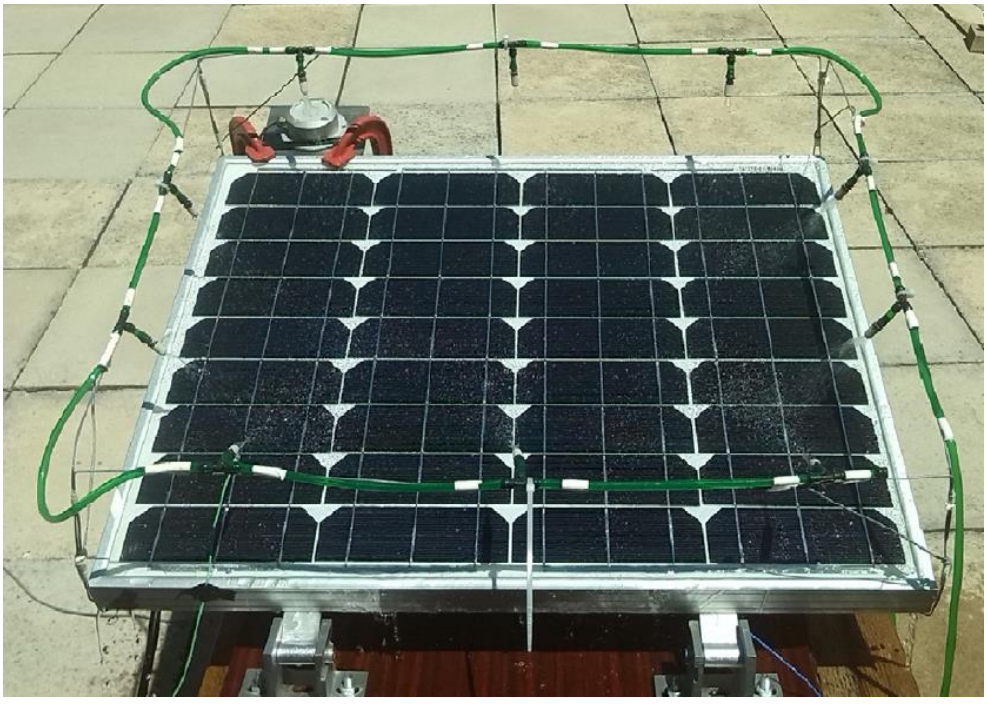

Figure 12: Front water sprinklers setup causing shading on the PV [75].

A continuous flow of water on the front of PV modules was also tested, achieving a net increase in daily energy yield of 5% in May while decreasing PV temperature from 55°C to below 40°C [77]. This setup was also tested in July with back insulation to simulate PV modules installed directly on roofs without ventilation. A net increase of 8.3% in daily energy yield was observed

with this configuration. Furthermore, this setup helps to keep the panels clean, thus, decreasing inefficiencies due to dust build-up and soiling. A laboratory-based experiment also investigated intermittent PV cooling by front water flow rates of 3 litres per minute (L/min), 5.3 L/min and 6.2 L/min and continuous flow of 0.6 L/min. For the intermittent cooling, water flow was initiated when the PV surface reached 40°C and stopped at 32°C, allowing the PV to go down to 29°C. Intermittent cooling achieved a 17.32% increase in average power, while continuous cooling achieved a 31.28% increase compared to a PV panel with no cooling installed [78]. Krauter [79] uses water flow on the front surface of a PV module. Apart from having a cooling effect on the PV module, the water (with a refractive index of 1.3) acts as an optical intermediary between air (η_{air}=1.0) and glass (η_{glass}=1.5), thus reducing reflection by 2 - 3.6%. Furthermore, the cooling effect of the water film decreases the cell temperatures by up to 22°C while achieving a net electrical yield of 8-9%, after considering pump energy consumption. The water film was created using twelve nozzles squirting water at a rate of 2 L/min. Another setup was constructed by the same author, which consisted of a PV module installed on a large water reservoir. However, this setup proved too heavy to be installed practically on a household rooftop.

A study [80] implemented a front-side pulsed water-cooling system that achieved a maximum increase in electrical efficiency of 2.4%. This system was, however, utilising an existing water flow, and therefore, no extra pump power was considered. Another possible disadvantage of cooling on the front side is that water can stain the front glass with limescale [81] or result in salt build-up (if using seawater). Limescale build-up occurs due to the formation of calcium and magnesium carbonates. Besides being difficult to clean, this deposit can also block some of the transmission of solar radiation to the solar cells, decreasing the efficiency of the photovoltaic module. Farrugia et al. [81] quantified the loss due to limescale build-up, which amounted to an average decrease of 2.38% in daily energy yield. Another setup implemented a front water-cooling system to keep a CPV module at low temperatures, despite the high light intensity level [77]. A peak-power output increase of 43% was observed with this setup. However, this setup leads to a high evaporation rate. Therefore, cooling water must be replenished frequently, and this could be challenging in locations where rainfall is scarce.

2.4.4.2 Back-side water-cooling

Various studies investigated the use of heat exchangers installed at the back of the PV module to create what is referred to as a photovoltaic thermal (PVT) systems. A PVT collector consists of a PV module with fluid flowing through structures underneath the PV to absorb heat from

this module [82]. The driving factor for research in PVTs is that approximately 78% of the incident solar radiation on a PV module is transformed to heat energy and not electrical energy [55]. The combined photovoltaic thermal system is usually integrated into buildings to contribute to the building's water heating system. Furthermore, this results in a cooling effect on the PV module since excess heat is used in water heating. There are two main types of PVT configurations, namely open-loop and closed-loop, as shown in Figure 13 [83]. In an open-loop configuration, the fluid is passed once underneath the PV at a set flow rate, and the heat absorbed by the fluid is utilised instantly. An application of an open-loop PVT system is in residential direct space heating, as shown in Figure 14 [83]. On the other hand, a closed-loop PVT system incorporates a circulating pump, which passes the fluid several times underneath the PV module to increase the amount of heat absorbed by the fluid [83]. A typical application of a closed-loop PVT system is in residential water heating. When looking at improving PV output efficiency, open-loop PVT systems are preferred since a closed-loop system favours water heating which would lead to the PV module reaching very high temperatures. This leads to a decrease in PV efficiency and possible delamination. A closed-loop PVT solar collector in thermosiphon mode is studied in [84], achieving an electrical power enhancement of 1.56% and a thermal efficiency of 10.73%. The negligible electrical power enhancement shows that a closed-loop system does not favour PV temperature and PV electrical efficiency.

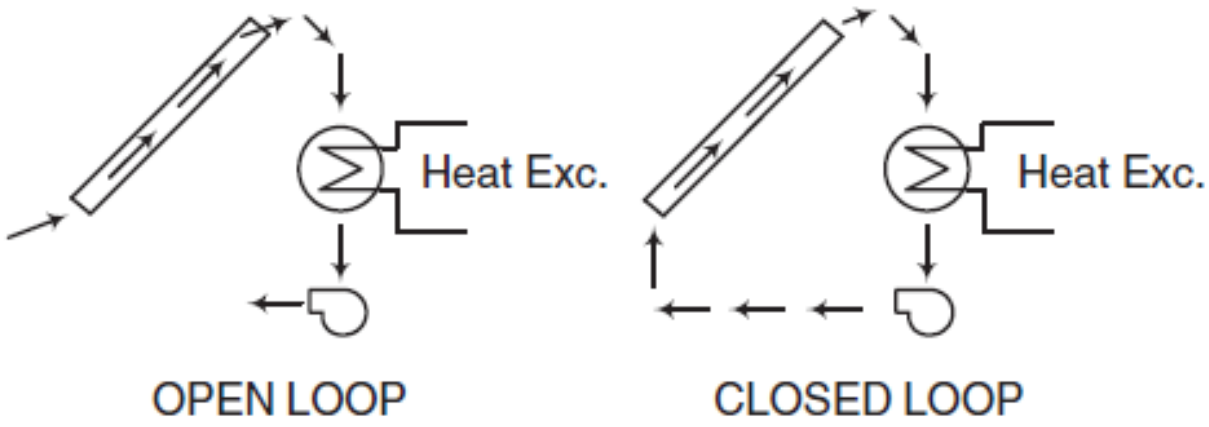

Figure 13: Comparison of an open-loop and a closed-loop PV/T system [83].

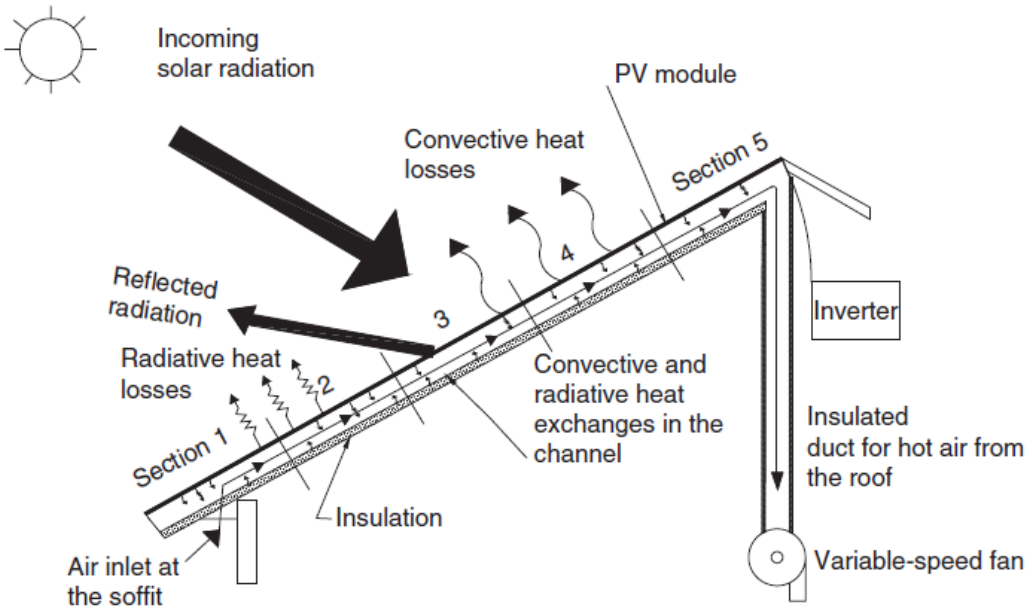

Figure 14: An application of an open-loop PV/T system [83].

Cooling channels installed at the back of PV modules can be of various materials. However, although plastic materials are easy to use, they have poor thermal conductivity, resulting in a low heat loss coefficient. Hence, metal ducts are preferred, and, in a particular study, these yielded a heat transfer coefficient of 45.09 W/m^2 [58]. In addition to metallic ducts, this study installed a metal sheet on the back-side of the PV panel to cool the back of the PV module uniformly.

Zondag et al. [85] compare four groups of combined PVT system collectors:

- Sheet and tube,
- Single channel on top,
- Free flow and
- Two-absorber collectors.

The two-absorber PVT collector yielded the highest thermal efficiency of 65-66%, while the sheet and tube PVT collector yielded the highest electrical efficiency. A feasibility study by Rebollo et al. [86] gives PV module temperature and efficiency priority over hot water generation. In this study, rectangular aluminium channels were installed at the back of the PV module, as shown in Figure 15 [86]. A 2% increase in electrical efficiency was obtained with this cheap setup. However, the author argues that the most significant limiting factor for heat transfer was the poor contact between the aluminium channels and the PV module. Another study [87] utilised a Solar Nor collector made from Poly(p-phenylene oxide) (PPO) plastic

channels filled with ceramic granulates to cool a combination of solar cells pasted on an absorber plate. A high heat transfer resistance was identified as one of the key factors contributing to reduced thermal efficiency compared to a conventional thermal absorber. H. Bahaidarah et al. [46] constructed a numerical model and verified it experimentally by installing a solar-thermal collector at the back of the PV module. This active cooling experiment achieved a 20% temperature drop and a 9% increase in PV panel efficiency.

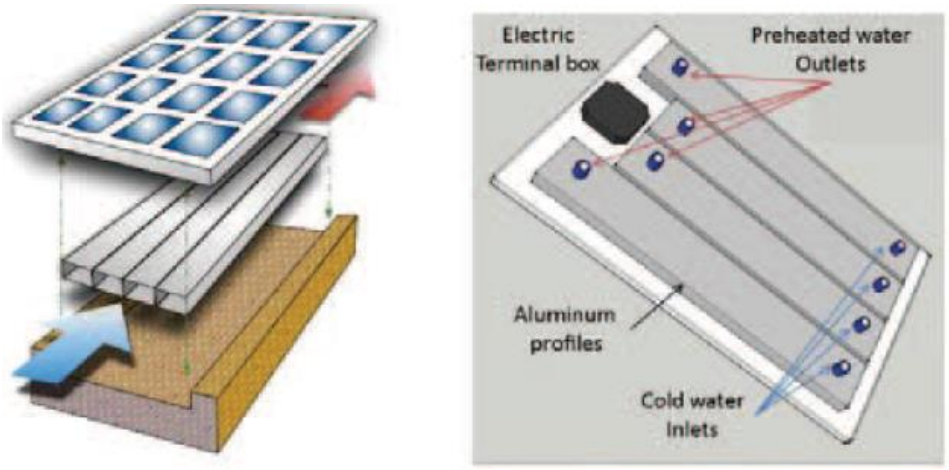

Figure 15: Cost-effective PV/Tw using rectangular aluminium channels [86].

Another cooling experiment [88] involved placing ice at the back of a PV module, resulting in a 47% increase in efficiency. However, since this setup was only experimental and impractical, another cooling system involving cooling channels installed at the back of PV modules was proposed. Such a system is reported to increase the power output of PV modules by 34.6%. Furthermore, when the cooling water was utilised for residential hot water requirements, the energy savings in water heating resulted in a total energy output increase of 107%. Also, this system was calculated to have a payback period of 12.1 years.

In another study [77], ice was also used to keep cool a continuous flow of water on the front of a PV module. This setup observed a maximum instantaneous power improvement of 24%. Another system [89] combines a back-side water spraying cooling system with a solar water heater. The cooling system alone increased the electrical efficiency by 1.4%. However, when acting as a pre-heater to a solar water heater, the overall system efficiency was 61.7%. Shalaby et al. published a cooling system involving a water flow through a configuration of Polyvinyl Chloride (PVC) pipes installed at the back of the PV module. This system achieved a maximum increase in power output of 5 to 13% [90]. However, this study did not factor in pumping power and water consumption. Furthermore, most of the above cooling systems do not address the

fact that when the water-cooling flow is stopped, the PV temperature in hot climates will increase again quickly. This will lead to a high pump switching frequency and increased power consumption, making it difficult for the cooling system to become financially viable while decreasing the lifetime of the water pump.

CPV modules can also be equipped with back-side water-cooling technology, as shown by Bin Du et al. [91]. In this research, a water mass flow rate of 0.05 kilograms per second (kg/s) increased the PV electrical efficiency from 7.35% to 8.25%.

2.4.5 Floating photovoltaics cooling technologies

When it comes to floating photovoltaic installations, cooling is an aspect to consider since the water supply is virtually unlimited and will thus add little or no extra cost to such a system. A system called “Floating Tracking Concentrated Cooling” implemented water sprinklers on top of the installed PV modules to attain the desired cooling effect [40][48]. Tina et al. [92] studied the performance of a fully submerged PV module at 4cm depth and concluded that the efficiency increase due to the cooling effect outweighs the loss due to the absorption of light by the water. The setups, shown in Figure 16 [93], were simulated at depths up to 50cm, and, at this depth, a reduction in efficiency of 20% for crystalline modules and 10% for thin-film modules were observed. However, it was also noted that in shallow waters, an increase in efficiency of 10-20% is possible. Another observation from this study was that, for the Catania experiment, glass shielding had a strong effect when the water depth was below 6cm [93] [94]. This effect was contributed to the incident light's reflection, refraction and absorption by the glass used to construct the experimental setup.

Another study analysed the performance of a PV module completely submerged in distilled water at different depths [95]. The PV module efficiency increased up to a depth of 6cm, after which it started decreasing again. A maximum efficiency gain of 11% was recorded at a depth of 6cm. The Mining Innovation Rehabilitation and Applied Research Corporation (MIRARCO) floating PV project consisted of floating thin film panels, utilising the cooling effect due to direct contact with the water underneath [38]. MIRARCO claim an increase in efficiency of 1% due to this cooling effect [96]. Ocean Sun’s floating PV design consists of a thin membrane stretched on a circular structure to create buoyancy, and PV panels installed directly on top. The company claims that this design can achieve up to a 10% increase in energy yield due to the cooling effect of the water underneath the floating membrane [97]. A floating PV installation in Aichi, Japan, was compared to a ground system. A maximum temperature

difference of 25 °C was recorded in August, attributed to the cooling effect of water underneath the floating panels [37].

Figure 16: Submerged PV setups in Pisa (left) and Catania (Right) [93].

In another study, the frame of an 80W PV module was replaced with buoyant material, and a heat sink was attached at the back to examine the performance of a floating PV module [98]. A power gain of 5.93% was observed at an irradiance of 1100W/m^2. PV module floats were also studied in Maltese waters as part of the Solaqua project, as shown in Figure 17 [10]. An average electrical output increase of 11% was observed, mainly attributed to the cooling effect of the seawater underneath [10]. In contrast, S. Oliveira-Pinto and J. Stokkermans [99] carried out an energy yield analysis using PVsyst and reported that although floating PVs perform better than land installations, the improvement in energy production ranges from 0.31% to 2.59%. However, this study also states that such energy improvements are highly dependent on the floating solar technology and the location of the installation.

Figure 17: Offshore PV module float in Maltese seawater [10].

2.4.6 Other methods to mitigate the effect of temperature

A solar cell receives photons at different energy levels. It is understood that sub-bandgap energy photons do not contribute to the photoconversion of single-junction solar cells. Thus, if the solar cells were designed in such a way as to reflect sub-bandgap photons, this would result in lower operating temperatures and, therefore, higher conversion efficiencies [55].

A possible solution would be to coat the solar cells with coatings that are transparent to photons with specific bandgap energies and reflective to sub-bandgap energy photons [55]. This technique was used for space applications by applying a coating on Gallium Arsenide (GaAs) solar cells. [100]. Similar solutions included a Spectrally Selective Reflector (SSR) added to a mirror, concentrating light on a c-Si cell. This reflector enables the mirror to only reflect photons with energies above the bandgap of the solar cell [101][55].

Other methods to reduce operating temperatures include slightly shifting the PV module's azimuth towards the east. The eastward shift can be effective because ambient temperature usually lags behind solar irradiance. This method allows the module to output peak power earlier during the day, when the ambient temperature is still lower [102]. Another method reported in the literature involves encapsulating PV cells in a vacuum to utilise the principles of Gay-Lussac's law. This method claims to decrease the PV operating surface temperature by 15°C [103].

Water-cooling is the most viable cooling technology for offshore photovoltaic installations due to the unlimited water resource. However, one faces various challenges when using water-cooling at sea, mainly due to salt deposition on panels and the corrosive effect of seawater. The impact of salt deposition can be avoided by applying water-cooling to the back-side of the PV installation. Furthermore, the corrosion effect can be reduced by applying protective coatings

or introducing sacrificial materials similar to the anodes included in standard water heaters. The state-of-the-art search shows a research gap in a feasible cooling system that does not impact incident solar radiation and does not require a high pump switching frequency, resulting in an efficient cooling flow.

2.5 Potential Induced Degradation (PID)

Potential Induced Degradation (PID) is a type of electrochemical degradation occurring in crystalline silicon and thin film photovoltaic modules. PID can sometimes be mitigated or even reversed. However, in some instances, it can also result in irreversible damage to the photovoltaic module.

PID occurs when high PV system potentials and leakage currents drive ion mobility between materials making up the modules, such as the glass and frame, and the semiconductor material [104]. In 1984, Jet Propulsion Laboratory [105] studied the occurrence of electrochemical corrosion, a type of PID. This degradation mechanism occurs due to a voltage potential between two cells or between solar cells and a grounded frame. This may cause the metallisation material to dissolve in the encapsulant surrounding the solar cells until the latter becomes insufficiently resistive to act as an insulator. A schematic of electrochemical corrosion can be seen in Figure 18 [105].

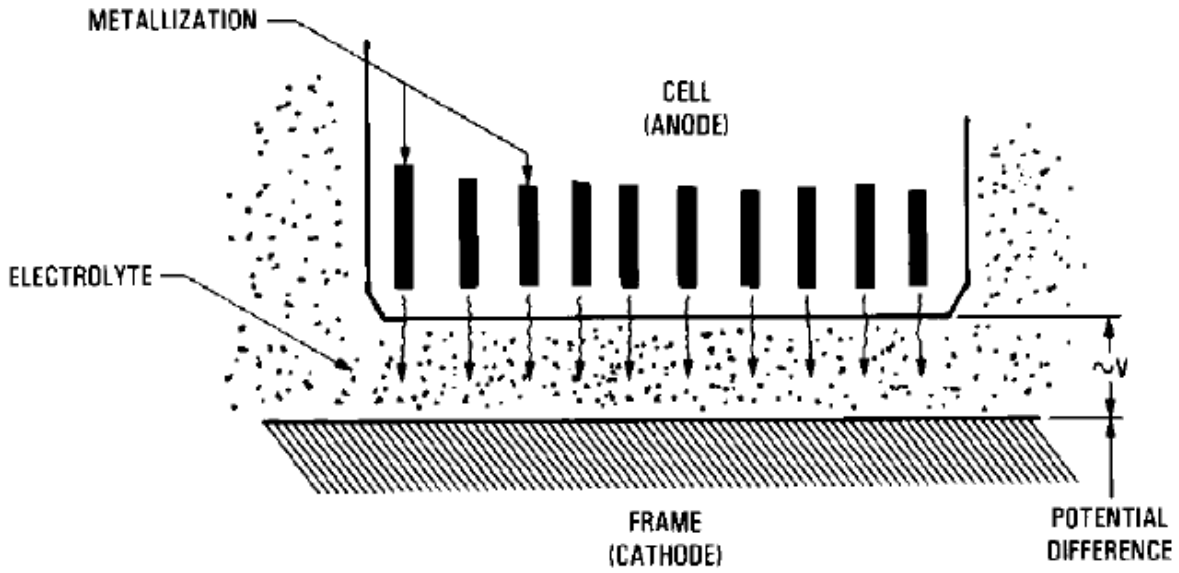

Figure 18: Schematic of electrochemical corrosion mechanism [105].

PID increases with environmental conditions, namely humidity and temperature. As discussed previously, module temperature can be controlled by applying cooling methods. In contrast,

humidity cannot be controlled, especially in offshore conditions. Water penetrating the PV module will lead to higher leakage currents due to increased conductivity between the solar cells' encapsulation, module glass, and frame [106]. Furthermore, the quality of the solar cell's base material also significantly affects the tendency of a solar cell to develop PID. Another factor affecting the PID rate in PV modules is the grounding topology adopted for both the PV installation and the inverter. The four basic classifications of grounding topologies are shown in Figure 19 [104], showing the variation of PV array voltage with grounding topology. PID is mainly associated with PV arrays with a negative voltage potential with reference to the ground [104].

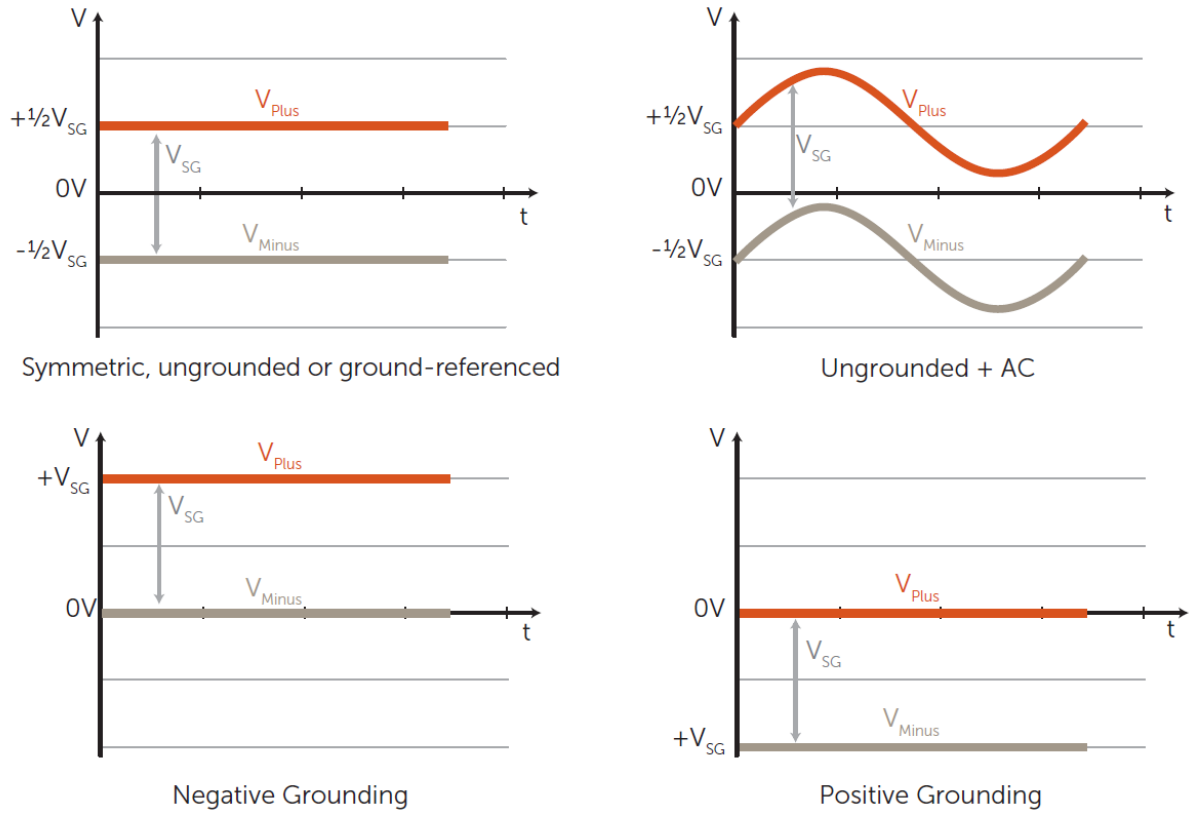

Figure 19: Four basic classifications of grounding topologies [104].

There are four main types of PID, namely the "corrosion of the transparent conductive oxide (TCO) layers in thin film modules", the dissolution of anti-reflective coatings (ARCs), the degradation of the metallisation in crystalline silicon modules and PID of the shunting type (PID-s) [107]. When a PV module is affected by PID-s, its parallel resistance decreases, leading to a decrease in fill factor and, as a result, a drop in maximum power output. Higher levels of PID-s effects on PV modules result in a drop in shunt resistance which causes an internal short circuit and a drop in open circuit voltage. PID can be effectively prevented by grounding the

negative pole of the PV output to only have a positive potential [106]. However, some modern inverters eliminated the use of transformers, making grounding the negative pole unsafe due to a lack of isolation. In a laboratory, PID is detected using a combination of flash testing and high-resolution electroluminescence.

S. Pingel et al. studied the effect of PID on a standard solar module and found a 32% power loss due to PID after the panel was subjected to a 1000V negative potential for 100 hours [106]. An important factor affecting the rate of PID in photovoltaic panels is the encapsulation material, and it was found that other materials could replace standard Ethyl Vinyl Acetate (EVA) to increase resistance to PID [106]. Swanson et al. [108] from SunPower Corporation investigated surface polarisation, one of the common factors leading to PID. Surface polarisation occurs due to charges developing from module leakage currents. However, this study shows that this surface polarisation effect can be avoided and reversed. To prevent this type of degradation, p-type front surfaces need to be installed at a positive potential with respect to the ground. In contrast, n-type front surfaces should be installed at a negative potential with respect to the ground. Furthermore, this study shows a module recovering from PID with an increase in power output from 140W to 203W after a negative 1000V was applied to the module for one hour. The IV curve before and after applying the negative voltage can be seen in Figure 20 [108].

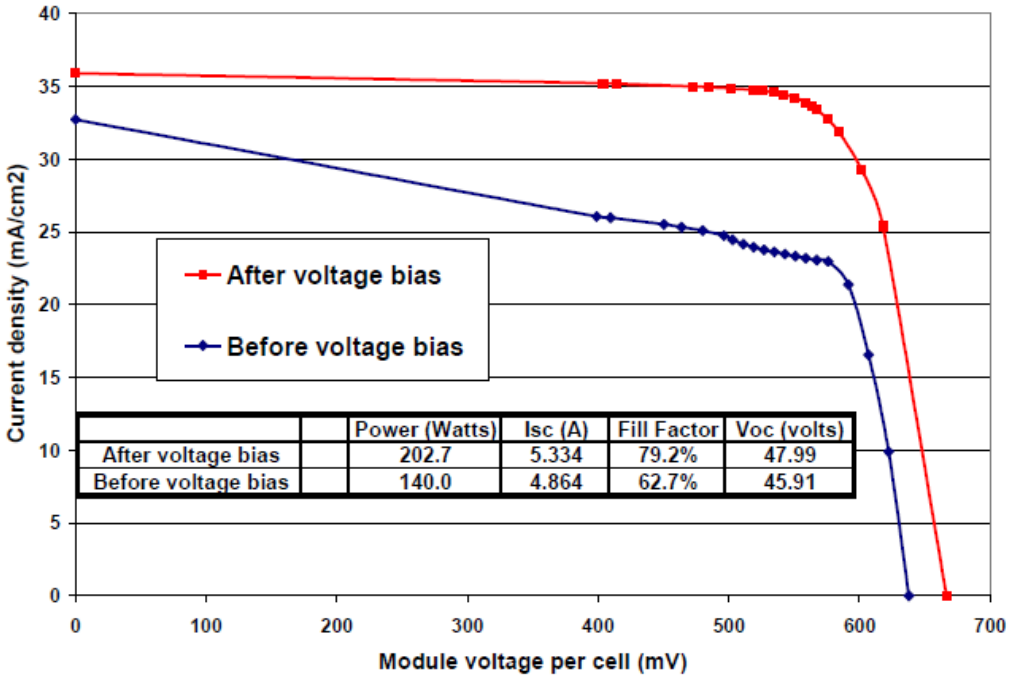

Figure 20: IV Curve of module recovering from the effect of PID [108].

Another study investigates the effects of electrochemical corrosion and electromigration on thin film modules, namely amorphous silicon (a-Si) and Cadmium Telluride (CdTe) [109]. While electrochemical corrosion is a result of a potential difference, electromigration is the diffusion of electrical conductors due to high current densities.

The high humidity environment in offshore conditions makes PID an issue to address when designing offshore photovoltaic installations. Surface polarisation can be avoided with the correct grounding techniques. Furthermore, the choice of photovoltaic modules is critical since, for example, SunPower have implemented a front surface conductive layer to shunt leakage currents and thus eliminate the polarisation effect [108].

2.6 Materials for marine environment

When designing offshore photovoltaic installations, one must consider adequate materials for the marine environment. Care must be taken when choosing materials for the PV modules, water pumps and installation fittings. These materials should have sufficient corrosion resistance and be resistant to ultraviolet (UV) radiation. Various materials have been used for offshore applications, including metals such as aluminium and stainless steel, and polymers. Although some materials are more robust, one must consider their corrosion resistance too.

There are three main polymer types [110], namely:

- thermoplastic,
- thermosetting and
- elastomers.

Thermoplastic polymers, commonly known as thermoplasts, can be re-formed into different shapes each time they are heated above a specific threshold temperature. Thermosetting polymers, widely known as thermosets, assume a fixed form after reaching their settling temperature. Elastomers are polymers that can be deformed when applying some force but retain their original shape when the force is released, provided that their elastic limit is not exceeded. Fibres are sometimes added to polymers to improve their properties, such as heat deflection and structural strength. Unlike metals, plastic materials do not usually have a corrosion rate since they would either be resistant to a specific condition such as UV or deteriorate rapidly when exposed to such conditions.

The most harmful weather component for polymers is long-term exposure to UV radiation. Therefore, care must be taken when choosing a polymeric material for photovoltaic installations since these will be constantly exposed to high levels of UV radiation. A sustainable solution would be to use recycled Polyethylene Terephthalate (PET). PET exhibits good mechanical properties and low moisture absorption. However, PET suffers from UV degradation when exposed outdoors. Hence, carbon black must be added to improve PET's UV resistance. Other polymers, such as Polyimide, are not degraded by UV while, for example, Polypropylene can be used in load-bearing applications, especially when glass fibres are added to it [110].

2.7 Conclusion

The literature review presented in this chapter shows that a solar cell's power output mostly depends on the following:

- The incident solar radiation on the solar cell,
- The solar cell's conversion efficiency,
- The temperature coefficient of the solar cell and
- The operating temperature of the solar cell.

The incident radiation is directly proportional to the power output and mainly affects the solar cells' short-circuit current. Higher solar cell operating temperatures result in a decrease in open circuit voltage. Although polycrystalline silicon solar cells exhibit a slight increase in short circuit current with increasing temperature, the reduction in open circuit voltage still results in a net decrease in power output. The extent of this effect depends on solar cell technology since different technologies result in solar cells with varying temperature coefficients.

Extensive research focused on achieving the optimal installation tilt and orientation angles to increase the incident solar radiation on photovoltaic modules. The general findings show that a surface with an inclination of 10° to 15° less than the latitude receives maximum insolation in summer, while in winter, a tilt of 10° to 15° more than the latitude is optimal. Furthermore, photovoltaic modules should be oriented towards the north or south, depending on the hemisphere in which they are installed. After reviewing the literature, it was noted that a research gap exists in evaluating the incident solar radiation on offshore photovoltaic installations. An offshore environment will result in quasi-continuous movement of the floating raft due to the response to incoming waves. These movements will result in changes in the

actual tilt and orientation of the module, and this effect was never studied in the scientific community. Therefore, part of this research will study this effect and create a tool to quantify it.

Different cooling technologies have been studied to lower the operating temperatures of photovoltaic modules. These technologies range from air-cooling, water-cooling, phase change materials (PCM), heatsinks, and thermoelectric coolers. Heatsinks result in very low gains at a high capital cost. Furthermore, phase change materials require further research to use non-toxic materials and increase economic feasibility. The low density, thermal conductivity and volumetric heat capacity of air result in air-cooling technologies having poor thermal performance. Finally, water-cooling is considered the best option, especially for offshore photovoltaic installations, due to the extensive water resource. However, applying water-cooling on the front side of a PV module can result in salt and limescale build-up. This could block some of the incident solar radiation on the solar cells and negatively affect power output more than the effect of temperature itself. The currently available technologies that cool PVs from the back usually involve sprinkler systems. These result in water wastage. While this would not be an issue for offshore photovoltaic installations, such a product would not be economically feasible on land since it would waste water, an essential and sometimes scarce resource. Furthermore, all the reviewed technologies have issues with either non-uniform solar cell temperatures or high pump switching frequencies. The latter is due to temperature rapidly increasing when water-cooling is switched off. Photovoltaic thermal (PVT) systems have been researched. However, these usually favour hot water generation, sometimes to the detriment of electrical efficiency. Therefore, there is a research gap on an adequate water-cooling technology that addresses all the above issues. The second part of this research will aim to address this gap.

Other factors affecting the performance of photovoltaic modules include degradation mechanisms such as potential induced degradation (PID). This degradation mechanism can be more prominent in an offshore environment due to the high humidity levels. Furthermore, due to the corrosive environment, care must be taken in choosing materials for an offshore photovoltaic system. However, this research will aim to analyse and optimise the negative effects on photovoltaic modules due to decreased incident solar radiation and high operating temperatures.

3. The effect of wave response motion on the insolation on fixed offshore photovoltaic installations

3.1 Introduction

As discussed in section 2.2 of this thesis, the tilt and orientation of PV modules play a key role in the energy production process. This is mainly due to the amount of irradiance on an inclined plane. Non-tracking PV systems have a fixed tilt and orientation, optimised for the location in which they are installed. However, offshore photovoltaics will not always stay in the designed tilt and orientation due to the response of the floating structure to incoming waves. Figure 21 depicts the effect that the reaction of a floating structure to incoming waves can have on the actual tilt of a PV module. Other movements can affect the azimuth of the PV installation or both tilt and azimuth. Therefore, this chapter presents a simulation tool that can be used to quantify the effect of wave response movements on incident radiation on fixed offshore PV installations. Furthermore, a simulation model validation and a parametric analysis are also presented. The results of this chapter were published in Elsevier's peer-reviewed journal Solar Energy Advances [111].

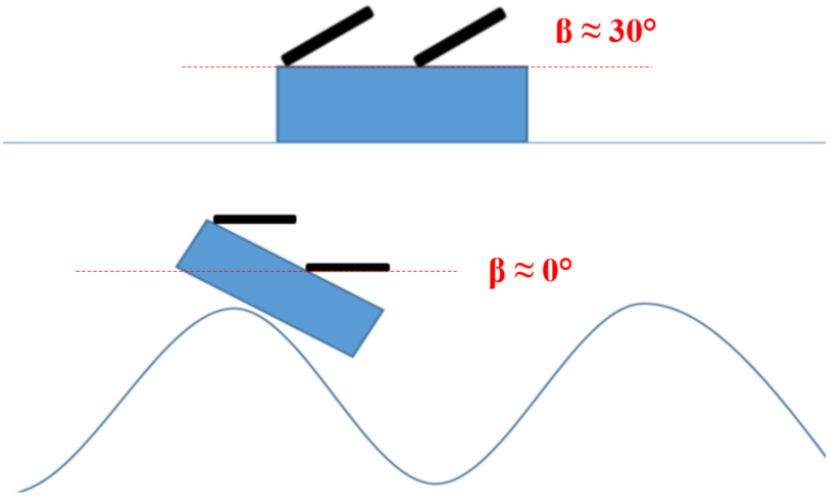

Figure 21: Floating platform at steady state (TOP) and floating platform responding to incoming wave (BOTTOM).

The motion of PV modules was divided into three degrees of freedom: pitch, yaw and roll movements, as shown in Figure 22. The effect of each movement on the insolation on offshore PV modules was studied in simulation and practice.

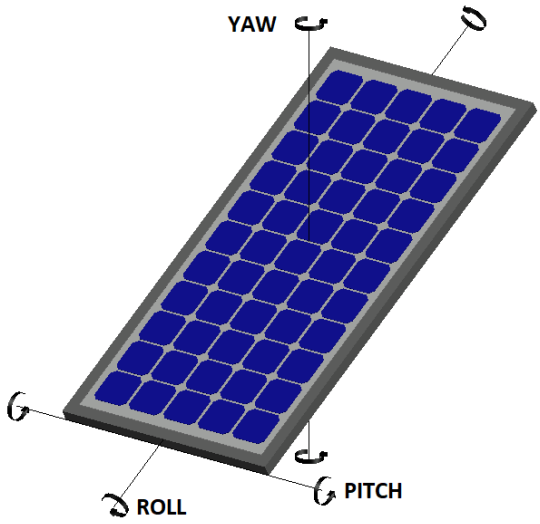

Figure 22: Pitch, Yaw and Roll movements on a PV panel.

3.2 Methodology

3.2.1 Position of the Sun

To predict the irradiance on a plane at any time during the year, one must know the Sun's position relative to a point on Earth at that given time. The Earth follows an elliptical orbit around the Sun. This means that the distance between the Sun and the Earth, r, is not a constant during the year and is denoted by equation (10) [112].

$$r = r_o \left[1 + 0.017 \sin \frac{360(N - 93)}{365}\right] \tag{10}$$

N is referred to as a Julian day, which is the day number starting from January 1st and r_o accounts for the deviation of the Earth's orbit from a circular path. This deviation is usually adequately expressed by a mean value of 1.496 x 10^8 km [112]. In addition, when calculating the Sun's position relative to a point on Earth, it is essential to include the eccentricity correction factor, given by equation (11) [112].

$$\varepsilon_o = \left(\frac{r_o}{r}\right)^2 = 1 + 0.033 \cos \frac{360\ N}{365} \tag{11}$$

It is well known that the Sun is higher in the sky in summer than it is in winter. This is because the Earth revolves once a day on its own axis, at an angle of circa 23.45° with the ecliptic plane. Hence, we define the solar declination angle, δ, defined by equation (12), which is the angle between the equatorial plane and a straight line drawn between the centre of the Earth and the centre of the Sun [112]. This equation holds for positive angles north of the equator and negative angles south of the equator. Figure 23 shows the variation in the solar declination angle during the year.

$$\delta = 23.45° \sin\left(\frac{360(N + 284)}{365}\right) \tag{12}$$

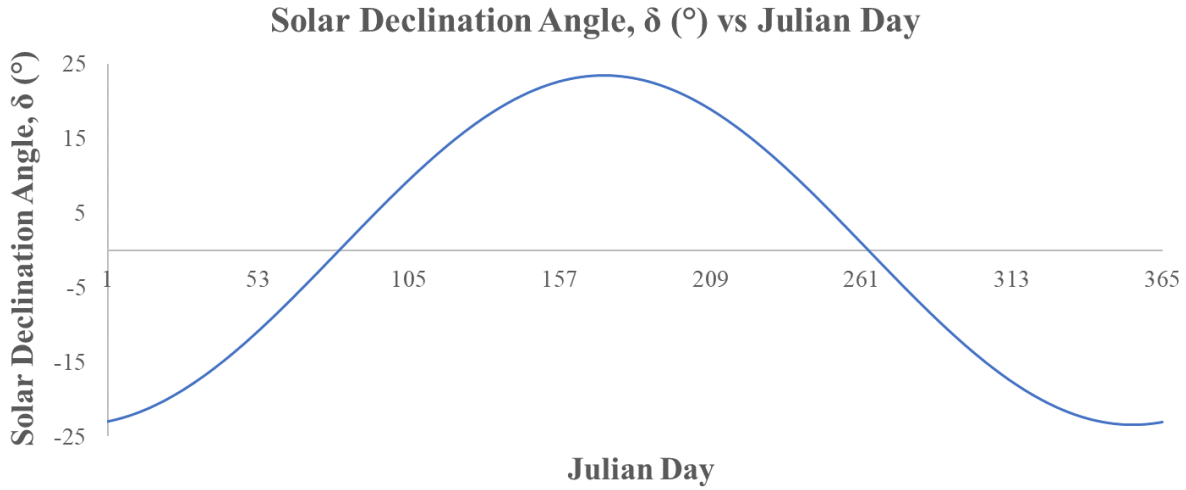

Figure 23: Variation of solar declination angle during the year.

As seen by an observer on Earth, the Sun's position usually does not coincide with the local standard time (LST). Hence, the Apparent Solar Time (AST) is used instead in solar calculations. To convert from LST to AST, one must apply two corrections namely the equation of time and longitude correction. The equation of time compensates for the variation in the Earth's orbital velocity due to the eccentricity of the Earth's orbit and the tilt of the Earth's axis with reference to its orbital plane [113]. The longitudinal correction compensates for the difference in longitude between the meridian on which the local standard time is based and the observer's meridian [19]. The difference in minutes between the Apparent Solar Time and the Local Standard Time is given by equation (13) [19].

$$AST - LST = 4(L_{ST} - L_{LOC}) + E \tag{13}$$

where L_{ST} is the standard meridian for the local time zone, and L_{LOC} is the longitude of the observer's location. The parameter *E* is the equation of time given by equation (14) where *B* is given by equation (15) [19].

$$E = 229.2(0.000075 + 0.001868\cos B - 0.032077\sin B \\ -0.014615\cos 2B - 0.04089\sin 2B) \quad (14)$$

$$B = (N-1)\frac{360}{365} \quad (15)$$

3.2.2 Total radiation on tilted surfaces

The total radiation on a tilted surface can be divided into two main components, namely Direct (Beam) Radiation B(β,γ) and Diffused Radiation D(β,γ). Diffused radiation is further divided into two main components, namely diffused radiation originating from the sky $D_a(\beta,\gamma)$, for example, due to reflections of clouds, and diffused radiation originating from the ground $D_g(\beta,\gamma)$, for example, reflections from ground material and buildings. The total radiation on a tilted surface G(β,γ) is given by equation (16).

$$G(\beta,\gamma) = B(\beta,\gamma) + D_a(\beta,\gamma) + D_g(\beta,\gamma) \quad (16)$$

To be able to calculate the beam radiation on a tilted surface given the beam radiation on a horizontal surface, we use the ratio between the two (R_{T-H}), given by equation (17); where θ_z is the Zenith angle equal to the angle of incidence of beam radiation on a horizontal surface and θ is the beam radiation angle of incidence on a tilted surface [19].

$$R_{T-H} = \frac{\cos\theta}{\cos\theta_z} \quad (17)$$

Equations (18) and (19) relate the angle of incidence of beam radiation on a surface to other known angles.

$$\cos\theta = \sin\delta\sin\emptyset\cos\beta - \sin\delta\cos\emptyset\sin\beta\cos\gamma + \cos\delta\cos\emptyset\cos\beta\cos\omega \\ + \cos\delta\sin\emptyset\sin\beta\cos\gamma\cos\omega + \cos\delta\sin\beta\sin\gamma\sin\omega \quad (18)$$

$$\cos\theta = \cos\theta_z\cos\beta + \sin\theta_z\sin\beta\cos(\gamma_s - \gamma) \quad (19)$$

where $\emptyset$ is the latitude of the tilted surface, γ is the azimuth of the tilted surface and ω is the hour angle. The hour angle is the angular displacement of the Sun east or west of the local meridian and is given by equation (20) [19] [113].

$$\omega = \frac{360}{24}(AST - 12) \tag{20}$$

Various sky models can predict the total incident radiation on a tilted surface. These can be divided into two main categories: the Isotropic and Anisotropic models. The differences between these two model categories lie in the way they look at diffuse radiation. Diffuse radiation can be divided into three parts:

- Isotropic radiation received uniformly from the entire sky dome,
- Circumsolar diffuse resulting from forward scattering in the part of the sky closest to the Sun, and
- Horizon brightening concentrated near the horizon. This has more effect on days with clear skies.

Figure 24 shows a schematic explaining the three parts of diffused radiation [19].

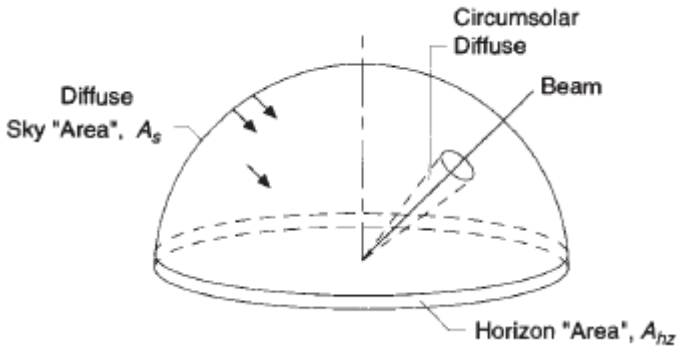

Figure 24: Schematic showing the three parts making up the diffused radiation on a surface.

3.2.3 Isotropic model

The isotropic model is the simplest model to predict the total radiation on an inclined surface. The basic form of this model assumes an isotropic combination of diffuse radiation from the sky and ground-reflected radiation. This means that diffused radiation on a tilted surface is always the same regardless of orientation. An improved version of this model is the isotropic diffuse model by Liu and Jordan [114] [19], which considers both isotropic sky diffused radiation, $D_a(\beta, \gamma)$, and diffuse radiation reflected from the ground, $D_g(\beta, \gamma)$. This model gives the total solar radiation on a tilted surface using equation (21)[19].

$$G(\beta,\gamma) = B(0,0)R_{T-H} + D_a(\beta,\gamma) + D_g(\beta,\gamma) \quad (21)$$

Where:

$$D_a(\beta,\gamma) = D(0,0)\left(\frac{1+\cos\beta}{2}\right)$$

And:

$$D_g(\beta,\gamma) = G(0,0) \times \rho_g \times \left(\frac{1-\cos\beta}{2}\right)$$

3.2.4 Anisotropic model

Anisotropic models provide a more accurate calculation of the global radiation on a tilted surface. Hay and Davies factor in the circumsolar diffuse radiation and consider it incident from the same direction as the beam radiation. The Perez Model [115][116] calculates in detail all three diffuse radiation components and, thus, includes horizon brightening. The diffused radiation on a tilted surface, according to Perez Model, is given by equation (22) [19]

$$D(\beta,\gamma) = D(0,0)\left[(1-F_1)\left(\frac{1+\cos\beta}{2}\right) + F_1\frac{a}{b} + F_2\sin\beta\right] \quad (22)$$

and $a = \max(0,\cos\theta), \qquad b = \max(0,\cos\theta_z)$

According to the definitions of 'a' and 'b', 'a / b' is equal to $R_{T\text{-}H}$ for the relevant parts of the day. Furthermore, F1 and F2 are circumsolar and horizon brightness coefficients. These coefficients are functions of the zenith angle θ_z, a clearness coefficient ε, and a brightness coefficient Δ given by equations (23) and (24) respectively.

$$\varepsilon = \frac{\left(1+\frac{B(0,0)}{\cos(\theta_z)\times D(0,0)}\right) + (5.535\times10^{-6})\theta_z^3}{1+(5.535\times10^{-6})\theta_z^3} \quad (23)$$

$$\Delta = \mathrm{m}\frac{D(0,0)}{G_{on}} \quad (24)$$

Where:

$$m = \frac{1}{\cos\theta_z} \quad (24.1)$$

$$G_{on} = G_{sc}(1.000110 + 0.034221\cos B + 0.001280\sin B + 0.000719\cos 2B + 0.000077\sin 2B) \quad (24.2)$$

$$B = (n-1)\frac{360}{365} \quad (24.2.1)$$

In the above equations, m is the air mass ratio, and G_{on} is the extra-terrestrial radiation incident on a plane normal to the radiation from the Sun. G_{sc} is the solar constant defined as the Sun's energy received by a unit area of a surface perpendicular to the direction of radiation, at an average Earth-Sun distance outside the atmosphere, per unit time. The World Radiation Centre takes this solar constant as an average of 1367 W/m^2 [19].

F1 and F2 in equation (22) are functions of statistically derived coefficients and they are calculated by equations (25) and (26) respectively.

$$F_1 = max\left[0, (f_{11} + f_{12}\Delta + \frac{\pi\theta_z}{180} f_{13}\right] \quad (25)$$

$$F_2 = f_{21} + f_{22}\Delta + \frac{\pi\theta_z}{180} f_{23} \quad (26)$$

Values for the coefficients mentioned in equations (25) and (26) are taken from Table 2 [19] [115], according to the value of the clearness coefficient.

Table 2: Brightness coefficients for Perez model [19] [115].

Range of $\boldsymbol{\varepsilon}$	$\boldsymbol{f_{11}}$	$\boldsymbol{f_{12}}$	$\boldsymbol{f_{13}}$	$\boldsymbol{f_{21}}$	$\boldsymbol{f_{22}}$	$\boldsymbol{f_{23}}$
1.000-1.065	-0.008	0.588	-0.062	-0.060	0.072	-0.022
1.065-1.230	0.130	0.683	-0.151	-0.019	0.066	-0.029
1.230-1.5	0.330	0.487	-0.221	0.055	-0.064	-0.026
1.5-1.950	0.568	0.187	-0.295	0.109	-0.152	0.014
1.950-2.800	0.873	-0.392	-0.362	0.226	-0.462	0.001
2.800-4.500	1.132	-1.237	-0.412	0.288	-0.823	0.056
4.500-6.200	1.060	-1.600	-0.359	0.264	-1.127	0.131
6.200-∞	0.678	-0.327	-0.250	0.156	-1.377	0.251

Therefore, the complete equation derived from Perez Model representing the irradiance on a tilted plane is given by equation (27) [19].

$$G(\beta,\gamma) = B(0,0)\frac{\cos\theta}{\cos\theta_z} + D(0,0)\left[\left((1-F_1)\left(\frac{1+\cos\beta}{2}\right) + F_1\frac{a}{b} + F_2\sin\beta\right)\right] + G(0,0)\rho\left(\frac{1-\cos\beta}{2}\right) \quad (27)$$

The chosen model only accounts for diffused reflections and does not consider specular reflection of the direct beam component. Purely specular reflection requires highly reflective smooth surfaces. While it is difficult to get such conditions when the sea is rough, specular reflection is possible in calm waters. Therefore, neglecting this effect could result in conservative losses. However, since specular reflection results in a source of light originating from a lower level than the PV installations, only front rows of PV modules could be subjected to it while inner rows would be shaded. Furthermore, specular reflection would result in rays with a high incidence angle on the photovoltaic surface. At such angles it was shown that the transmittance through glass decreases [19], which would result in an even lower impact. Future studies can investigate this effect and possibly consider it in software updates.

3.2.5 Simulation

Firstly, a simulation file was created to compare the performance of Isotropic and Anisotropic (Perez) models in predicting irradiance on a tilted surface from data of irradiance on a horizontal surface. Weather data was obtained from a weather station installed at the Institute for Sustainable Energy (ISE) in Marsaxlokk, Malta.

A model from the United States National Oceanic and Atmospheric Administration (NOAA) [117] was used to accurately find the Sun's position on particular dates and at given times. This acquired position was then applied to the Isotropic and Anisotropic (Perez) models to derive the total irradiance on a tilted plane. Simulations were carried out for a surface facing South at an inclination of 33° (G(33,0)) and compared to real data for three types of sky, namely, clear (Figure 25), cloudy (Figure 26) and overcast. Figure 27 shows the graphical user interface of the simulation file and the result for the overcast sky. An albedometer was used to measure the albedo of the weather station area and was found to be 0.35. The deviations of simulation models from actual data for the three scenarios are tabulated in Table 3.

Table 3: Comparison of simulation to practical data for Isotropic and Perez models.

Type of Sky	Average Deviation from Real Data (Perez Model)	Average Deviation from Real Data (Isotropic Model)
Clear	0.50%	3.15%
Cloudy	0.58%	2.85%
Overcast	4.21%	7.66%

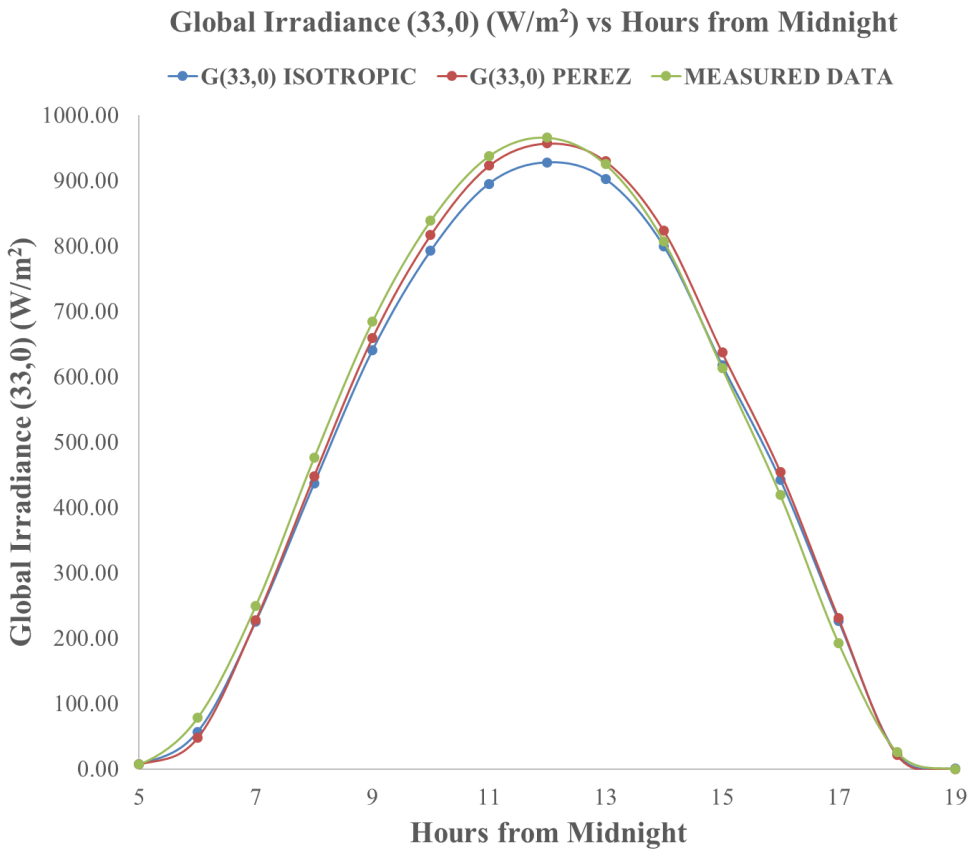

Figure 25: Clear sky simulation result.

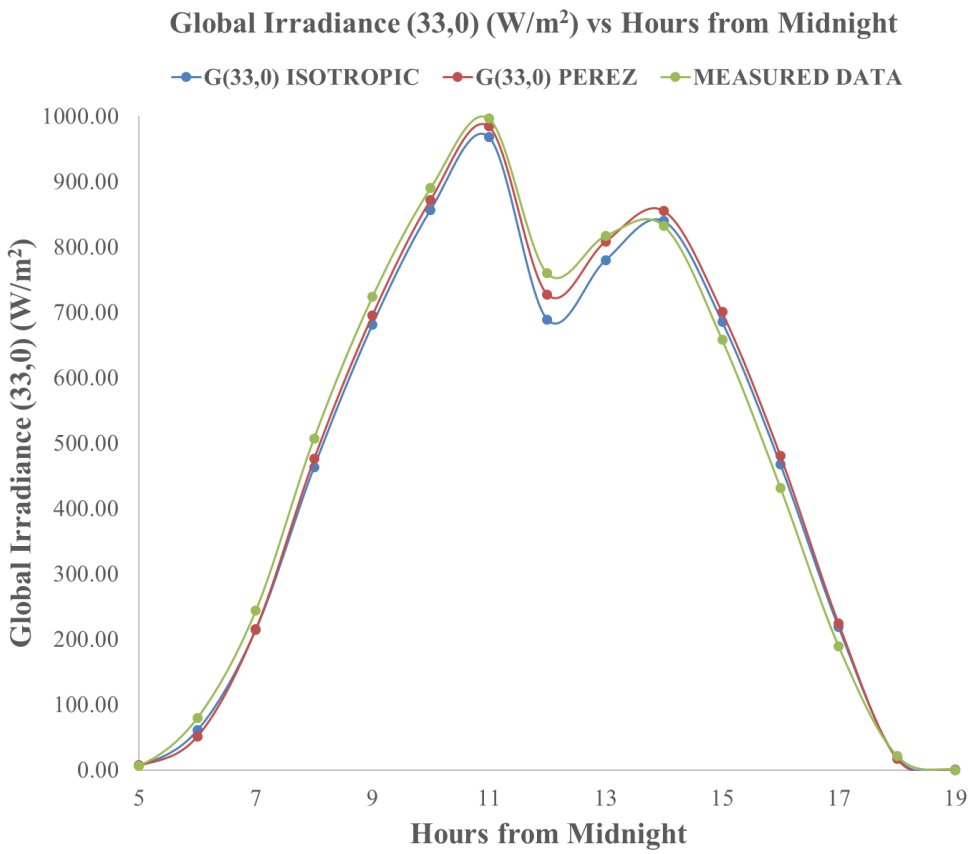

Figure 26: Cloudy sky simulation result.

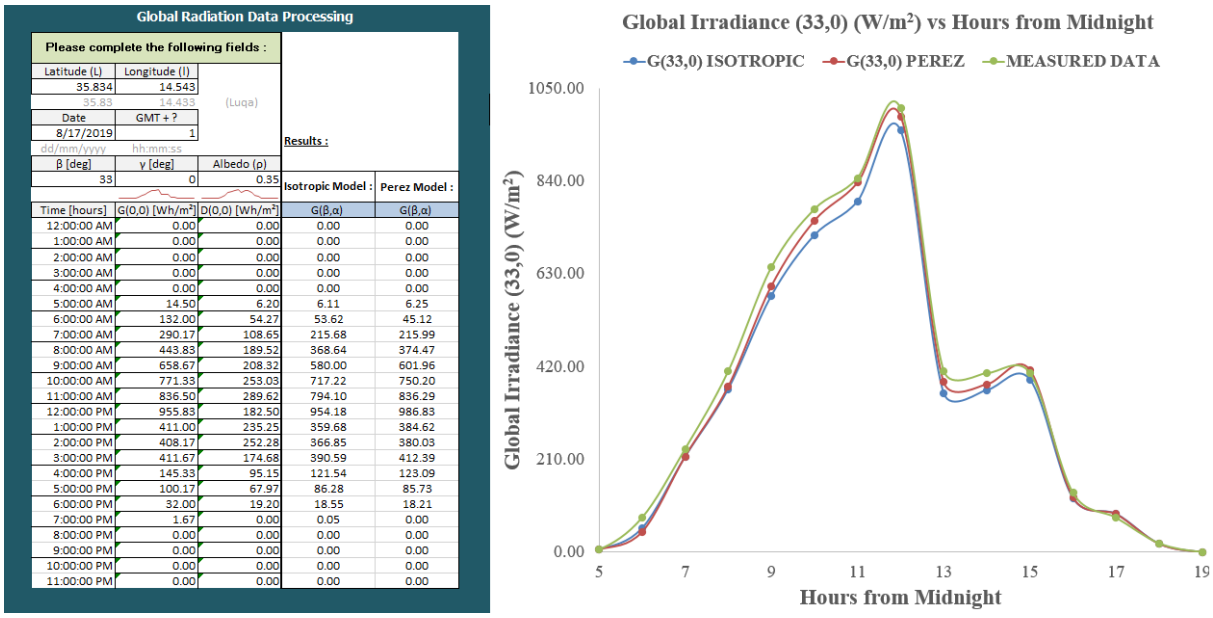

Global Radiation Data Processing

Please complete the following fields :

Latitude (L)	Longitude (l)	
35.834	14.543	
35.83	14.433	(Luqa)

Date	GMT + ?
8/17/2019	1
dd/mm/yyyy	hh:mm:ss

β [deg]	γ [deg]	Albedo (ρ)
33	0	0.35

Results :

Time [hours]	G(0,0) [Wh/m²]	D(0,0) [Wh/m²]	Isotropic Model : G(β,α)	Perez Model : G(β,α)
12:00:00 AM	0.00	0.00	0.00	0.00
1:00:00 AM	0.00	0.00	0.00	0.00
2:00:00 AM	0.00	0.00	0.00	0.00
3:00:00 AM	0.00	0.00	0.00	0.00
4:00:00 AM	0.00	0.00	0.00	0.00
5:00:00 AM	14.50	6.20	6.11	6.25
6:00:00 AM	132.00	54.27	53.62	45.12
7:00:00 AM	290.17	108.65	215.68	215.99
8:00:00 AM	443.83	189.52	368.64	374.47
9:00:00 AM	658.67	208.32	580.00	601.96
10:00:00 AM	771.33	253.03	717.22	750.20
11:00:00 AM	836.50	289.62	794.10	836.29
12:00:00 PM	955.83	182.50	954.18	986.83
1:00:00 PM	411.00	235.25	359.68	384.62
2:00:00 PM	408.17	252.28	366.85	380.03
3:00:00 PM	411.67	174.68	390.59	412.39
4:00:00 PM	145.33	95.15	121.54	123.09
5:00:00 PM	100.17	67.97	86.28	85.73
6:00:00 PM	32.00	19.20	18.55	18.21
7:00:00 PM	1.67	0.00	0.05	0.00
8:00:00 PM	0.00	0.00	0.00	0.00
9:00:00 PM	0.00	0.00	0.00	0.00
10:00:00 PM	0.00	0.00	0.00	0.00
11:00:00 PM	0.00	0.00	0.00	0.00

Figure 27: User interface of comparison file and overcast sky simulation result.

As expected from the literature [19], the Isotropic model is the simplest to implement but gives very conservative estimates of global radiation on a tilted surface. Furthermore, the Perez model is more complex to implement but gives more accurate results, although slightly overestimated at times. Hence, the Perez Model was chosen to develop a Microsoft Excel simulation file to predict the loss or gain in yield due to movements in pitch, yaw and roll. This simulation focuses on the difference in the irradiance received by a fixed plane and a plane moving due to incoming waves.

The user inputs an equation that characterises the response of the offshore structure to incoming waves in terms of pitch, yaw and roll. Furthermore, weather data is required for that particular day. The essential weather data required by the simulation file are any two of the following:

- Global irradiance on a horizontal plane
- Diffuse radiation on a horizontal plane
- Direct Beam Radiation on a horizontal plane

Hence, the file runs two separate algorithms combining a model by the United States National Oceanic and Atmospheric Administration (NOAA) [117] to find an accurate position of the Sun and the Perez model to find the global irradiance on a tilted plane. One algorithm derives the global irradiance on a plane with a fixed tilt and orientation. In contrast, the other algorithm varies the tilt and orientation based on the response characteristic equation inputted by the user. Finally, both results of global irradiance are compared together. A parametric simulation compared a fixed installation on land with a non-tracking offshore installation installed on a floating structure moving in response to incoming waves. A pure sinusoidal wave was assumed for all movements. The parameters used for the simulation are shown in Table 4.

Hence, another simulation was performed using a movement amplitude of 20° and selecting a day for each month of the year. The days chosen were close to the 21st of each month to include important solar events, such as equinoxes and solstices. However, care was taken to select days with similar sky clarity. A 30° fixed tilt south-facing installation was chosen since these parameters result in the highest yearly energy yield in Malta. Furthermore, a 5° fixed tilt south-facing installation was also chosen since offshore photovoltaics are expected to have a low tilt angle to reduce the effect of wind and get a higher energy density for each offshore raft, thus making the system more financially viable.

Table 4: Parameters used for irradiance comparison simulation.

Fixed Tilt Angle (β)	Fixed Azimuth Angle (γ)	Movement and Amplitude			
30°	0°	Pitch 5°	Pitch 10°	Pitch 15°	Pitch 20°
		Yaw 5°	Yaw 10°	Yaw 15°	Yaw 20°
		Roll 5°	Roll 10°	Roll 15°	Roll 20°
5°	0°	Pitch 5°	Pitch 10°	Pitch 15°	Pitch 20°
		Yaw 5°	Yaw 10°	Yaw 15°	Yaw 20°
		Roll 5°	Roll 10°	Roll 15°	Roll 20°

3.2.6 Experimental setup

The experimental setup, shown in Figure 28, was designed to verify simulation results in a practical scenario. Poly (methyl methacrylate) material was used to construct two lightweight bases rotating on two axes, similar to the structure of a two-axis solar tracker. Kipp & Zonen Silicon Pyranometers were attached to these bases to obtain irradiance data. High-torque servo motors were used to achieve the desired movements. Hence, an Arduino UNO board utilising an ATMEGA328 microcontroller was programmed to control the servo motors. The program asks the user to enter the desired Amplitude and then outputs a sinusoidal wave using the inputted parameters. This sinusoidal signal is transferred to the servo motors, and the desired movements are achieved. Finally, a DATAQ DI-808 data logger was connected to the pyranometers, and a 10Hz sampling rate was set to accurately acquire all the data points required to represent the response signal. Data was acquired with six decimal places precision and an accuracy of ±0.05% of the full range. Figure 29 shows a data sample representing the effect of pitch movements on the insolation on non-tracking offshore photovoltaic installations.

Figure 28: Effect of waves on irradiance experimental setup.

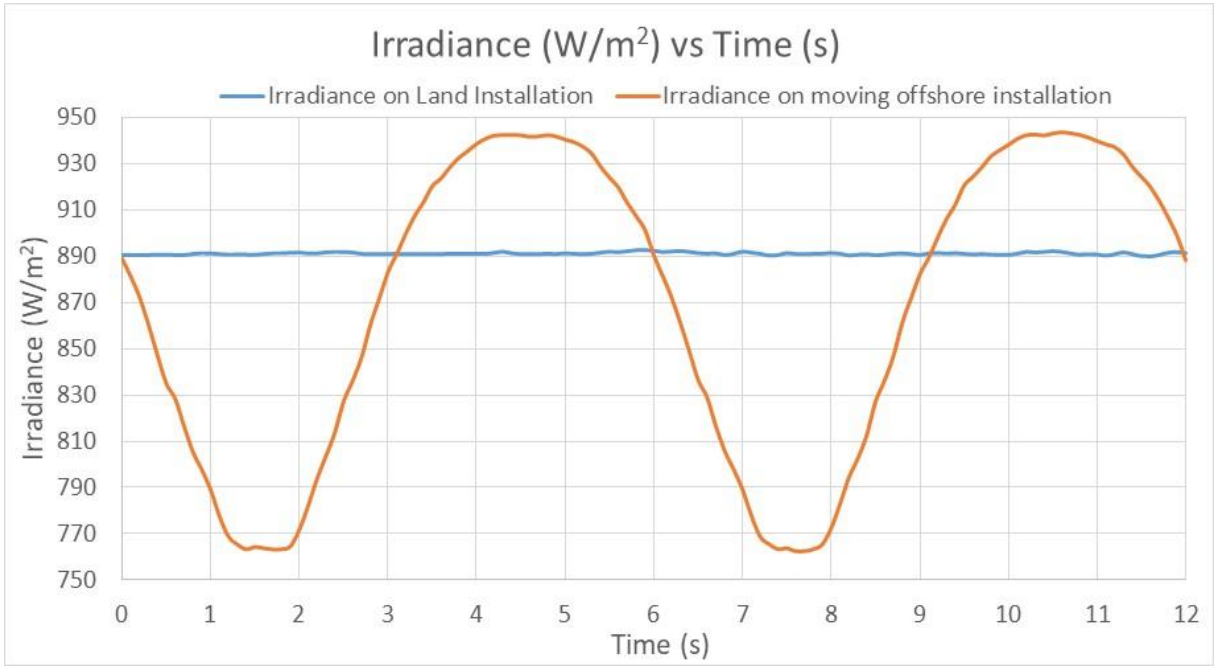

Figure 29: Data sample showing the effect of pitch movements.

Initially, a calibration procedure was performed for the two pyranometers to get the same irradiance output for the same conditions. It was noted that the available pyranometers' outputs varied slightly, and the variation was not constant during the day. This slight difference is due to instrument errors and different deviations from factory calibration over time. While this small difference will not affect the regular operation of the pyranometers, it would affect the experiment results since the margin of error needs to be minimal. The percentage difference between the moving and the fixed pyranometers was expected to be very small from the simulation; therefore, accuracy was essential.

Hence, a calibration procedure was performed immediately before taking readings for each hour. An experimental procedure described in the flowchart in Figure 30 was adopted hourly. The algorithm is initially idle prompting the user to enter initial tilt and orientation angles. It uses the inputted angles as the centre of oscillations. Once an adequate input is received, the microcontroller signals the servo motors to move to the positions instructed by the user. The user is then prompted to enter an amplitude selector from zero to three corresponding to sinusoidal oscillation amplitudes of 20° to 5°, respectively. The user is further asked to select if the movement should be applied to tilt only, orientation only or both. Next a high digital output, signals the datalogger to create a new file and start recording data. Hence, the microcontroller signals the servo motors to produce sinusoidal oscillations with an amplitude equal to that selected by the user. When a complete cycle is performed, a low digital output signals the datalogger to stop recording data and close the file. The algorithm then automatically increments the amplitude selector to perform a cycle of oscillations with a lower amplitude. This algorithm loop reaches an end once a cycle of oscillations is completed at the lowest amplitude of 5°. Therefore, at the end of a single program loop, the user will have separate files with data corresponding to irradiance incident on a plane oscillating at different amplitudes compared with a plane having a fixed tilt and orientation. The complete algorithm code is presented in Appendix D – Control algorithms.

Pitch and Yaw movements for a tilted surface could be performed directly with the designed setup. However, a slight modification was required to perform roll movements for a tilted surface. An extra piece of wood was cut at the required angle and added on top of the setup to create the initial tilt of the pyranometers. Finally, data was analysed and compared to the simulation and the results are presented in the following section

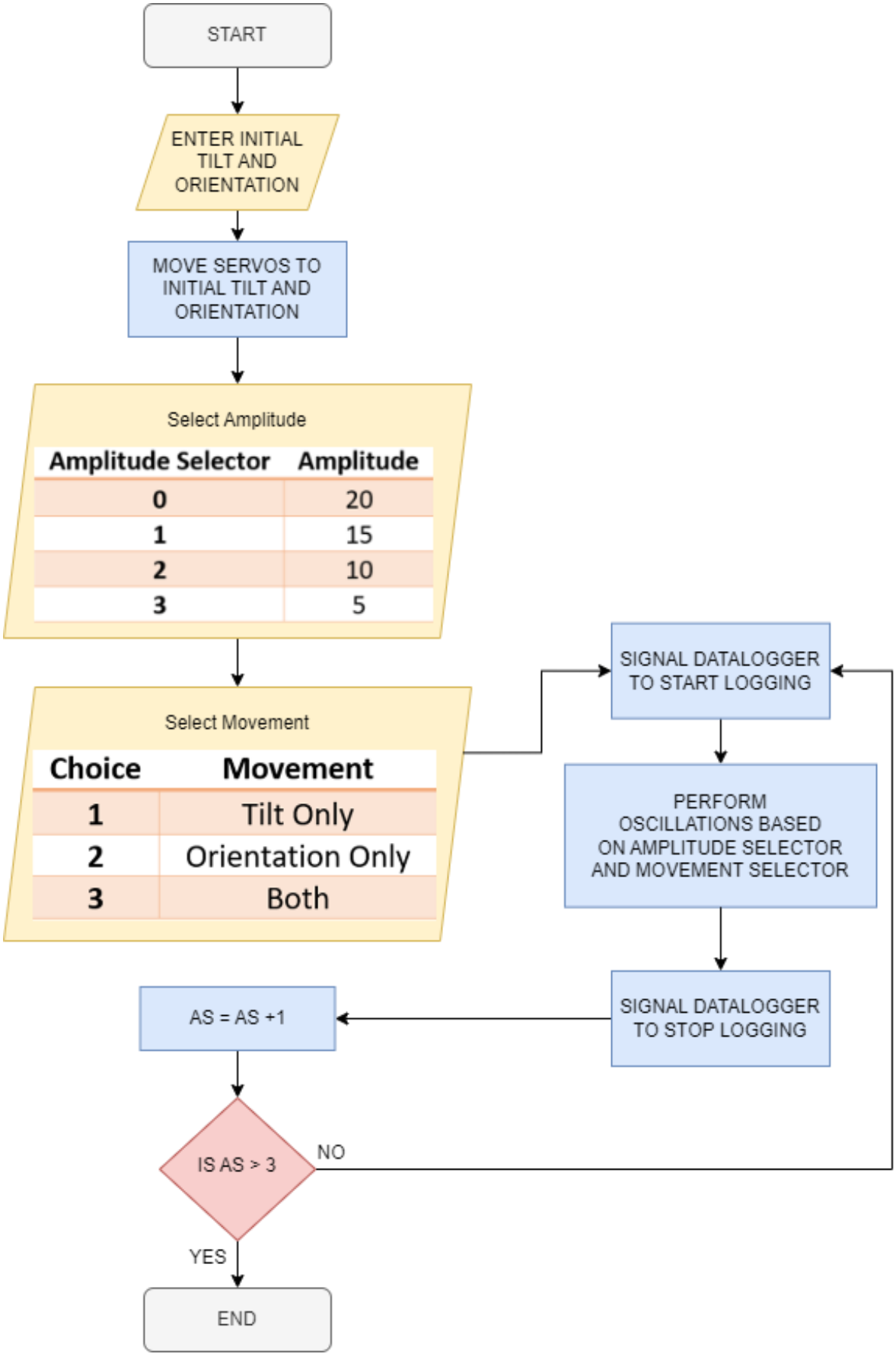

Figure 30: Irradiance experiment flow chart.

3.3 Results and discussion

3.3.1 Verification of simulation data

The percentage insolation deviation of an offshore photovoltaic installation from a fixed structure on land due to Pitch, Yaw and Roll movements can be seen in Figure 31, Figure 32 and Figure 33, respectively. These results were obtained in June 2019 for an installation designed with a fixed tilt of 30° and a fixed orientation of 0°. Table 5 shows the maximum and minimum insolation deviation of offshore installations from fixed installations on land from data obtained from both simulation and experimental setups. Table 5 also shows the average errors between simulation and experimental results. These results show that the most significant yield loss is obtained with pitch movements since these movements directly affect the actual installation tilt of the PV modules. The average error between simulation and real data tends to vary with oscillation amplitudes. This is attributed to the varying jitter present in the servo motors.

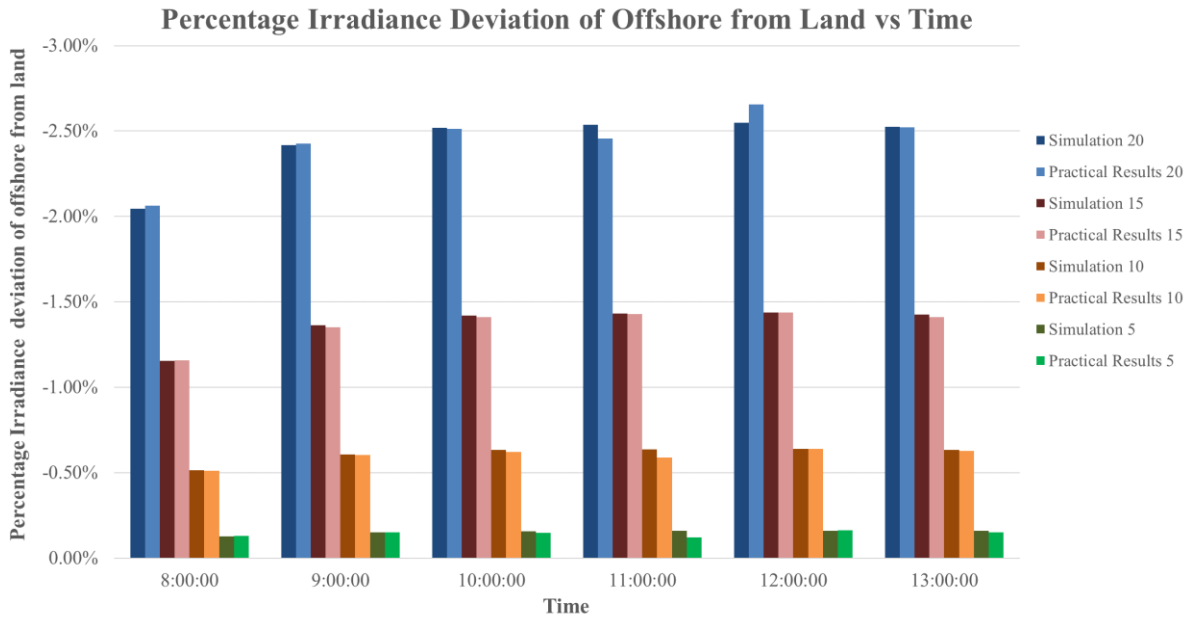

Figure 31: Comparison between simulation and experimental data: Percentage irradiance deviation of offshore from land due to pitch movements (03/06/2019, β=30°, γ=0°).

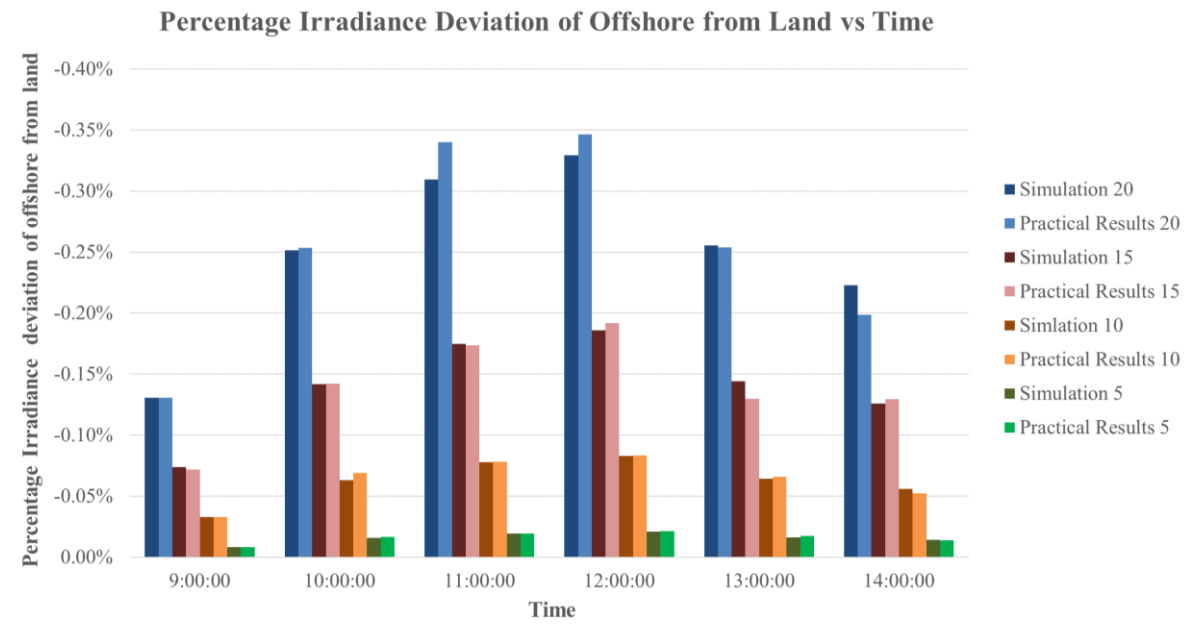

Figure 32: Comparison between simulation and experimental data: Percentage irradiance deviation of offshore from land due to yaw movements (06/06/2019, β=30°, γ=0°).

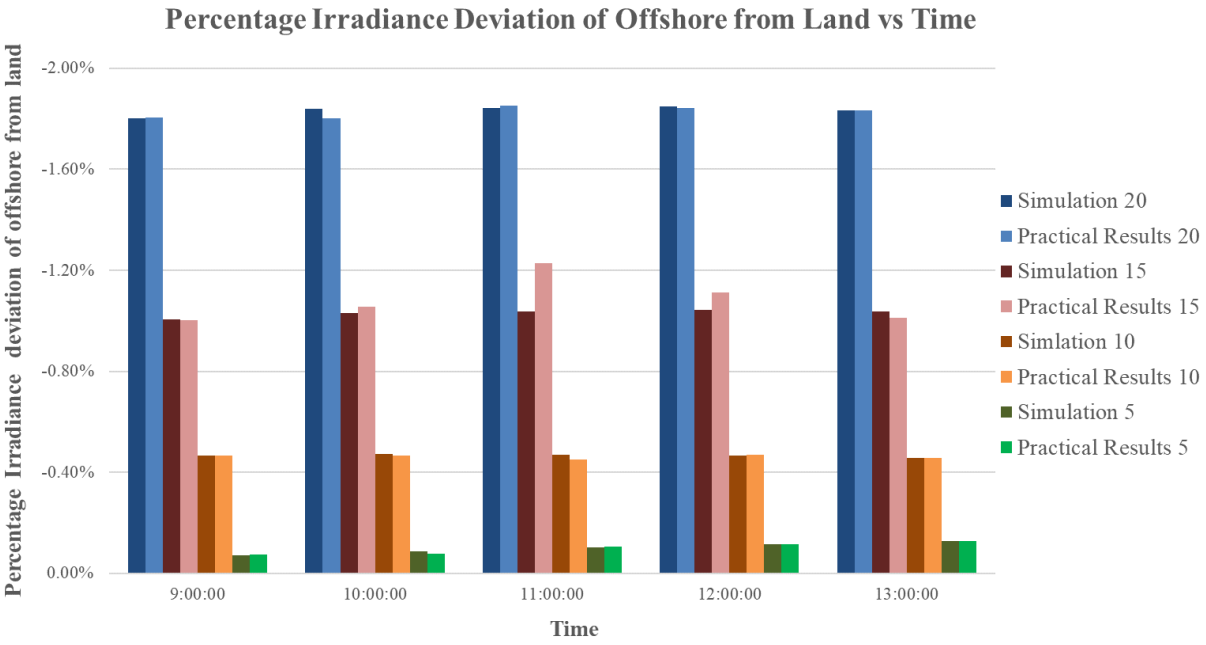

Figure 33: Comparison between simulation and experimental data: Percentage irradiance deviation of offshore from land due to Roll movements (11/06/2019, β=30°, γ=0°) .

Table 5: Statistical comparison between simulation and experimental data.

β = 30° γ = 0°	**Irradiance deviation of Offshore from Land (Simulation)**			**Irradiance deviation of Offshore from Land (Experimental)**			**Average Error between Simulation and Experiment (%)**
Movement	MIN	MAX	Average	MIN	MAX	Average	
Pitch 20°	-2.418%	-2.550%	-2.484%	-2.428%	-2.655%	-2.470%	0.037%
Pitch 15°	-1.365%	-1.439%	-1.402%	-1.351	-1.430%	-1.381%	0.008%
Pitch 10°	-0.608%	-0.641%	-0.625%	-0.589%	-0.640%	-0.605%	0.012%
Pitch 5°	-0.152%	-0.161%	-0.156%	-0.123%	-0.162%	-0.145%	0.009%
Yaw 20°	-0.131%	-0.329%	-0.257%	-0.131%	-0.346%	-0.262%	0.026%
Yaw 15°	-0.074%	-0.186%	-0.145%	-0.072%	-0.192%	-0.139%	0.014%
Yaw 10°	-0.033%	-0.083%	-0.065%	-0.033%	-0.083	-0.065%	0.006%
Yaw 5°	-0.008%	-0.021%	-0.016%	-0.008%	-0.021%	-0.017%	0.002%
Roll 20°	-1.800%	-1.848%	-1.83%	-1.802%	-1.850%	-1.83%	0.009%
Roll 15°	-1.005%	-1.041	-1.03%	-1.003%	-1.227%	-1.09%	0.053%
Roll 10°	-0.458%	-0.472%	-0.47%	-0.451%	-0.471%	-0.46%	0.007%
Roll 5°	-0.072%	-0.129%	-0.10%	-0.074%	-0.127%	-0.10%	0.004%

3.3.2 Simulation of low installation angle

Parametric simulations were performed to analyse the effect of wave response motion on the insolation on offshore photovoltaics installed with a designed fixed tilt of 5°. This simulation is of interest since a low angle might be the way forward for offshore photovoltaics since this reduces the effects of wind on the installation and allows more PV modules to be installed on each floating structure, thus increasing the energy density. Figure 34, Figure 35 and Figure 36, respectively show the effects of Pitch, Yaw and Roll movements on the insolation on a 5° tilt offshore installation. Additionally, Table 6 presents a statistical representation of these effects.

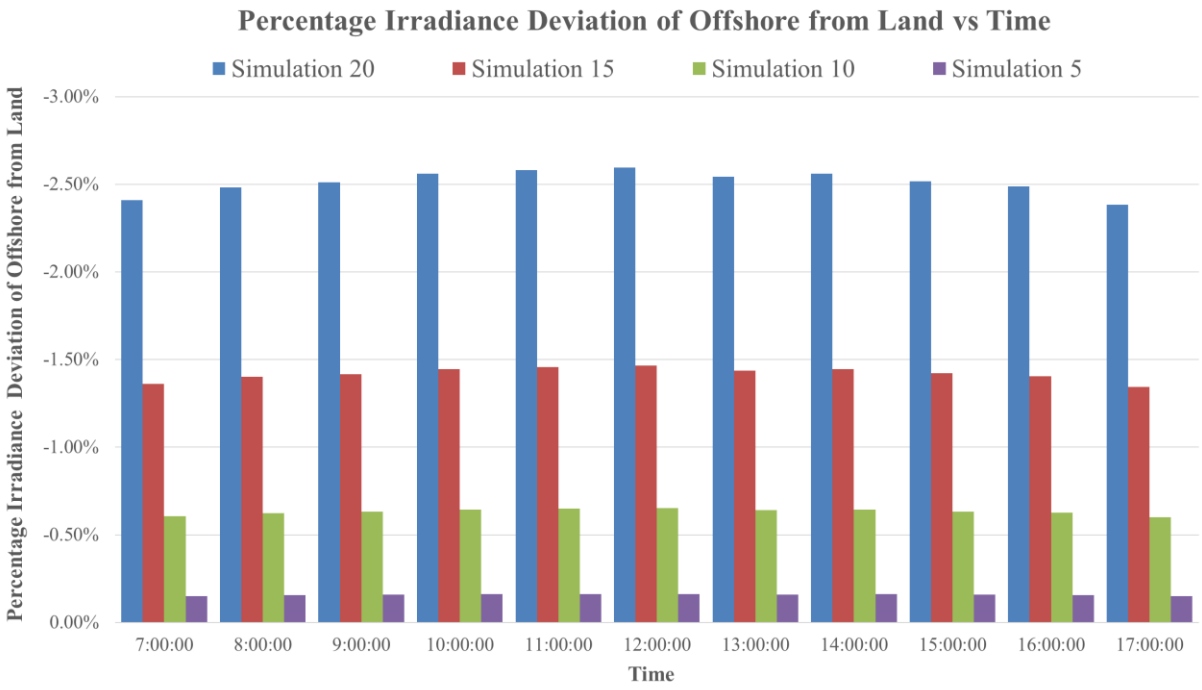

Figure 34: Percentage irradiance deviation of offshore from land due to pitch movements (05/06/2019, β = 5°, Fixed γ= 0°).

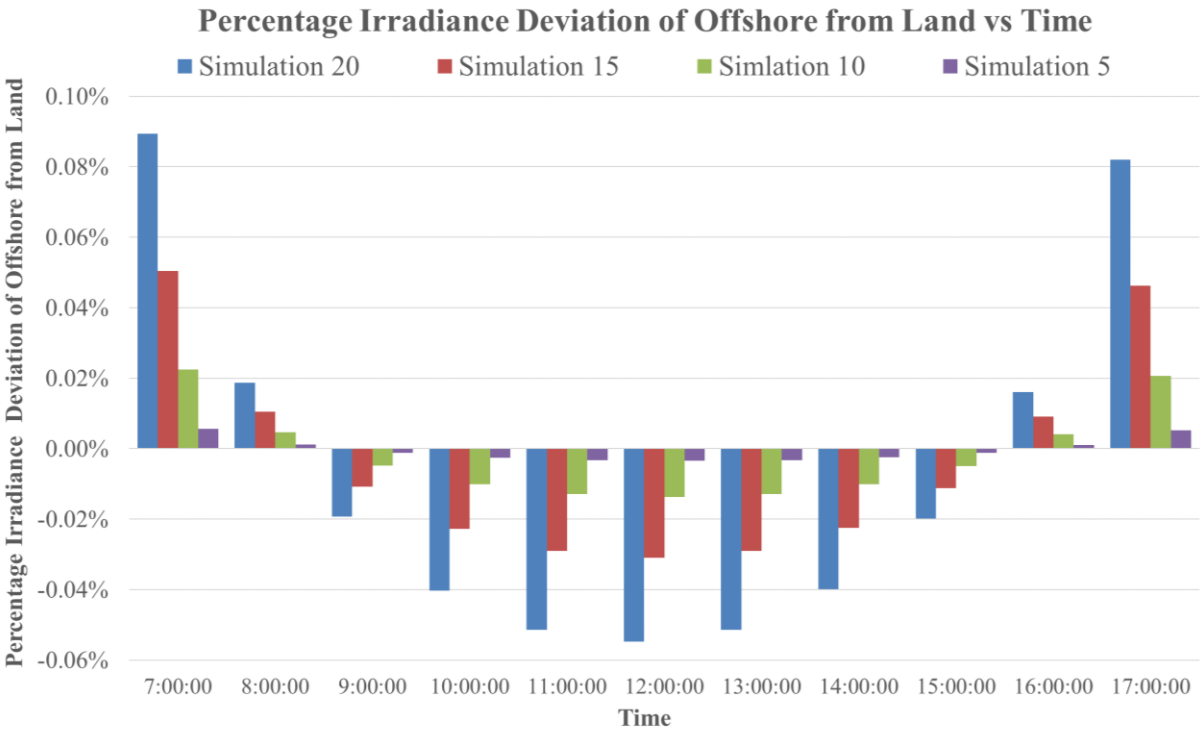

Figure 35: Percentage irradiance deviation of offshore from land due to yaw movements (10/06/2019, β = 5°, Fixed γ= 0°).

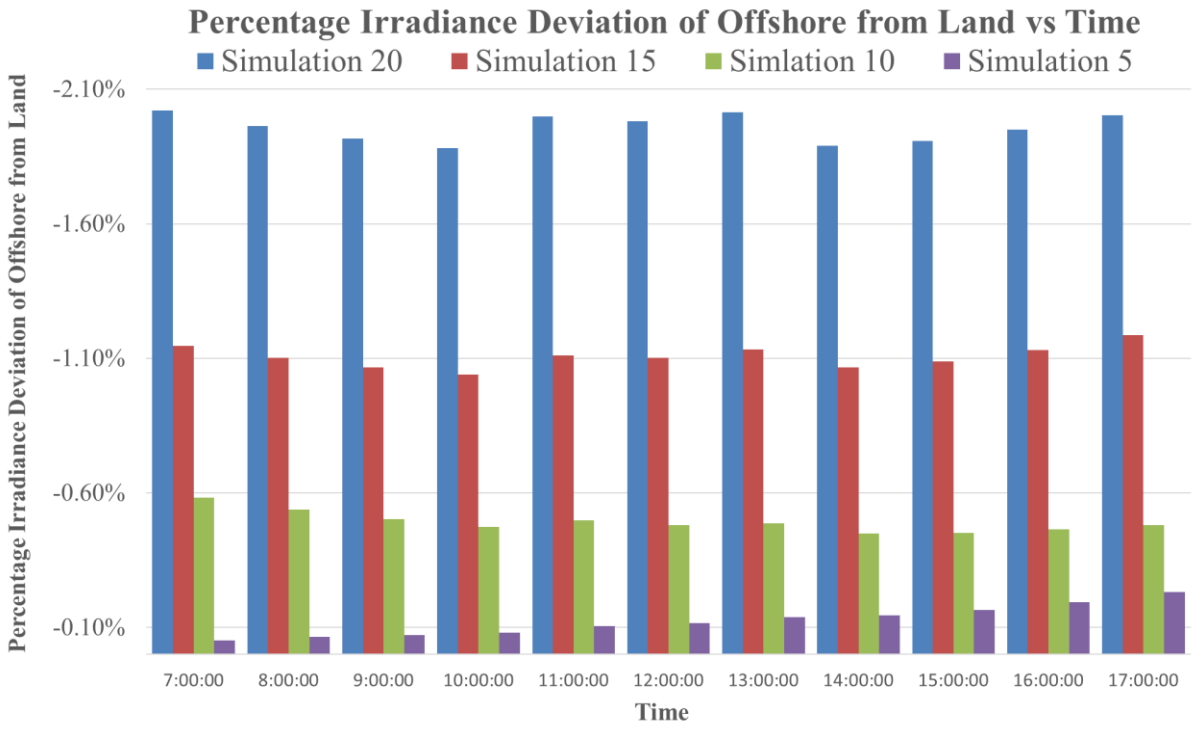

Figure 36: Percentage irradiance deviation of offshore from land due to roll movements (13/06/2019, β = 5°, Fixed γ= 0°).

Table 6: Statistical analysis of simulation data for the irradiance deviation of an offshore installation from land, for a designed fixed tilt of 5° and orientation of 0°.

β = 5°, γ= 0°	**Irradiance deviation of Offshore from Land (Simulation)**		
Movement	**Minimum**	**Maximum**	**Average**
Pitch 20°	-2.409%	-2.594%	-2.532%
Pitch 15°	-1.360%	-1.464%	-1.429%
Pitch 10°	-0.606%	-0.652%	-0.637%
Pitch 5°	-0.152%	-0.163%	-0.159%
Yaw 20°	+0.016% -0.019%	+0.089% -0.055%	-0.022%
Yaw 15°	+0.009% -0.011%	+0.050% -0.031%	-0.013%
Yaw 10°	+0.004% -0.005%	+0.022% -0.014%	-0.006%
Yaw 5°	+0.001% -0.001%	+0.006% -0.003%	-0.001%
Roll 20°	-1.881%	-2.020%	-1.95%
Roll 15°	-1.039%	-1.186%	-1.10%
Roll 10°	-0.448%	-0.583%	-0.48%
Roll 5°	-0.051%	-0.231%	-0.12%

3.3.3 Yearly simulations

Parametric simulations were also performed to analyse the effect of Pitch, Yaw and Roll movements on the insolation on offshore photovoltaics, throughout all the months of the year. Sinusoidal responses with an amplitude of 20° were chosen for these simulations. To perform these simulations, weather data for 2019 was taken for days close to the 21st of each month to include the major solar events, namely equinoxes and solstices. However, another criterion that was imposed on the choice of the day was that the sky clearness had to be similar to be able to

compare different times of the year. Figure 37 and Figure 38 show the results of these simulations for fixed tilts of 5° and 30°, respectively.

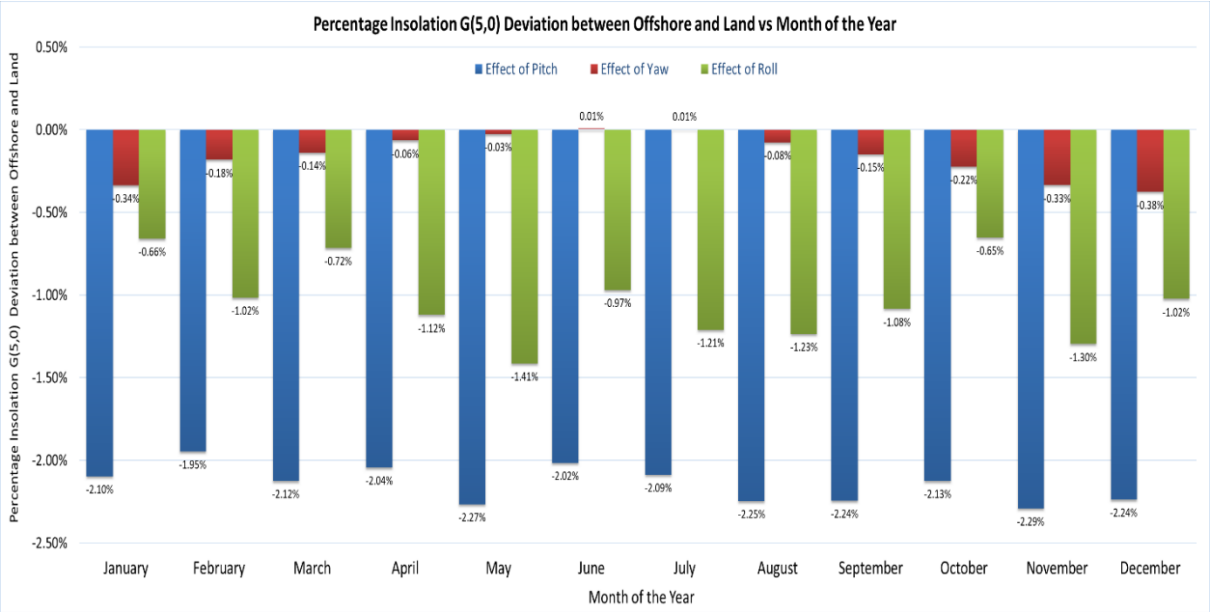

Figure 37: Percentage insolation deviation between offshore and land throughout the year for a β of 5° and γ of 0°.

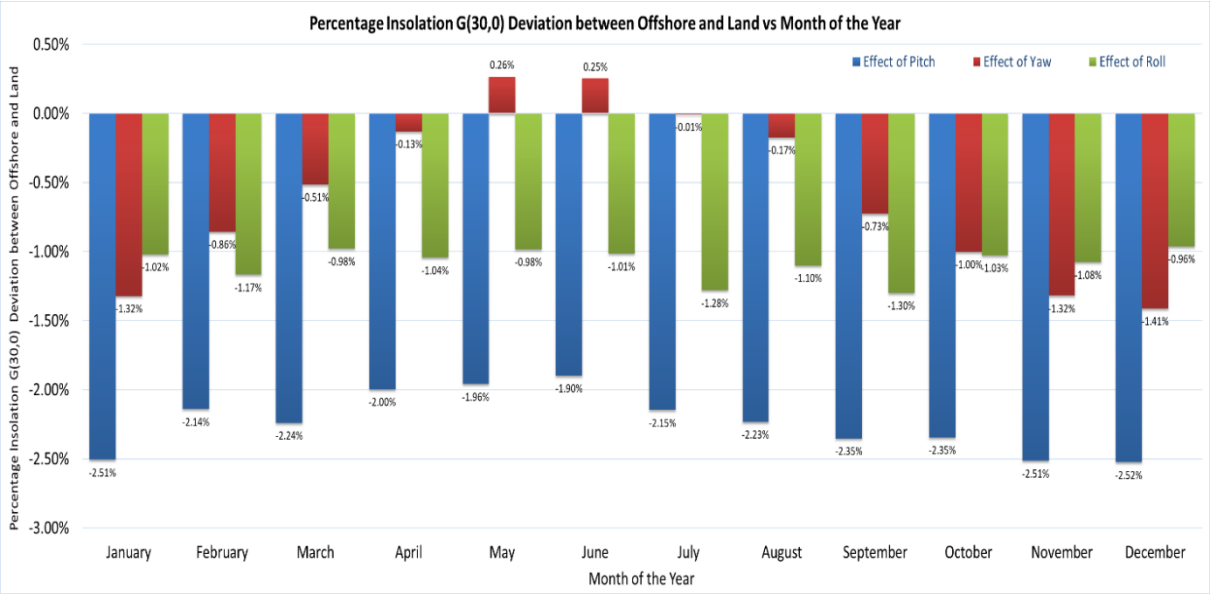

Figure 38: Percentage insolation deviation between offshore and land throughout the year for a β of 30° and γ of 0°.

3.3.4 Discussion

The parametric simulations used the same albedo value for both offshore and land installations. This was decided because the offshore installations we envision will likely require large floating rafts rather than installing PVs close to the sea surface, as in the case of floating photovoltaic (FPV) installations. However, in the tool created, albedo can be varied for both offshore and land installations once such data is available. The results presented were simulated based on weather data for the year 2019.

From the yearly simulations, one can note that Yaw movements in December have a much higher negative effect on the insolation than the same movements in May. This is because the irradiance on a tilted plane follows a cosine function. Therefore, although the change in incidence angle is lower in January than in June, the change in cos (θ) is higher. Yaw movements had the highest negative effect of -1.41% in December, while a positive effect of up to 0.26% was observed in May.

It can be noted from Figure 37 and Figure 38 that pitch movements have the highest effect on the insolation. This is because pitch movements directly affect the actual tilt of the installation. Moreover, this effect on an installation with a designed fixed tilt of 30° is more predominant in December than June. This is because the centre of oscillations is closer to the optimal installation tilt angle in June than in December. This is evidenced again in Figure 37 where, for low tilt angles, seasonal variations in the effect of pitch movements on the insolation are minimal. Pitch movements had the highest negative effect of -2.52% in December and the least negative effect of -1.90% in June. Roll movements had the highest negative effect of -1.41% in May and the least negative effect of -0.65% in October. These movements considerably impacted the insolation since they change both the actual tilt and orientation of the PV modules.

3.4 Conclusion

Offshore photovoltaic installations have various benefits; however, being a new technological advancement, they also come with unknowns. This study investigated the effect of wave response motion on the insolation on offshore photovoltaic installations. A simulation tool was created to allow a system designer to assess the impact that the wave response motion of the floating structure will have on the incident solar radiation on photovoltaic modules. The Microsoft Excel-based simulation tool was verified with an experimental setup that simulated sinusoidal wave responses. Finally, a parametric analysis was performed for photovoltaic

installations facing south and with fixed tilts of 30° and 5°. This parametric analysis was also performed for each month of the year taking days close to the 21st of each month to include the major solar events while still keeping a similar sky clearness. Pitch movements resulted in the most predominant negative effects on the insolation (up to −2.52%) since these movements directly affect the tilt of the installation. Yaw movements had a minimal impact on low tilt angle installations (less than −0.38%) since the effect of orientation on such systems is minimal. Finally, this research showed that roll movements could considerably affect the insolation on an offshore photovoltaic installation since these movements change both the actual tilt and orientation of the PV modules.

4. The effect of wave response motion on the insolation on tracking offshore photovoltaic installations

4.1 Introduction

Tracking systems can considerably increase the energy yield of photovoltaic installations, as discussed in section 2.2.1. However, offshore tracking installations will face various challenges to reach a mature, viable technology. Firstly, active tracking algorithms will find it difficult to accurately follow the Sun while the raft underneath is constantly moving due to incoming waves. Furthermore, once the algorithm successfully tracks the Sun, any movement caused by the response of the floating raft to incoming waves will change the amount of incident radiation on the photovoltaic panels. This movement can have a positive or negative effect depending on the type of tracking system implemented. For example, any movement after an accurate dual-axis tracking algorithm should result in the photovoltaic panels receiving less irradiance when compared to the same tracking system installed on land. However, this effect has never been quantified in the literature. Therefore, this chapter presents the optimisation of the simulation tool presented in the previous chapter to include HSAT, VSAT and dual-axis offshore tracking. The new simulation tool was termed Offshore Solar Irradiance Calculator (OSIC) and its logo is shown in Figure 39. This chapter has been published in MDPI Energies [118]

Figure 39: Official OSIC software logo.

4.2 Methodology

After the simulation tool described in Chapter 3 was published [111], it generated considerable interest in researchers worldwide. However, this tool was operated in Microsoft Excel and executed long calculations very slowly. This factor and a lack of a Graphical User Interface (GUI) made the simulation tool less adequate to be distributed. Hence, it was decided to optimise the simulation tool by re-programming it using C-language, in Visual Studio 2022 Integrated Development Environment (IDE). This part of the research aimed to create a user-friendly software that includes a GUI and can process inputs and give results in a fraction of the time it took for the Excel-based tool. Furthermore, North-South axis HSAT, VSAT and Dual-Axis tracking were added to the tool, making it the first tool (at the time of writing) that can calculate the effect of wave response motion on both fixed and tracking offshore photovoltaic installations.

Once again, the floating raft's movement was divided into Pitch, Yaw and Roll. In the Excel file, the pitch was affecting the tilt, the Yaw was affecting the Azimuth, and the Roll was affecting both. Also, azimuth and tilt angles after Roll movements were obtained for every wave characteristic equation using the 3D environment in PVSYST. The OSIC software needed to allow the user to have different orientations for the solar panels and the floating raft. It also needed to automatically calculate the tilts and orientations of the solar panels without requiring third-party software. Therefore, rotational matrices were used to calculate new tilt and orientation angles after particular movements, as explained in section 4.2.3 of this chapter.

4.2.1 General operation of OSIC

A graphical user interface (GUI) was created using the open-source GTK library [119]. This library uses computer objects called widgets that can be combined to create a graphical interface, therefore, facilitating the addition of text, buttons and other features. Furthermore, an application called Glade [120] was used to facilitate the placement of these widgets. This application also helps the programmer work more efficiently since one can visualise the graphical interface without having to execute the code.

In addition, the pbPlots [121] library was used for the interface to be able to plot graphs. This library allows the program to create and save .png graphics files, allowing users to keep the graphs after the application is closed.

Hence, the GUI was split into three sections, namely:

- The input section, shown in Figure 40
- The graphical results section and
- The numerical results section.

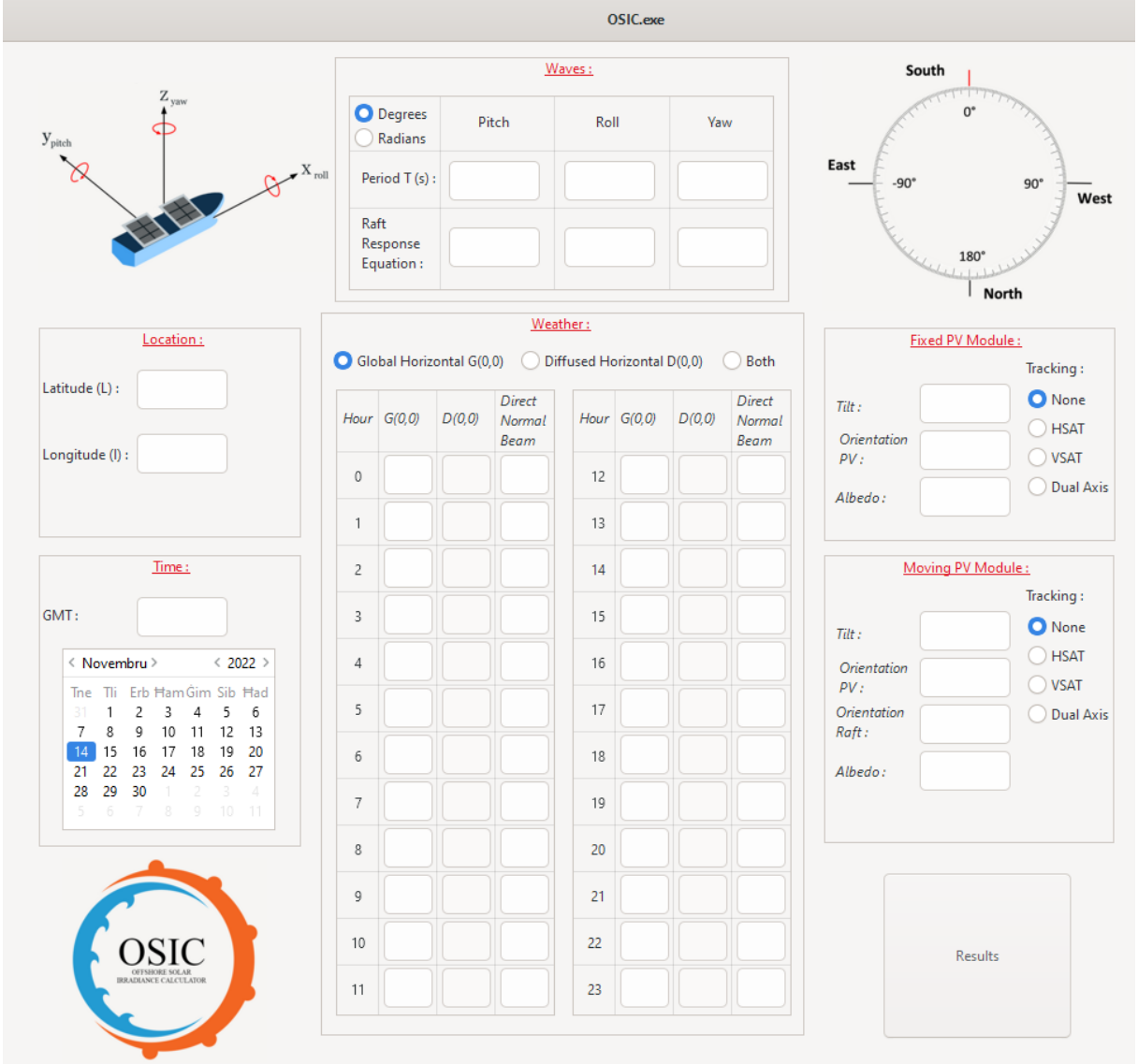

Figure 40: The input section of the OSIC Graphical User Interface.

The user first has to input the longitude and latitude of the installation, the Greenwich Mean Time (GMT), and the date on which the calculations are to be made. The date is input by choosing the correct day and year from the calendar on the left-hand side of the user interface. The calendar widget was included to ensure the correct format was used when inputting the date. Similar to the Excel file, this information is then used by a NOAA calculator [117] to find the Sun's position for every hour of the day. Hence, if the user selects a tracking system, the

software will calculate the solar panels' tilt and azimuth based on the Sun's position during the day. On the other hand, if the user selects a fixed installation, the tilt and azimuth angles will be set to the values entered by the user. Hence, the user has to enter hourly data for Direct Normal Beam and either global horizontal radiation G(0,0) or diffused horizontal radiation D(0,0) or both. If the user enters only one of the global or diffused radiation, the software will automatically calculate the other parameter.

Next, if a movement is required, the user has to enter a characteristic equation of this movement under one of the three movement categories. For the software to understand and compute this user input, a string parsing method was used to read the different parts of the equation. When the user enters an equation, the program only records a series of characters and does not understand what each character means. Therefore, specific instructions related to each character had to be programmed so that when the program reads each character independently, it could understand and execute the correct instruction. With this part of the code, the software could recognise various mathematical functions and symbols, such as trigonometric functions and pi. If the user enters a periodic equation, it has to be accompanied by an input for the period. Hence, the software will compute the amplitudes from these equations at a time step of 0.1s until the period value is reached. The right-hand rule was used as a movement convention, as shown in Figure 41, and users must adhere to this rule to obtain correct results.

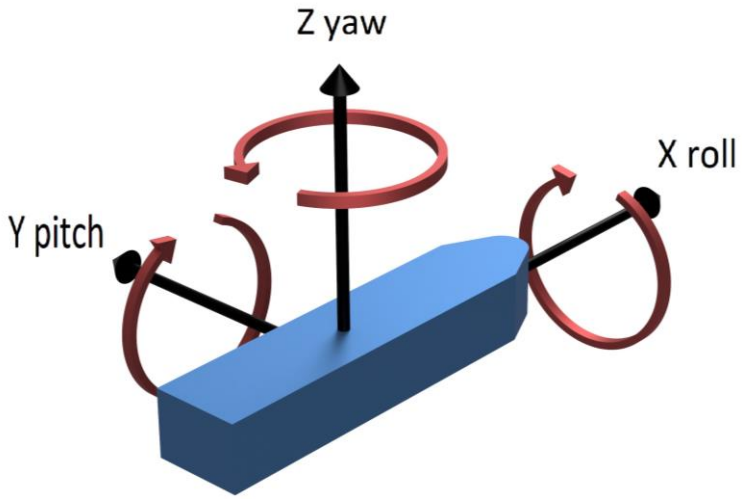

Figure 41: Right-hand rule convention for Pitch, Yaw and Roll movements.

After the user inputs the characteristic equations for pitch, yaw and roll movements, one must also choose between “Degrees” and “Radians” to inform the software how it should handle trigonometric functions. Finally, details must be input for the “Fixed PV Module” and the “Moving PV Module”. These details include the designed tilt and orientation of the PV for

non-tracking installations, the installation locations' albedo and the raft's orientation, which can differ from that of the solar panels. The "Orientation PV" refers to the azimuth of the PV installation. In contrast, the "Orientation Raft" refers to the orientation of the front of the raft abiding with the convention shown in Figure 41. If dual-axis or HSAT tracking is selected, the "Tilt" and "Orientation PV" boxes will be greyed out and will not allow any input, while if VSAT is selected, only the "Orientation PV" box will be greyed out.

Care was taken when transposing equations used in Excel into C language. For example, since we are using the NOAA calculations, the application needs to calculate the number of days that have passed since the beginning of the Gregorian calendar, which was introduced on the 15th of October, 1582 [117]. Software such as Microsoft Excel uses an Epoch to calculate the time since a specific date. This is an arbitrary date from which the software counts the number of seconds that have passed since the first of January 1900. This date is much later than the beginning of the Gregorian calendar. Therefore, the Excel simulation tool first calculates the number of days from the Excel epoch to the desired date and then adds the number of days between 1 January 1900 and 15 October 1582. However, the C language does not use the same epoch and uses the 1st of January 1970 instead [122]. It was therefore necessary to apply a correction and add the number of days between the two epochs.

Data inputs were protected against unexpected entries to prevent the software from crashing. For example, if a user inputs a negative period for the wave equations, a pop-up window will prompt the user to fix this before continuing, as shown in Figure 42. Once all the required fields have been filled in, the user clicks on the "Results" button, and the software runs all the calculations while the GUI changes to the graphical results section shown in Figure 43. This section is composed of six graphs, two for each raft movement. The top graphs show the irradiance incident on the fixed solar panels in blue and the irradiance incident on the offshore solar panels in orange. On the other hand, the second graph shows the percentage difference between the two irradiances when subtracting the fixed from the moving. This means that a negative percentage difference indicates that the moving PV installation receives a lower irradiance than the fixed installation.

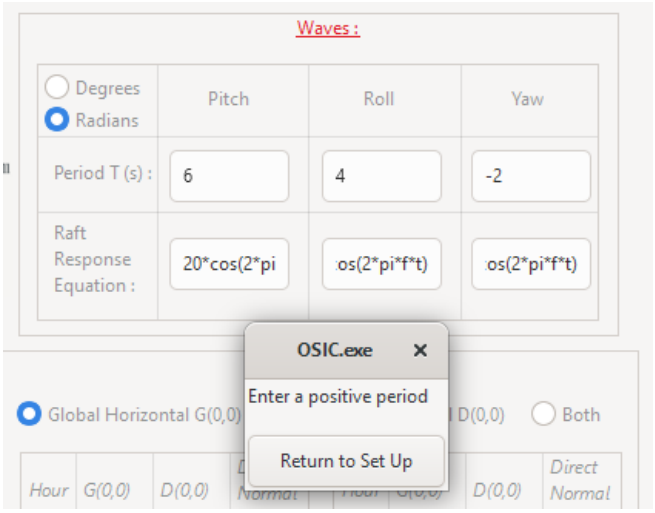

Figure 42: Pop-up window prompting the user to enter a positive period.

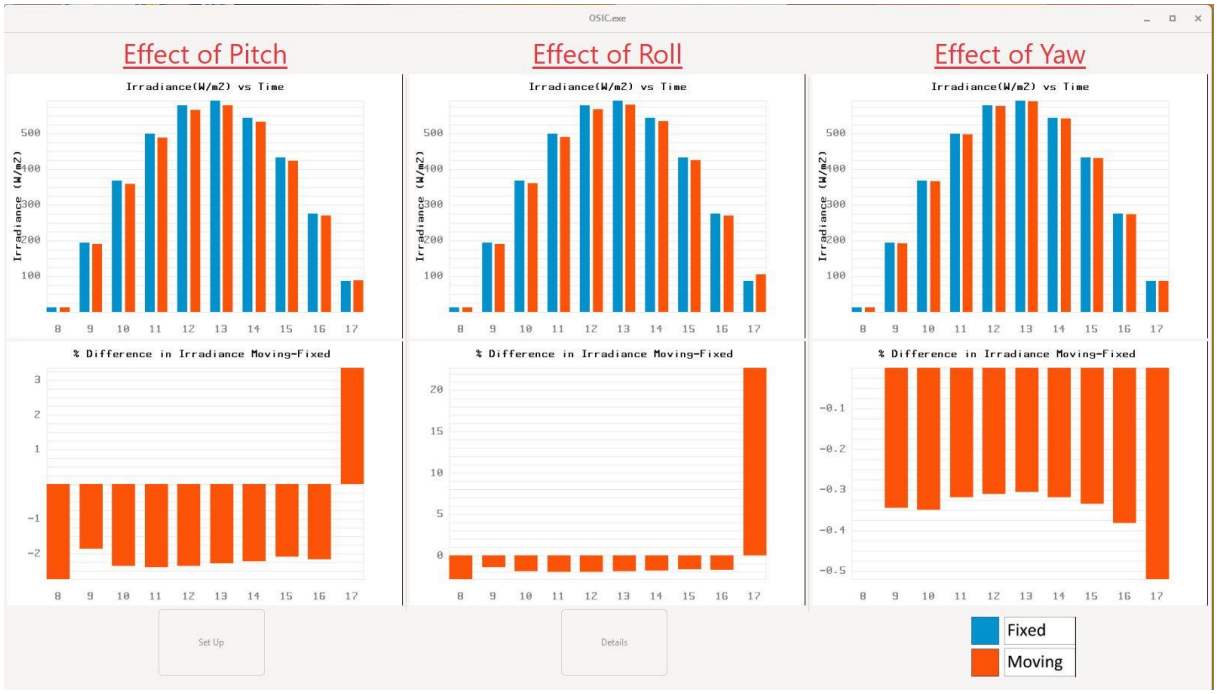

Figure 43: Graphical results section of the OSIC GUI.

Hence, the user can either click on the “Set Up” button to return to the GUI input section and modify some parameters or click on the “Details” button to view the GUI numerical results section, shown in Figure 44. This section shows the numerical values of the irradiance for every hour for both the fixed and moving PVs. In addition, this section also displays the percentage difference between the irradiance incident on the moving and the fixed solar panel, following the same convention as the graphical results section. Moreover, both results sections are dynamic and only show hours with irradiance values above zero to minimise the number of

calculations performed by the application and have a cleaner GUI. The data presented in this section can be copied and pasted into other third-party software for further processing and analysis. Finally, from this window, one can return either to the graphical results section or the input section.

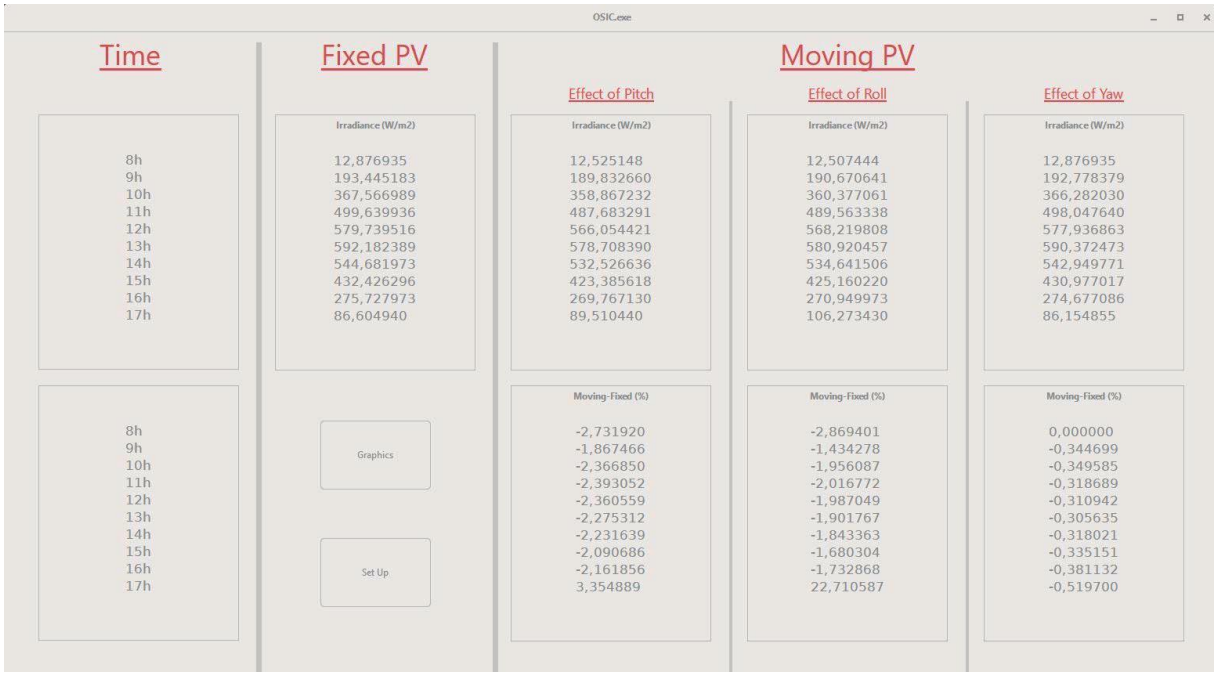

Figure 44: Numerical results section of the OSIC GUI.

The OSIC simulation tool was extensively tested, and any discovered bugs were corrected. The software robustness was increased by optimising any memory leaks occurring in the code and correctly handling unexpected user inputs without crashing. Furthermore, the software can check for weather data that does not make sense, and a pop-up message is shown to the user allowing them to continue or modify the input parameters. Moreover, information messages are shown when the pointer moves on various software parts to guide the user better.

4.2.2 Calculation of tilt and azimuth after movement.

To find the incident radiation for each wave-induced movement, it is necessary to know the exact tilt and azimuth of the offshore solar panels. These new tilts and azimuths are calculated every 0.1 seconds during a given period. However, it is not necessary to recalculate them every hour since the wave response equations of the raft are assumed to be the same throughout the day. A number of conventions had to be used to calculate the new tilt and azimuth. Firstly, the orthonormal frame of reference in which the boat is located follows the right-hand rule defined in Figure 41. In this figure, the red arrow indicates the positive direction of rotation. For

example, the yaw angle will be considered negative if the raft turns clockwise. The orthonormal reference is composed of the three vectors defined in equation (28).

$$\vec{x} = (1 \quad 0 \quad 0);\ \vec{y} = (0 \quad 1 \quad 0);\ \vec{z} = (0 \quad 0 \quad 1) \tag{28}$$

Rotation matrices must be used in order to calculate the rotations made by the solar panel. Rotation matrices calculate the new object's position after a rotation around one of the three principal axes passing through the origin of the orthonormal reference frame in which this object is located (represented in Figure 41 by the X, Y and Z axes). These new positions are then defined with reference to the basic orthonormal reference frame. It is possible to define rotation matrices both clockwise and counter-clockwise. However, OSIC software uses the clockwise matrix of rotation. The three rotation matrices for the pitch, yaw and roll movements are defined in Equations (29), (30) and (31) respectively.

$$R_{pitch} = \begin{bmatrix} \cos(x) & 0 & \sin(x) \\ 0 & 1 & 0 \\ -\sin(x) & 0 & \cos(x) \end{bmatrix} \tag{29}$$

$$R_{yaw} = \begin{bmatrix} \cos(x) & -\sin(x) & 0 \\ \sin(x) & \cos(x) & 0 \\ 0 & 0 & 1 \end{bmatrix} \tag{30}$$

$$R_{roll} = \begin{bmatrix} 1 & 0 & 0 \\ 0 & \cos(x) & -\sin(x) \\ 0 & \sin(x) & \cos(x) \end{bmatrix} \tag{31}$$

Assuming that:

- The vector $\vec{x}$ in front of the raft is oriented South
- The orientation of the PV module is the same as that of the raft
- The tilt of the panel is 0°; that is, it is lying horizontally on the raft.

Hence, a vector $\vec{a}$ normal to the plane formed by the solar panel is defined in equation (32).

$$\vec{a} = \begin{pmatrix} 0 \\ 0 \\ 1 \end{pmatrix} \tag{32}$$

When an object performs several rotations, it is possible to combine rotation matrices to create a new rotation matrix that describes the complete set of rotations. Hence, this new combined rotation matrix is multiplied by the normal vector of the base solar panel to obtain the new normal vector of the solar panel, after undergoing a set of rotations. When a photovoltaic system is installed on a floating raft, its orientation could differ from that of the raft. This means

that if we take the raft's orientation as a reference, a rotation around the z-axis (yaw) must be performed to describe the PV's orientation. If the angle between the orientation of the PV and the orientation of the raft is ψ , then this rotation can be described by a rotation matrix A defined by equation (33).

$$A = \begin{bmatrix} \cos(\psi) & -\sin(\psi) & 0 \\ \sin(\psi) & \cos(\psi) & 0 \\ 0 & 0 & 1 \end{bmatrix} \tag{33}$$

Once this rotation is complete, the main orthonormal frame may differ from the PV module's orthonormal frame. It is then possible to perform an extrinsic rotation around one of the axes of the main frame or an intrinsic rotation around one of the axes of the new PV frame itself. If an extrinsic rotation, described by matrix B, is performed after another rotation described by matrix A, the multiplication B*A is performed. If, on the other hand, an intrinsic rotation is performed after a rotation matrix A, the A*B multiplication is performed. After the rotation to match the orientation of the PV panel (described by matrix A), it is necessary to perform an intrinsic rotation to achieve the designed tilt of the PV panel. For this purpose, a rotation around the Y-axis of the orthonormal reference frame of the PV panel is performed. If θ represents the angle of this rotation, the matrix B describing this rotation is given by equation (34). This matrix is then multiplied by matrix A to obtain the rotation matrix C defined by equation (35). This rotation matrix is used as the basis for calculating the three rotation matrices for the roll, pitch and yaw effects of the waves on the raft.

$$B = \begin{bmatrix} \cos(\theta) & 0 & \sin(\theta) \\ 0 & 1 & 0 \\ -\sin(\theta) & 0 & \cos(\theta) \end{bmatrix} \tag{34}$$

$$C = AB = \begin{bmatrix} \cos(\psi) & -\sin(\psi) & 0 \\ \sin(\psi) & \cos(\psi) & 0 \\ 0 & 0 & 1 \end{bmatrix} \begin{bmatrix} \cos(\theta) & 0 & \sin(\theta) \\ 0 & 1 & 0 \\ -\sin(\theta) & 0 & \cos(\theta) \end{bmatrix}$$

$$C = \begin{bmatrix} \cos(\psi)\cos(\theta) & -\sin(\psi) & \cos(\psi)\sin(\theta) \\ \sin(\psi)\cos(\theta) & \cos(\psi) & \sin(\psi)\sin(\theta) \\ -\sin(\theta) & 0 & \cos(\theta) \end{bmatrix} \tag{35}$$

To calculate the effect of the roll on the position of the solar panel, the rotation matrix of the roll must be used. This is an extrinsic rotation because the effect of the waves is linked to the position of the raft and not to the position of the solar panels. Therefore, the main orthonormal reference frame must be used. If ϕ represents the angle of this rotation, the Matrix D describing

a roll movement is defined by Equation (36). This matrix is then multiplied by matrix C to obtain a new combined matrix E, as shown in Equation (37).

$$D = \begin{bmatrix} 1 & 0 & 0 \\ 0 & \cos(\phi) & -\sin(\phi) \\ 0 & \sin(\phi) & \cos(\phi) \end{bmatrix} \tag{36}$$

$$E = DC$$

$$= \begin{bmatrix} \cos(\psi)\cos(\theta) & -\sin(\psi) & \cos(\psi)\sin(\theta) \\ \cos(\phi)\sin(\psi)\cos(\theta) + \sin(\phi)\sin(\theta) & \cos(\phi)\cos(\psi) & \cos(\phi)\sin(\psi)\sin(\theta) - \sin(\phi)\cos(\theta) \\ \sin(\phi)\sin(\psi)\cos(\theta) - \cos(\phi)\sin(\theta) & \sin(\phi)\cos(\psi) & \sin(\phi)\sin(\psi)\sin(\theta) + \cos(\phi)\cos(\theta) \end{bmatrix} \tag{37}$$

Hence, the next step is to calculate the normal vector to the solar panel $\vec{v}$ after undergoing the roll effect. This is done by multiplying the normal vector of the solar panel before rotation, $\vec{a}$, by the matrix E, as shown in equation (38).

$$\vec{v} = E\vec{a} = \begin{pmatrix} \cos(\psi)\sin(\theta) \\ \cos(\phi)\sin(\psi)\sin(\theta) - \sin(\phi)\cos(\theta) \\ \sin(\phi)\sin(\psi)\sin(\theta) + \cos(\phi)\cos(\theta) \end{pmatrix} \tag{38}$$

The next calculation is the new tilt angle of the solar panel (β_n) after the roll movement, which corresponds to the angle between the vector $\vec{v}$ and the plane of the flat solar panel and is given by equation (39).

$$\beta_n = 90 - \arcsin\left(\frac{|\vec{v}.\vec{a}|}{\|\vec{v}\|.\|\vec{a}\|}\right) \tag{39}$$

$$\beta_n = 90 - arcsin\left(\frac{|\sin(\phi)\sin(\psi)\sin(\theta) + \cos(\phi)\cos(\theta)|}{\sqrt{(\cos(\psi)\sin(\theta))^2 + (\cos(\phi)\sin(\psi)\sin(\theta) - \sin(\phi)\cos(\theta))^2 + (\sin(\phi)\sin(\psi)\sin(\theta) + \cos(\phi)\cos(\theta))^2}}\right)$$

To calculate the orientation of the solar panel after the roll movement, the angle, α, between the vector $\vec{x} = (1 \quad 0 \quad 0)$ and the projection of the vector $\vec{v}$ on the plane composed of the vectors $\vec{x}$ and $\vec{y}$ must be calculated. The projection of the vector $\vec{v}$ is given by equation (40), while the angle α is calculated using equation (41).

$$\hat{v} = proj_v\vec{x} + proj_v\vec{y} = \begin{bmatrix} \cos(\psi)\sin(\theta) \\ \cos(\phi)\sin(\psi)\sin(\theta) - \sin(\phi)\cos(\theta) \\ 0 \end{bmatrix} \tag{40}$$

$$\alpha = \arccos\left(\frac{\vec{x}.\hat{v}}{\|\vec{x}\|.\|\hat{v}\|}\right)$$

$$\alpha = \arccos\left(\frac{\cos(\psi)\sin(\theta)}{\sqrt{(\cos(\psi)\sin(\theta))^2 + (\cos(\phi)\sin(\psi)\sin(\theta) - \sin(\phi)\cos(\theta))^2}}\right) \quad (41)$$

However, the result of α is an unsigned angle which does not necessarily show the correct orientation, abiding by the convention shown in Figure 45. To get more information on the sign of α, the angle between the projection $\hat{v}$ and the vector $\vec{y} = (0 \quad 1 \quad 0)$ is calculated using equation (42). If this angle, σ, is between 0 and 90, then α will be negative. Otherwise, it will be positive. Finally, the orientation of the raft as inputted by the user is added and the result is the true azimuth of the solar panel after a particular movement.

$$\sigma = arcos\left(\frac{\cos(\phi)\sin(\psi)\sin(\theta) - \sin(\phi)\cos(\theta)}{\sqrt{(\cos(\psi)\sin(\theta))^2 + (\cos(\phi)\sin(\psi)\sin(\theta) - \sin(\phi)\cos(\theta))^2}}\right) \quad (42)$$

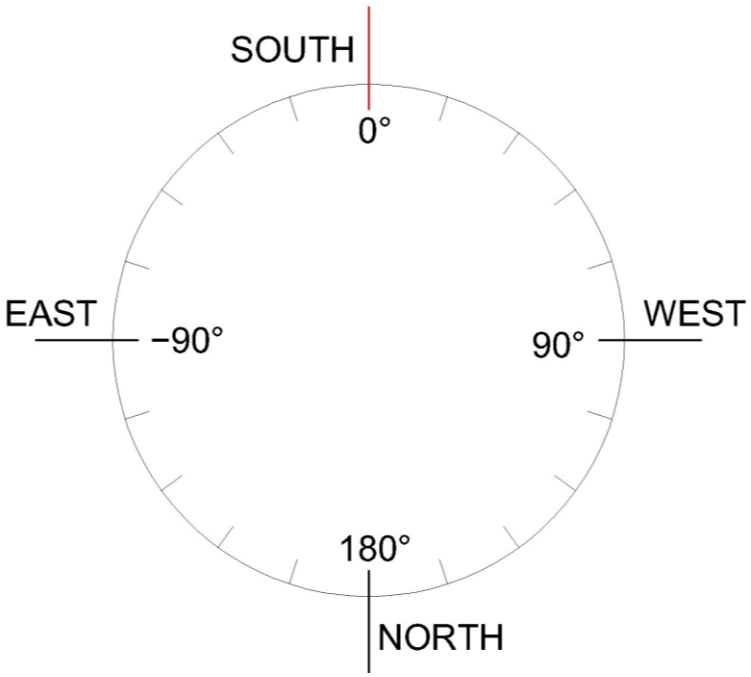

Figure 45: Convention of azimuth angles.

The calculations above give the tilt and azimuth angles of the solar panel after a roll movement. To obtain the tilt and azimuth angles after a yaw or a pitch movement, it is necessary to replace the matrix D in equation (36) with other matrices. Matrix F in equation (43) must be used for

yaw movements, where τ is the angular amplitude. Likewise, matrix G in equation (44) must be used for pitch movements, where n is the angular amplitude.

$$F = \begin{bmatrix} \cos(\tau) & -\sin(\tau) & 0 \\ \sin(\tau) & \cos(\tau) & 0 \\ 0 & 0 & 1 \end{bmatrix} \tag{43}$$

$$G = \begin{bmatrix} \cos(n) & 0 & \sin(n) \\ 0 & 1 & 0 \\ -\sin(n) & 0 & \cos(n) \end{bmatrix} \tag{44}$$

The new tilt and orientation after a yaw movement are calculated using equations (45) and (46), respectively.

$$\beta_n = 90 - arcsin\left(\frac{|\cos(\theta)|}{\sqrt{(\cos(\tau)\cos(\psi)\sin(\theta) - \sin(\tau)\sin(\psi)\sin(\theta))^2 + (\sin(\tau)\cos(\psi)\sin(\theta) + \cos(\tau)\sin(\psi)\sin(\theta))^2 + (\cos(\theta))^2}}\right) \tag{45}$$

$$\begin{aligned} \alpha &= \arccos\left(\frac{\cos(\tau)\cos(\psi)\sin(\theta) - \sin(\tau)\sin(\psi)\sin(\theta)}{\sqrt{(\cos(\tau)\cos(\psi)\sin(\theta) - \sin(\tau)\sin(\psi)\sin(\theta))^2 + (\sin(\tau)\cos(\psi)\sin(\theta) + \sin(\phi)\cos(\theta))^2}}\right) \\ \sigma &= arcos\left(\frac{\sin(\tau)\cos(\psi)\sin(\theta) - \cos(\tau)\sin(\psi)\sin(\theta)}{\sqrt{(\cos(\tau)\cos(\psi)\sin(\theta) - \sin(\tau)\sin(\psi)\sin(\theta))^2 + (\sin(\tau)\cos(\psi)\sin(\theta) + \sin(\phi)\cos(\theta))^2}}\right) \end{aligned} \tag{46}$$

The new tilt and orientation after a pitch movement are calculated using equations (47) and (48), respectively.

$$\beta_n = 90 - arcsin\left(\frac{|-\sin(n)\cos(\psi)\sin(\theta) + \cos(n)\cos(\theta)|}{\sqrt{(\cos(n)\cos(\psi)\sin(\theta) + \sin(n)\cos(\theta))^2 + (\sin(n)\sin(\theta))^2 + (\sin(n)\cos(\psi)\sin(\theta) + \cos(n)\cos(\theta))}}\right) \tag{47}$$

$$\begin{aligned} \alpha &= \arccos\left(\frac{\cos(n)\cos(\psi)\sin(\theta) + \sin(n)\cos(\theta)}{\sqrt{(\cos(n)\cos(\psi)\sin(\theta) + \sin(n)\cos(\theta))^2 + (sin(n)\,sin(\theta))^2}}\right) \\ \sigma &= arcos\left(\frac{\sin(\psi)\sin(\theta)}{\sqrt{(\cos(n)\cos(\psi)\sin(\theta) + \sin(n)\cos(\theta))^2 + (sin(n)\,sin(\theta))^2}}\right) \end{aligned} \tag{48}$$

4.2.2.1 Practical Example

Considering a scenario where a user inputs details of a panel installed with a tilt of 30 degrees facing south, on a raft with an azimuth of 20 degrees, which rolls 5 degrees from East to West. The vector normal to the plane formed by the solar panel is still equal to equation (32).

Furthermore, ψ is the angle between the orientation of the raft and the azimuth of the solar panel which is equal to 20 degrees, resulting in a matrix A, as shown in equation (49).

$$A = \begin{pmatrix} \cos(20) & -\sin(20) & 0 \\ \sin(20) & \cos(20) & 0 \\ 0 & 0 & 1 \end{pmatrix} \tag{49}$$

θ is the original tilt angle which is equal to 30 degrees. Therefore, matrices B and C are given by equations (50) and (51), respectively.

$$B = \begin{pmatrix} \cos(30) & 0 & \sin(30) \\ 0 & 1 & 0 \\ -\sin(30) & 0 & \cos(30) \end{pmatrix} \tag{50}$$

$$C = \begin{pmatrix} \cos(20)\cos(30) & -\sin(20) & \cos(20)\sin(30) \\ \sin(20)\cos(30) & \cos(20) & \sin(20)\sin(30) \\ -\sin(30) & 0 & \cos(30) \end{pmatrix} \tag{51}$$

Following the convention in Figure 41, since the roll is from the East to the West, the angle of the roll, ϕ, is positive and is equal to 5 degrees. Therefore, the matrix D and E are given by equations (52) and (53), respectively. Also, the normal vector to the solar panel after undergoing the roll movement, $\vec{v}$, is shown in equation (54).

$$D = \begin{pmatrix} 1 & 0 & 0 \\ 0 & \cos(5) & -\sin(5) \\ 0 & \sin(5) & \cos(5) \end{pmatrix} \tag{52}$$

$$E = \begin{pmatrix} \cos(20)\cos(30) & -\sin(20) & \cos(20)\sin(30) \\ \cos(5)\sin(20)\cos(30) + \sin(5)\sin(30) & \cos(5)\cos(20) & \cos(5)\sin(20)\sin(30) - \sin(5)\cos(30) \\ \sin(5)\sin(20)\cos(30) - \cos(5)\sin(30) & \sin(5)\cos(20) & \sin(5)\sin(20)\sin(30) + \cos(5)\cos(30) \end{pmatrix} \tag{53}$$

$$\vec{v} = \begin{pmatrix} \cos(20)\sin(30) \\ \cos(5)\sin(20)\sin(30) - \sin(5)\cos(30) \\ \sin(5)\sin(20)\sin(30) + \cos(5)\cos(30) \end{pmatrix} \tag{54}$$

This results in a new solar panel tilt, β_n, of **28.64°** after the effect of the roll, as shown in equation (55)

$$\beta_n = 90 - arcsin\left(\frac{|\sin(5)\sin(20)\sin(30) + \cos(5)\cos(30)|}{\sqrt{(\cos(20)\sin(30))^2 + (\cos(5)\sin(20)\sin(30) - \sin(5)\cos(30))^2 + (\sin(5)\sin(20)\sin(30) + \cos(5)\cos(30))^2}}\right) = 28.64° \tag{55}$$

The projection of the vector $\vec{v}$ is shown in equation (56), while the unsigned azimuth and the sign test are shown in equation (57).

$$\hat{v} = \begin{pmatrix} \cos(20)\sin(30) \\ \cos(5)\sin(20)\sin(30) - \sin(5)\cos(30) \\ 0 \end{pmatrix} \tag{56}$$

$$\alpha = \arccos\left(\frac{\cos(20)\sin(30)}{\sqrt{(\cos(20)\sin(30))^2 + (\cos(5)\sin(20)\sin(30) - \sin(5)\cos(30))^2}}\right)$$

$$\alpha = 11.42°$$

$$\sigma = arcos\left(\frac{\cos(5)\sin(20)\sin(30) - \sin(5)\cos(30)}{\sqrt{(\cos(20)\sin(30))^2 + (\cos(5)\sin(20)\sin(30) - \sin(5)\cos(30))^2}}\right) \tag{57}$$

$$\sigma = 78.58°$$

Since σ is between 0 and 90, one can then deduce that α is negative. Therefore, the final step would be to add the original azimuth of the raft (20°) to α so as to obtain the real azimuth of the solar panel, Γ, as shown in equation (58).

$$\Gamma = -11.42 + 20 = \mathbf{8.58}° \tag{58}$$

4.2.3 Calculation of irradiance on tracking surfaces

When calculating the irradiance on a tracking surface, the anisotropic model was used, similar to that described in section 3.2.4 Anisotropic model. A dual-axis tracker adjusts both the tilt and azimuth of the solar panel to maintain its surface always perpendicular to the Sun throughout the day [112]. This implies that the tilt angle of the solar panel is always equal to the solar zenith angle while the azimuth of the solar panel is always equal to the solar azimuth. A vertical single-axis solar tracker (VSAT) has a fixed tilt set during the installations while its azimuth changes during the day and is equal to the solar azimuth. The incidence angle is found by subtracting the surface's fixed tilt from the solar zenith angle.

A horizontal N-S single-axis tracker (HSAT) tracks the Sun from East to West on a horizontal axis. This implies that the tilt constantly changes during the day while the orientation is either towards the East or towards the West. The solar panel's tilt angle is a function of the solar azimuth angle γ_S and the solar altitude α_S, given by Equation (59). The solar incident angle on the tilted surface, θ, is found using equation (*60*) [112].

$$\beta_n = \tan^{-1}\left|\frac{\sin\gamma_S}{\tan\alpha_S}\right| \tag{59}$$

$$\theta = \cos^{-1}\left(\cos\delta \times \sqrt{[(\sin\omega)^2 + (\cos\emptyset\cos\omega + \tan\delta\sin\emptyset)^2]}\right) \tag{60}$$

4.2.4 Description of OSIC code

The programming of the OSIC tool was done in C language using Microsoft Visual Studio 2022 IDE. The program was organised into multiple files, each handling different parts of the software. A file named Source1.c contains all the functions required to setup the user interface. A main() function is called, and communication with the GTK library [119] is initiated to set up the user interface. Furthermore, data from the Glade project [120] file is read, and each GUI widget is associated with variables to be used by other parts of the program.

The OSIC interface needed to work on screens with different resolutions and sizes. Therefore, after all widgets are initialised, a GetSystemMetrics() function is called to find the size of the user's screen. This function returns the screen's pixel width and height, which are then divided by the base width and height defined in the Glade software (1920x1080). This step enables us to find the percentage reduction required to have all widgets in the user interface shown as intended. Hence, after finding this percentage, it is applied to all widgets and the GUI is adapted to the user's display.

Another function, on_radioButton_clicked, is used to grey out areas to avoid unexpected or conflicting inputs. For example, if the user selects "Dual Axis Tracking", the software will calculate the PV tilt and orientation angles based on the Sun's position. Therefore, the corresponding GUI fields are greyed out, and the user cannot input any values. After the user adjusts all parameters in the "Set Up" section, the "Results" button is pressed. This triggers a function on_button1_clicked() which reads all the parameters entered by the user and sends them to the main function for further processing and plotting. Hence, the following functions are linked to the "Details", "Graph" and "Set Up" buttons, respectively:

- on_buttonNumbers1_clicked()
- on_buttonGraphs1_clicked()
- on_buttonSetUp1_clicked()

These functions enable the user to quickly switch between the different sections of the software.

A Calcul.c file contains the major mathematical equations used by the simulation tool. This file is responsible for creating the time and date corresponding to the calculated data. This is done by creating a timeAndDate[] array of 24 spaces corresponding to every hour of the day. Hence, a calculTimeAndDate() function reads the GMT Zone of the location of the PV installation and uses the timeAndDate[] array to calculate all variables for every hour of the day. After having the time and date in the desired format, a calculSun() function is called, which uses adapted NOAA equations to calculate all variables related to the Sun's position for every hour of the day. This function also uses two other functions conversionDegreesRadians() and conversionRadiansDegrees(), to convert angles from degrees to radiance and vice versa.

Weather data entered by the user is stored in a 24-spaces weather[] array. Hence, a calculWeather() function takes information from a calculationsSun[] array to calculate any missing weather data. Next, if tracking is selected, tracking algorithm equations are executed for all hours of the day. Hence, Isotropic and Anisotropic (Perez) calculations are carried out. However, the current software version only displays the results of the Anisotropic model. The calculPerezFixed() function accesses various stored variables and constants required to calculate the Perez model equations [115], [116], as described in section 3.2.4 above.

A main.c file calls various functions stored in the Calcul.c file and performs other calculations and memory management operations. The angles corresponding to the wave characteristic equations are calculated every 0.1 seconds for a whole cycle, defined as the time between two wave peaks. A two-dimensional dynamic array was created since the wave period is a variable the user enters. This array consists of 24 spaces corresponding to every hour of the day. Each of these spaces consists of a dynamic array corresponding to rotation angles calculated every 0.1 seconds for the duration of a wave period. Hence, as shown in Figure 46, the malloc() function was used to allocate the required memory to store data in the dynamic array.

When memory is manually allocated, it is crucial to release the allocation as soon as the program no longer needs it. This step is essential to avoid what is known as "memory leaks", which would continuously increase computer memory use until the resource runs out. This would impact the operation of all applications running on the computer since the memory resource would be depleted. Therefore, the free() function was used to deallocate memory. Since we were dealing with a two-dimensional array, it was necessary to deallocate memory in the reverse order of its allocation, as shown in Figure 47.

```
    int sizeRoll=(int)floor(wave.periodRoll/0.1);
    int sizePitch=(int)floor(wave.periodPitch/0.1);
    int sizeYaw=(int)floor(wave.periodYaw/0.1);

    roll=malloc(24*sizeof(Rotations *));
    yaw=malloc(24*sizeof(Rotations *));
    pitch=malloc(24*sizeof(Rotations *));

int i=0;
    for(i = 0; i < 24; ++i){
        roll[i]=malloc(sizeRoll*sizeof(Rotations));
        yaw[i]=malloc(sizeYaw*sizeof(Rotations));
        pitch[i]=malloc(sizePitch*sizeof(Rotations));
    }

    if(roll==NULL||pitch==NULL||yaw==NULL){
        exit(0);
    }
```

Figure 46: Allocating memory to a dynamic two-dimensional array.

```
for(int i = 0; i < 24; ++i)
{
    free(roll[i]);
    free(yaw[i]);
    free(pitch[i]);
}
free(roll);
free(yaw);
free(pitch);
```

Figure 47: Releasing manually allocated memory for a two-dimensional array.

A calculWave() function calculates the tilt and azimuth angles of the solar panels every 0.1 seconds and stores data for roll, pitch and yaw effects to be used by other functions. This function uses a string parsing method to understand the equation inputted by the user and execute the corresponding mathematical functions such as addition, multiplication or trigonometry. Finally, the finalResults() function performs the statistical calculations. This function calculates the average of the irradiance models for every hour for the fixed and the three movements scenarios. Hence the percentage difference is calculated using equation (*61*).

$$Percentage\ Difference = 100 \times \left(\frac{Offshore\ Irradiance}{Fixed\ Iradiance} - 1\right) \quad (61)$$

The output of the finalResults() function is plotted using the pbPlots library [121]. Also, this function uses the printString() function to display the numerical results in the "Details" section of the OSIC software. In cases where, for example, very high latitudes are chosen, resulting in no insolation during the day, a message is printed stating: "*There are 0 hours of Sunshine during the selected period*".

4.3 Results and discussion

The OSIC simulation tool was used to perform a parametric analysis for all three types of tracking systems and for each month of the year. A day was chosen for every month, and weather data for that day was used to obtain the results. Clear days were chosen with the least clouds possible and close to the 21st of each month to include equinoxes and solstices. Equation (62) was inputted for all three movements and a period of 6s was chosen. The results obtained are shown in Table 7.

$$f(t) = 20 \times \cos(2 \times pi \times f \times t) \quad (62)$$

The first observation from the results in Table 7 is that an HSAT system with N-S horizontal axis and with the raft's orientation facing south is mostly affected by roll movements compared to pitch and yaw movements. This is because yaw movements will only change the azimuth of the PV, while pitch movements will slightly change both azimuth and tilt. In contrast, roll movements directly affect the PV's tilt, which means that such movements are going against the HSAT algorithm designed to capture the maximum irradiance for such an installation. Therefore, OSIC software informs a raft designer that if such a tracking system is installed, care must be taken to limit response movements to incoming waves in the roll direction. Figure 48 shows the hourly effects on an HSAT caused by Roll, Pitch and Yaw movements for the months of June and December. Yaw movements have no effect on an HSAT system during the middle part of the day since the algorithm sets the PV to a horizontal inclination during this time. In contrast, pitch movements have a higher effect during this period since these movements result in a considerable change in tilt.

Table 7: Parametric analysis of insolation deviation of offshore tracking systems from land.

Insolation deviation of offshore from land - HSAT			
Month	**Effect of Pitch**	**Effect of Roll**	**Effect of Yaw**
January	-0.93%	-2.31%	-1.33%
February	-0.96%	-2.00%	-1.06%
March	-0.98%	-2.16%	-1.14%
April	-1.06%	-2.06%	-0.96%
May	-1.15%	-2.35%	-1.20%
June	-1.11%	-2.31%	-1.13%
July	-1.18%	-2.38%	-1.14%
August	-1.10%	-2.33%	-1.18%
September	-1.00%	-2.28%	-1.24%
October	-0.94%	-2.20%	-1.21%
November	-0.98%	-2.28%	-1.31%
December	-0.88%	-2.21%	-1.34%
Insolation deviation of Offshore from Land – VSAT β=30°			
Month	**Effect of Pitch**	**Effect of Roll**	**Effect of Yaw**
January	-2.07%	-1.41%	-1.47%
February	-1.71%	-1.55%	-1.07%
March	-1.66%	-1.83%	-1.04%
April	-1.53%	-1.95%	-0.82%
May	-1.53%	-2.31%	-0.95%
June	-1.48%	-2.28%	-0.89%
July	-1.54%	-2.30%	-0.92%
August	-1.58%	-2.16%	-0.99%
September	-1.70%	-1.93%	-1.12%
October	-1.83%	-1.60%	-1.22%
November	-2.09%	-1.43%	-1.46%
December	-2.15%	-1.30%	-1.55%

Insolation deviation of offshore from land – DUAL AXIS TRACKER			
Month	**Effect of Pitch**	**Effect of Roll**	**Effect of Yaw**
January	-1.95%	-1.08%	-2.13%
February	-1.53%	-1.32%	-1.60%
March	-1.41%	-1.75%	-1.47%
April	-1.30%	-1.94%	-1.10%
May	-1.26%	-2.28%	-1.26%
June	-1.23%	-2.25%	-1.18%
July	-1.29%	-2.30%	-1.20%
August	-1.31%	-2.16%	-1.32%
September	-1.45%	-1.83%	-1.57%
October	-1.65%	-1.40%	-1.79%
November	-1.96%	-1.05%	-2.12%
December	-2.05%	-0.90%	-2.23%

Figure 49 shows the hourly effects on a VSAT caused by Roll, Pitch and Yaw movements for the months of June and December. This figure clearly shows that Yaw movements in December have a higher negative effect on the insolation than in June. This is because the irradiance on a tilted plane follows a cosine function. Therefore, although the change in incidence angle is lower in December than in June, the change in cos (theta) is higher. This figure also shows that roll movements in the mornings and evenings have a higher effect in summer than in winter. This is because, during these times of the day, roll movements have a major effect on the tilt of the solar panel. Since, in summer, the chosen tilt is close to the optimum, any deviation will always result in less irradiance incident on the solar panel.

The results in Table 7 show that Yaw has the biggest effect on dual-axis trackers compared to the other tracking mechanisms. This is because the tracking algorithm always orients the PV into a quasi-optimal tilt and orientation. Therefore, any movement will always result in a deviation from the optimal, which means a loss in irradiance incident on the PV. Moreover, Yaw movements on a dual-axis tracker have a higher negative impact in winter than other tracking systems since tilts are higher and therefore changes in azimuth have a higher effect on the incident radiation. Pitch movements in the mornings and evenings slightly alter the tilt and

orientation and therefore do not have the same effect magnitude as roll movements. Although the effect of pitch movements increases in the middle of a summer day since they start affecting the tilt, roll movements still have a considerable negative effect since, at this time, they vary considerably both tilt and orientation. In contrast, during a winter midday, the panel is oriented towards a low-elevation Sun which means it is at a high tilt. Therefore, roll movements are less important than pitch movements since the latter considerably affects the tilt while the former slightly varies both tilt and orientation.

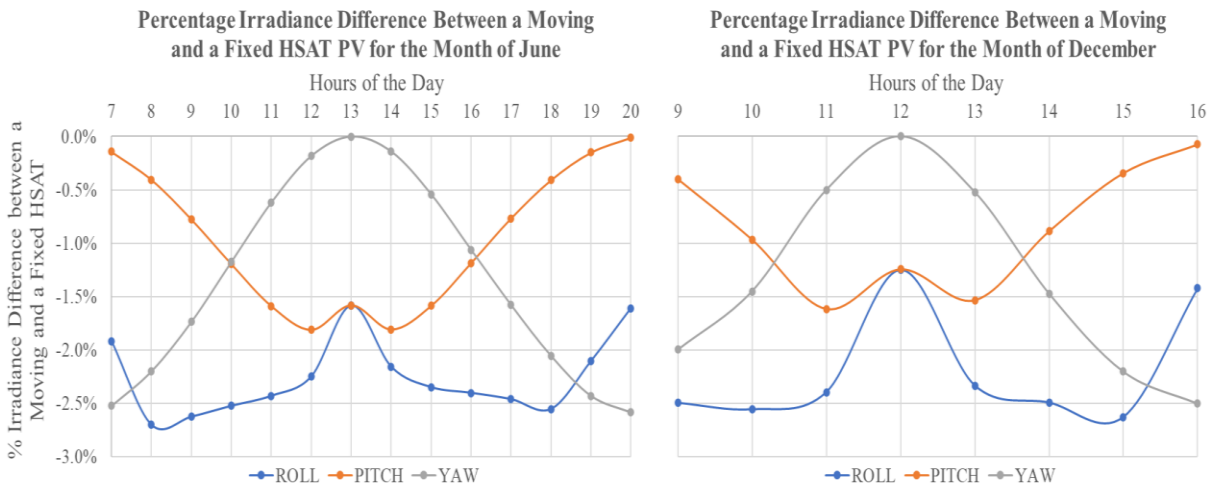

Figure 48: Percentage irradiance difference between a moving and a fixed HSAT PV for the months of June and December.

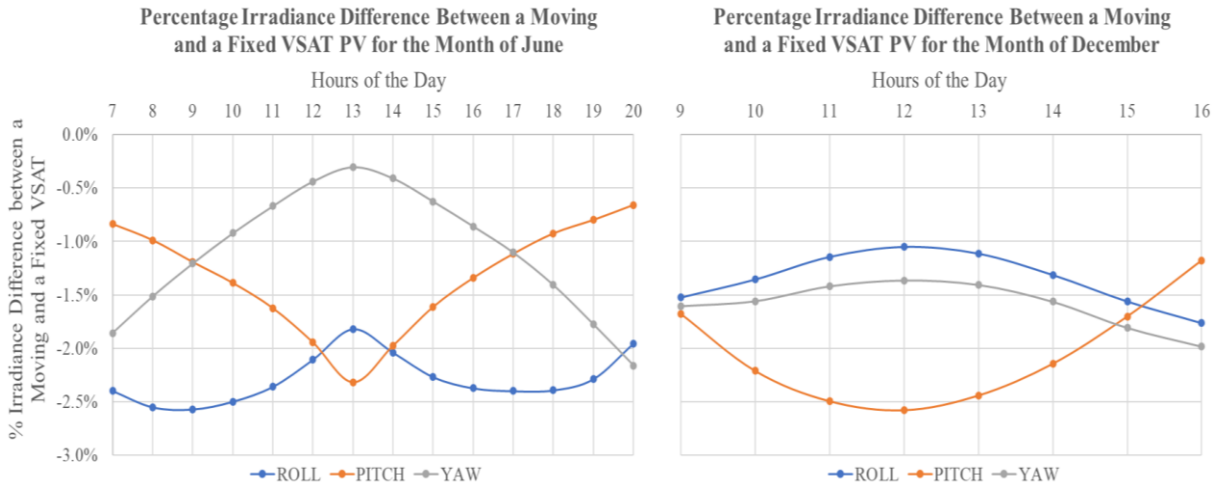

Figure 49: Percentage irradiance difference between a moving and a fixed VSAT PV for the months of June and December.

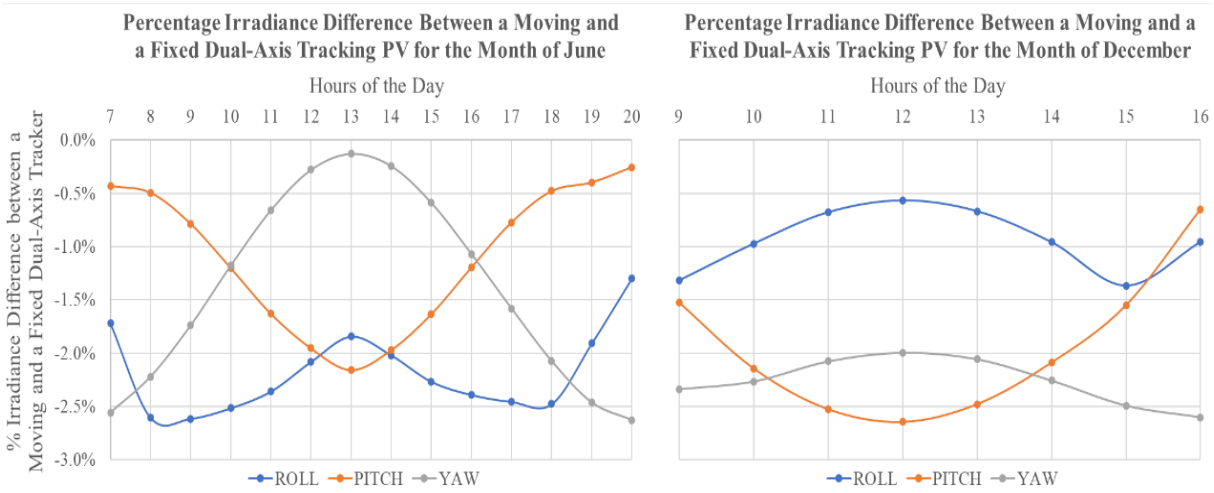

Figure 50: Percentage irradiance difference between a moving and a fixed Dual-Axis tracking PV for the months of June and December.

A final parametric analysis was performed to observe the changes in the effects of waves with varying oscillation amplitudes on a June day. These amplitudes were varied between 0° and 50°. The results for Dual-Axis Tracker and HSAT are shown in Figure 51 and Figure 52 respectively. Furthermore, three fixed tilts were chosen for the VSAT, namely 5°, 30° and 50° and the results were tabulated in Table 8.

These results show that the relationship between the percentage difference in irradiance and the amplitude of oscillations is not linear for the chosen wave. Furthermore, roll effects are more predominant in tracking systems when compared to fixed systems, previously reported in section 3.3 of this thesis. This is because, as previously discussed, roll movements in an HSAT directly influence the tilt of the PV. In comparison, roll movements for other tracking systems result in a deviation in tilt and orientation, both of which are already quasi-optimised by the tracking algorithm. These results were published in the peer-reviewed journal MDPI Energies [118].

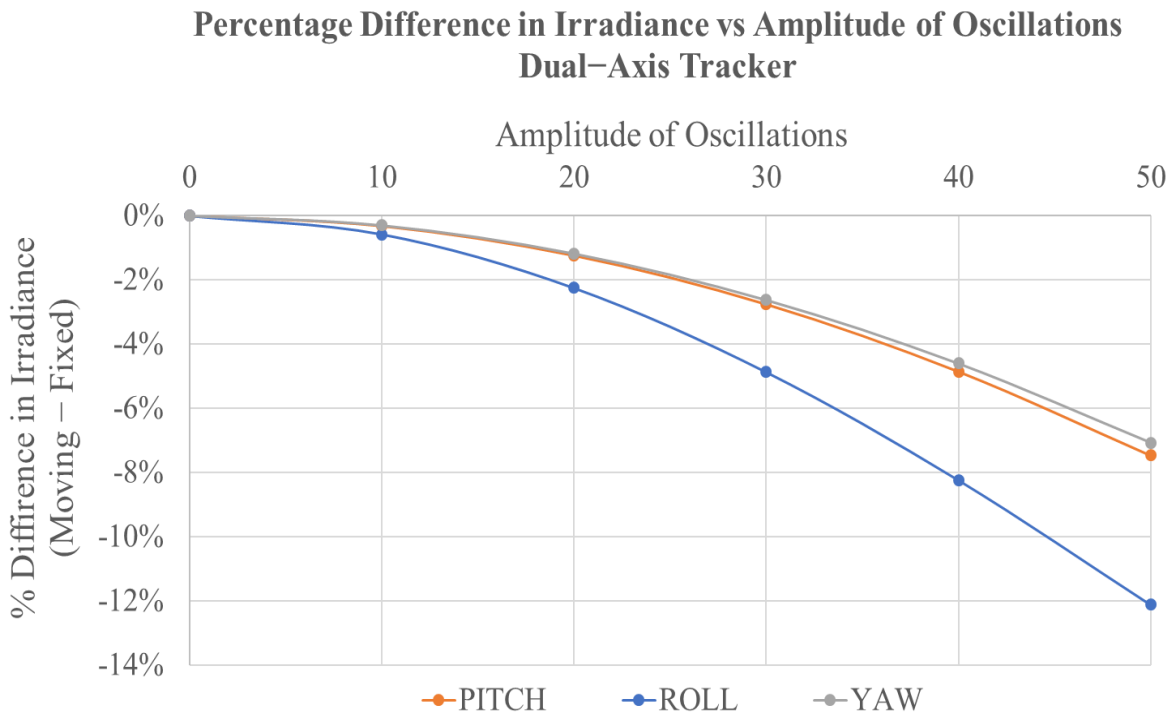

Figure 51: Percentage irradiance difference between a moving and a fixed Dual-Axis tracking PV for different amplitude of oscillations in a day in June.

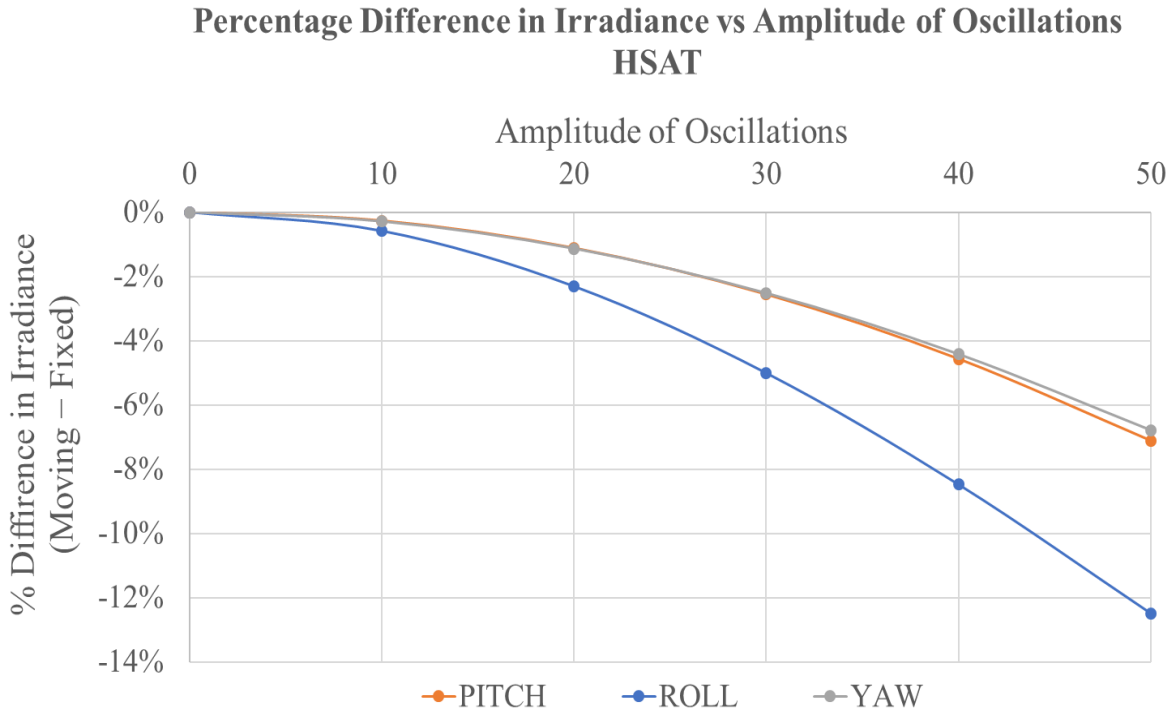

Figure 52: Percentage irradiance difference between a moving and a fixed HSAT PV for different amplitude of oscillations in a day in June.

Table 8: Percentage irradiance difference between a moving and a fixed VSAT PV for different tilts and amplitude of oscillations in a day in June.

VSAT Tilt	Effect of Pitch	Effect of Roll	Effect of Yaw
Wave Amplitude = 10°			
5°	-0.31%	-0.39%	-0.05%
30°	-0.37%	-0.57%	-0.22%
50°	-0.30%	-0.57%	-0.33%
Wave Amplitude = 20°			
5°	-1.49%	-1.56%	-0.19%
30°	-1.48%	-2.28%	-0.89%
50°	-1.18%	-2.27%	-1.31%
Wave Amplitude = 30°			
5°	-3.63%	-3.49%	-0.42%
30°	-3.31%	-5.06%	-1.99%
50°	-2.64%	-5.07%	-2.93%
Wave Amplitude = 40°			
5°	-6.73%	-5.99%	-0.74%
30°	-5.82%	-8.78%	-3.48%
50°	-4.63%	-8.88%	-5.14%
Wave Amplitude = 50°			
5°	-10.74%	-8.92%	-1.14%
30°	-8.98%	-13.28%	-5.35%
50°	-6.81%	-12.07%	-7.89%

4.4 Conclusion

This chapter presented the optimisation of a simulation tool to include the effects of wave response motion on offshore HSAT, VSAT and dual-axis PV tracking systems. This new simulation tool was termed the Offshore Solar Irradiance Calculator (OSIC), which, at the time of writing, is the only available tool that allows the user to quantify the effect of waves on offshore photovoltaic installations. A parametric analysis was performed using a characteristic wave equation, and the effects of pitch, roll and yaw movements were observed and presented. Roll movements resulted in the maximum negative effects, with HSATs and VSATs demonstrating a maximum loss of −2.38%, while a −2.3% loss was observed for the dual-axis tracker. Furthermore, a parametric analysis of the effects of different wave-response amplitudes

on the incident irradiance was presented. The greatest effect was observed for a 50° amplitude wave response, with losses exceeding −12%. Moreover, this part of the research showed that, for the same wave type, the effect of a moving raft varies for non-tracking and tracking installations.

This study's limitation is that it assumes that wave response movement occurs after the tracking algorithm has successfully reached its objective. In reality, it is hypothesised that implementing offshore tracking will face other challenges since the tracking algorithm has to work in a constantly moving environment. This can be confusing for the control algorithm since it would constantly receive varying feedback from the irradiance sensors. This limitation can be overcome by slightly sacrificing tracking accuracy and implementing an open-loop tracking algorithm based on a tilt and orientation database, that is dependent on the time of the year. Furthermore, the effect of shading caused by the movement of the floating raft was not quantified in this study. In offshore installations, PVs will most likely be installed at very low angles to decrease the forces acting on them and increase the energy density by fitting more modules on each floating raft. Therefore, although not considered by this study, the effect of PV row shading is expected to be minimal. Similarly, the same albedo was used for land and offshore installations so as to isolate the effect caused by wave response motion. The difference in albedo between installations has a further effect on the incident radiation. However, if large concrete-based rafts are used for such installations, albedo values will become more comparable.

5. Photovoltaic back-side cooling using the space inside a conventional frame (IPCoSy)

5.1 Introduction

Various cooling methodologies have been adopted for PV modules to reduce the negative effect of rising temperature on power output. However, from the literature, it was evident that water-cooling is the most feasible technology for offshore photovoltaic installations due to the very large water resource. In this section, a modified back-side water-cooling system was studied due to its various benefits both offshore and on land. The first part of this chapter, concerning the small-scale design and experiments, was published in Future Energy journal [123].

5.2 Hypothesis

From the literature, one can find various implementations of back-side cooling. The hypothesis studied in this research is that if one creates a water chamber at the back of the PV modules, the added specific heat capacity will keep the modules cooler during the day, thus, working more efficiently. Furthermore, a new modified flow is being proposed where a water flow is initiated to lower the PV module's temperature. After reaching the required low-temperature threshold, the water is stored in a chamber in contact with the back of the PV module instead of being discarded. With this setup, the PV module should take longer to reach the high-temperature threshold and therefore, the pump switching frequency is reduced, prolonging the pump's lifetime and decreasing the power consumed. The photovoltaic cooling system was termed Innovative Photovoltaic Cooling System (IPCoSy) and the official logo for this innovation is shown in Figure 53.

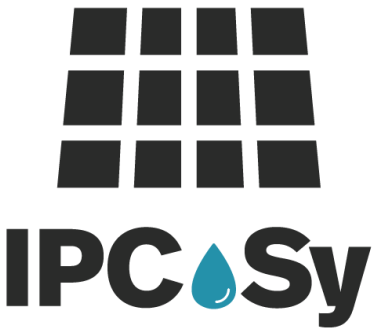

Figure 53: IPCoSy official logo.

5.3 Small scale methodology

5.3.1 Prototype design

Initially, two different prototypes were designed and implemented to test the above hypothesis. The first prototype involved the modification of an existing photovoltaic module consisting of a top glass cover, a polymer back sheet and an aluminium frame. Small 5W ET solar panels were used to facilitate in-house prototyping. The dimensions of the active area were 30.5cm by 12.5cm, while the dimensions of the water chamber were 38.5cm by 16cm by 2.5cm. This resulted in a volume of water of 1.54L or 40.4L per m^2 of PV active area. A cross-section of a conventional photovoltaic module can be seen in Figure 54. The idea of this prototype was to close the back-side of the module, thus creating a closed chamber underneath, as shown in the design in Figure 55. In practice, this can be achieved by welding an aluminium sheet; however, for the scope of this research, a 5mm Poly (methyl methacrylate) sheet was used instead.

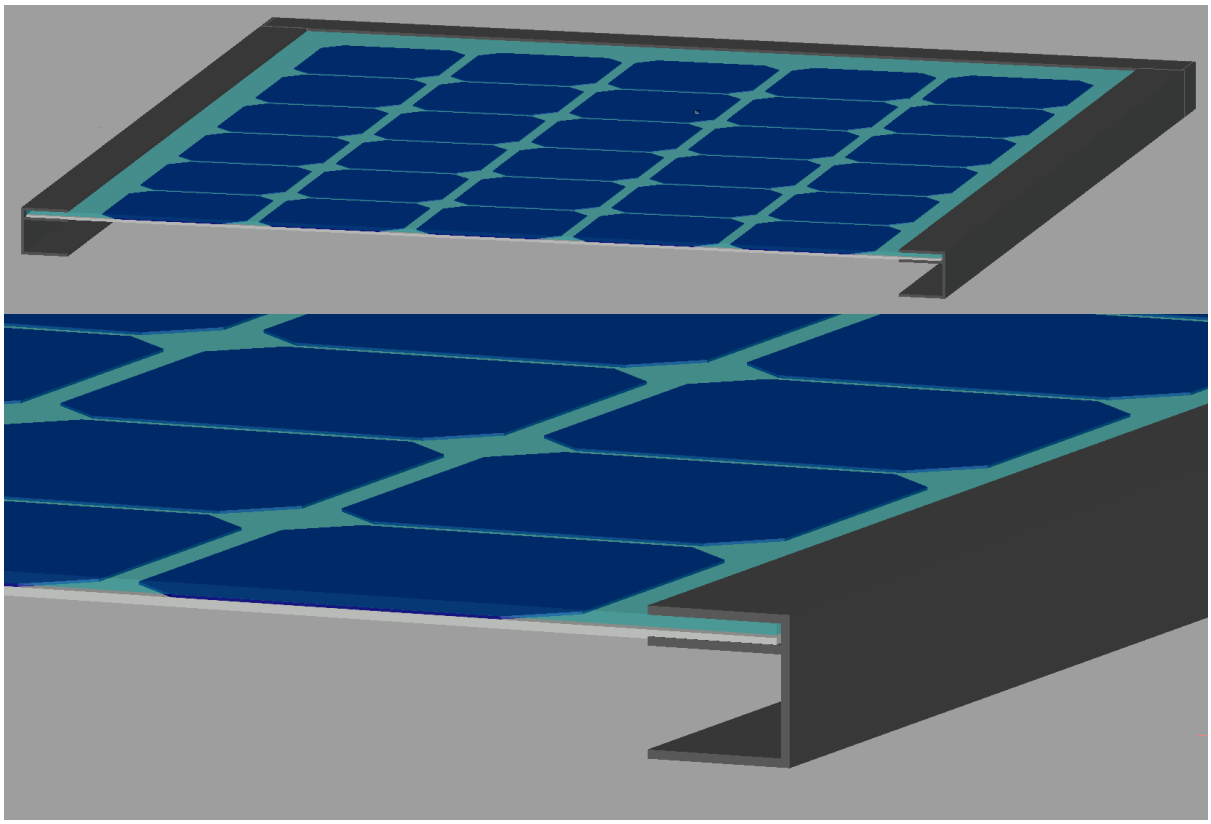

Figure 54: Cross-sections of a standard photovoltaic module.

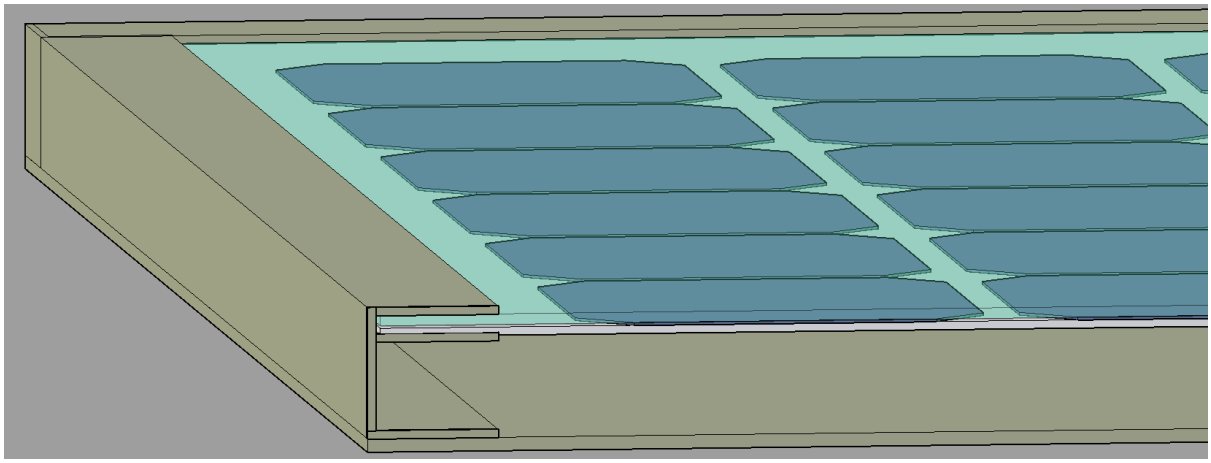

Figure 55: First prototype design with the frame's back-side closed.

Since the water would be in direct contact with the back sheet of the PV module, it was necessary to seal the junction box containing the electrical connections. If this box is not properly sealed off, the water will create a short between the positive and negative contacts of the PV module, forcing the module to only work in short circuit current mode, thus producing no actual power. Therefore, the contact box was electrically insulated by pouring a liquid resin mixture inside and allowing it to cure. Furthermore, two Hep_2O fittings were fitted on the short sides of each module to enable water flow underneath the photovoltaic cells. In addition, waterproof Negative Temperature Coefficient (NTC) Thermistors were installed at the back of each PV module to monitor the PV cells' temperature. These three modifications are shown in Figure 56. Finally, the 5mm Poly (methyl methacrylate) sheet was attached to the back of the PV module frame using a strong sealing and bonding agent.

Figure 56: Junction box electrically insulated with resin, and Hep_2O fittings installed.

The first prototype involved the modification of an existing PV module, making it an easy manufacturing process. However, this has its disadvantages in practice. Firstly, for larger modules, one would need a thicker sheet and structural support to avoid bulging caused by hydrostatic pressure. Therefore, it would be ideal if the photovoltaic module production is modified from the factory stage to have new modules on the market ready with a back-side cooling chamber. Hence, with this aim in mind, a second prototype was designed.

The second prototype differs from the first one mainly in the frame type. The design of the second prototype involves a seamless closed cuboid serving as the frame, with the only open side being the top side to house the encapsulated PV cells and glass. The design for the second prototype is shown in Figure 57. The dimensions of the PV active area were 19.5cm by 10.5cm. The water chamber was constructed with dimensions of 12.5cm by 20.5cm by 3.2cm to keep similar conditions between both prototypes. This resulted in a 0.82L volume of water and a 40L water volume per m^2 of active photovoltaic area. For this design, it was possible to place the contact box outside of the water chamber. This would allow for future maintenance, including the replacement of bypass diodes.

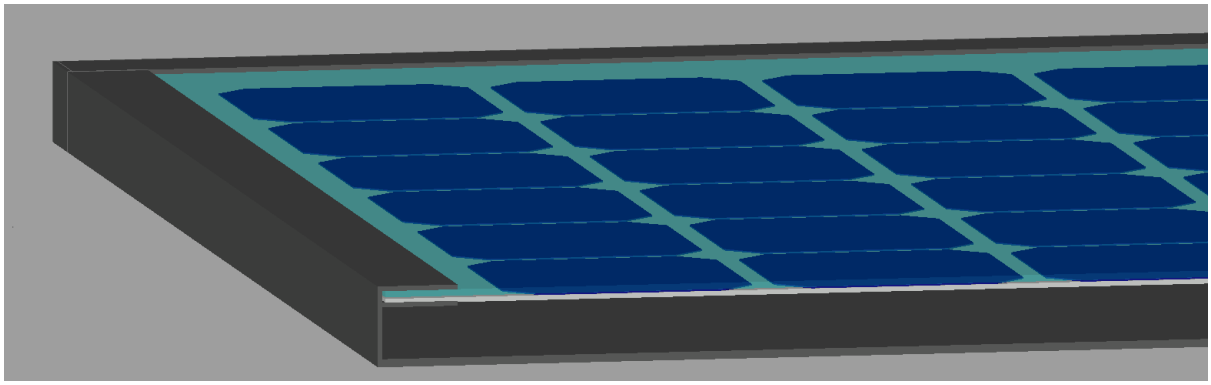

Figure 57: Design of the second prototype.

Due to the limited production capabilities, small encapsulated PV Cells with glass on top were used. However, it was noted that the back sheet of these cells consisted of an absorbing material similar to paper. Therefore, the first step was to apply three coats of acrylic sealer on the back sheet to stop it from absorbing any water. Furthermore, waterproof Negative Temperature Coefficient (NTC) Thermistors were installed at the back of each PV module to monitor the PV cells' temperature. Hence, a 5mm Poly (methyl methacrylate) sheet was bent using an electric heater to create a seamless U-shape. Due to the lack of moulding manufacturing capabilities, the other two sides of the cuboid had to be installed separately.

Hep_2O fittings were installed on these two sides to enable water flow. Furthermore, tracks were routed in the U-shape structure and filled with a sealing agent to mimic a seamless finish. Hence, the remaining two sides of the cuboid were tightly fit inside these tracks. Similarly, the glass, PV cells and back sheet combination were tightly fit in other grooves routed on the top side of the frame. In a practical scenario, a moulding machine would be used to implement the seamless design. Another advantage of this concept is that such a prototype could be manufactured from recycled plastics with the necessary additives to make them UV resistant. The finished second prototype can be seen in Figure 58.

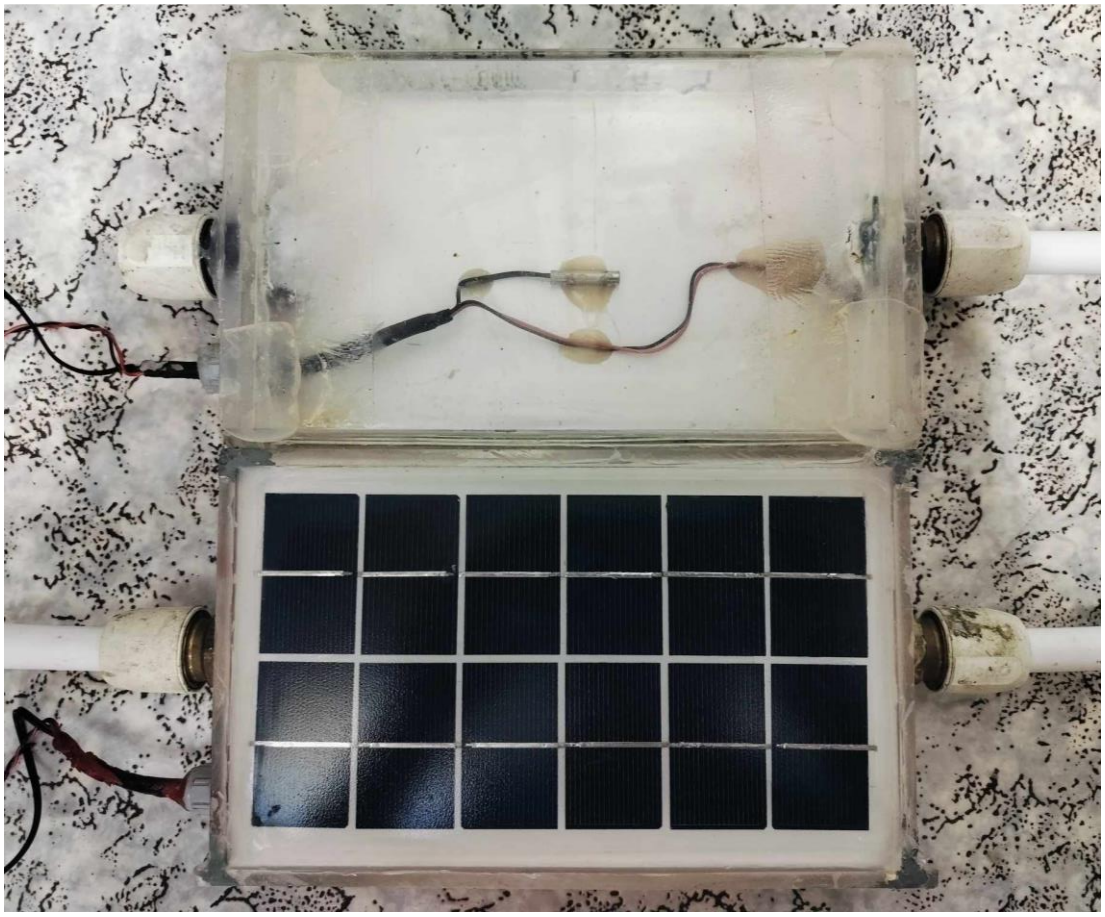

Figure 58: Back-side cooling Prototype 2.

5.3.2 Design failure points

During the initial prototype testing, it was noted that, when pressure was applied to the first prototype, the bonding agent between the aluminium and the polymer sheet failed. This resulted in water leaking making it impossible to test the IPCoSy concept. Hence, a different approach was taken where an aluminium sheet was used instead of Perspex. A general-purpose sealer was placed between the aluminium sheet and the PV's aluminium frame, and blind-sealed rivets were used to tightly fix both aluminium parts together. This new manufacturing approach

proved effective since it eliminated any water leakage. However, the front PV glass shattered upon increasing the internal water pressure up to 3 Bar, as shown in Figure 59. This showed that reinforcing the back-side shifted all the stresses to the front glass, making it the new failure point. Finally, it was decided that we should keep the riveted back-side manufacturing process for the small prototypes but avoid applying pressure larger than the hydrostatic pressure. This would allow us to test the cooling effect without having to go into design optimisation for a small PV panel.

Figure 59: Shattered PV glass at 3 Bar water pressure.

5.3.3 Experimental setup

Experiments were designed to test the prototypes mentioned in the sections before. For each experiment, two modified PVs were used together with a control PV module consisting of the same material composition but without the water chamber underneath the PV cells. The idea was to monitor and compare power and temperature for a conventional module with no cooling, a new prototype with a standard back-side cooling flow, and a new prototype with a modified back-side cooling flow, which always leaves water stored underneath the PV module. The standard back-side cooling flow involved filling the water chamber with water during cooling and allowing it to drain when cooling is switched off. This allowed us to have similar dimensions and conditions to IPCoSy while implementing a different cooling operation, similar to the back-side cooling found in the literature. A 9W DC submersible water pump was used to control the flow, and a flow rate of 145L/hour was achieved.

The Negative Temperature Coefficient (NTC) thermistors used in these experiments were initially placed in heating water with a calibrated thermocouple to obtain their respective

temperature-resistance characteristics. Hence, the Steinhart and Hart empirical equation, shown in equation (63), was used to derive accurate temperatures from NTC resistance values.

$$\frac{1}{T} = A + B \ln R + C(\ln R)^3 \tag{63}$$

Where: T is the Temperature in kelvins

R is the NTC resistance (in Ohms) at Temperature T.

A, B and C are empirically determined Steinhart-Hart Coefficients

Figure 60 shows a block diagram of the designed experimental setup while Figure 61 shows the implemented control algorithm. Figure 62 illustrates the experimental setup implemented in practice. The PV modules were connected to a fixed resistive load, calculated using equation (64), for the PVs to operate close to their maximum power point. The resistive loads were overrated in terms of power and attached to a heatsink using a thermal paste to dissipate heat and decrease errors due to thermal drift. Furthermore, water solenoid valves and water flow sensors were connected to the PV modules to control and measure water flow respectively. A thermocouple was fitted in one of the elbow fittings to monitor the input water temperature. Finally, mechanical water valves were fitted in line with each PV module to be able to fine-tune the water flow.

$$R_{LOAD} = \frac{V_{MP}}{I_{MP}} \tag{64}$$

where R_{LOAD} is the resistive load

V_{MP} and I_{MP} are the PV Voltage and Current outputs at the maximum power point.

A DATAQ DI-808 Data-logger was used to record data from the experimental setup, including PV Temperature, PV Power Output, Water Flow and Water Temperature. This data logger logged data from thermocouples with an accuracy of ± (0.1% of span + 2) while voltage data were recorded with an accuracy of ± (0.05% of span + 10μV). Data was mainly collected at a 0.2Hz frequency, while some data sets were gathered at a 5Hz frequency to study the cooling flow in detail. Furthermore, the data-logger was programmed in such a way as to output alarms if the module temperatures were not within the desired range. Hence, a control board was designed using an ATMEL MEGA328P microcontroller programmed with Arduino Integrated Development Environment (IDE). A Printed Circuit Board (PCB), shown in Figure 63, was designed and manufactured to enable connections with the Arduino board. The control board

was programmed to monitor the alarm states output by the data logger. Hence, based on the alarm states, the control board would signal a relay board to open or close the water solenoid valves connected to the PV modules and switch ON or OFF the cooling pump. Hence, a set of experiments were carried out by varying flow control parameters as shown in Table 9.

Table 9: Cooling experiments flow control parameters

Experiment	Prototype with Modified Flow	Prototype with Standard Flow
1	Temperature independently controlled between 35°C and 45°C	Temperature independently controlled between 35°C and 45°C
2	Temperature independently controlled between 35°C and 40°C	Temperature independently controlled between 35°C and 45°C
3	Prototype filled with water in the morning with no water changes during the day	

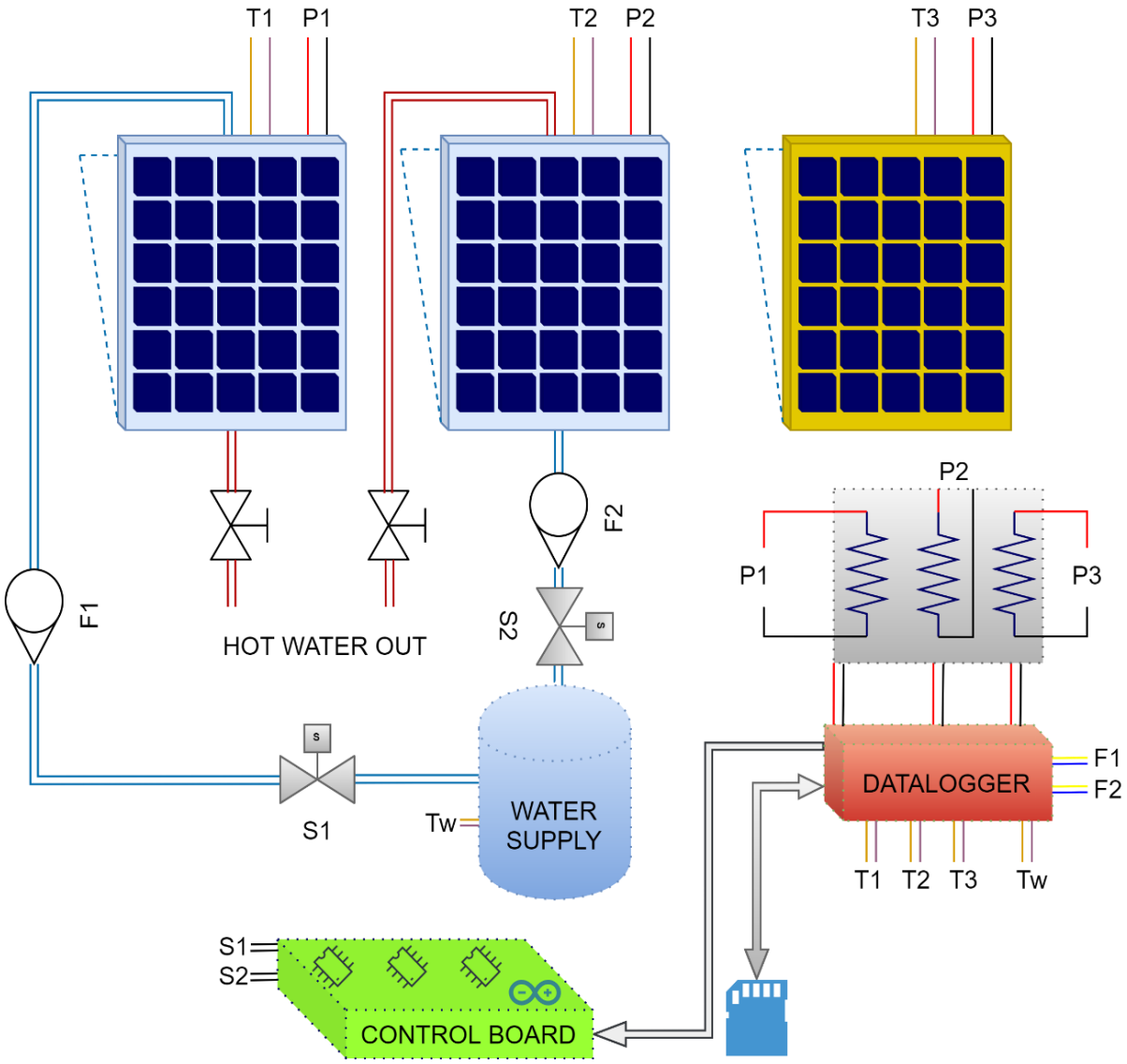

KEY

P1,P2,P3	PVs POWER OUTPUT
T1,T2,T3,TW	PV AND INLET WATER TEMPERATURES
S1,S2	WATER SOLENOID VALVES
F1,F2	WATER FLOW METERS

Figure 60: Block diagram of back-side cooling experimental setup.

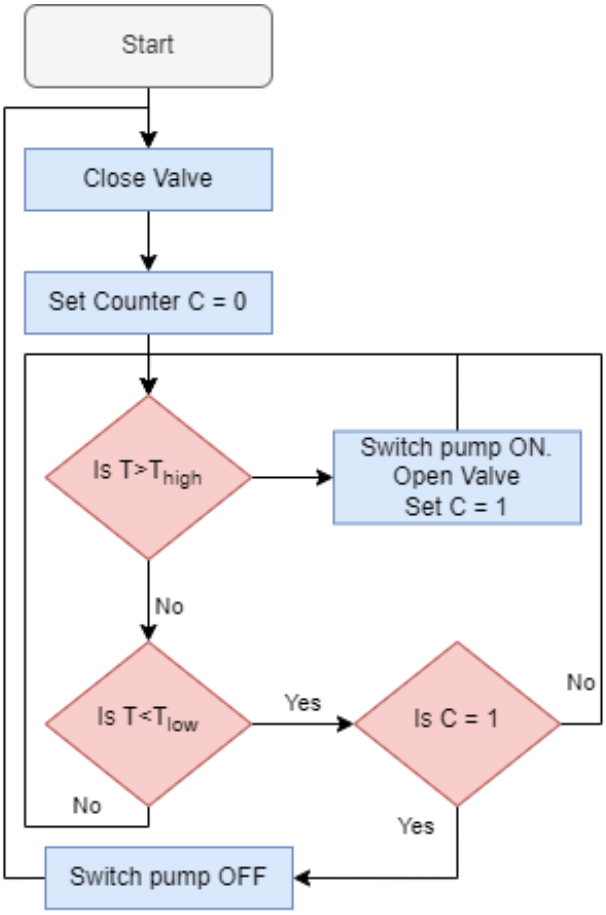

Figure 61: Cooling experiment program flowchart.

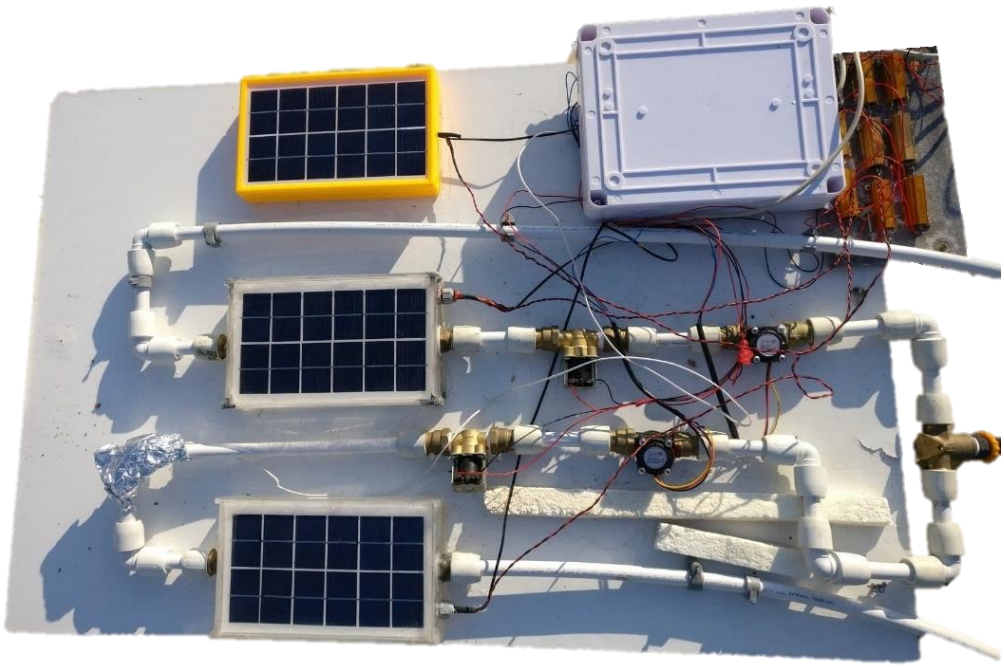

Figure 62: Experimental setup of back-side cooling.

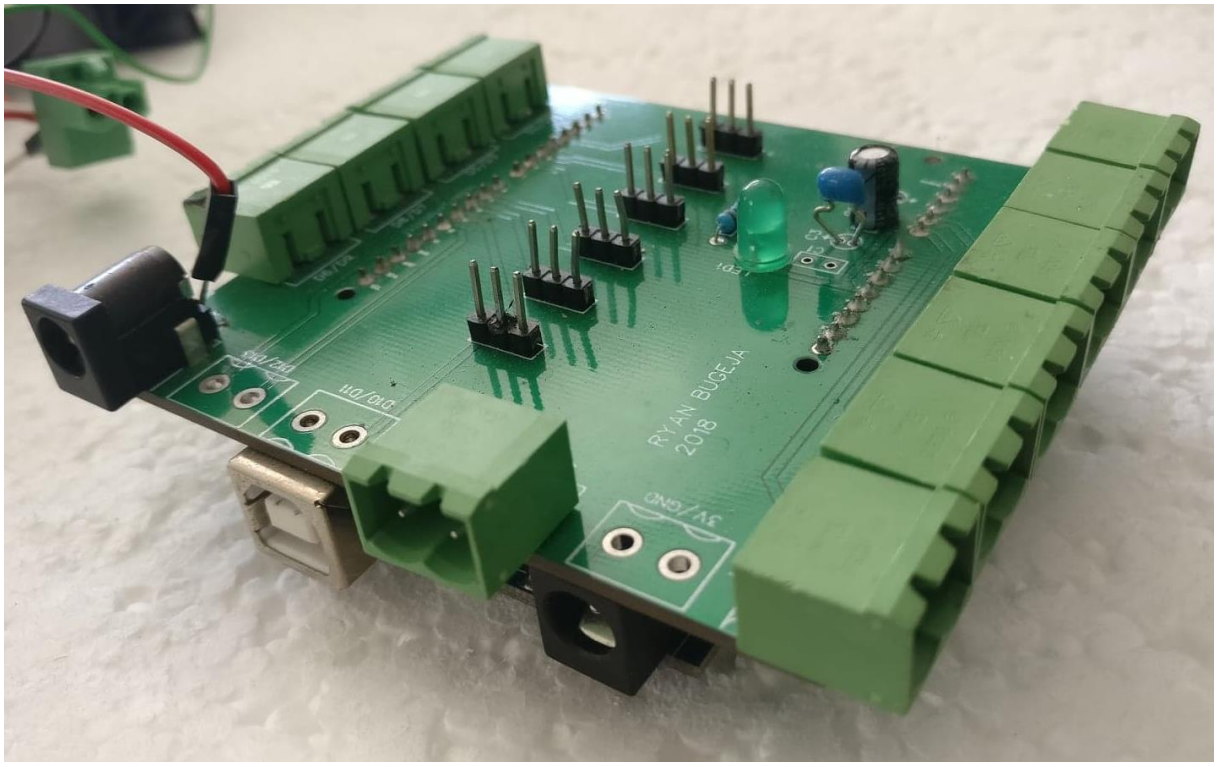

Figure 63: PCB to enable connections with Arduino board.

5.4 Small scale results and discussion

The results obtained from testing the small-scale prototypes are presented in this section. An important observation is that since small-scale panels were used for these experiments, the ratio of pump power to PV power is very high. Therefore, the net energy gain will most of the time be minimal or even negative. A smaller pump could not be used since lower power would result in a lower pump head not sufficient to carry out experimentations. This will be optimised when the concept is up-scaled to full-size PVs and is presented in section 5.5. The percentage gross and net energy differences between the test PVs and the control (uncooled) PV were calculated using equations (65) and (66), respectively.

$$\%\ Gross\ Energy\ Difference = \left(\frac{Test\ PV_{Energy} - Control\ PV_{Energy}}{Control\ PV_{Energy}}\right) \times 100 \quad (65)$$

$$\%\ Net\ Energy\ Difference = \left(\frac{(Test\ PV_{Energy} - Pump_{Energy}) - Control\ PV_{Energy}}{Control\ PV_{Energy}}\right) \times 100 \quad (66)$$

5.4.1 Comparison to standard back-side cooling

The IPCoSy prototype was first tested against standard back-side cooling that does not retain water when the cooling is switched off. Test1 consisted of setting similar thresholds for both cooling technologies. The control system was configured to switch on the cooling flow when the PV panels reached a temperature of 45°C and switch off the flow at 35°C. Figure 64 compares the different cooling technologies with the same control thresholds (Test1). The top graph (a) shows the evolution of PV back-side temperature during the day for the three PVs under test while the bottom graph (b) shows the power output of the three PVs during the day. The drop in temperature around 13:00 is due to the presence of clouds as evidenced by the power curves.

These results show that, although both technologies manage to keep the PV temperatures within the desired thresholds, the IPCoSy module achieved this with a much lower pump switching frequency. In this figure, the blue and the orange curves have similar cooling rates, when the cooling flow is switched on at 45°C. However, as soon as the panels reach the 35°C threshold and the cooling is switched off, the blue curve has a much higher heating rate than the orange curve. This phenomenon is because the IPCoSy panel has a volume of cool water still in contact with the back-side of the PV panel even when the cooling flow is switched off. This results in a higher PV module specific heat capacity, resulting in a slower heating rate. This confirms the initial hypothesis. For Test2, the PV with standard cooling was given thresholds of 35°C to 45°C while the IPCoSy PV was set between 35°C and 40°C. Results are tabulated in Table *10*.

Table 10: Comparison between different cooling technologies.

Test 1	**Standard Back-side Cooling**	**IPCoSy Cooling**	**Uncertainty**
Gross Energy Difference	5.91%	6.01%	±0.45%
Net Energy Difference	-9.13%	3.06%	
Test 2	**Standard Back-side Cooling**	**IPCoSy Cooling**	
Gross Energy Difference	5.55%	7.59%	±0.45%
Net Energy Difference	-9.29%	2.42%	

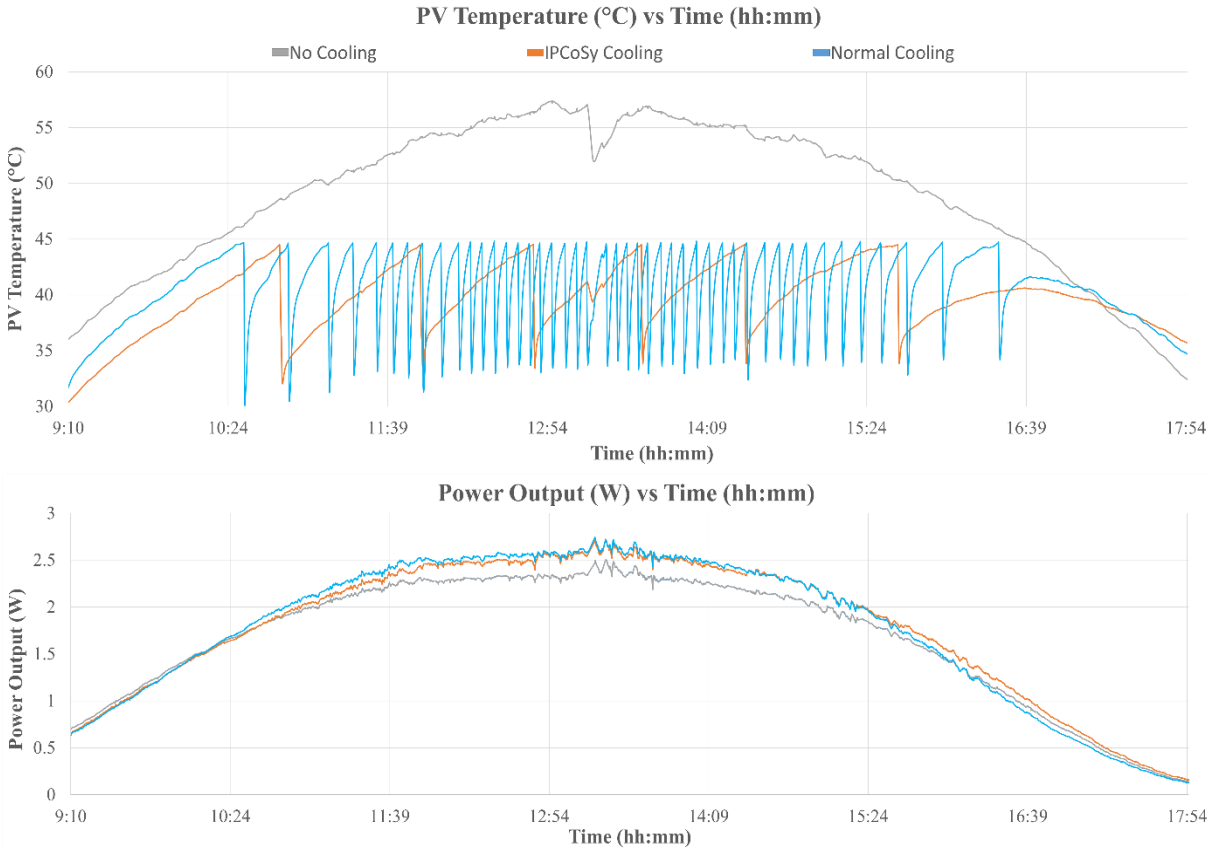

Figure 64: Comparison between different cooling technologies with the same control thresholds (Test1).

In this test, the IPCoSy cooling technology achieved a higher net energy difference than the PV with standard back-side cooling. However, although the 35°C to 40°C setting achieved a higher percentage gross energy gain, this resulted in a lower percentage net energy gain, when compared to the 35°C to 45°C setting. This effect is attributed to the higher pump switching frequency resulting in an increased pump energy consumption. This result is in agreement with the optimal temperature settings published by Moharram et al. [74].

5.4.2 IPCoSy testing with no flow.

Another set of experiments involved filling the IPCoSy prototype with water and having no extra forced flow during the rest of the day. The hypothesis was that the added specific heat capacity would keep the IPCoSy PV cooler and therefore operate at a higher efficiency. Figure *65* shows the results of these experiments. The round and square orange markers respectively show the difference in average and maximum temperatures between the Control PV and the IPCoSy PV. The results obtained showed an increase in daily energy yield by up to 3.34% ±0.41%.

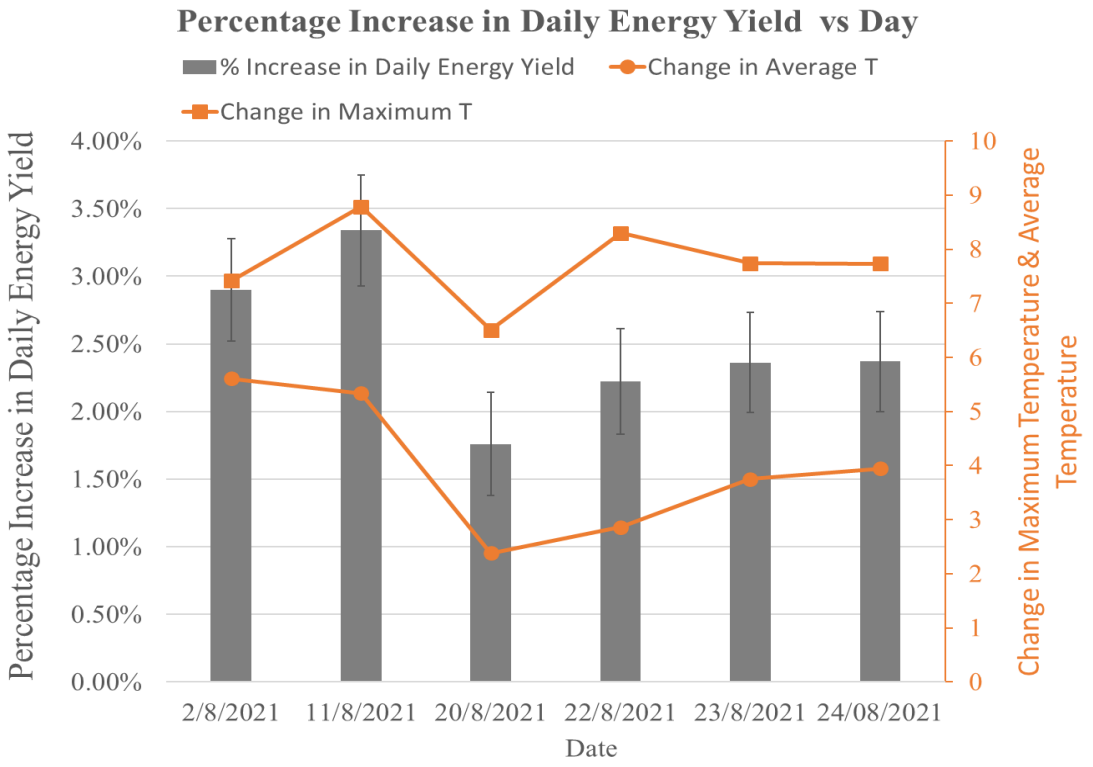

Figure 65: Results for experimentation with no flow.

The panel filled with water took longer to heat up in the morning, when compared to the control panel. However, during the afternoon, the control panel cooled down faster than the IPCoSy panel. Although, this resulted in the control panel working at a higher efficiency in the afternoon, the IPCoSy panel worked at a higher efficiency during peak solar radiation. Therefore, this contributed to the overall increase in daily energy yield. This effect is shown in the sample graph in Figure 66.

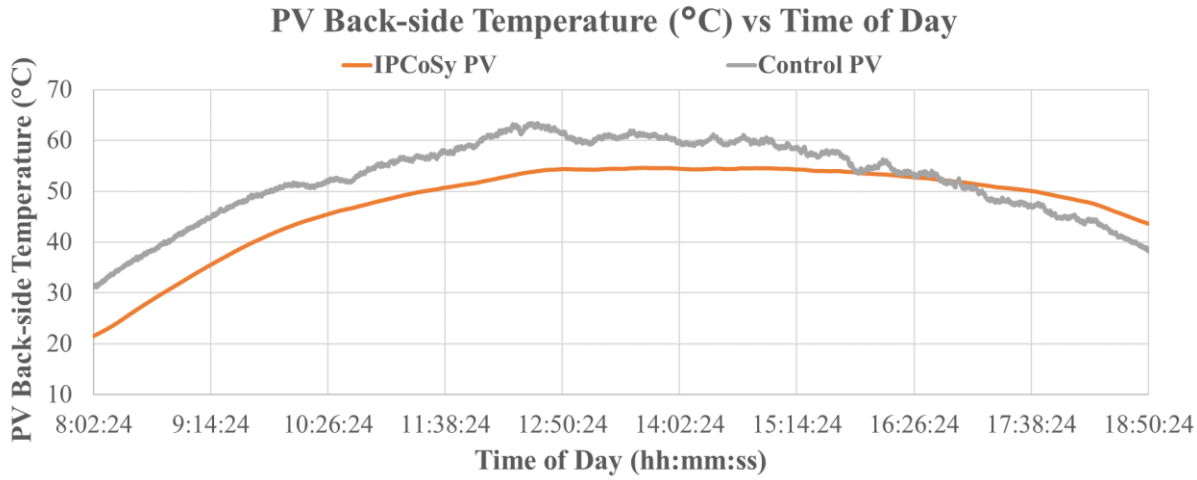

Figure 66: Sample graph of experimentation with no flow.

5.4.3 IPCoSy testing with a controlled flow.

The final set of experiments involved setting different cooling thresholds for the IPCoSy prototype. The cooling flow is switched on when the PV temperature reaches a certain high threshold. Hence, the PV temperature will start decreasing and the cooling flow will be switched off when it reaches a certain low-temperature threshold. These experiments aimed to test the possible gains that can be achieved with this cooling technology and to determine ideal threshold temperatures to achieve efficient cooling. Table 11 summarises the results obtained through this set of experimentations. The results in Table 11 show that the 35°C to 45°C range produced the highest net energy yield, in agreement with a previous study by Moharram et al. [74].

Figure 67 shows the dependency of the net energy to gross energy ratio on:

- the difference between the lower control temperature threshold and the water supply temperature and
- the difference between the upper control temperature threshold and the maximum temperature reached by the control panel.

The data shows that when lower control temperature thresholds are set close to the water supply temperature, the pump consumption increases due to the longer cooling time required to reach the desired threshold. Furthermore, setting a maximum temperature much lower than the control panel's maximum temperature, will result in the pump switching on at a higher frequency, consuming more energy. These results show that, for the best-case scenarios, the difference between the upper control temperature and the maximum temperature of a non-cooled PV should be in the range of 12°C to 16°C. In contrast, the difference between the lower temperature threshold and the supply water temperature should not be less than 8°C.

Table 11: Results of testing with controlled flow.

Date	Net Energy Difference from Control	Gross Energy Difference from Control	Uncertainty
Temperature Thresholds: 35°C to 45°C, Flow Rate: 145L/hour			
03/08/2021	3.75%	5.18%	0.38%
05/08/2021	4.36%	6.27%	0.38%
06/08/2021	3.59%	5.63%	0.38%
07/08/2021	5.42%	7.47%	0.38%
08/08/2021	4.11%	5.77%	0.39%
Temperature Thresholds: 25°C to 37°C, Flow Rate: 145L/hour			
09/08/2021	-4.92%	9.2%	0.39%
10/08/2021	-10.49%	10.81%	0.40%
Temperature Thresholds: 25°C to 45°C, Flow Rate: 145L/hour			
12/08/2021	-1.94%	4.00%	0.40%
13/08/2021	-1.63%	4.66%	0.38%
15/08/2021	-0.39%	7.87%	0.39%
16/08/2021	-6.63%	6.47%	0.38%
Temperature Thresholds: 35°C to 37°C, Flow Rate: 145L/hour			
17/08/2021	1.7%	7.43%	0.39%
18/08/2021	2.6%	7.57%	0.39%
Temperature Thresholds: 30°C to 35°C, Flow Rate: 145L/hour			
28/08/2021	1.83%	10.82%	0.38%
29/08/2021	0.9%	9.60%	0.42%
Temperature Thresholds: 30°C to 40°C, Flow Rate: 145L/hour			
30/08/2021	2.08%	5.77%	0.39%
31/08/2021	2.35%	6.48%	0.40%
01/09/2021	0.27%	4.03%	0.45%
02/09/2021	2.89%	5.99%	0.38%
05/09/2021	1.92%	6.89%	0.41%
06/09/2021	1.37%	3.63%	0.39%
Temperature Thresholds: 30°C to 37°C, Flow Rate: 145L/hour			
17/09/2021	1.56%	5.20%	0.39%

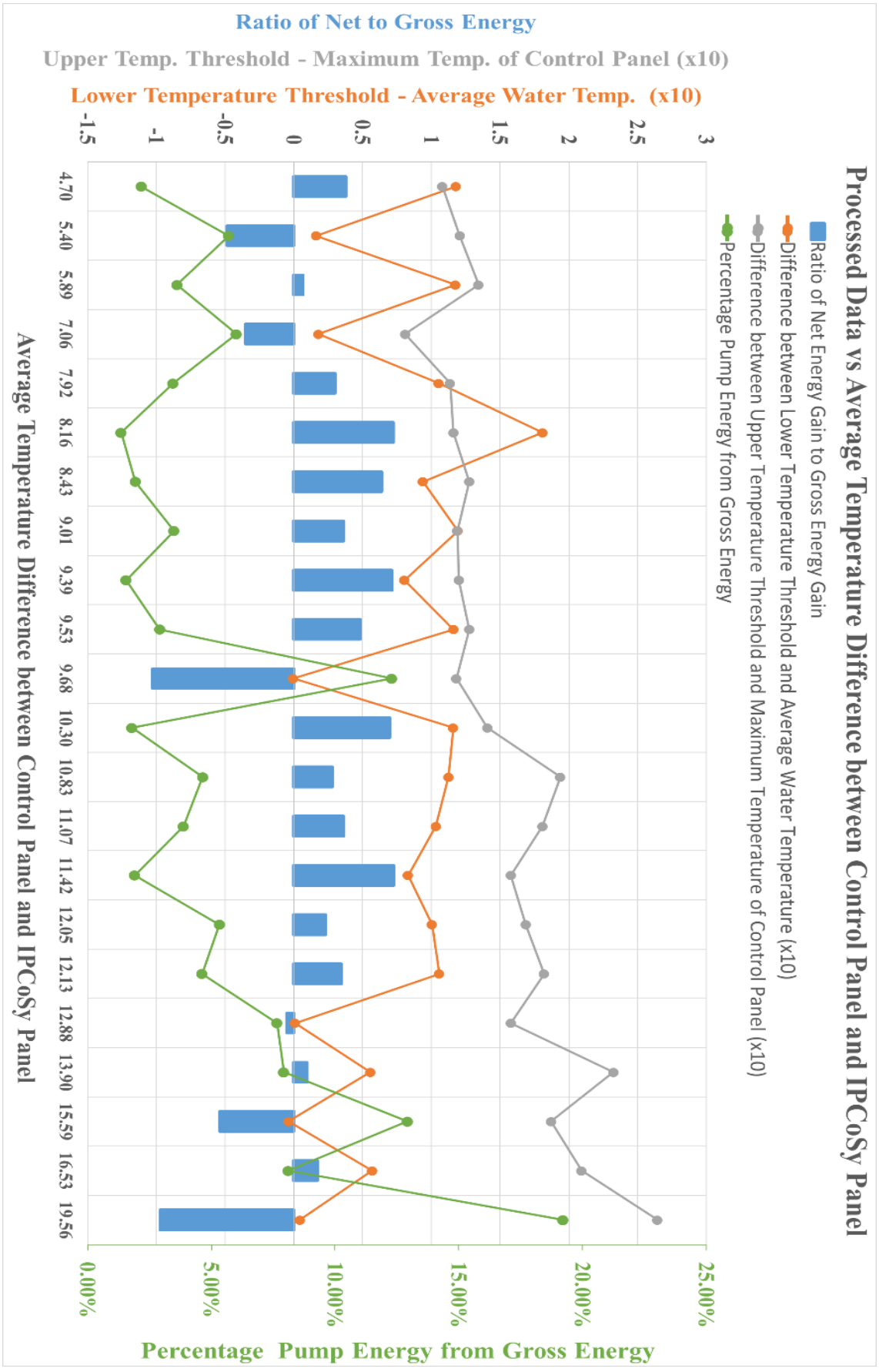

Figure 67: Data analysis of forced flow experiment.

5.5 Large scale methodology

5.5.1 Introduction

The results presented in section 5.4 confirmed the initial hypothesis and the potential of the back-side water-cooling system IPCoSy. Hence, the next step was to study if this cooling solution could be scaled up to include it in existing commercial full-size PV panels. Two funding applications were granted by the Energy and Water Agency (EWA) and Malta Marittima through the Maritime Seed Award (MARSA). The former funding was used to design and test the full-scale prototypes while the latter to cover the patenting process. Through EWA funding we got support on mechanical and computational fluid dynamics (CFD) simulations. The expected challenges were the mechanical strength of the modified PV module due to its dimensions and the internal fluid dynamics to cool the solar cells quickly and uniformly. This part of the research aimed to obtain working full-scale prototypes that can be proposed to potential investors for further development and better manufacturability.

5.5.2 Patent

After a thorough literature search by the University of Malta Knowledge Transfer Office and REINHOLD COHN Intellectual Property Group, IPCoSy was deemed as innovative. Therefore, we proceeded in filing a patent to protect the following:

- The general idea
- Various aspects of the design.
- A completely new photovoltaic module incorporating the cooling technology, as shown in Figure 68. This involves a closed PV frame to create a water chamber at the back of the solar cell assembly.
- An after-market kit that can be installed on existing PV modules to add the cooling technology. This can be a solid water tank, as shown in Figure 69, or a flexible tank that is fitted at the back of a PV module in the space between a conventional aluminium frame.
- Different manufacturing possibilities including different materials such as aluminium and recycled plastics.
- Various possible applications, such as offshore PVs, available rooftops, industrial water heating and Reverse Osmosis (RO) plants as shown in Figure 70.

The patent was officially granted on the 2nd of January, 2023 and is in force until August 2027 [124].

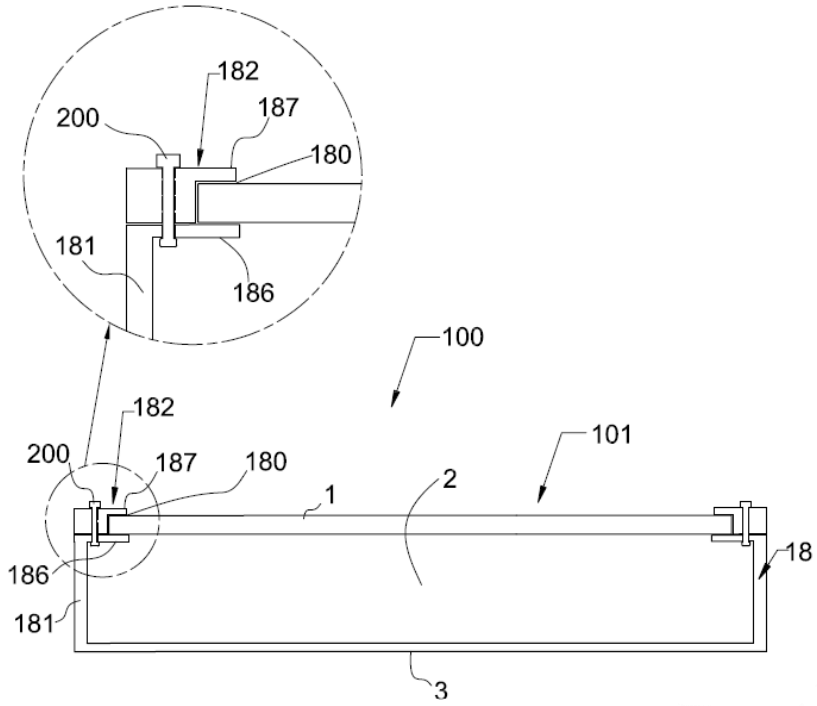

Figure 68: Patent diagram of completely new photovoltaic module incorporating cooling technology [124].

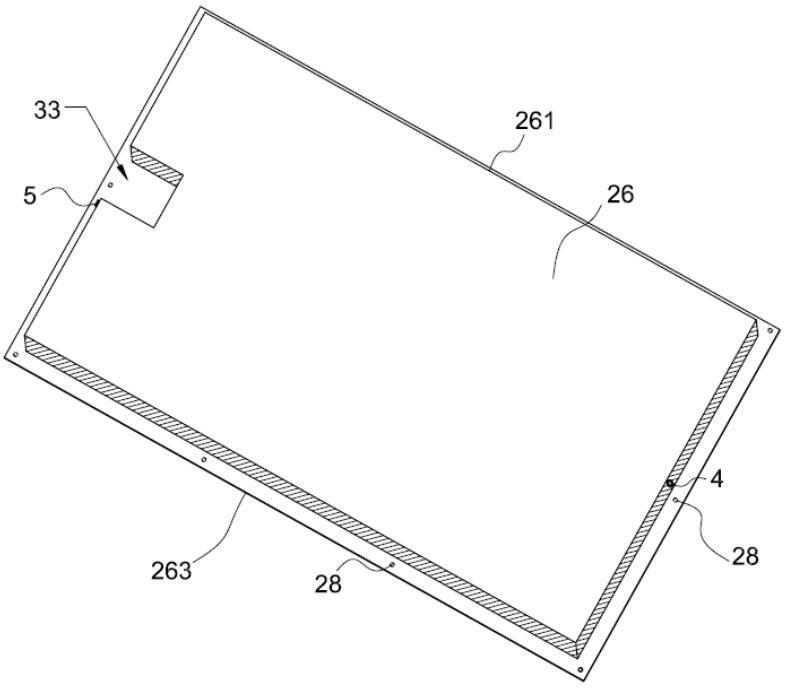

Figure 69: Patent diagram of an after-market kit to include the cooling technology to existing PV modules [124].

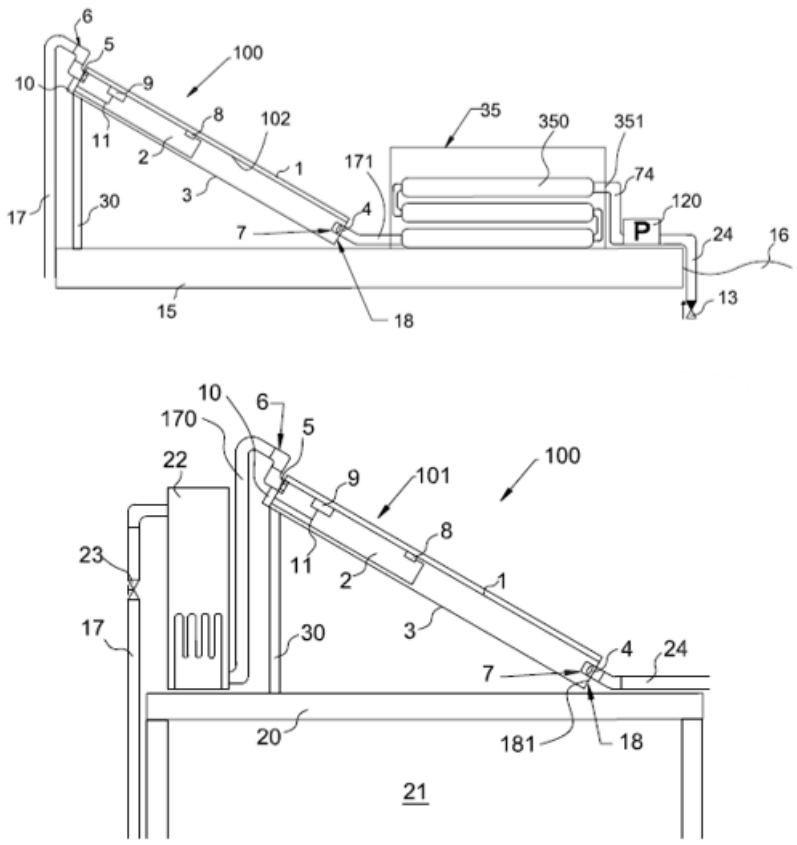

Figure 70: IPCoSy patent diagrams of reverse osmosis (TOP) and industrial water heating (BOTTOM) applications [124].

5.5.3 Prototype design

The first prototype designs were done using Autodesk FUSION 360. This software allows the user to not only design in 3D but also perform some mechanical simulations on the designed prototype. This part of the research focused on two main designs: a completely new photovoltaic module modified to incorporate the cooling technology and an after-market kit that can be easily installed at the back of existing commercial PV panels to achieve the cooling effect. Throughout this chapter, the prototype involving the modification of a PV module and having the water in direct contact with the back sheet will be referred to as Type 1, while the after-market prototype will be referred to as Type 2.

The essential components required for the construction of the Type 1 prototype are presented in a cross-section taken from the patent documents, shown in Figure 71. The solar cell assembly **(1)** consists of solar cells encapsulated in EVA, with solar glass on top and a back sheet **(102)** at the back. The solar cell assembly is housed in a frame **(18)**, closed off at the back using a sheet of various possible materials **(3)**. The conventional junction box **(9)** is sealed-off, and

connections are shifted to a new junction box **(10)** outside the PV module. With this modification, one can conduct necessary testing and replace bypass diodes. A T-shaped stream spreader **(7)** is fitted at the inlet **(4)** to distribute the input water and create turbulence. This turbulent flow helps to cool the PV panel quicker and more efficiently. At the output, two 45° elbows are hydraulically coupled to allow the PV to be installed at any tilt angle while ensuring the water chamber is always full. Adding these fittings at the output forces the water to fill the whole chamber **(2)** before overflowing through the output of the two 45° elbows **(6)**. A temperature sensor **(8),** such as a thermocouple, is attached at the back of the solar cell assembly to give temperature readings to the cooling control algorithm.

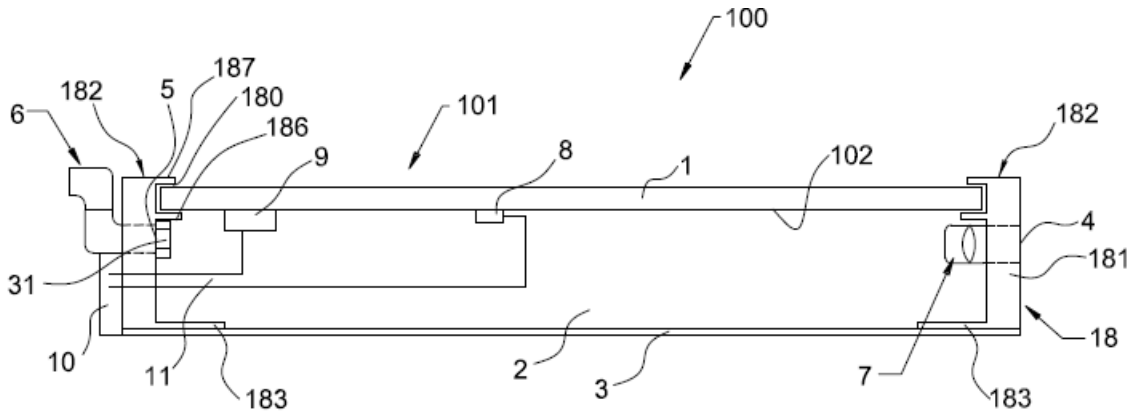

Figure 71: Patent diagram of the modified PV panel to incorporate cooling (Type 1) [124].

Figure 69 above shows the essential components making up the after-market design. This design consists of a water tank that can be composed of various materials. The top of the water tank **(26)** must be a conductive material such as aluminium since this will be responsible for the heat transfer between the back-side of the solar cell assembly and the water inside the tank. An inlet **(4)** and an outlet **(5)** are present on opposite sides of the tank to enable a water flow. A space **(33)** is left to house junction boxes, conventionally found in commercial PV modules. Finally, holes **(28)** are present on the sides of the tank to enable a strong fix with the aluminium frame of the PV modules. Therefore, to include cooling on an existing PV module, one would simply attach this tank at the back of the module as shown in the cross-section in Figure 72.

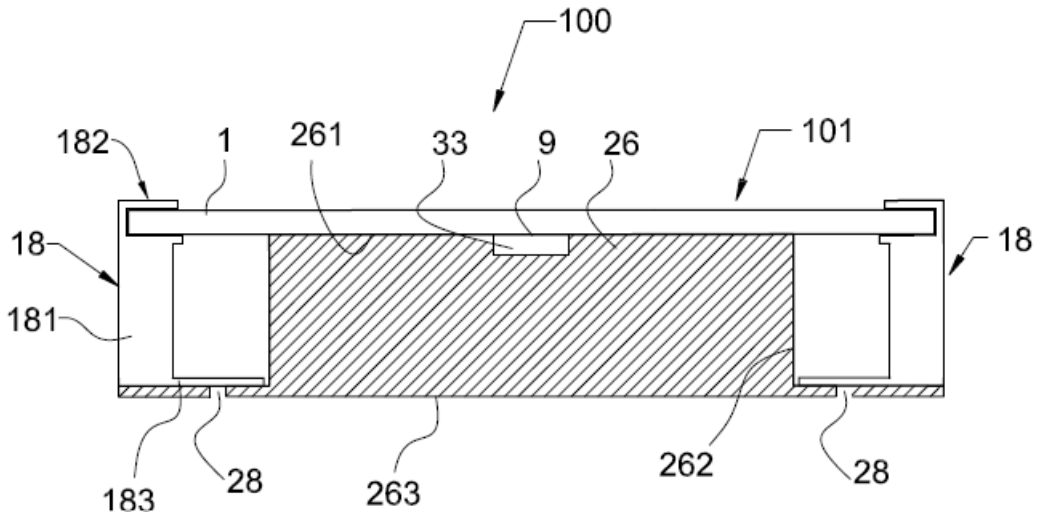

Figure 72: After-market design attached to the back-side of a PV module (Type 2) [124].

From the lessons learnt from designing the small-scale prototypes, it was essential to initially ensure that the seal between the bottom plate and the aluminium frame was not compromised under hydrostatic pressure. Therefore, mechanical simulations were essential in designing structurally sound prototypes. These simulations would highlight the mechanical stresses and deformation resulting from hydrostatic pressures. Maximum hydrostatic pressure occurs when the module is completely filled with water and positioned vertically and in a portrait orientation. It was expected that both the glass and the back plate would deform under pressure however, the extent of this deformation was unknown. The bottom plate was expected to deform considerably due to its thickness. Therefore, extra support would be needed to decrease the stress on the seal binding the plate to the aluminium frame. However, reducing the deformation of the back plate by introducing stiffeners would increase the stresses exerted on the glass, resulting in a potential failure. Mechanical simulations were therefore performed to investigate ways to reduce the deformation in the glass and the aluminium back plate, without exceeding the maximum tensile strength of the solar glass.

5.5.4 Mechanical simulations

As seen in the previous sections, finding the right balance between bottom rigidity and stresses on the top glass was important. Hence, simulations on ANSYS MECHANICAL were sub-contracted to obtain feedback aimed at optimising the design.

5.5.4.1 Mechanical simulations on glass

The dimensions considered for the glass were 1630mm in length, 980mm in width and 3.2mm in thickness. Typically, the glass used in PV panels is toughened or pre-stressed. Toughened glass was considered, with a tensile bending strength of 120MPa, Young's Modulus, E, of 73GPa and Poisson coefficient, ν, of 0.24. The four faces around the panel, which usually make up the PV panel's aluminium frame, were selected as fixed supports. Three stress probes were initially studied in casually selected positions to perform a mesh convergence analysis. Three mesh sizes of 3, 5 and 10mm were chosen, and the results of maximum principal stresses are shown in Figure 73. Since convergence was obtained and computational resource was scarce, we selected 10mm as the final mesh size for the glass model.

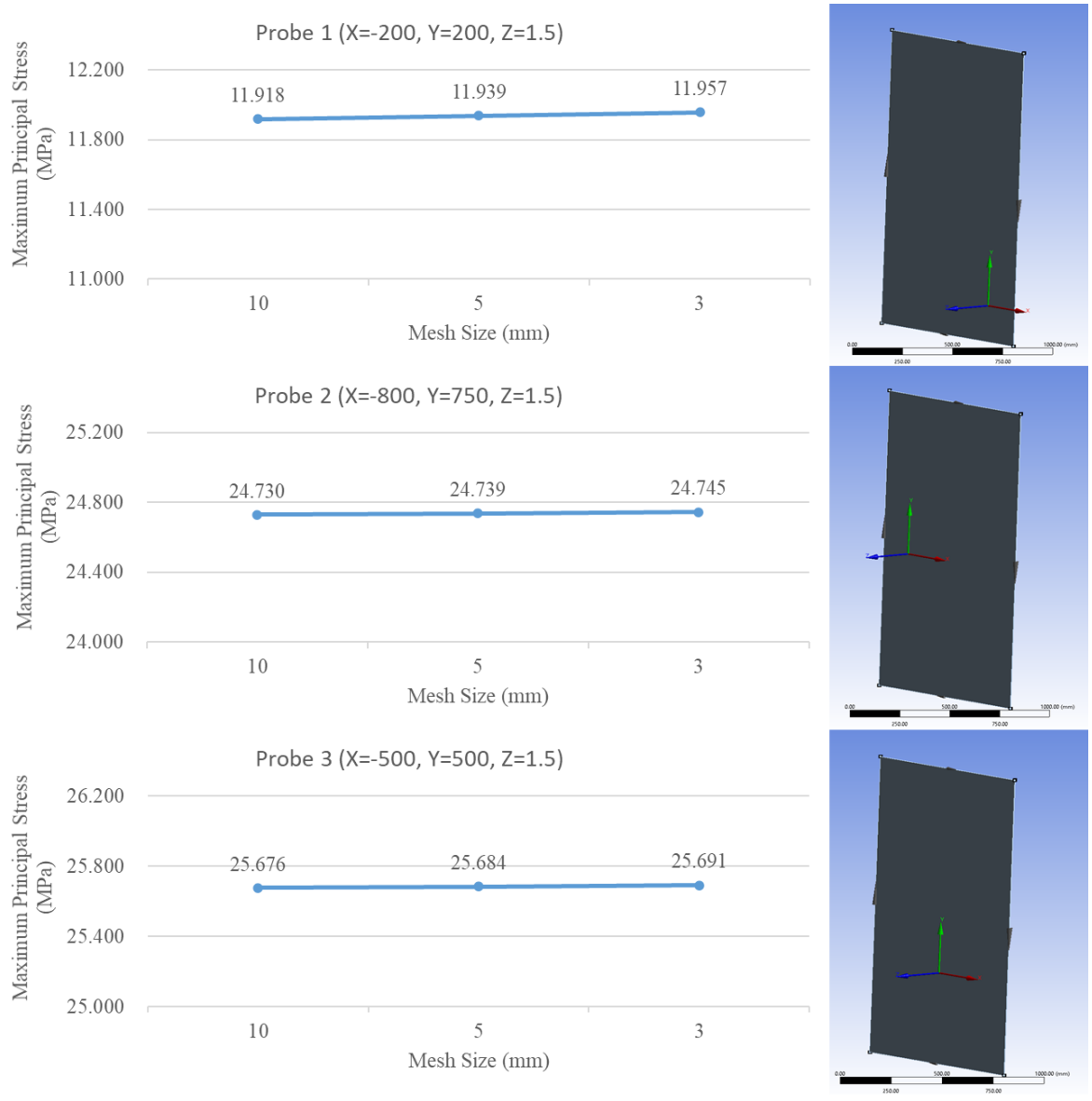

Figure 73: Three test probes chosen at random positions to analyse mesh convergence.

Hence, simulations were conducted to investigate the deformation and stresses on the front glass at different inclinations for both portrait and landscape installations. The results of these simulations are presented in Table 12. Maximum Principal Stress was chosen for this analysis since glass is a brittle material and therefore failure usually occurs when tensile stress reaches a critical value.

Table 12: Mechanical simulations of hydrostatic pressure on the front glass.

Inclination	Hydrostatic Height (mm)	Max. Deformation (mm)	Maximum Principal Stress (MPa)
		Portrait	
10°	321.0	6.30	53.67
20°	597.2	7.95	83.82
30°	855.3	9.06	108.17
90°	1650	11.73	180.41
		Landscape	
10°	208.1	5.14	43.07
20°	374.9	6.39	64.14
30°	530.3	7.24	81.24
90°	1000.0	9.02	124.59

Simulation shows that the glass will not fail for all landscape positions, except for the 90° case. Hence, care must be taken during the panel installation to avoid placing it at 90° when full of water. Therefore, the panel must be installed at the desired inclination and filled with water afterwards. The next highest value of maximum principal stress for landscape positions is 81.24MPa at a 30° inclination, while toughened glass theoretically fails at 120MPa.

When the panel is placed in a portrait position at 10°, the maximum principal stress is 53.67MPa. The results in Table 12 show that all the portrait inclinations above 30° have maximum principal stresses close to the theoretical limit, with the 90° inclination exceeding this limit. This suggests that the glass could fail under hydrostatic pressure. Even if the panel does not break, the probable bulging of the glass could create cracks in the solar cells and affect their efficiency. Also, additional internal pressure during the filling should be avoided because of the glass's fragility. Therefore, during a cooling flow, the pressure of the piping system must

be regulated to prevent the build-up of internal pressure and risk damaging the front glass of the panels.

5.5.4.2 Mechanical simulations on aluminium back-plate

The dimensions considered for the aluminium back-plate were 1580mm in length, 930mm in width and 2mm in thickness. The support stiffeners chosen were angle profiles of 25.4mm by 25.4mm by 3.2mm. The material selected for the back plate and stiffeners was Aluminium 6061 T6, found in the ANSYS Library. The four faces around the panel, which usually make up the PV panel's aluminium frame, were selected as fixed supports. Three stress probes were initially studied in casually selected positions to perform a mesh convergence analysis. Six mesh sizes of 3, 5, 7, 10, 15 and 20mm were chosen, and the results of maximum principal stresses are shown in Figure 74. Since convergence was obtained and computational resource was scarce, we selected 7mm as the final mesh size for the aluminium back-plate model.

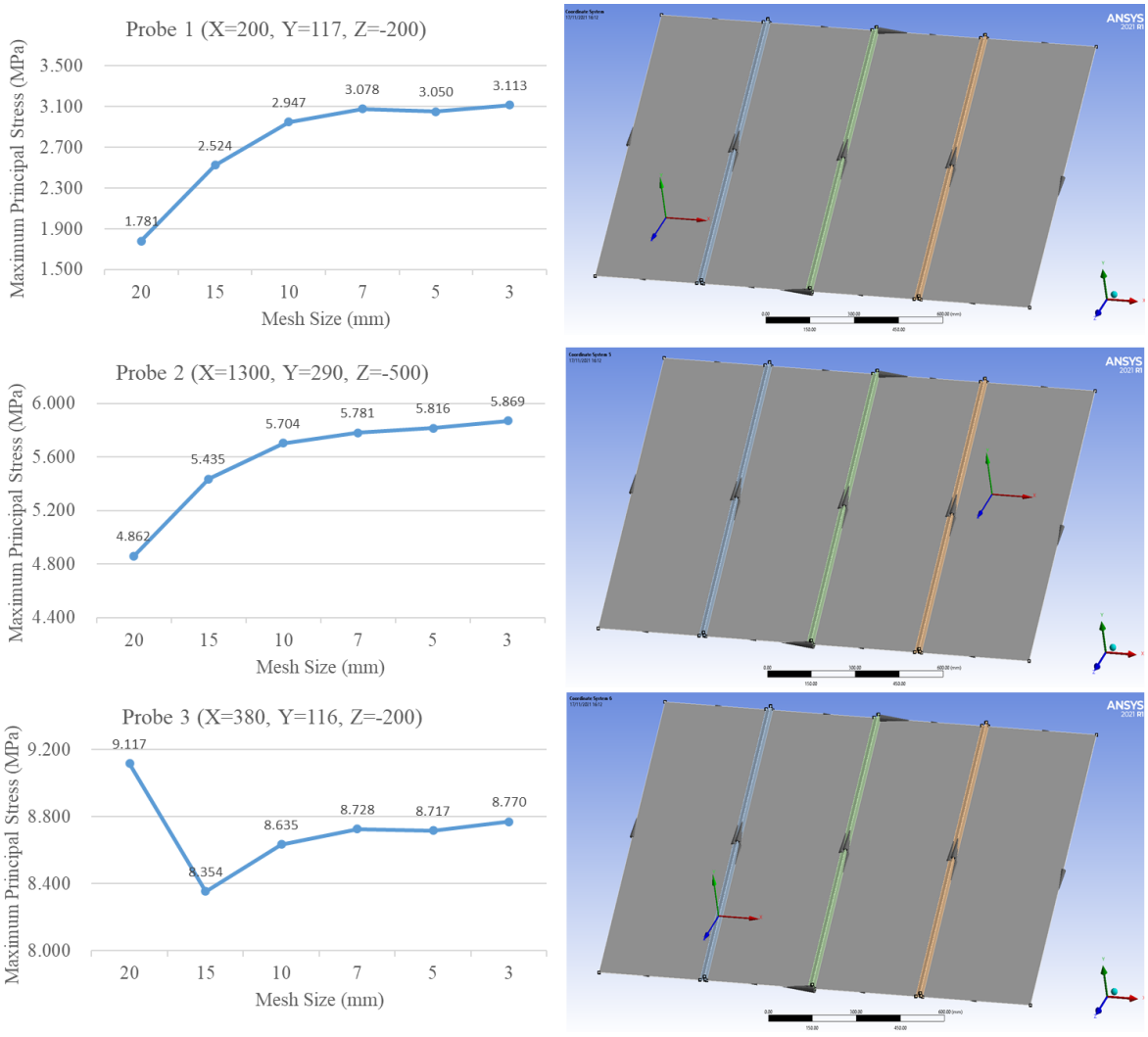

Figure 74: Three test probes chosen at random positions to analyse mesh convergence.

Hence, simulations were conducted to investigate the deformation of the aluminium back-plate at different inclinations for both portrait and landscape installations. The results of these simulations are presented in Table 13.

Table 13: Mechanical simulations of hydrostatic pressure on aluminium back-plate.

Number of Stiffeners	Inclination	Hydrostatic Height (mm)	Max. Deformation (mm)
Portrait			
0	10°	321.0	7.20
	20°	597.2	8.89
	30°	855.3	10.05
	90°	1650	12.54
2	10°	321.0	5.71
	20°	597.2	7.71
	30°	855.3	9.06
	90°	1650	11.91
3	10°	321.0	5.24
	20°	597.2	7.45
	30°	855.3	8.91
	90°	1650	11.92
Landscape			
0	10°	208.1	6.05
	20°	374.9	7.33
	30°	530.3	8.23
	90°	1000.0	10.12
2	10°	208.1	4.52
	20°	374.9	6.11
	30°	530.3	7.2
	90°	1000.0	9.46
3	10°	208.1	3.49
	20°	374.9	5.12
	30°	530.3	6.26
	90°	1000.0	8.63

Simulations at an inclination of 30° in a portrait position with three stiffeners show a deformation of 8.91mm against 9.06mm when two stiffeners are used. The simulation shows deformation of 7.2mm in the landscape position with two stiffeners and 6.27mm with three stiffeners. Since the maximum deformation in the Aluminium back-plate does not change significantly, using two stiffeners in the final prototype design was deemed more financially viable.

5.5.4.3 Verification of mechanical simulations

Simulations showed that the principal stress acting on the glass due to hydrostatic pressure could exceed the maximum tensile bending strength of the glass. However, simulations are based on several assumptions, so it was necessary to verify these results in practice.

This was achieved by modifying damaged PV panels donated to us by Bajada New Energy Ltd. to incorporate the cooling system. Firstly, the internal edges of the PV panel were sealed using a strong marine sealer. Hence, a 2mm aluminium sheet was cut to size, and three aluminium angle channels of 25.4 by 25.4 by 3.2mm were attached to one side of the sheet using marine sealer and blind-sealed rivets, as shown in Figure 75. These angle channels would serve as stiffeners to the aluminium sheet. Two holes were drilled in the aluminium frame walls on the short sides of the PV panel, and water fittings were threaded in place. This inlet and outlet would allow the filling of the chamber with water while allowing air to vent out from the other side. Finally, the PV panel aluminium frame was lightly sanded to create a rough surface, and the aluminium sheet was attached to it using a multipurpose sealant and blind-sealed rivets. After the sealer cured, the modified PV panel was filled with water, ensuring all the air was pushed out. Hence, the inlet and outlet were closed, and the PV panel was erected up to an inclination of 90° in a portrait position. Contrary to that suggested by the mechanical simulations, the glass did not fail at any inclination angle, although glass bending was visible at high inclinations. Figure 76 shows the back-side of the modified prototype and the glass bending caused by hydrostatic pressure due to high inclination angles.

This test provided essential information on design specifications such as the size of bolts, pressure limitations, type of sealant and possible failure points. Furthermore, these results increased our confidence in obtaining successful full-scale prototypes that can be tested without damage.

Figure 75: PV Panel with sealed internal edges (Left) and Aluminium sheet with three stiffeners attached (Right).

Figure 76: Aluminium sheet attached to the back of PV panel (Left) and filled PV panel at a high inclination angle showing bending of glass (Right).

5.5.5 Final prototype designs

Four prototype designs were finalised following the mechanical simulations presented in the section above. The designs involved two options for a Type 1 prototype and two for a Type 2 prototype.

5.5.5.1 Type 1.1 prototype

The Type 1.1 prototype design involves a modification of an existing PV module to incorporate a cooling chamber at the back of the solar cell assembly. The water inlet and outlet are placed on the back aluminium sheet on opposite ends of the long sides of the PV module. A T-shaped stream spreader is installed internally at the water inlet to create turbulence and achieve quicker and more uniform cooling. Two aluminium angle channels are used to stiffen the aluminium back sheet. These stiffeners have routed slots to allow water to flow through them. This prototype has a quarter-inch water inlet and a half-inch water outlet to avoid pressure build-up during cooling flows. Finally, the aluminium back sheet has another outlet to be fitted with a water-tight electrical grommet to transfer the internal junction box to a new external junction box. This enables the installation and replacement of bypass diodes. Figure 77 shows the design of the Type 1.1 prototype with the top removed to view internal design details.

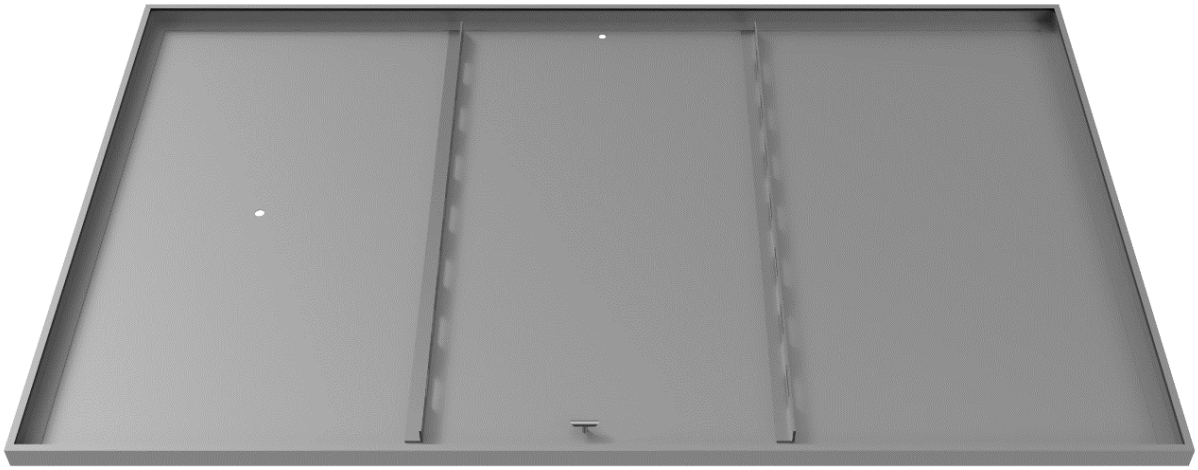

Figure 77: Design of Type 1.1 prototype with an open top.

5.5.5.2 Type 1.2 prototype

The Type 1.2 prototype also involves a modification of an existing PV module to incorporate cooling. However, the water inlet and outlet are placed on the back aluminium sheet on opposite corners of the PV module. Similar to the Type 1.1 prototype, a T-shaped stream spreader is installed internally at the water inlet, while two aluminium angle channels are used

to stiffen the aluminium back sheet. The stiffeners have holes routed to allow water to flow through them. Furthermore, water inlet and outlet sizes are similar to the Type 1.1 prototype, and the aluminium back sheet also has an outlet to transfer the internal junction box to a new external junction box. Figure 78 shows the design of the Type 1.2 prototype with the top removed to view internal design details.

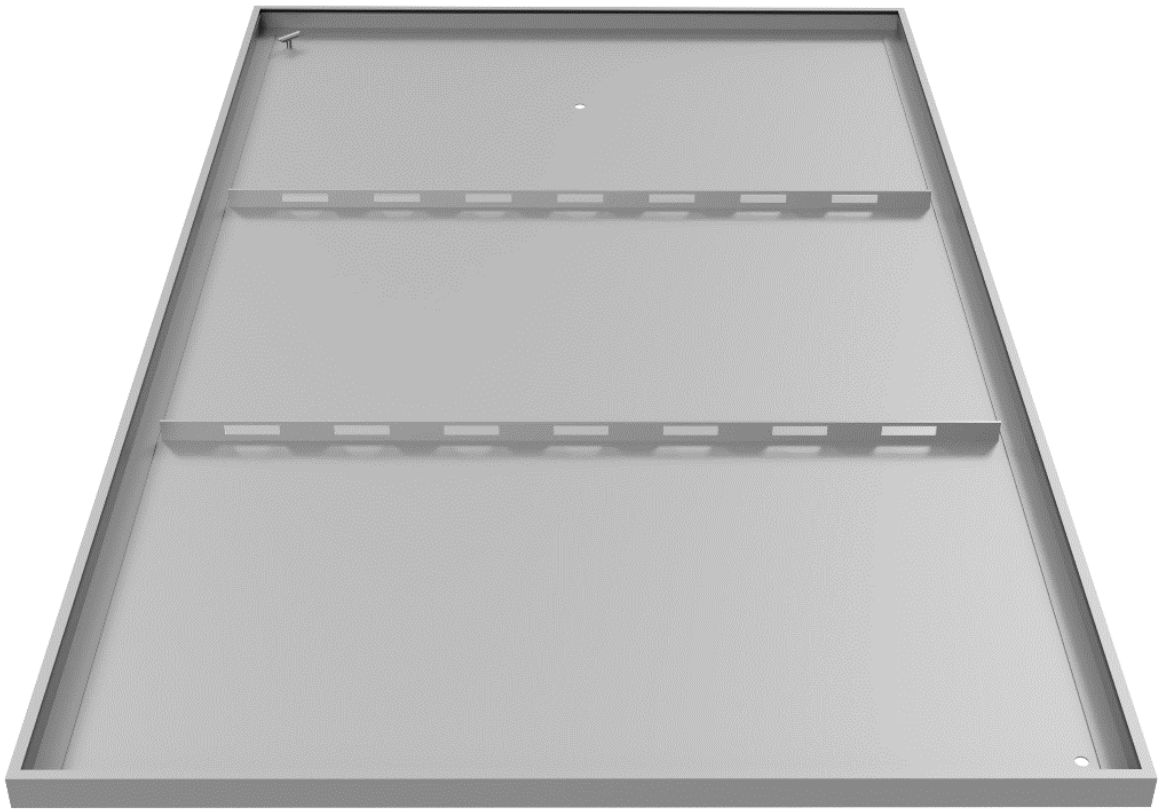

Figure 78: Design of Type 1.2 prototype with an open top.

5.5.5.3 Type 2.1 prototype

The Type 2.1 prototype aims to achieve an after-market cooling system that can be attached to existing PV panels. Therefore, an aluminium tank was designed to have eight aluminium stiffeners. The stiffeners consist of aluminium U channels with holes routed to allow water to flow through them. These stiffeners are glued to both the top and bottom aluminium plates, creating rigidity and avoiding buckling as much as possible. Any buckling in the top aluminium plate would result in poor contact with the back of the PV module, resulting in a poor and non-uniform heat transfer. Therefore, besides the stiffeners, the top plate was designed with a thickness of 5mm, while the bottom plate would have a thickness of 2mm. The water inlet and outlet are placed on the back aluminium sheet on opposite corners of the PV module, and their sizes are similar to those for the Type 1 prototypes. A T-shaped stream spreader is installed

internally at the water inlet. The shape of the aluminium tank was designed in such a way as to allow space for the junction box, which is situated at one of the short sides of standard commercial PV modules. Figure 79 shows the design of the Type 2.1 prototype with the top removed to view internal design details.

Figure 79: Design of Type 2.1 prototype with an open top.

5.5.5.4 Type 2.2 prototype

The Type 2.2 prototype involves an aluminium tank having eight aluminium stiffeners, each alternatively attached to an opposite side of the long sides of the PV module. The stiffeners consist of solid aluminium U channels glued to the top and bottom aluminium plates. These stiffeners are used to avoid buckling of the top aluminium plate and create a sinusoidal path for the water to flow from the inlet to the outlet. Therefore, unlike the other prototypes, in the Type 2.2 prototype, water has to follow a specific path dictated by the stiffeners before exiting from the outlet. Inlet and outlet sizes are similar to the other prototypes. However, a T-shaped stream spreader was omitted from this design since the aluminium tank is compartmentalised into

smaller sections and therefore, controlling the direction of the inlet water flow was unnecessary. Figure 80 shows the design of the Type 2.2 prototype with the top removed to view internal design details.

Figure 80: Design of Type 2.2 prototype with open top.

5.5.6 Computational fluid dynamic simulations

The next step of the design was to compare various design ideas and analyse their effectiveness for cooling the PV module quickly and uniformly. This was done by subcontracting computational fluid dynamic simulations of different IPCoSy designs.

The first simulations involved the flow analysis of a Type 1.1 prototype without an inlet stream spreader. This analysis aimed to determine the validity of the hypothesis that without a stream spreader, a big part of the cool water will flow directly from the inlet to the outlet, thus resulting in a lengthy and inefficient cooling flow. Figure 81 shows a CFD simulation on a cross-section along the long part of a Type 1.1 prototype. The presented images reflect intervals of approximately one hundred eighty seconds from the start of a cooling flow, shown in the top left image. This figure shows that as soon as cooling is started, the flow direction is predominant from the inlet directly to the outlet. As cooling time progresses, as shown in the middle row of images, water at the lowest temperature escapes from the outlet, with most of the water chamber still at elevated temperatures. This means that pump power and water resource are being wasted since it is not efficiently contributing to the cooling of the PV panel. Furthermore, if such a system is designed to feed a water heating system, it would be feeding

it with cold water, thus decreasing the overall system efficiency. Finally, another observation from Figure 81 is that the points furthest from the water inlet, such as the corners, take very long to cool down since they are not being reached by the cool water entering the water chamber and instead have to cool down by quasi-natural convection towards the cooler water in adjacent places.

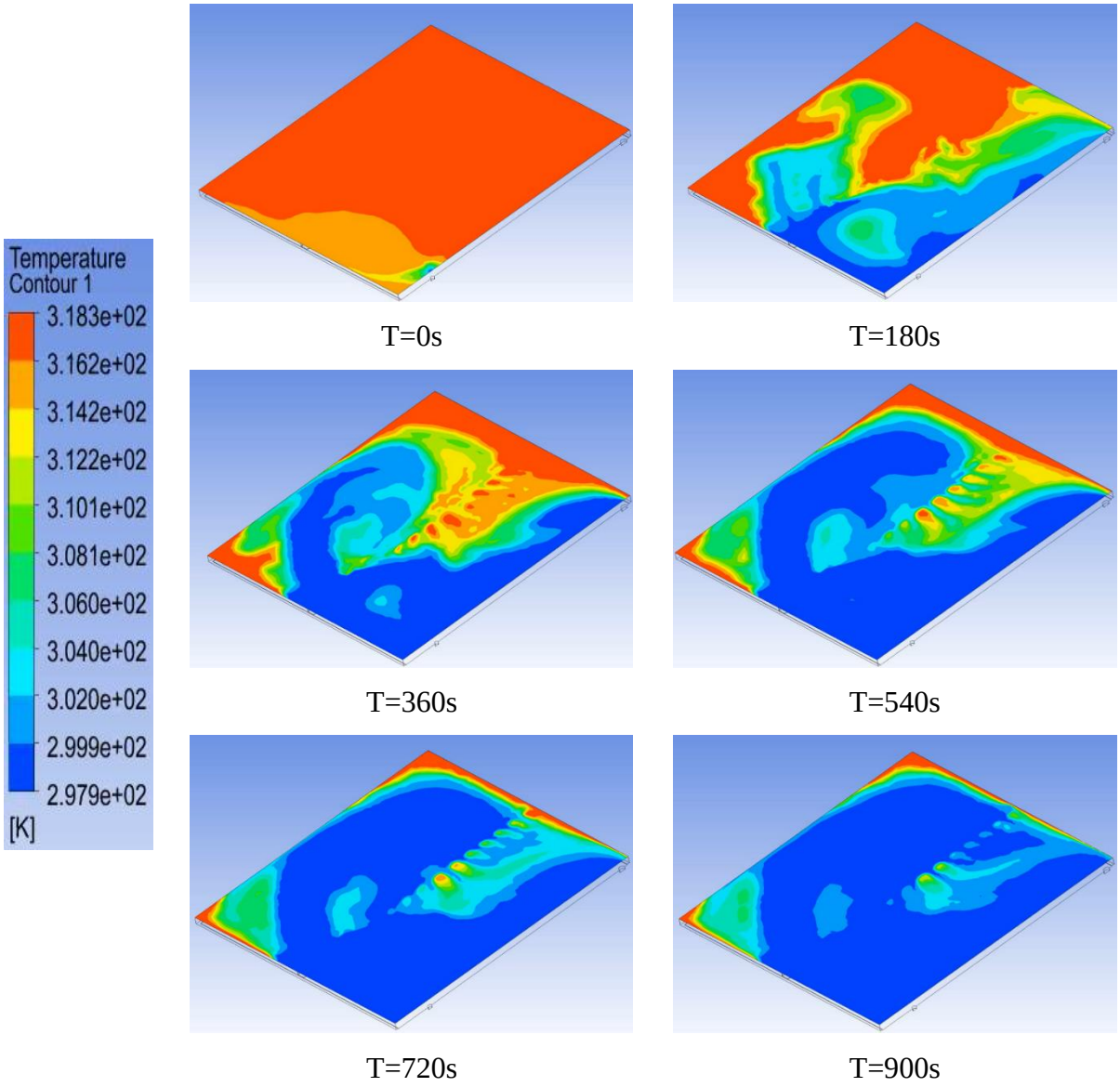

Figure 81: CFD analysis of Type 1.1 prototype without an inlet stream spreader.

Therefore, once the hypothesis that one needs to force a direction on the water inlet was proven, it was essential to decide on the design of the stream spreader. Hence, two slightly different designs for the inlet stream spreader were proposed, and a CFD analysis would determine the best out of the two. One of the designs, shown in Figure 82 (left), involved a Tee fitting with the opposite edges cut at a 45 degree angle while the other design, shown in Figure 82 (right), consisted of a tee coupled with two 45 degree fittings. The main difference between the two

designs lies in the initial directional path the water will follow when entering the cooling chamber.

Figure 82: Two inlet stream spreader designs.

Figure 83 shows a CFD simulation on a cross-section along the long part of a Type 1.1 prototype, with the figures on the left having a stream spreader consisting of a tee fitting and two 45 degree elbows. The images shown in this figure correspond to different time steps with the top images being the first time step and the bottom images corresponding to the last time steps. In contrast, the figures on the right have a stream spreader comprised of a tee-fitting cut at a 45-degree angle. From this simulation, it is clear that for the tee fitting with the 45° elbows, as soon as water exits the spreader, it hits one of the sides of the frame of the PV module. This causes some of the water to continue flowing to the rest of the PV module while a part of it is reflected towards the outlet. This partial reflection causes cold water to exit from the outlet before reaching the rest of the PV module, as shown in the second and third row of pictures in Figure 83.

In contrast, the spreader consisting of a cut Tee fitting has the inlet water flowing towards parts of the cooling chamber that are furthest from the water inlet. This type of flow is desirable since the warmer water is displaced and pushed out by the colder water. This is further evidenced by the last two rows of images in Figure 83 which show that while the prototype on the right has achieved uniform cooling, the prototype on the left still has various areas at different temperatures. The latter behaviour is not desirable when cooling PV panels since having a series combination of solar cells at different temperatures will still result in a current output limited by the hottest solar cell. Therefore, these simulations show that the inlet water flow needs to be directed towards the area that is furthest away from the inlet and the outlet to create a ‘piston effect’, pushing out the hot water. Hence, with this result in mind, it was concluded that the most adequate stream spreader would consist of a tee fitting with the long sides cut at a 45-degree angle.

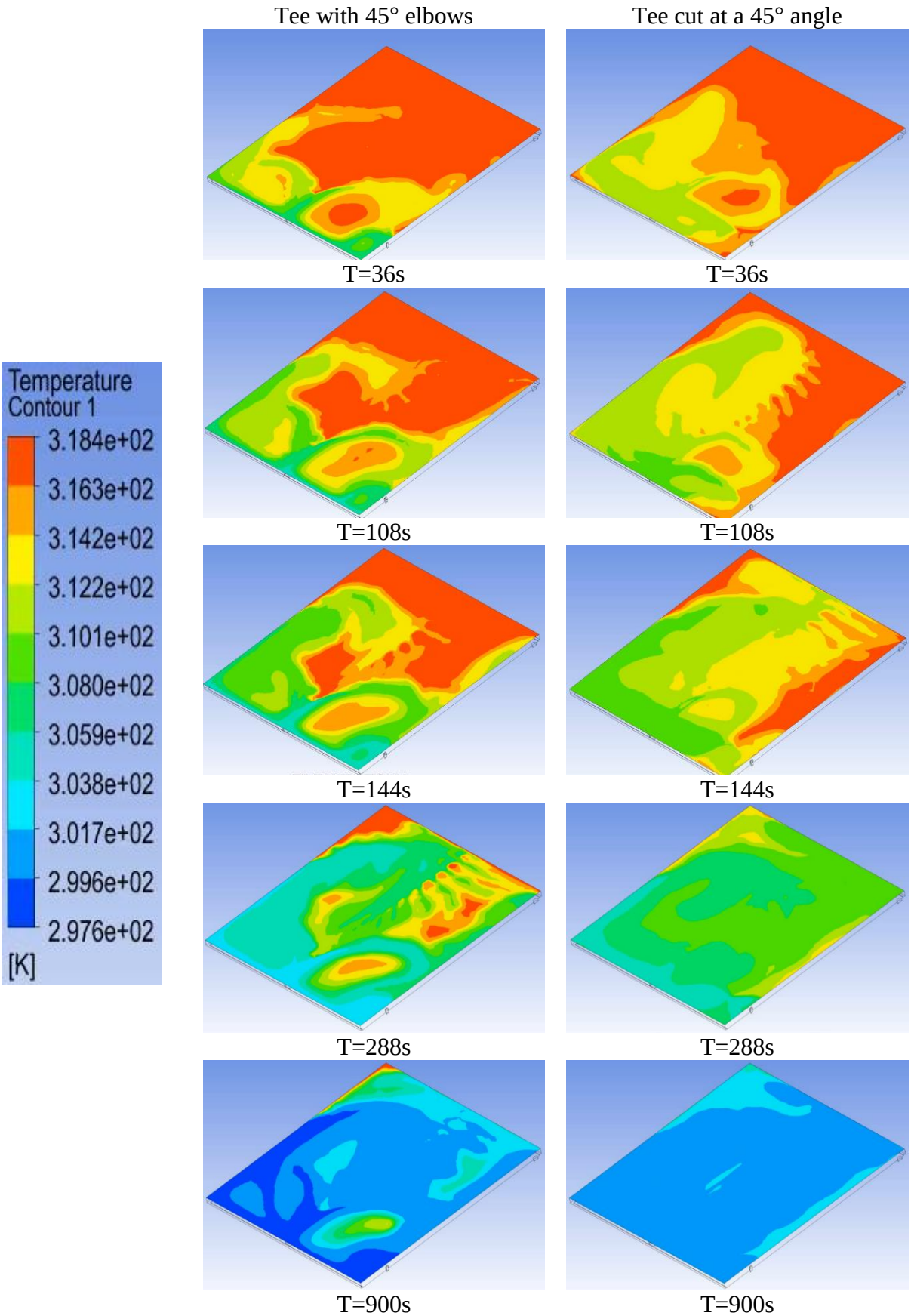

Figure 83 CFD analysis of Type 1.1 prototype with two different stream spreader designs.

Another CFD simulation, shown in Figure 84, involved a previous design of the Type 2.1 prototype where the stream spreader was placed opposite the water outlet in a central position, similar to the Type 1.1 prototype. The images shown in this figure correspond to different time steps with the top images, left to right, being the first two time steps and the bottom images, left to right, corresponding to the last time steps. This CFD simulation showed that due to the proximity and a large number of stiffeners present in this prototype, the directional flow caused by the stream spreader was encountering too much resistance and was still resulting in most of the cool input water flowing directly to the output without pushing any of the hot water present in the cooling chamber. Therefore, this configuration would still result in an inefficient cooling flow.

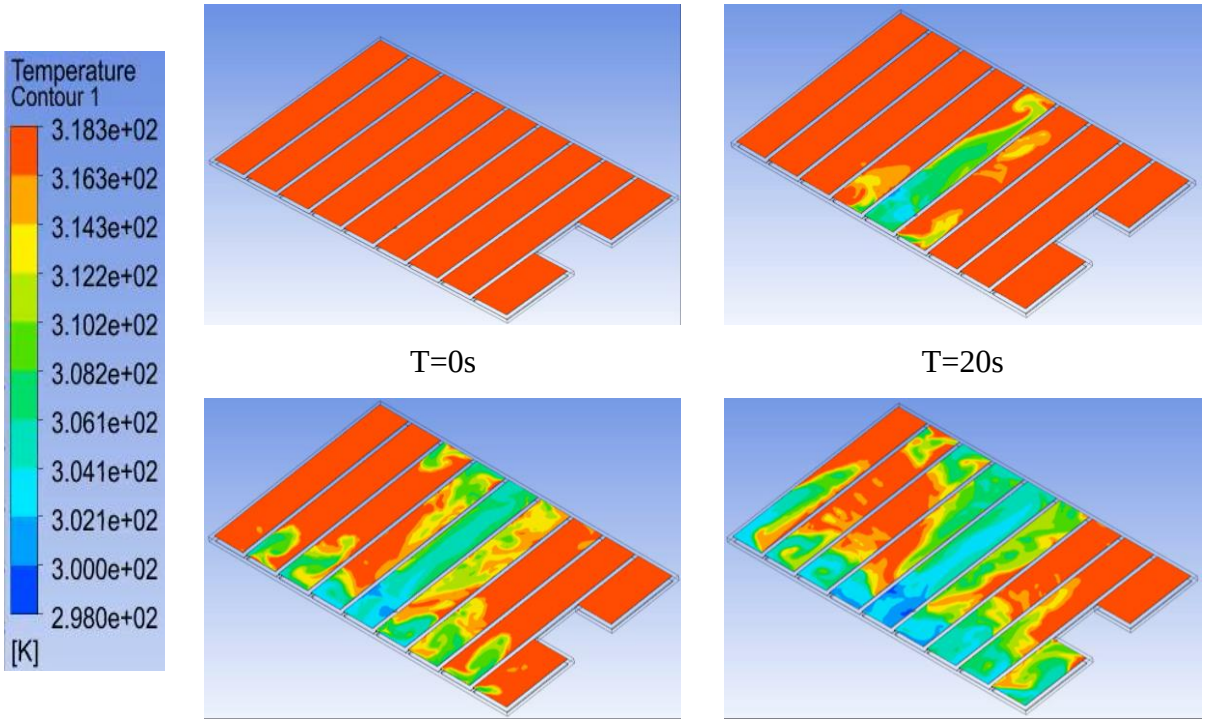

Figure 84: CFD analysis of Type 2.1 prototype with inlet and outlet opposite each other in a central position.

Hence, it was decided that the stream spreader and the output would be placed in opposite corners of the prototype, similar to the Type 1.2 prototype. A CFD simulation was again performed on this new configuration, and as shown in Figure 85 and Figure 86, when the results are compared to the old design, the increase in cooling efficiency is evident. The images shown in this figure correspond to different time steps with the top images, left to right, being the first two time steps and the bottom images, left to right, corresponding to the last time steps. Furthermore, this simulation highlights the benefits of adding a stream spreader since one side

of the stream spreader directs the water towards the part of the prototype where the tank shape changes to allow space for a conventional PV junction box. This stream of water effectively cools this area, which would otherwise be very difficult to cool since water would keep flowing toward the water outlet on the opposite side.

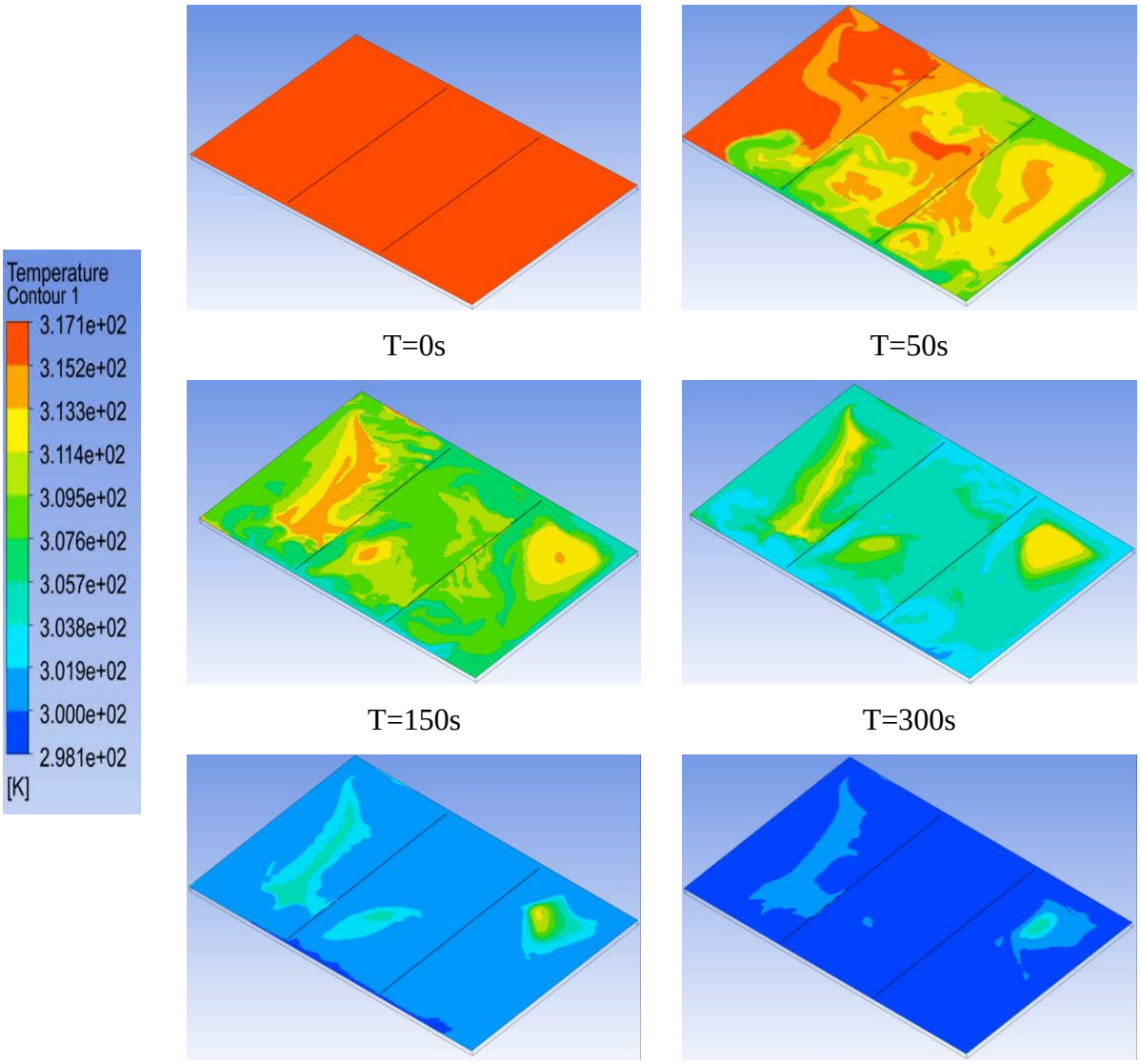

Figure 85: CFD analysis of Type 1.2 prototype.

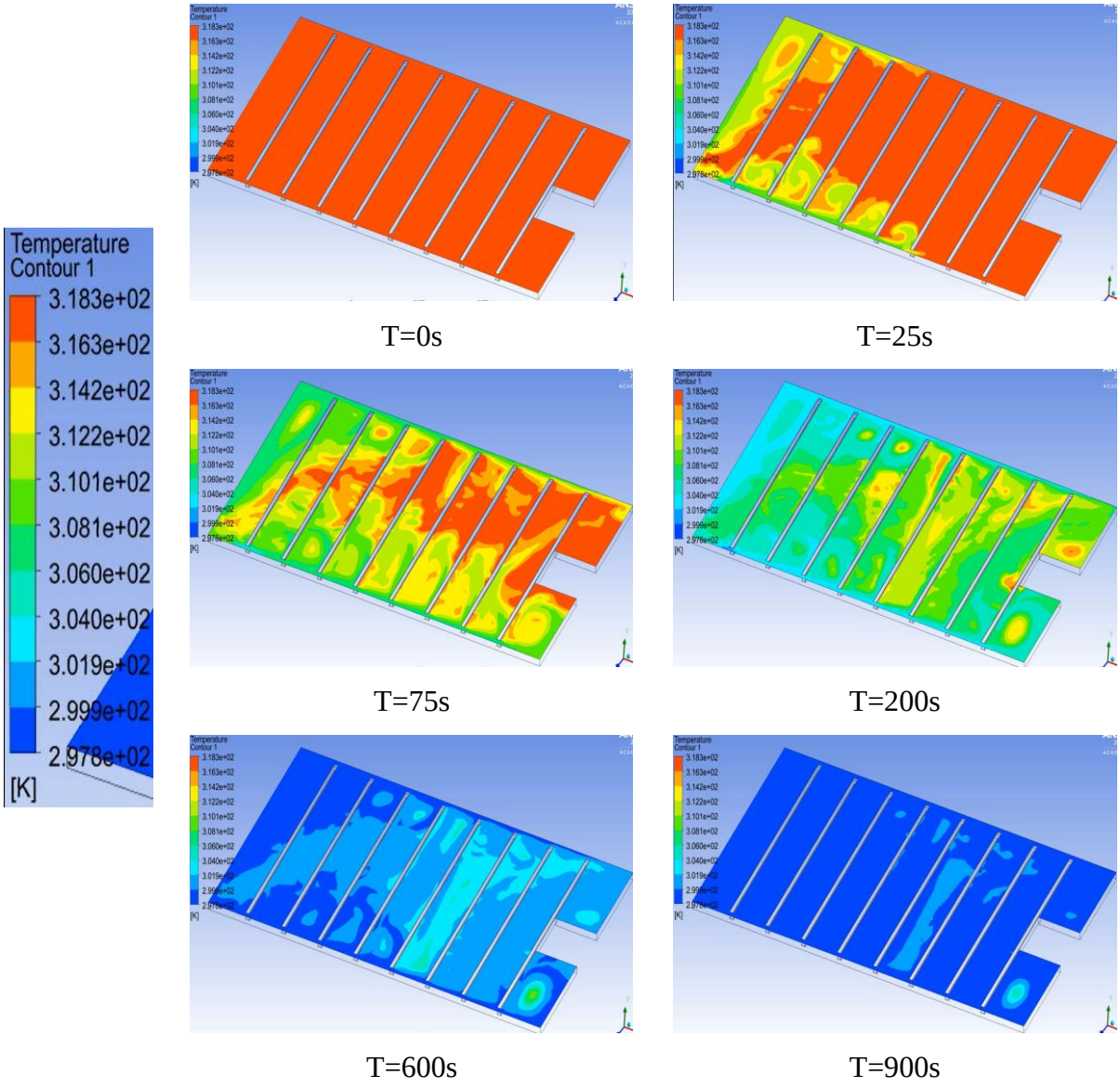

Figure 86: CFD analysis of Type 2.1 prototype with inlet and outlet situated in opposite corners.

The final CFD simulation was carried out on the Type 2.2 prototype to confirm its viability. The images shown in Figure 87 correspond to different time steps with the top images, left to right, being the first two time steps and the bottom images, left to right, corresponding to the last time steps. This simulation produced results that were in line with expectations. Cool water flowed from the inlet to the outlet pushing the hot water out and creating the desired “piston effect”. The area next to the junction box was cooled efficiently due to the lack of space between the last stiffener and the edge of the tank. This small distance allowed the entire area to be filled with cold water before exiting through the outlet.

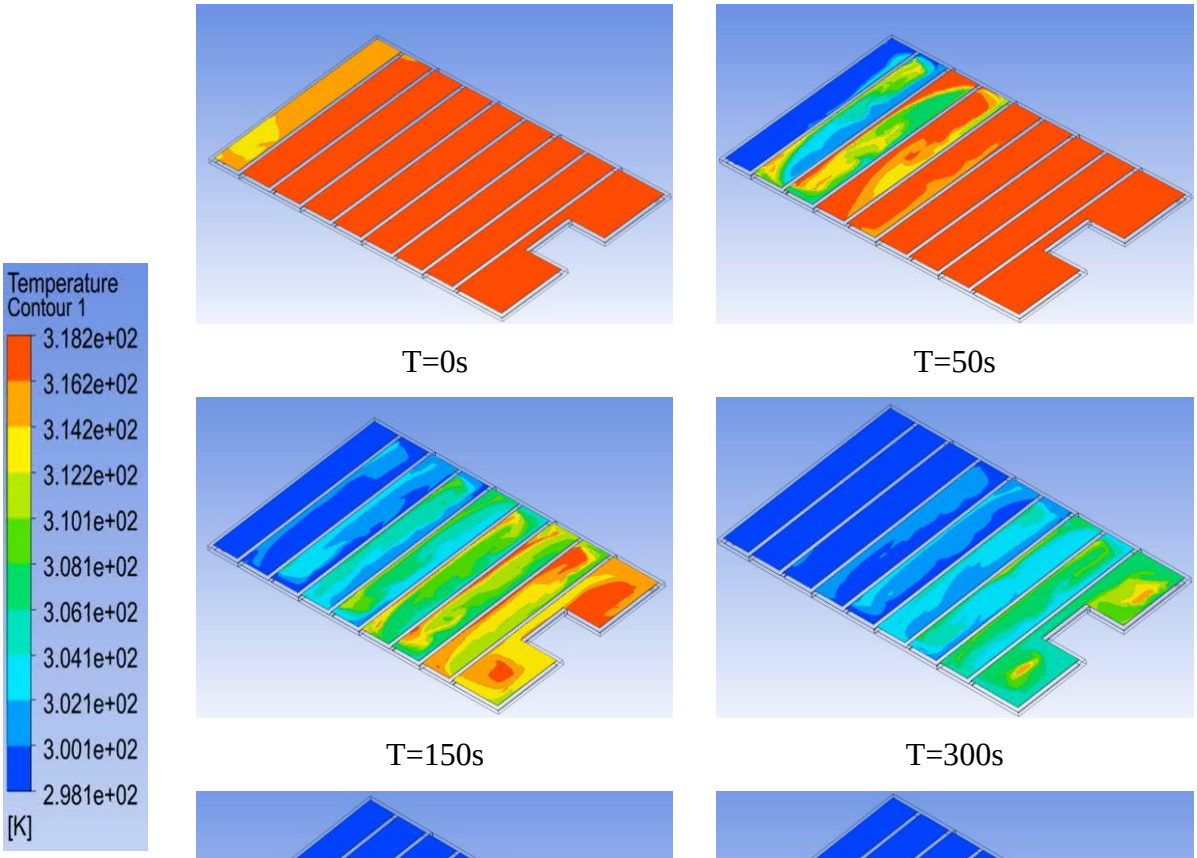

Figure 87: CFD analysis of Type 2.2 prototype.

5.5.7 Prototype manufacturing

The four final prototype designs described in the sections above were sent to EMPAV ENGINEERING Ltd. for further processing and manufacturing. These designs are shown in Appendix F. The junction box of the Type 1 prototype was sealed using marine sealer instead of pouring hot resin, as shown in Figure 88 (left). This was done since the chemical reaction when mixing the resin could result in a temperature rise that could damage the solar cell assembly. Furthermore, a four-core cable was soldered with the contacts inside the junction box, and the bypass diodes were removed to transfer everything to a new junction box placed outside the closed PV panel. Figure 88 (right) shows the new external junction box without a cover. Hence, the internal edges and corners were sealed using a marine sealant. Aluminium

corners were manufactured to fit inside the PV module's inner corners to ensure that water does not leak through these corners, as shown in Figure 89 (left). Furthermore, two type T thermocouples were attached to the back sheet of the solar cell assembly using their own glue. A thin layer of marine sealant was poured on top of the attached thermocouples to protect them from coming into direct contact with the cooling water, as shown in Figure 89 (right). A type T thermocouple was chosen since, at the expected temperature ranges, these thermocouples have the highest accuracy out of all the base metal thermocouples. The predicted accuracy of Type T thermocouples is up to ±1℃ in accordance with the standard ANSI/ASTM E230 [125].

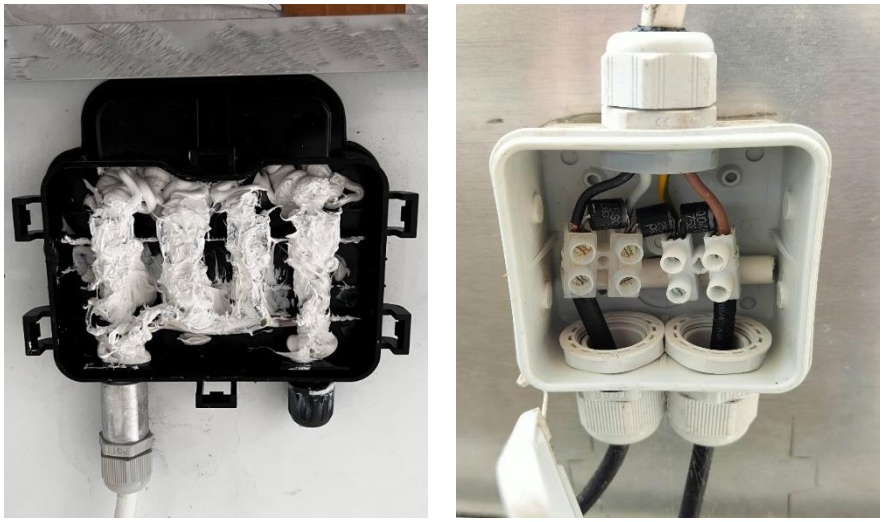

Figure 88: Sealed internal junction box (left) and new external junction box (right).

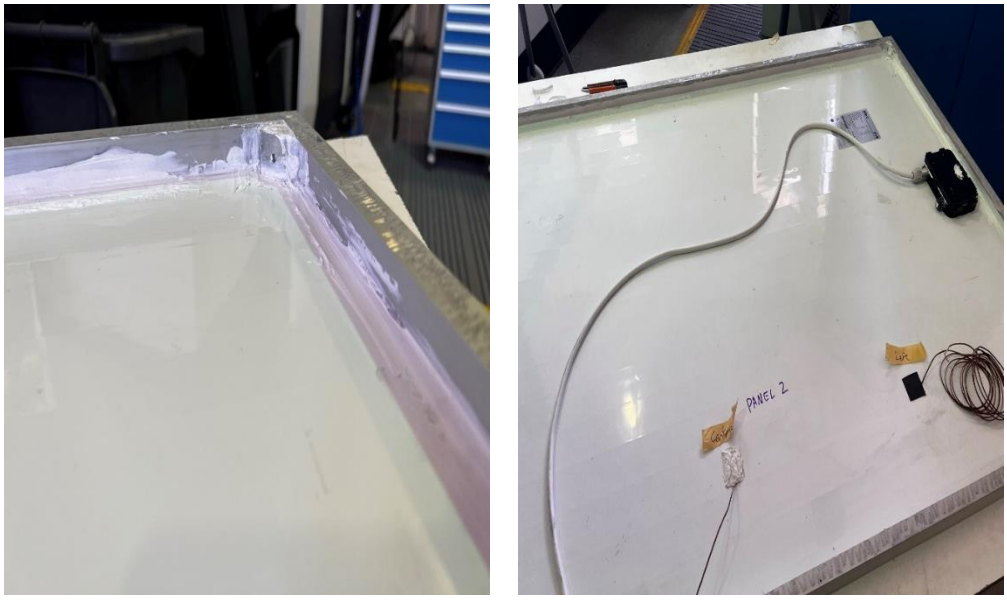

Figure 89: Type 1 prototype with sealed edges (left) and attached thermocouples (right).

For manufacturing the Type 2.1 and Type 2.2 prototypes, 3mm aluminium sheets were cut and bent to form U channels. Some U channels were joined together to form the frame of the aluminium water tank, and the rest were used as stiffeners. Furthermore, for the Type 2.1 prototype shown in Figure 90, the channels used for stiffeners had five-centimetre slots routed in one of their faces to allow water to flow through them. The Type 2.2 prototype stiffeners only had one slot routed at the very edge; hence, they were attached in alternating orientations to create the desired water path. A 5mm aluminium sheet was used to close off the part of the tank that would be in contact with the back-side of the PV module, while a 3mm back sheet was used to close off the other side of the tank. The sheets and stiffeners were attached together using marine glue and sealant. Furthermore, countersunk holes were drilled in the aluminium sheets, and self-tapping screws were inserted to provide more rigidity and structural integrity. Two type T thermocouples were attached to the 5mm aluminium sheet. Marine sealant was poured on top of the attached thermocouples to protect them from coming into direct contact with the cooling water. Figure 91 shows two of the final manufactured prototypes ready for installation.

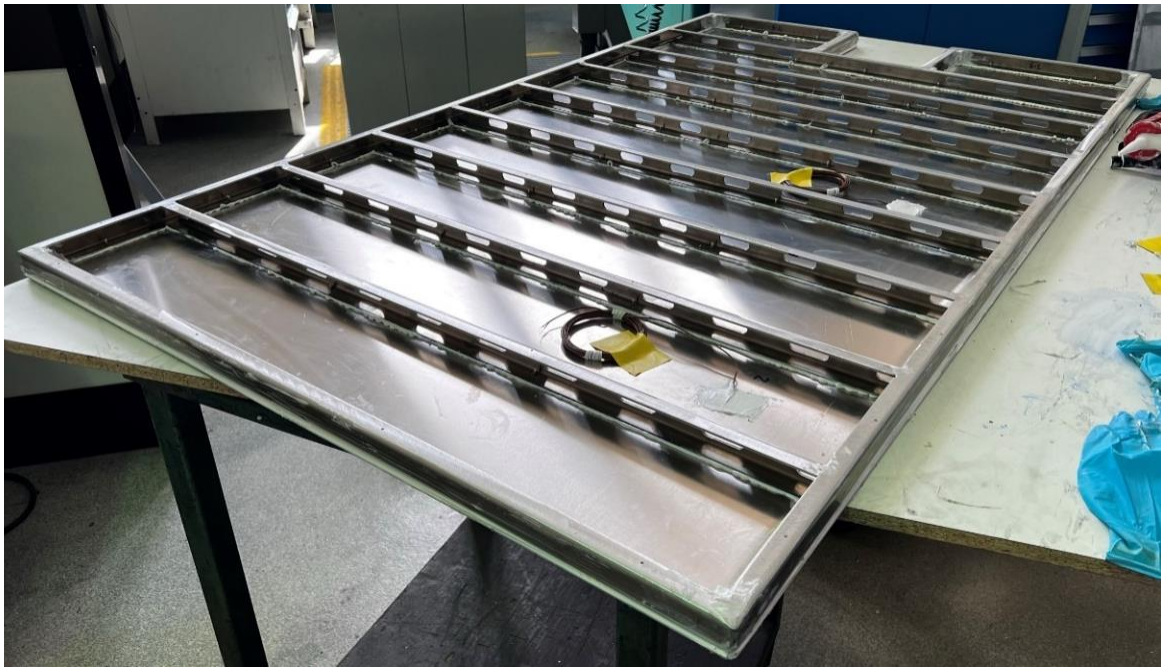

Figure 90: Type 2.1 prototype during manufacturing.

Figure 91: Final Type 1.1 (Left) and Type 2 (right) prototypes.

5.5.8 Experimental setup

The next phase of this research was to implement an experimental setup, shown in Figure 92, to compare the different types of prototypes and contrast a conventional PV module with IPCoSy PV modules.

A call for quotations was issued for seven monofacial solar panels having a standard residential size and a standard type and position for the junction box. Seven ALEO X59 photovoltaic modules were chosen together with Enphase IQ7+ micro-inverters. The ALEO panels had dimensions of 1.66m by 0.99m with a 300W maximum power rating at standard test conditions (STC) and a 222W rating at nominal conditions. The PV module had a white polymer back sheet and 3.2mm front toughened solar glass. Solar cells used in these panels were Passivated Emitter and Rear Contact (PERC) monocrystalline Silicon technology, and each module had a total of 60 solar cells. Micro-inverters were chosen over other solutions to have each panel generating power completely independent from the rest to enable comparisons. An installation angle of 10° was chosen to minimise the hydrostatic pressure on the IPCoSy modules and reduce the risk of damage during experimentation.

The IPCoSy prototypes were fitted with a male thread to Hep_2O converters to be able to use Hep_2O fittings for all the pipework. A 300L water tank was placed under the PV installation to be shaded from direct Sunlight. A 12V 20W DC submersible pump was placed inside the tank to circulate water continuously through a TECO TK-2000 water chiller. The chiller was introduced to control the water supply temperature and achieve temperature stability to simulate installations where the water resource is much larger, such as in an offshore environment. The chiller was placed in a well-shaded area, and water pipes from the chiller to the water tank were insulated to decrease the chiller's load. Furthermore, the chiller was placed at a lower elevation than the water tank to ensure it always remains full of water, even during a power outage. The chiller power consumption will not be considered in the net energy calculations of the cooling system since this would not be present in everyday scenarios.

The temperature in the water tank was measured by placing a submersible thermocouple consisting of a type T thermocouple attached to an aluminium plate and sealed from water entry. A water pressure regulator was installed in line with the PV system to avoid any accidental build-up of pressure that could result in the prototypes' permanent damage. A second 12V 20W DC submersible pump was placed inside the 300L water tank to supply water to the IPCoSy cooling chambers when the control system switches on the cooling flow.

Figure 92: IPCoSy full-scale experimental setup.

A flexible polyurethane tank was placed under one of the PV modules to test a flexible solution for IPCoSy. However, after the first test, it was noted that, when filled with water, the tank would keep stretching beyond the design requirements, resulting in warping of the PV panel. Therefore, it was decided to scrap the idea of a flexible solution for the purposes of this research. However, the flexible tank was emptied and left installed under the PV module to simulate a PV with limited forced cooling due to wind speed. Hence, the system had conventional PV panels acting as experimental control, IPCoSy types 1 and 2 prototypes and a conventional PV module with the back-side shielded from the effect of wind.

Since each micro-inverter could output a maximum of 1.39A of continuous current, miniature circuit breakers with a 2A tripping current were chosen to protect each individual PV and inverter. Therefore, the whole PV installation was expected to have a maximum continuous current output of 9.73A. Hence, a further 10A-rated Miniature Circuit Breaker (MCB) and a 30mA Residual Current Device were installed to protect the overall circuitry.

The sizing of the required current carrying capacity for the Alternating Current (AC) cable carrying the power of all seven PV modules was calculated using equation (67) [126]. In this equation, I_z is the required current carrying capacity while I_N is the current rating of protection devices which in our case is the 10A rating of the MCB. C_a, C_g and C_{gT} are derating factors for ambient temperature, circuit grouping factor and ground temperature respectively. A 40 °C ambient temperature was chosen to slightly overcompensate for possible elevated temperatures, resulting in a derating factor of 0.87. Furthermore, a 40°C ground temperature was considered resulting in a 0.77 derating factor. Finally, no circuit grouping factor was required since only a single circuit was present.

$$I_Z = \frac{I_N}{C_a \times C_g \times C_{gT}} = \frac{10A}{0.87 \times 1 \times 0.77} = 14.93A \quad (67)$$

Since the cable was not routed through a conduit, reference method C (clipped direct) was chosen from Table 4D2A of the Institution of Electrical Engineers (IEE) regulations [126]. According to this table, a cable with a conductor cross-sectional area of 1.5mm^2 has a current carrying capacity of up to 19.5A. However, apart from the current carrying capacity, one must also take care of the voltage drop for such a cable. PV installation guidelines allow up to a 3% voltage drop, equating to 6.9V. According to Table 4D2B of the IEE regulations, a 1.5mm^2 cable has a voltage drop of 29mV/A/m, meaning that a 16m cable would have an acceptable voltage drop of 3.68V. To further increase the accuracy of the experimental setup and eliminate

the loss variable, we decided to opt for a conductor cross-sectional area of 2.5mm^2 with a voltage drop rating of 18mV/A/m, resulting in a total drop of 2.3V (equivalent to 1%).

A Simex MultiCon CMC-141 datalogger, shown in Figure 93, was chosen due to its versatility in accepting various inputs by adding specific cards. A TC12 card was used to read twelve independent thermocouples with a 0.1% precision. Seven SGT-22 transmitters were used to measure AC current and convert it into a standard output signal using a Root Mean Square (RMS) value algorithm. These sensors measure current with an accuracy of 0.2% and a nonlinearity of 0.025%. The output of the seven current sensors is read by an SlAi-8 module which can sample analogue data from up to eight devices and send this data to the datalogger through the RS-485 protocol. The SlAi-8 can sample data at an approximate frequency of 10Hz from every channel with an accuracy of ±0.25%. The final current sensing and protection distribution board is shown in Figure 94.

Figure 93: Simex MultiCon CMC-141 datalogger.

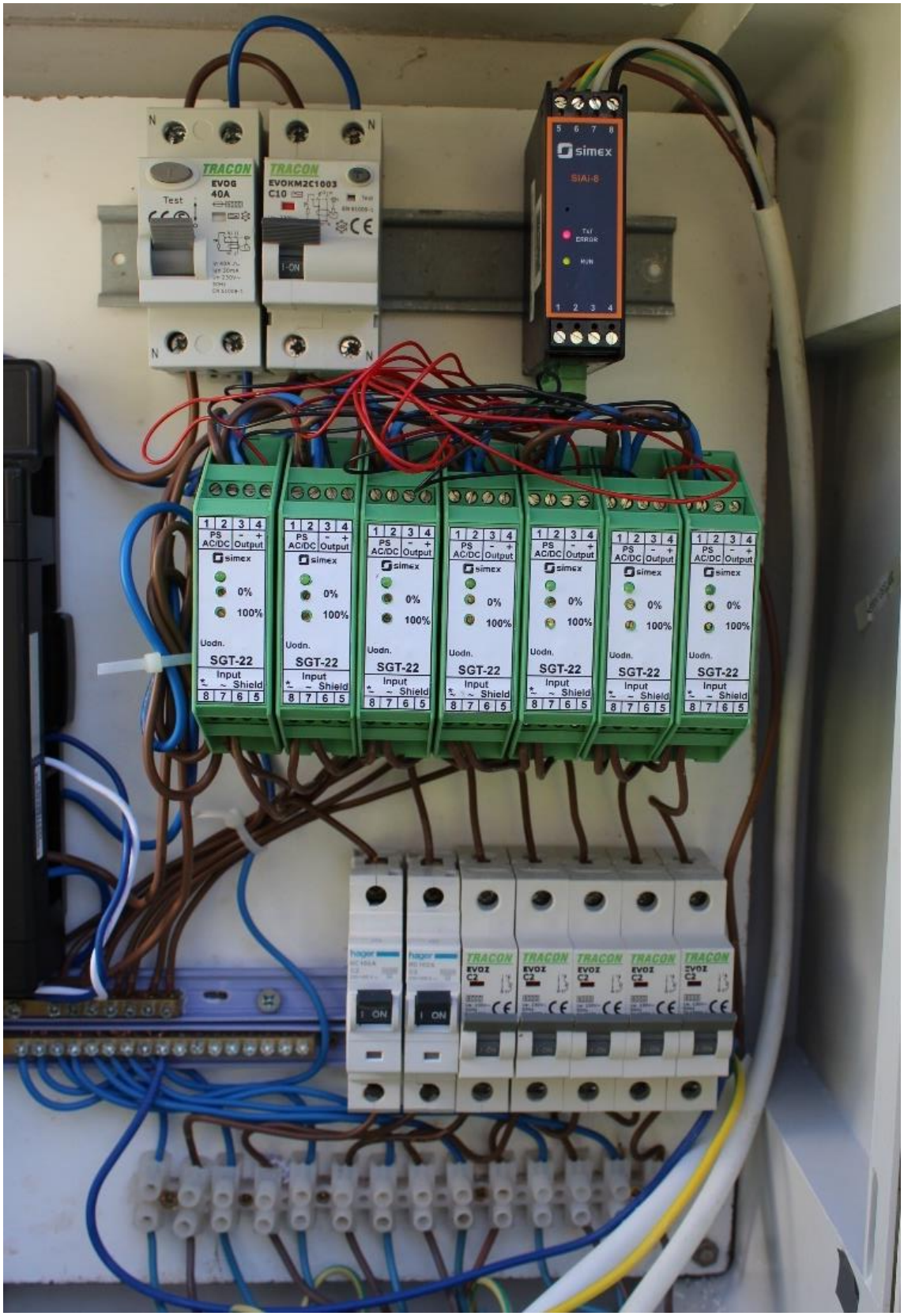

Figure 94: Current sensing and protection distribution board.

After initial testing, it was noted that during production, the internal thermocouples of the Type 1.1 and Type 2.1 prototypes were damaged, and no signal could be read. Furthermore, the junction box of the Type 1.1 prototype was not adequately sealed, and when filled with water, the connections were shorted, and the PV panel stopped producing power. Due to the limited time and financial resources, it was impossible to fix these manufacturing errors. Therefore, it was decided that research could still be conducted by comparing the Type 1.2 and Type 2.2 prototypes with conventional PV panels shielded and unshielded from wind cooling.

Before sending the PV panels for manufacturing and modification, the PV system was set up, including the dataloggers and sensors mentioned above and left operating for 55 consecutive days to obtain calibration factors. These calibration factors were essential to remove any discrepancies in the output of the PVs and inverters resulting from manufacturing tolerances. Therefore, after these calibration factors are applied to the acquired data, any discrepancies noted can be attributed to the experiment in question, which in this case, would be the cooling effect. Figure 95, Figure 96 and Figure 97 show the plots of the control PV against Type 1.2, Type 2.2 and shielded PV respectively. Calibration equations were obtained using linear regression with the assumption that the output of all PVs intersects at the zero power point.

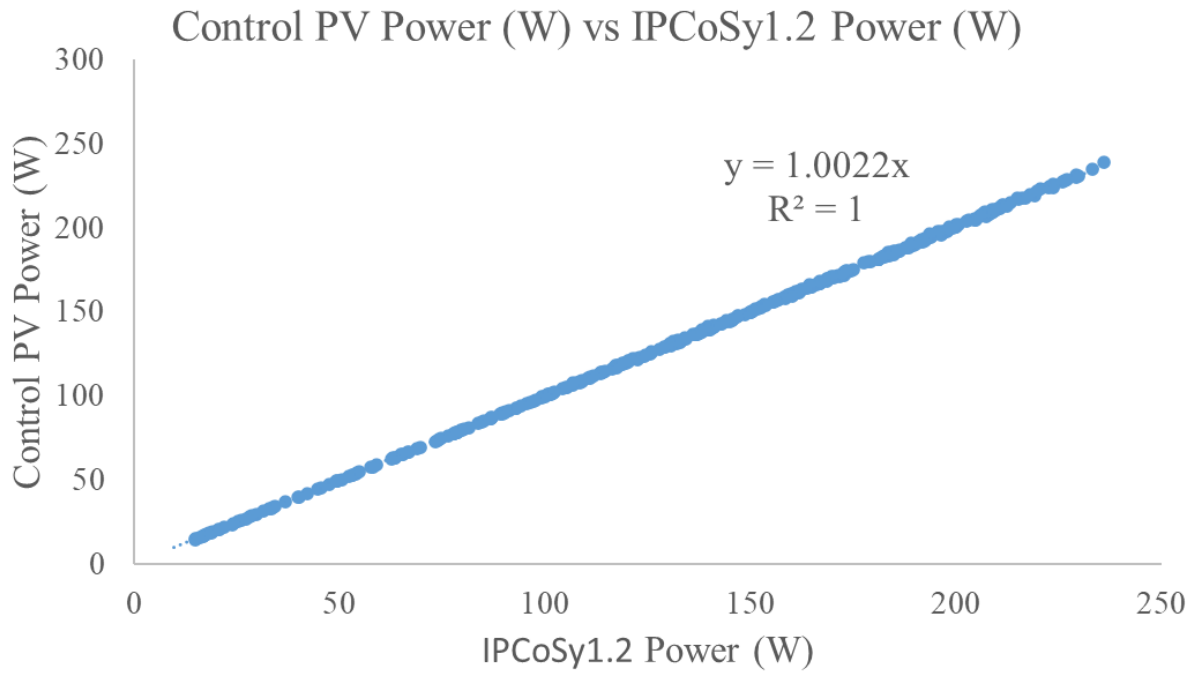

Figure 95: Calibration factor for Type 1.2 prototype.

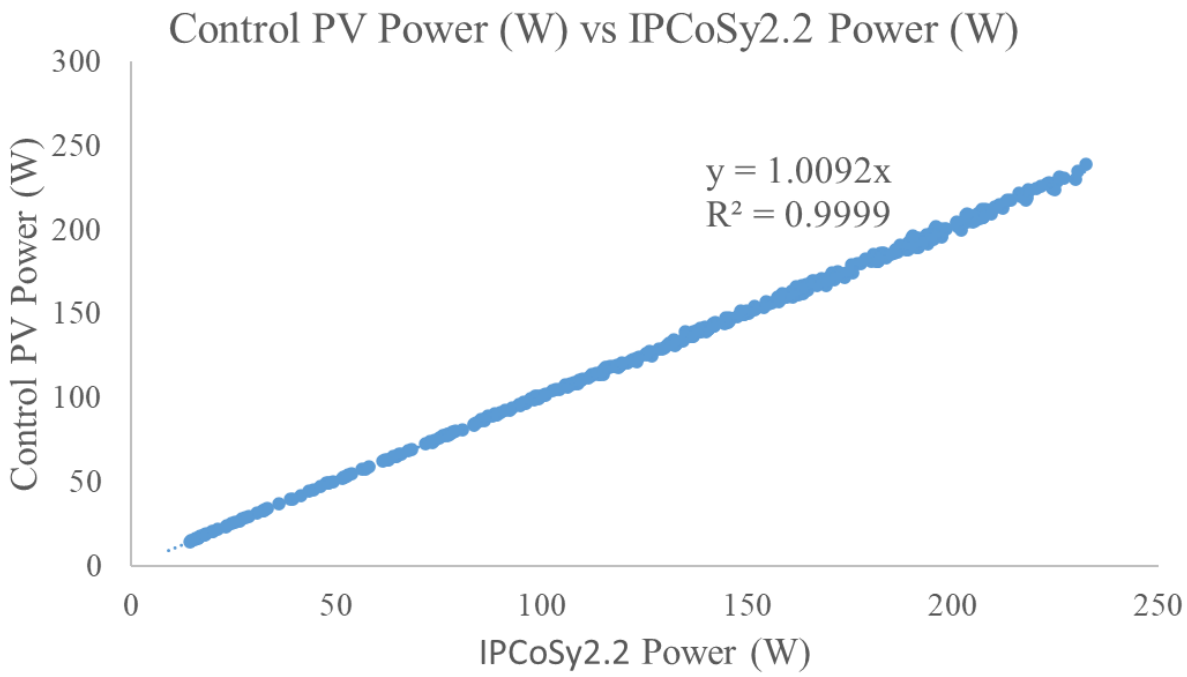

Figure 96: Calibration factor for Type 2.2 prototype.

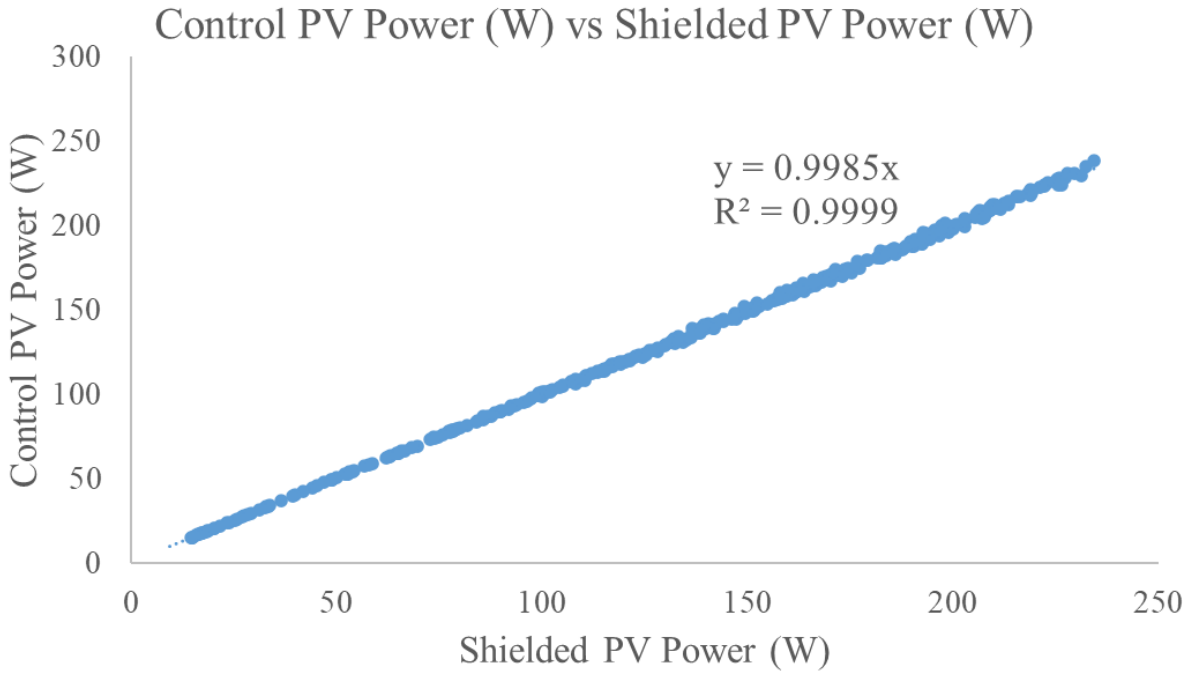

Figure 97: Calibration factor for shielded PV.

Figure 98 represents a typical plot of temperature data (in °C) recorded on the 2nd of September 2022. On this day the IPCoSy 2.2 prototype was operated with a controlled flow between 35°C and 40°C. In contrast the IPCoSy 1.2 prototype was filled with water and left operating without

further flow. Figure 99 presents a typical plot of PV output power (in Watts) recorded on the 2nd of September 2022. Details and results of these experiments will be presented in the following sections of this chapter.

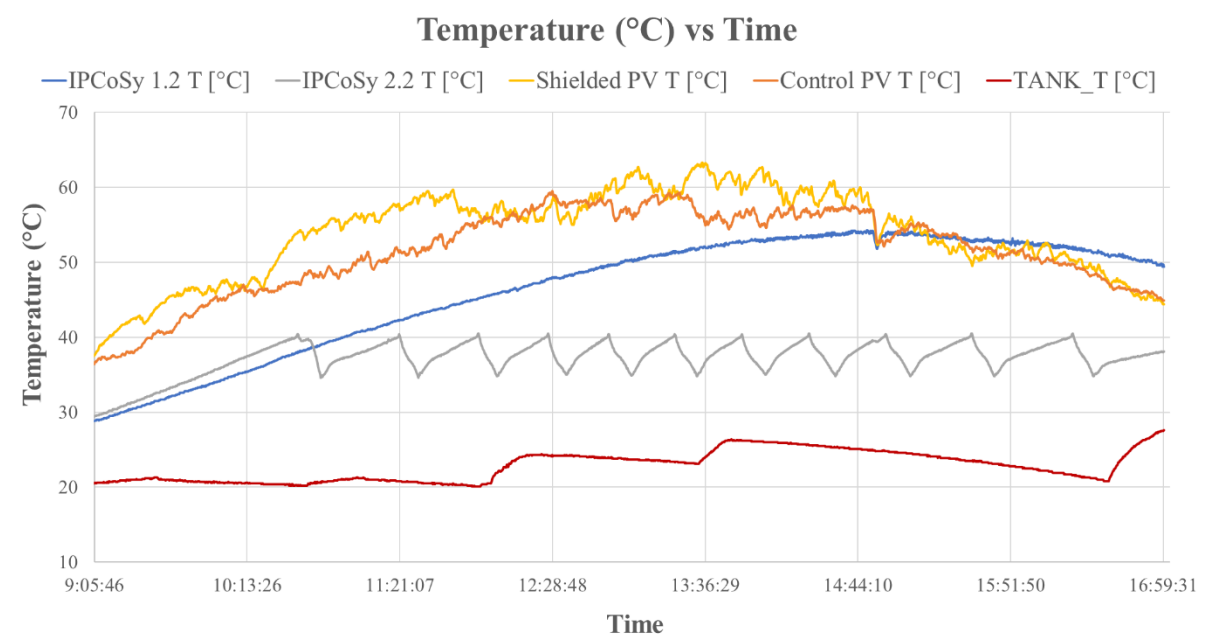

Figure 98: Recorded temperature data for the 2nd of September 2022.

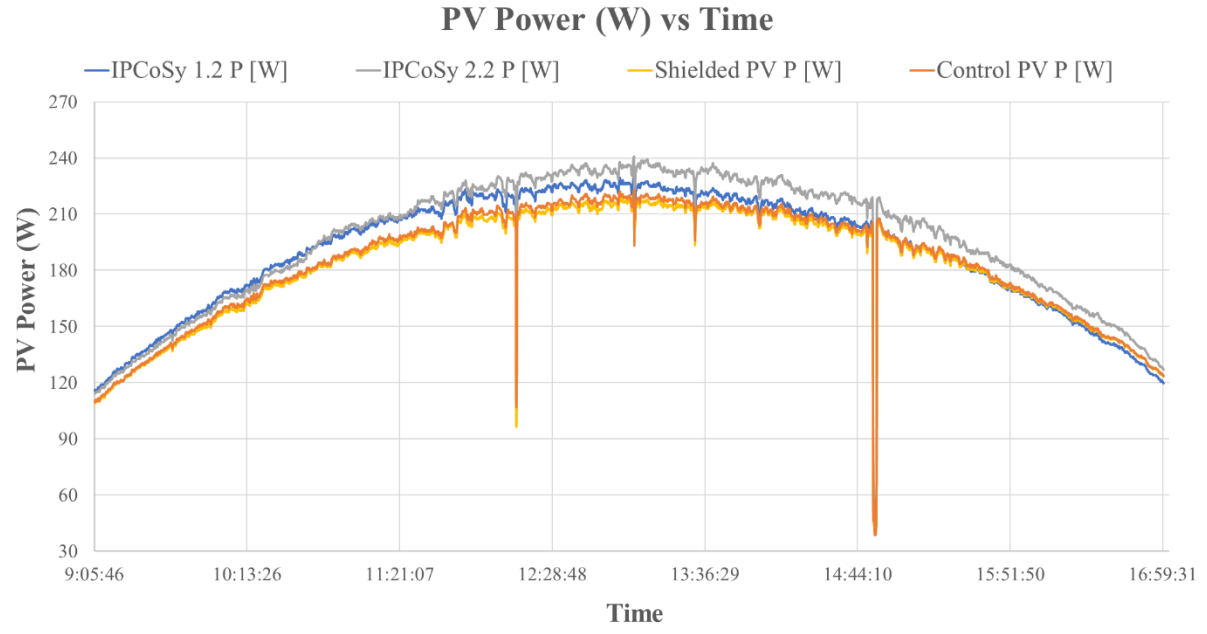

Figure 99: Recorded power data for the 2nd of September 2022.

5.5.9 Testing with no flow

5.5.9.1 Introduction

After gathering data from experimentation, a temperature model was required to represent the new prototypes' thermal performance. Two temperature models were considered: the Faiman Model [127] and SANDIA National Laboratories Model [54].

The Faiman Temperature model is utilised by PVSYST, a PV simulation software that is widely used in industry. This model, given by equation (68), consists of a modification of the Hottel-Whillier-Bliss equation [128] [129] to predict the PV module temperature, T_{mod}, using the ambient temperature T_a, the irradiance incident on the plane of the PV module G_{inc}, the wind speed *v* and two heat transfer coefficients U_0 and U_1. U_0 represents a constant heat transfer coefficient, while U_1 represents the convective heat transfer coefficient due to wind. This equation shows that if one had to plot G_{inc} / (T_{mod} - T_a) against v, the fitted straight line would have a y-intercept and gradient corresponding to U_0 and U_1 respectively.

$$T_{mod} = T_a + \frac{G_{inc}}{U_0 + U_1 \times v} \tag{68}$$

The Sandia Model, given by equation (69), is an empirically-based thermal model utilising the irradiance incident on the plane of the PV module G_{inc}, wind speed *v*, ambient temperature T_a and two empirically determined coefficients *a* and *b*. Hence, if the natural log of {(T_{mod} - T_a) / G_{inc}} is plotted against the wind speed, the fitted straight line would have a y-intercept and gradient corresponding to a and b respectively. Table 14 [54] shows some empirically determined values for *a* and *b* for different PV module types and different installation scenarios.

$$T_{mod} = G_{inc} \times \{e^{a+b\times v}\} + T_a \tag{69}$$

Table 14: Empirically determined Sandia thermal model coefficients.

Module Type	Mount	a	b
Glass/cell/glass	Open rack	-3.47	-0.0594
Glass/cell/glass	Close roof mount	-2.98	-0.0471
Glass/cell/polymer sheet	Open rack	-3.56	-0.0750
Glass/cell/polymer sheet	Insulated back	-2.81	-0.0455
Polymer/thin-film/steel	Open rack	-3.58	-0.113
22x Linear Concentrator	Tracker	-3.23	-0.130

This part of the research aimed to find a new thermal model that describes the IPCoSy prototypes when filled with water and left to operate without any further water changes. The experimentations with the small prototypes showed that the increase in specific heat capacity results in a delayed rise in temperature, and the maximum PV temperature never reaches that of a standard PV panel. To obtain such a model, weather data was required, namely the irradiance incident on the plane of the PV module in W/m^2, the wind speed in m/s, and the ambient temperature and the PV module temperature in ℃. Irradiance, wind speed and ambient temperature were obtained from the Institute for Sustainable Energy's weather station, which is situated very close to the experimental setup. The module temperature was measured directly from the thermocouples attached to the back-side of the PV modules.

5.5.9.2 Wind measurement

The Institute for Sustainable Energy's weather station anemometer is situated 6.82m above ground level on which the experimental setup was installed. Furthermore, besides being installed at ground level, the experimental setup had various wind shielding from nearby structures such as buildings and trees. Therefore, to get a more accurate temperature model, it was necessary to adjust the measured wind speed to reflect better the conditions at the level of the experimental setup. This was done by installing an elliptical anemometer from BARANI DESIGN Technologies next to the weather station's anemometer at the same height. This was essential to calibrate any discrepancies between the two anemometers and afterwards be able to compare data with both anemometers installed in different places. Linear and second-order polynomial regressions were fitted to the gathered data.

The linear regression shown in equation (70) achieved a fit with a root mean square error of 0.4065 and an R^2 of 0.9467. The second-order polynomial regression shown in equation (71) achieved a fit with a root mean square error of 0.3924 and an R^2 of 0.9504. Hence, although both regressions were adequate, it was decided to use the second-order polynomial regression due to its slightly better fit. Figure 100 shows the data plot from the BARANI DESIGN Technologies anemometer against the ISE weather station anemometer before and after applying the calibration equation.

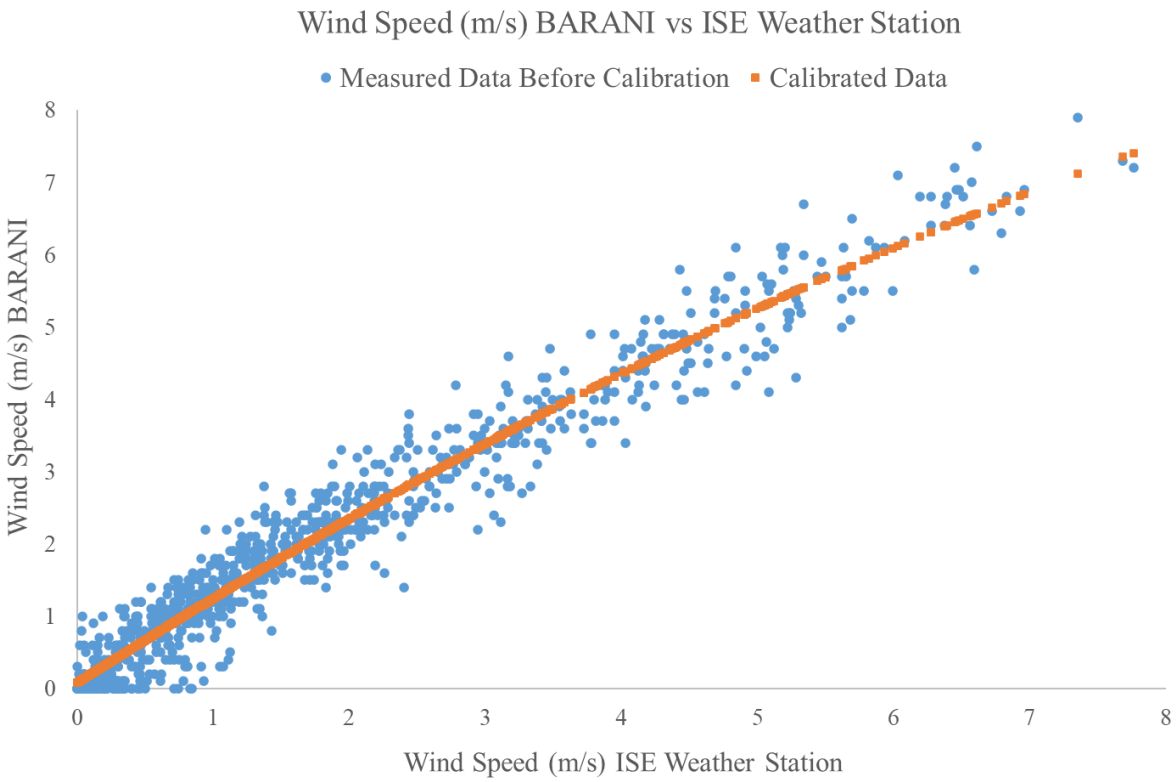

Figure 100: Plot of data from BARANI anemometer against ISE weather station anemometer before and after calibration.

$$v_{BARANI} = (1.0148 \times v_{station}) + 0.2224 \quad (70)$$

$$v_{BARANI} = (-0.0333 \times {v_{station}}^2) + (1.2029 \times v_{station}) + 0.0787 \quad (71)$$

The next step was to transpose wind speed data gathered from the weather station height to wind speed at the height and location of the experimental setup. Hence, the BARANI DESIGN Technologies anemometer was installed at the site of the experimental setup and a height of 1m above ground level. Data was gathered from the ISE weather station and the BARANI anemometer for several days to find an empirical characteristic equation between the two locations. The most common equations used to transpose wind measurements to different heights are the power law, shown in equation (72), and the log law, shown in equation (73). In these equations, z and z_r are the target and reference heights respectively, while U(z) and U(z_r) are the wind speeds at these heights. Furthermore, z_0 is the surface roughness length that varies for different terrains and conditions and is usually taken from a predetermined set of tables or

found empirically. Similarly, the power law exponent α is generally taken as either 0.143 or else chosen from an empirically derived set of values [130].

$$\frac{U(z)}{U(z_r)} = \left(\frac{z}{z_r}\right)^{\alpha} \tag{72}$$

$$\frac{U(z)}{U(z_r)} = \frac{\ln\left(\frac{z}{z_0}\right)}{\ln\left(\frac{z_r}{z_0}\right)} \tag{73}$$

Four equations were used to obtain the best wind transposition, namely the Power Law, the Log Law, a linear regression and a second-order polynomial regression. Table 15 shows the equations and statistical analysis comparing the predicted values transposed from the ISE weather station to data measured at the location of the experimental setup.

As explained above, the power and log laws are more general equations and should be used for most applications requiring transposing wind measurements to different heights. A Power Law exponent of 0.3682 was found, corresponding to terrain in suburbs and urban areas with tall buildings. Although this does not reflect the topography in which the experimental setup was installed, the resultant power law exponent value agrees with the range published by Farrugia [131] in a study carried out in the Maltese islands. In addition, the surface roughness length of the log law was found to be 0.1601, corresponding to terrain with few trees [130]. To increase the accuracy of this research, it was decided that the polynomial regression equation should be used to transpose wind data instead of the other equations. Figure 101 compares measured wind data at the location of the experimental setup to wind data transposed from the ISE weather station.

Table 15: Statistical analysis of wind transposition equations.

	Power Law	**Log Law**	**Linear Regression**	**Polynomial Regression**
Details	$\alpha = 0.3682$	$z_0 = 0.1601$	$y = 0.5248x - 0.1246$	$y = -0.0133x^2+0.6781x-0.4458$
RMSE	0.3866	0.3866	0.3790	0.3629
R^2	0.9333	0.9333	0.9359	0.9412

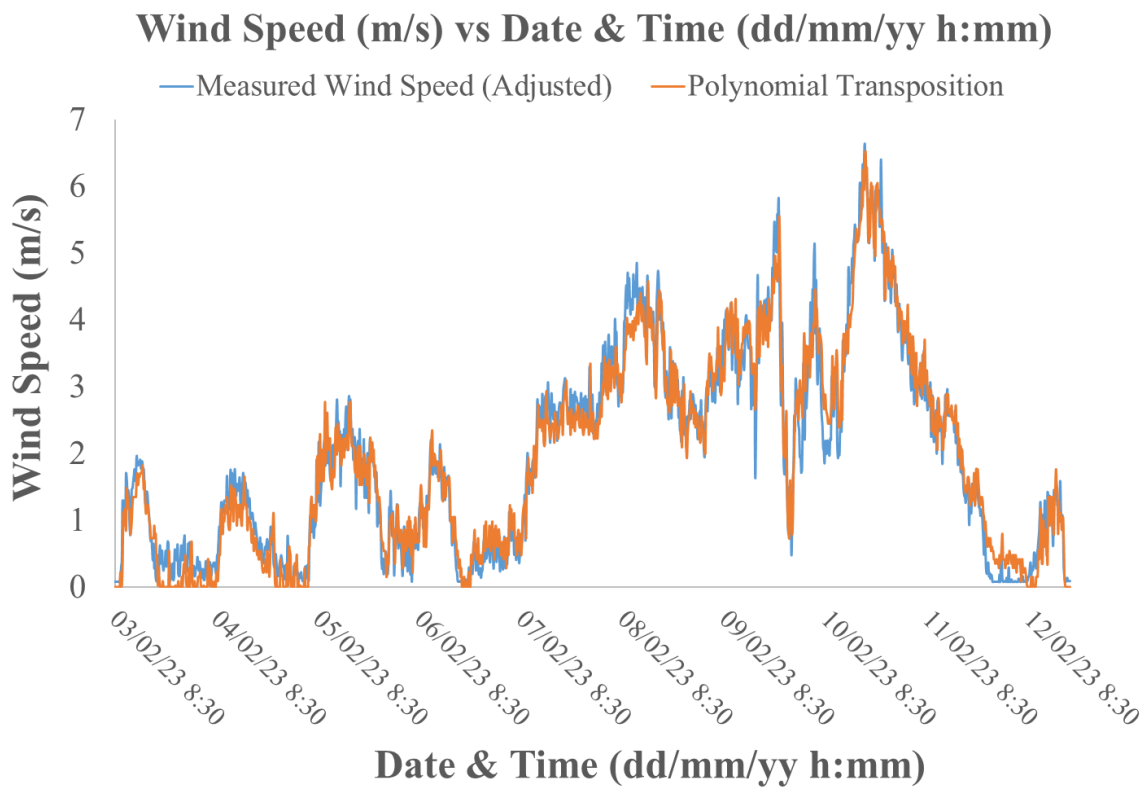

Figure 101: Measured and transposed wind speeds.

5.5.9.3 Temperature model

After the experimental setup was implemented, the IPCoSy panels were filled with water and testing commenced. One set of experiments involved filling the IPCoSy panels with water, closing off all valves and allowing the PV modules to operate without further interference. The objective of these tests was to observe the effect of the added PV module specific heat capacity with the introduction of a water body always in contact with the back-side of the PV module.

Sixteen days of adequate no-flow test data were gathered for the Type 1.2 prototype, while six days were recorded for the Type 2.2 prototype. Data was recorded between August and December 2022. The Microsoft Excel solver add-in was used to perform iterations and find values for *a* and *b* for the Sandia temperature model and U_0 and U_1 for the Faiman temperature model. Although the resulting models were adequate for predicting the PV module temperature of the control modules, none of these models seemed to be accurate when it came to the IPCoSy prototypes. This phenomenon was attributed to IPCoSy prototypes having higher thermal inertia, which is not considered in the two temperature models. This increased thermal inertia comes from adding a high specific heat capacity fluid at the back of the PV module.

Hence, the way forward was to modify the temperature model equations to incorporate a time factor in minutes from midnight based on a 1-hour offset from the Coordinated Universal Time (UTC+1). Therefore, PV temperatures were plotted against time in minutes from midnight to get an idea of the relationship between the two. From the plot shown in Figure 102, it was determined that a logarithmic relationship would best describe the effect of time on the increase in temperature for an IPCoSy prototype. Therefore, a factor of C1.ln(t)+C2 was added to both the Sandia and Faiman temperature models, where t is the time in minutes from midnight and C1 and C2 are two empirically determined constants. Hence, the Microsoft Excel solver was used to compute iterations and deduce the temperature model constants that give the least root mean square errors. The resultant modified Sandia temperature model equations that describe the thermal behaviour of the IPCoSy 1.2, IPCoSy 2.2 and Control PV modules are shown in equations (74), (75) and (76), respectively.

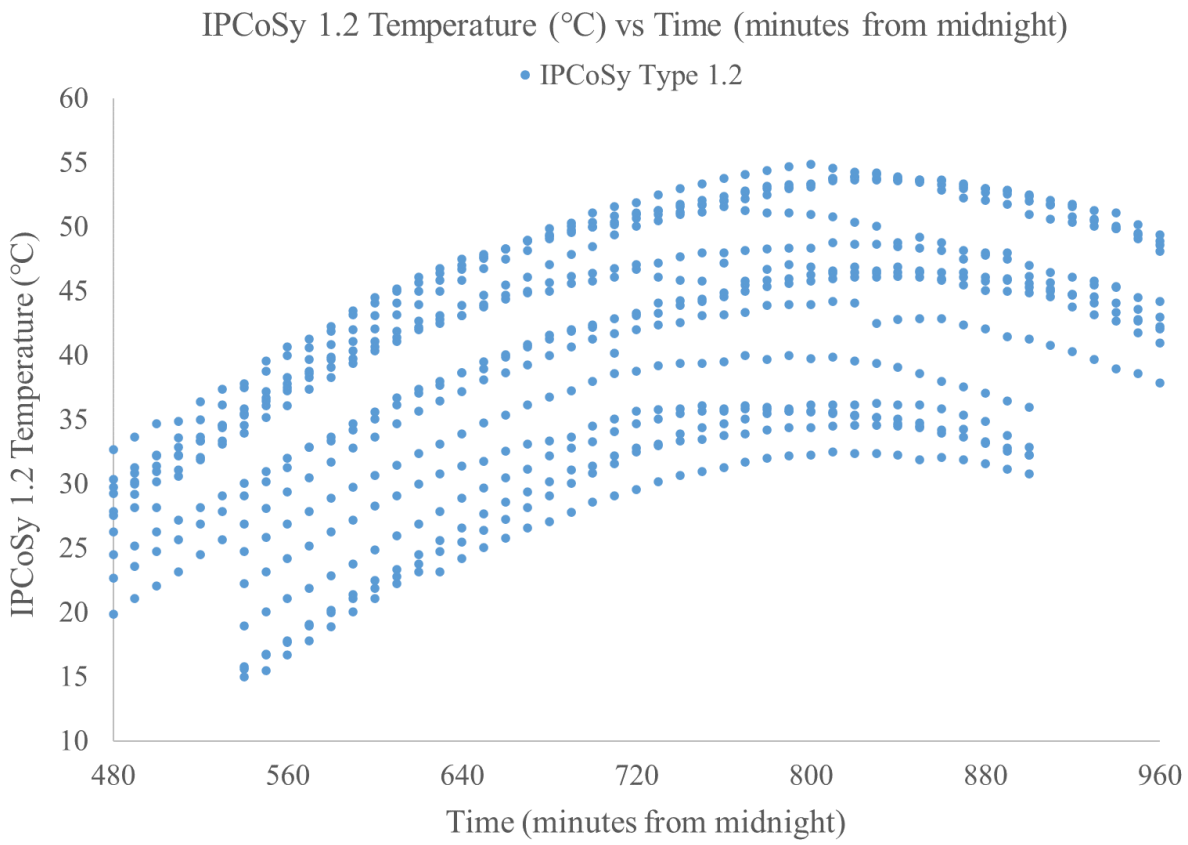

Figure 102: IPCoSy PV temperature against time in minutes from midnight.

The resultant modified Faiman temperature model equations that describe the thermal behaviour of the IPCoSy 1.2, IPCoSy 2.2 and Control PV modules are shown in equations (77), (78) and (79), respectively.

$$T_{IPCoSy\ 1.2} = G_{inc} \times \{e^{-10.0918+(-0.0166\times v)+(2.1946\times ln(t)-8.3808)}\} + T_a \quad (74)$$

$$T_{IPCoSy\ 2.2} = G_{inc} \times \{e^{-9.6970+(-0.1707\times v)+(1.9686\times ln(t)-6.9196)}\} + T_a \quad (75)$$

$$T_{Control} = G_{inc} \times \{e^{-3.974+(-0.089\times v)+(0.3553\times ln(t)-1.942)}\} + T_a \quad (76)$$

$$T_{IPCoSy\ 1.2} = T_a + \frac{G_{inc}}{453.3072 + (1.778 \times v) + (-109.1724 \times ln(t) + 321.9602)} \quad (77)$$

$$T_{IPCoSy\ 2.2} = T_a + \frac{G_{inc}}{293.8376 + (7.5440 \times v) + (-84.2909 \times ln(t) + 301.0609)} \quad (78)$$

$$T_{Control} = T_a + \frac{G_{inc}}{62.62 + (3.5605 \times v) + (-14.07 \times ln(t) + 65.62)} \quad (79)$$

Finally, a multiple linear regression was performed on the gathered data to obtain a regression temperature model. The resultant regression temperature model equations that describe the thermal behaviour of the IPCoSy 1.2, IPCoSy 2.2 and Control PV modules are shown in equations (80), (81) and (82) respectively. Table 16 shows that all statistical P-values for the different parameters are very low, meaning they are all statistically significant and contribute considerably to the multiple linear regression temperature model.

$$T_{IPCoSy\ 1.2} = -29.8461 - 0.5444 \times v + 1.2028 \times T_a + 0.0188 \times G_{inc} + 0.0336 * t \quad (80)$$

$$T_{IPCoSy\ 2.2} = -37.66 - 2.244 \times v + 1.4901 \times T_a + 0.0199 \times G_{inc} + 0.0367 * t \quad (81)$$

$$T_{Control} = -8.2162 - 1.8444 \times v + 1.116 \times T_a + 0.027 \times G_{inc} + 0.0078 * t \quad (82)$$

Statistical analysis was carried out for all three temperature models, the IPCoSy prototypes, and the control PV module. Table 17 shows the Root Mean Square Error (RMSE), Mean Absolute Error (MAE), Standard Deviation (STD) of the MAE and R^2 for all temperature models. The fact that RMSE is greater than MAE shows some variation in the magnitude of the errors. However, the small difference between RMSE and MAE does not indicate the presence of substantial errors. Figure 103, Figure 104 and Figure 105 present plots of the RMSE for all three temperature models for IPCoSy and Control PV modules on different testing dates. Since the Multiple Linear Regression model resulted in the lowest errors, it would

be the ideal model to represent the PV modules. However, it was noted that this model did not perform well in time periods that were outside the time range at which the analysed data was gathered. Hence, it was decided to focus on the modified Sandia model since, although it results in a slightly higher error, it performed well during all times of the day. Figure 106, Figure 107 and Figure 108 show the measured temperatures on particular days compared to temperatures predicted by the three models discussed above.

Table 16: P-values for different parameters in the multiple linear regression.

Parameter	**P-Value**		
	IPCoSy 1.2	**IPCoSy 2.2**	**Control**
Intercept	2.0947×10^{-289}	2.06×10^{-24}	5.81118×10^{-55}
Wind Speed	1.66932×10^{-05}	1.22×10^{-23}	5.52451×10^{-47}
Air Temperature	0	3.54×10^{-27}	0
Solar Irradiance	3.0182×10^{-208}	6.29×10^{-71}	0
Time	0	1.8×10^{-112}	5.4864×10^{-55}

Table 17: Statistical analysis of the three temperature models.

Statistic	**IPCoSy 1.2**		
	Sandia	**Faiman**	**Multiple Linear Regression**
RMSE	2.272	2.4694	1.5904
Mean Average Error	1.7345	1.8585	1.2669
STD of MAE	1.4674	1.6261	0.9614
R^2	0.9391	0.9281	0.9702
	IPCoSy 2.2		
RMSE	2.1796	2.3680	1.8061
Mean Average Error	1.5784	1.7749	1.4225
STD of MAE	1.5032	1.5676	1.1128
R^2	0.9298	0.9171	0.9518
	Control		
RMSE	2.0177	2.0227	1.9161
Mean Average Error	1.6233	1.6280	1.5932
STD of MAE	1.1984	1.2003	1.0645
R^2	0.944	0.9438	0.9495

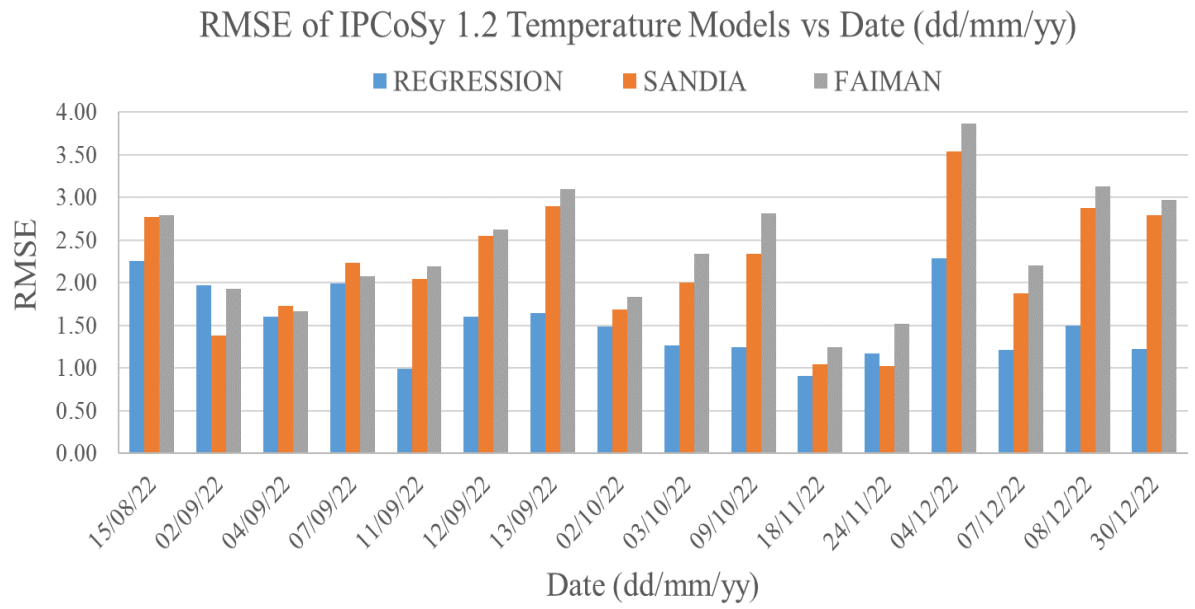

Figure 103: RMSE of IPCoSy 1.2 temperature models.

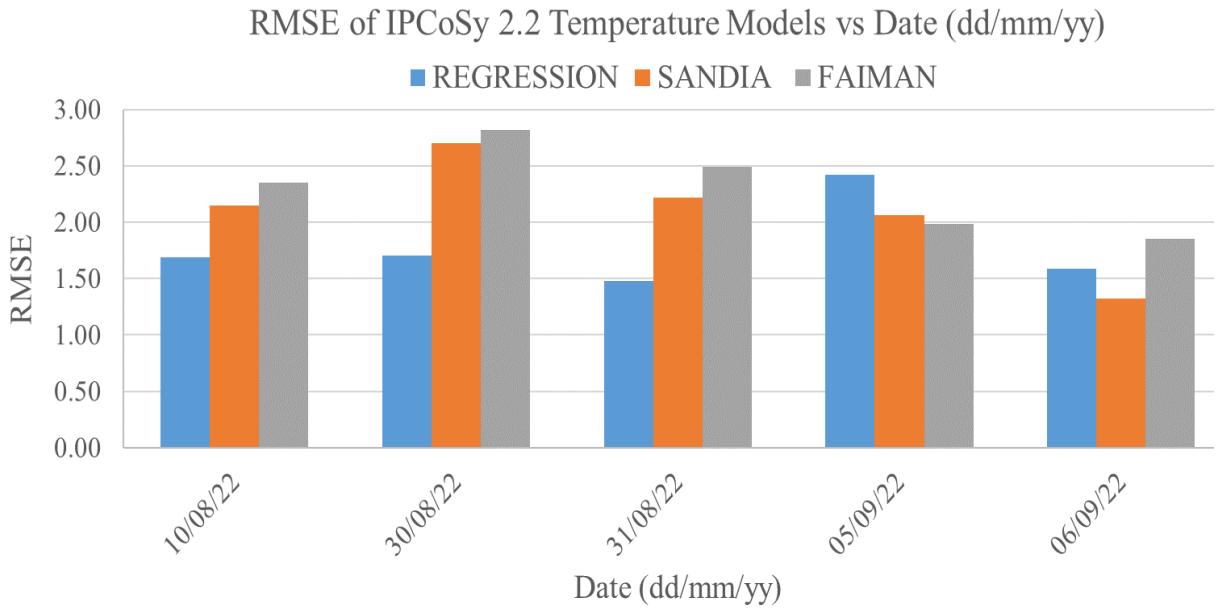

Figure 104: RMSE of IPCoSy 2.2 temperature models.

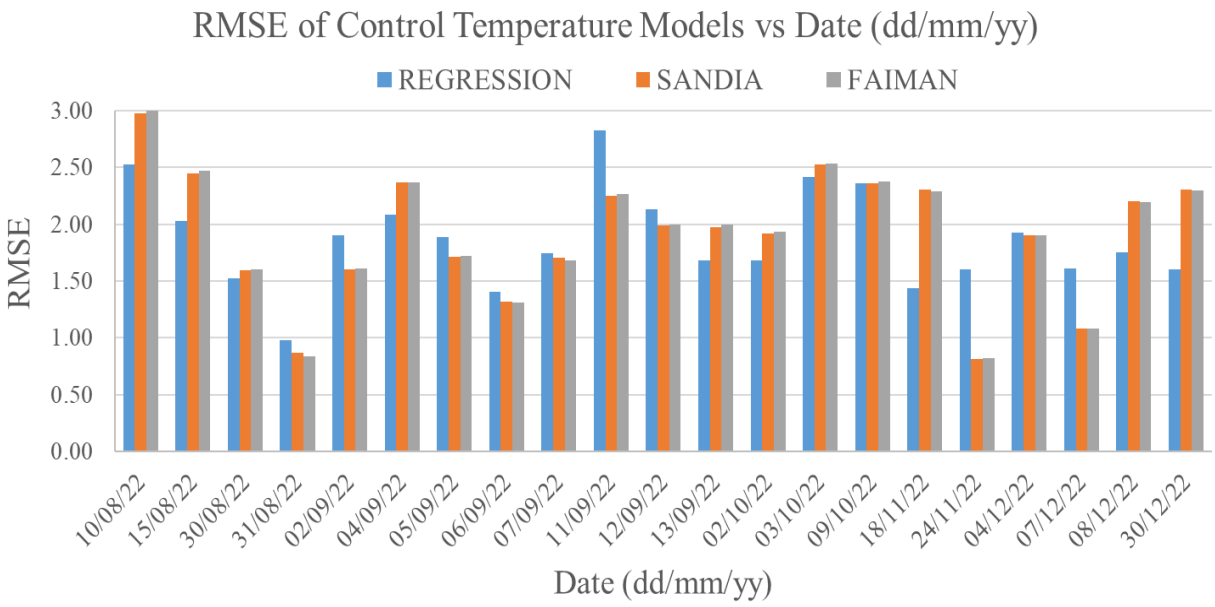

Figure 105:RMSE of Control temperature models.

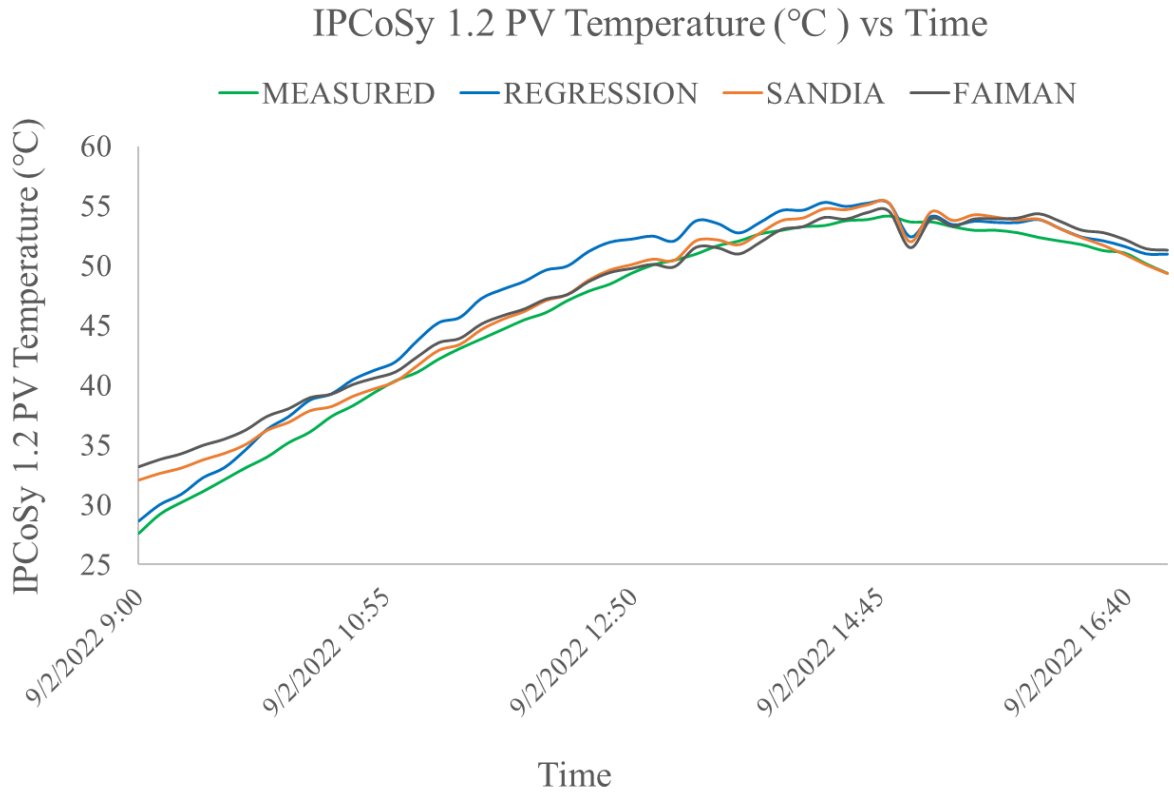

Figure 106: Measured and predicted temperatures for IPCoSy 1.2.

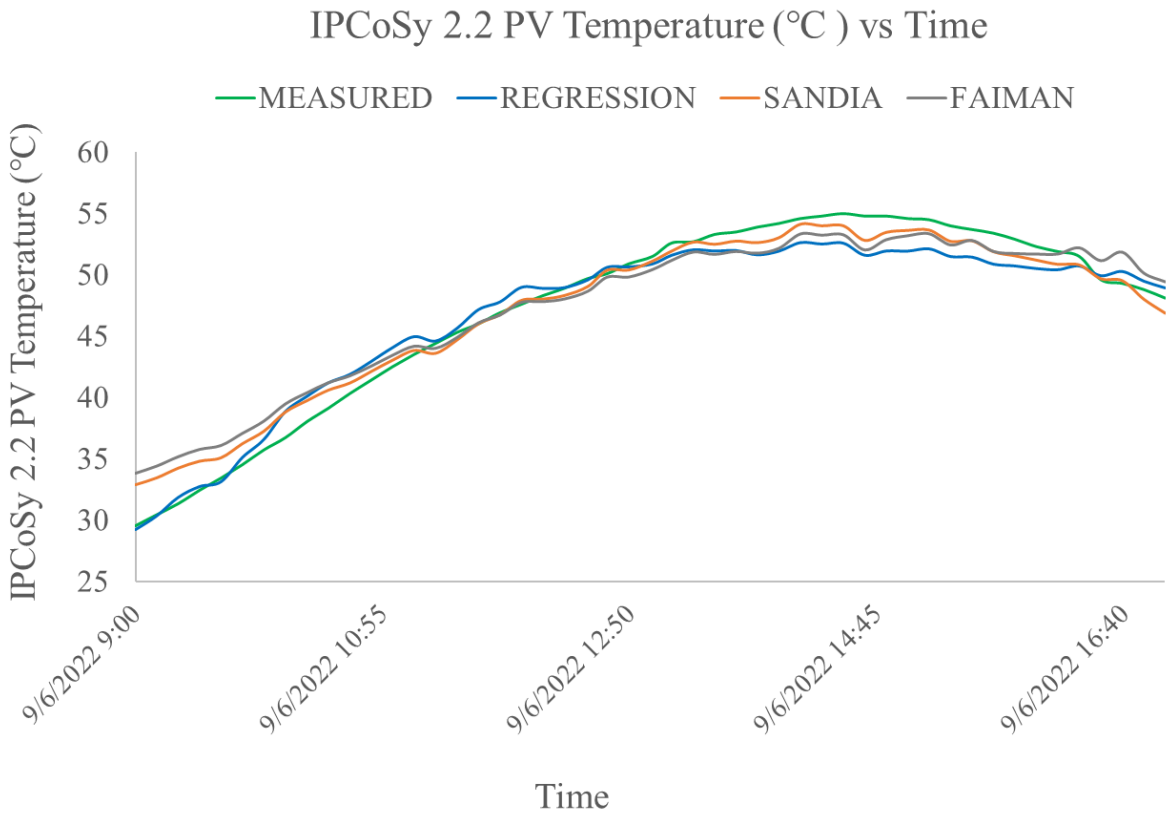

Figure 107: Measured and predicted temperatures for IPCoSy 2.2.

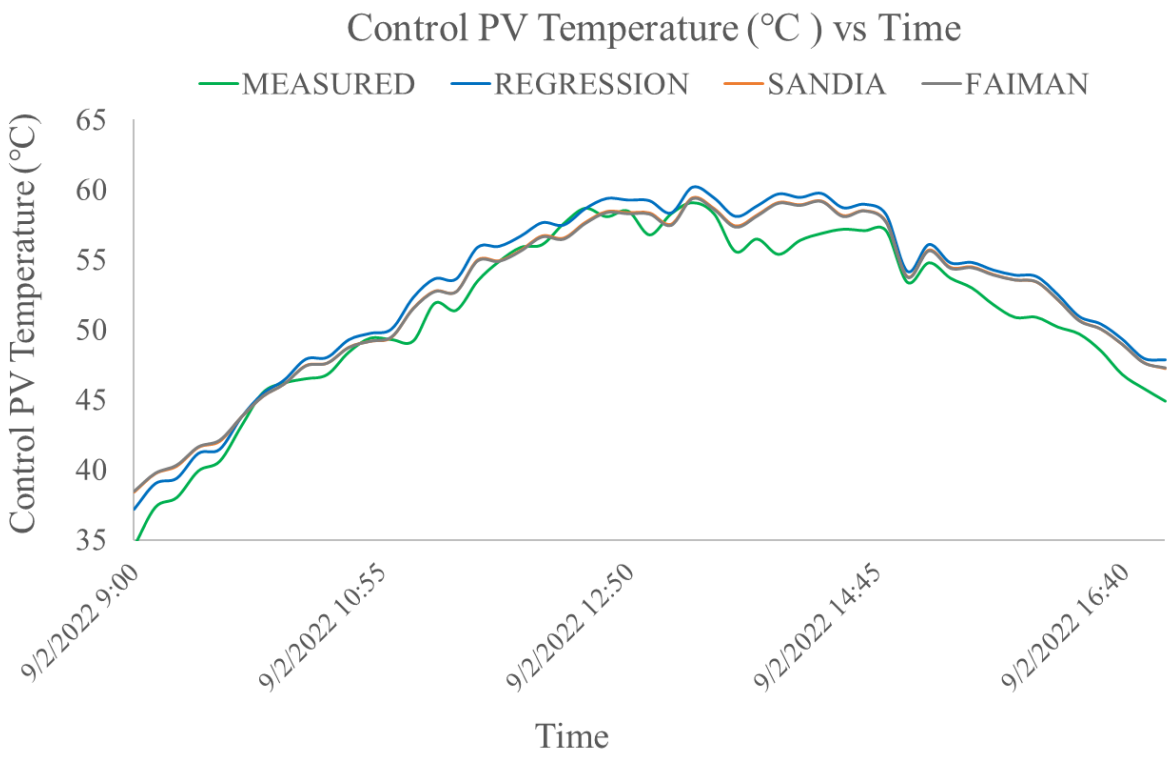

Figure 108: Measured and predicted temperatures for Control PV.

5.5.9.4 Annual simulation

Following the decision to focus on the modified Sandia models, a year of data with a ten-minute interval was gathered from the ISE weather station to apply the derived temperature models and predict the gain in energy generated throughout the year. Figure 109 shows the monthly maximum predicted PV temperatures for the IPCoSy and control PV modules. This figure shows that the control module has the highest maximum temperature throughout the year. Furthermore, the IPCoSy 2.2 module has a higher maximum temperature than the IPCoSy 1.2 module throughout the year. This effect is attributed to the design of the IPCoSy 2.2 cooling tank fitting at the back of a PV module. This results in the cooling tank having double side walls, an extra aluminium sheet on top and a thicker aluminium sheet at the back. These design components make heat transfer to the environment less efficient than the IPCoSy 1.2, and therefore a higher maximum temperature is expected. Figure 110, shows the corresponding monthly percentage gains in energy yield. These values agree with the range of values obtained in the small-scale experiments discussed above and also with similar large-scale experiments, which will be discussed later in this chapter.

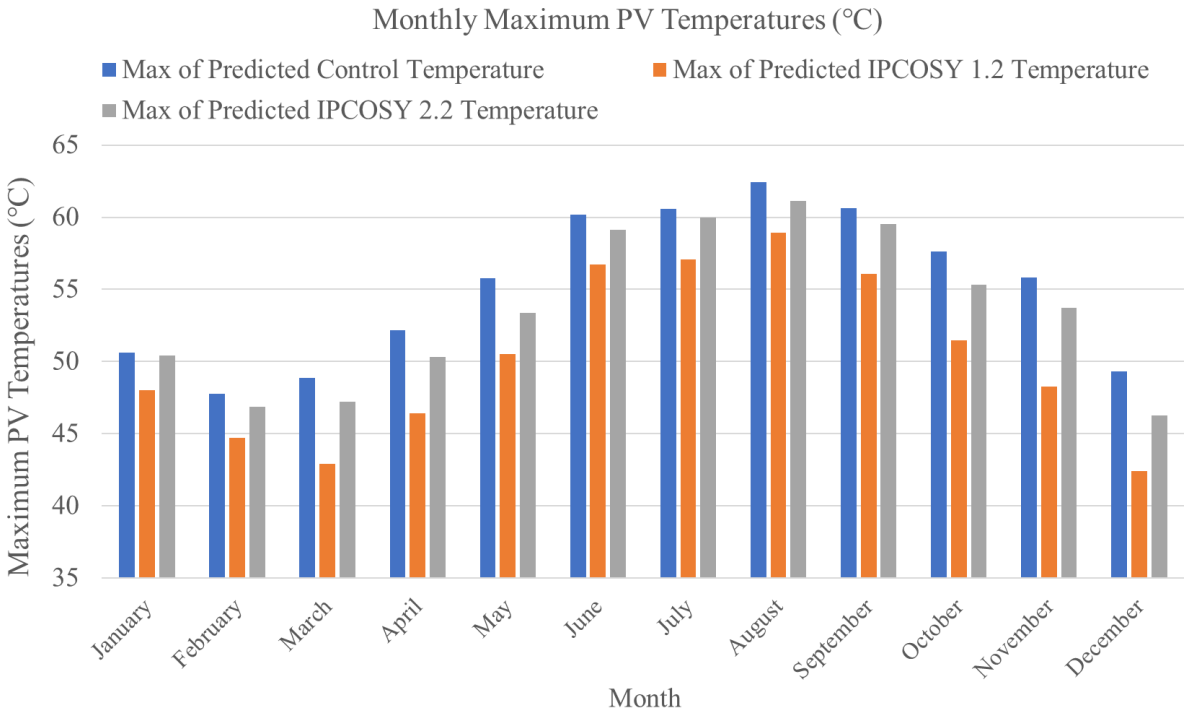

Figure 109: Monthly maximum predicted PV temperatures.

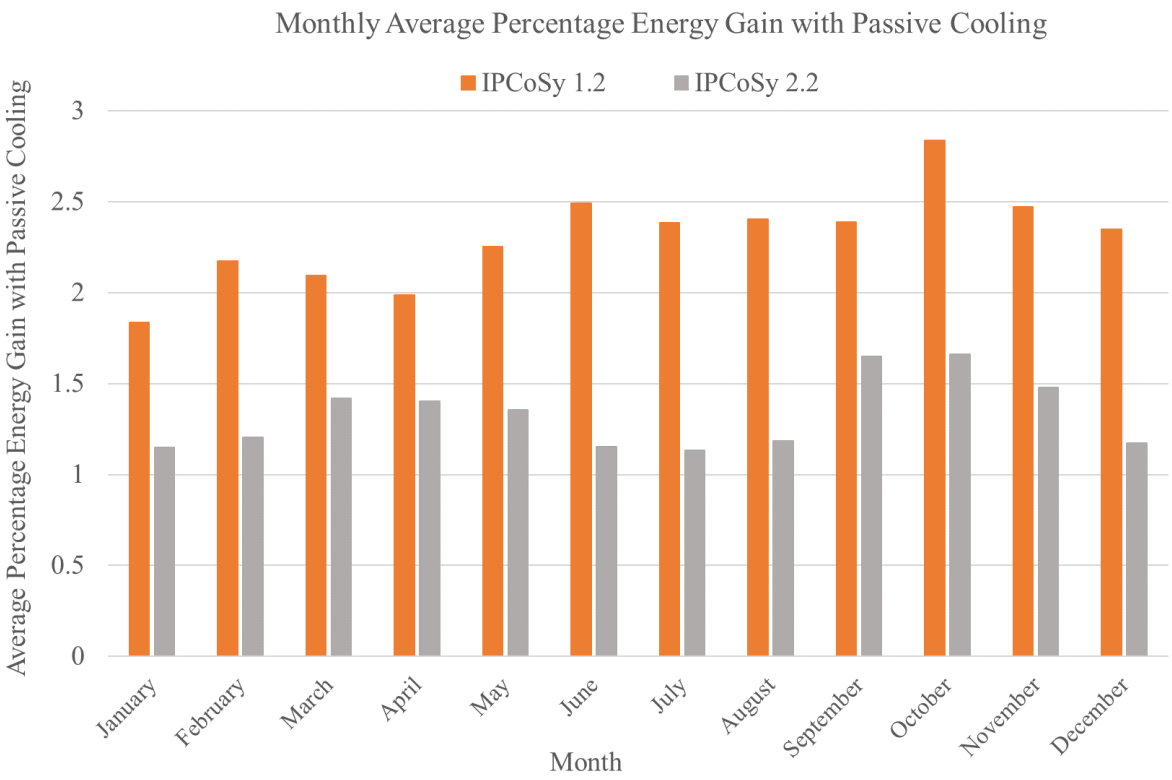

Figure 110: Monthly average percentage energy gain.

5.5.9.5 Experimental results and discussion

Power measurements were also recorded throughout the no-flow experiments described in the above section. Figure 111 and Figure 112 show the percentage gain in daily energy yield for IPCoSy 1.2 with no flow, when compared to a control PV module and a back-side shielded PV module, respectively. Compared to the control PV module, the IPCoSy 1.2 prototype registered gains ranging from 1.15% ±0.40% to 3.29% ±0.41%. In comparison, when compared to a back-side shielded PV module, the IPCoSy 1.2 prototype registered gains ranging from 1.68% ±0.41% to 4% ±0.42%. Moreover, Figure 113 plots the percentage gain in daily energy yield for an IPCoSy 1.2 prototype, against average temperature differences from a standard PV module. The gradient of a linear regression fitted to the data points approximates the power temperature coefficient of the PV module under test. The resulting power temperature coefficient of 0.46 %/°C is close to the 0.4%/°C reported by the PV's manufacturer.

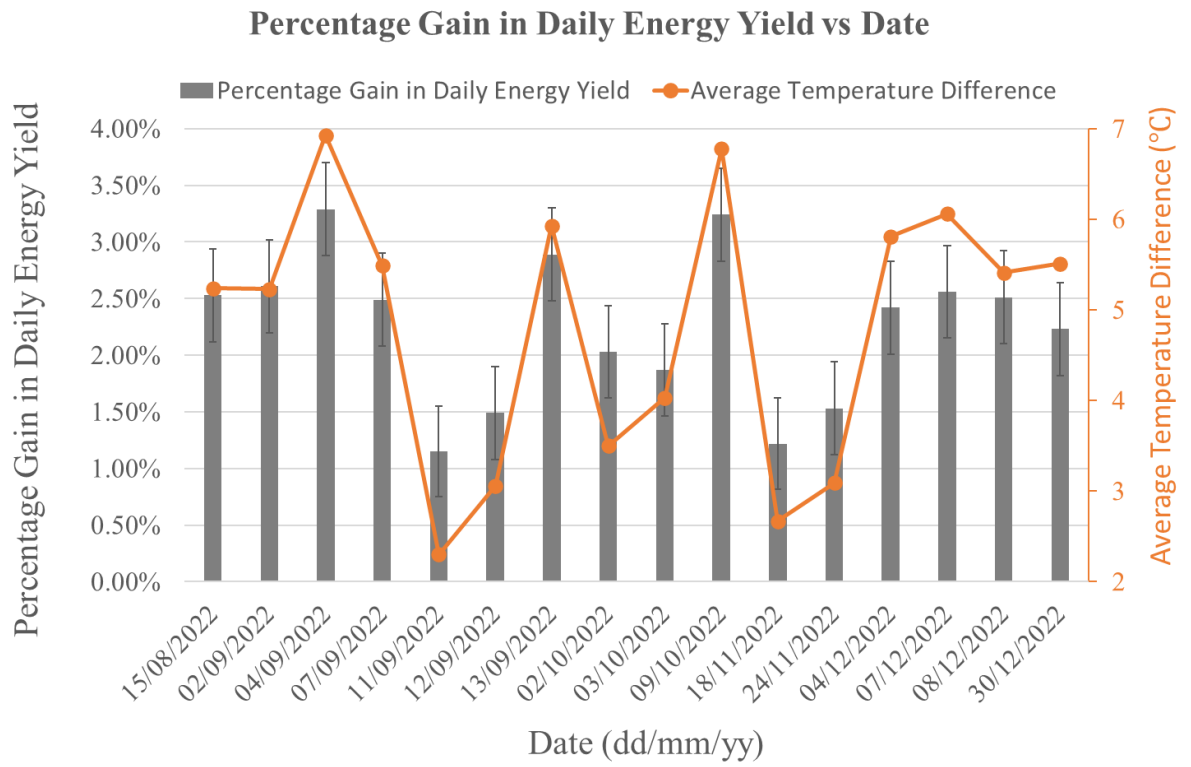

Figure 111: Percentage gain in daily energy yield for IPCoSy 1.2 with no flow when compared to a control PV module.

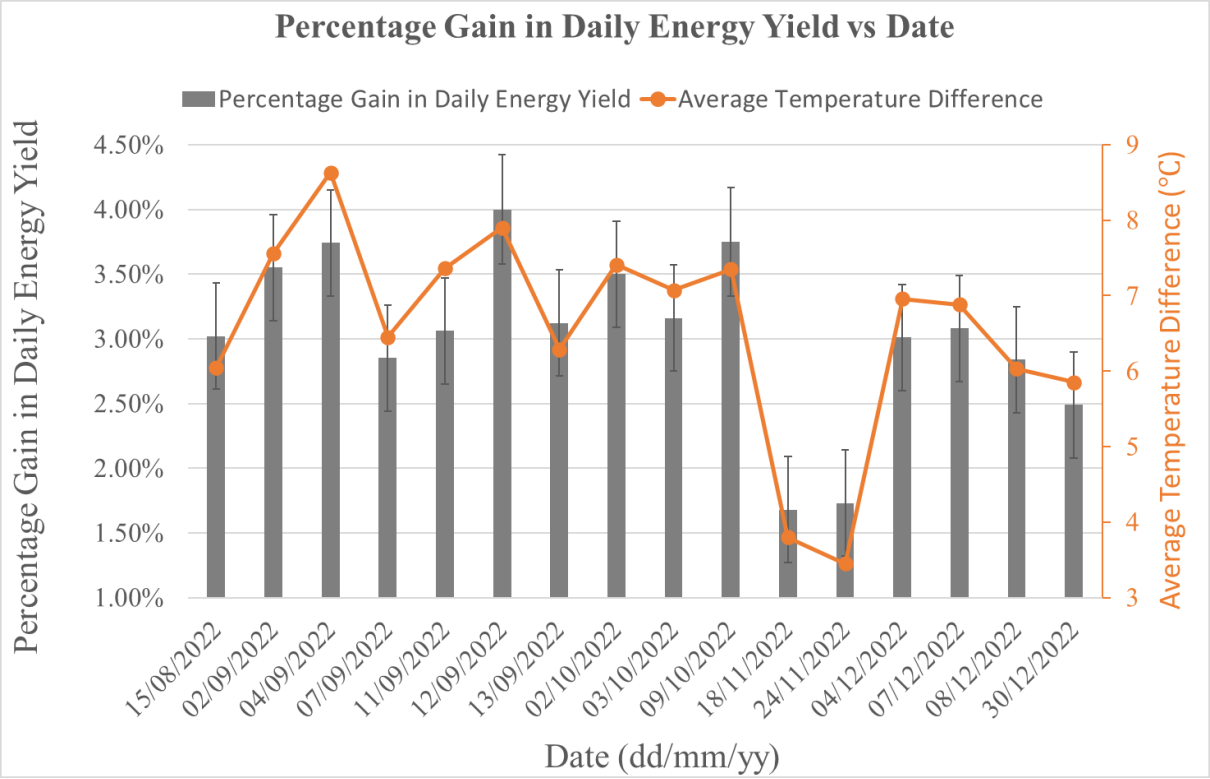

Figure 112: Percentage gain in daily energy yield for IPCoSy 1.2 with no flow when compared to a shielded PV module.

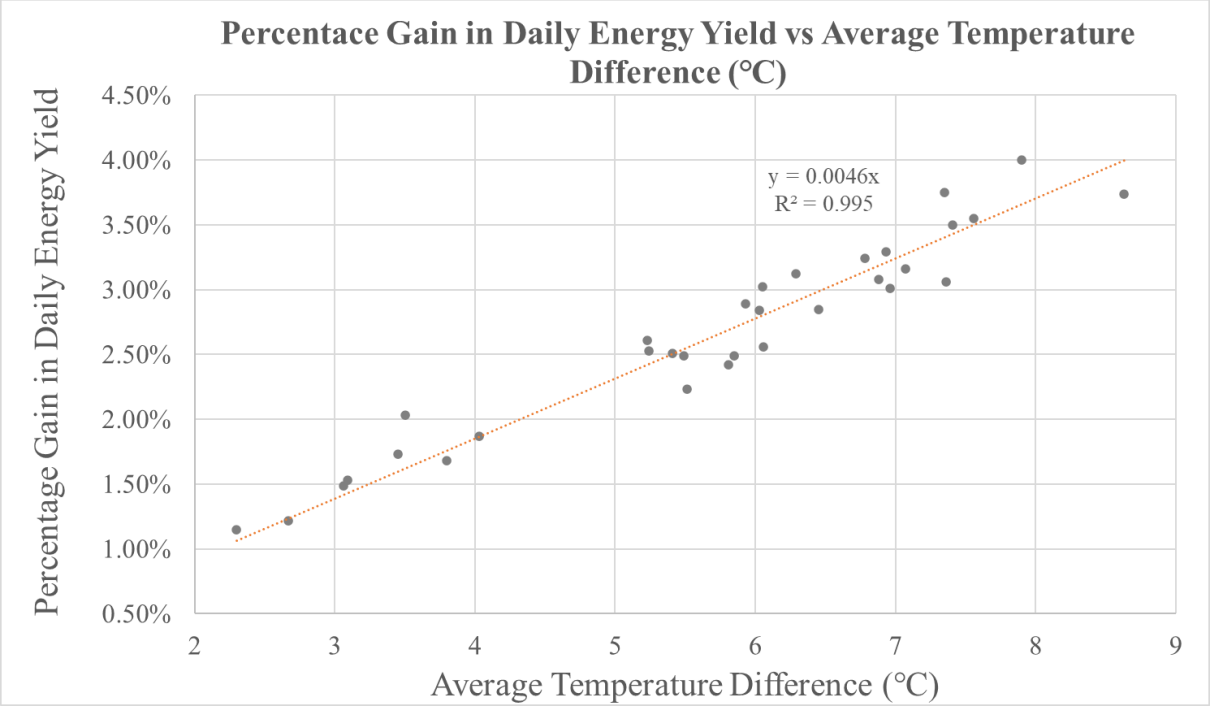

Figure 113: Percentage gain in daily energy yield against average temperature differences from a standard PV module.

Figure 114 and Figure 115 show the percentage gain in daily energy yield for IPCoSy 2.2 with no flow when compared to a control PV module and a back-side shielded PV module respectively. The error bars in these figures represent uncertainty in results due to instrumentation accuracy. Compared to the control PV module, the IPCoSy 2.2 prototype registered gains ranging from 0.60% ±0.43% to 0.96% ±0.43%. In comparison, when compared to a back-side shielded PV module, the IPCoSy 2.2 prototype registered gains ranging from 1.05% ±0.43% to 2.86% ±0.43%. The energy gains are less than the values observed for the IPCoSy 1.2 prototype. This effect could be attributed to a less efficient heat transfer between the solar cells and the cooling water due to the added aluminium sheet in contact with the PV's back sheet. Furthermore, PV modules fitted with IPCoSy 2.2 prototypes have a less efficient heat transfer to the environment since they have a double aluminium wall with an air gap in between and an extra 5mm aluminium sheet in contact with the PV's back sheet. Moreover, since the cooling chamber does not cover the whole PV area due to the space allowed for the PV's junction box, there could be non-uniformities in solar cell temperatures which result in a decreased energy gain.

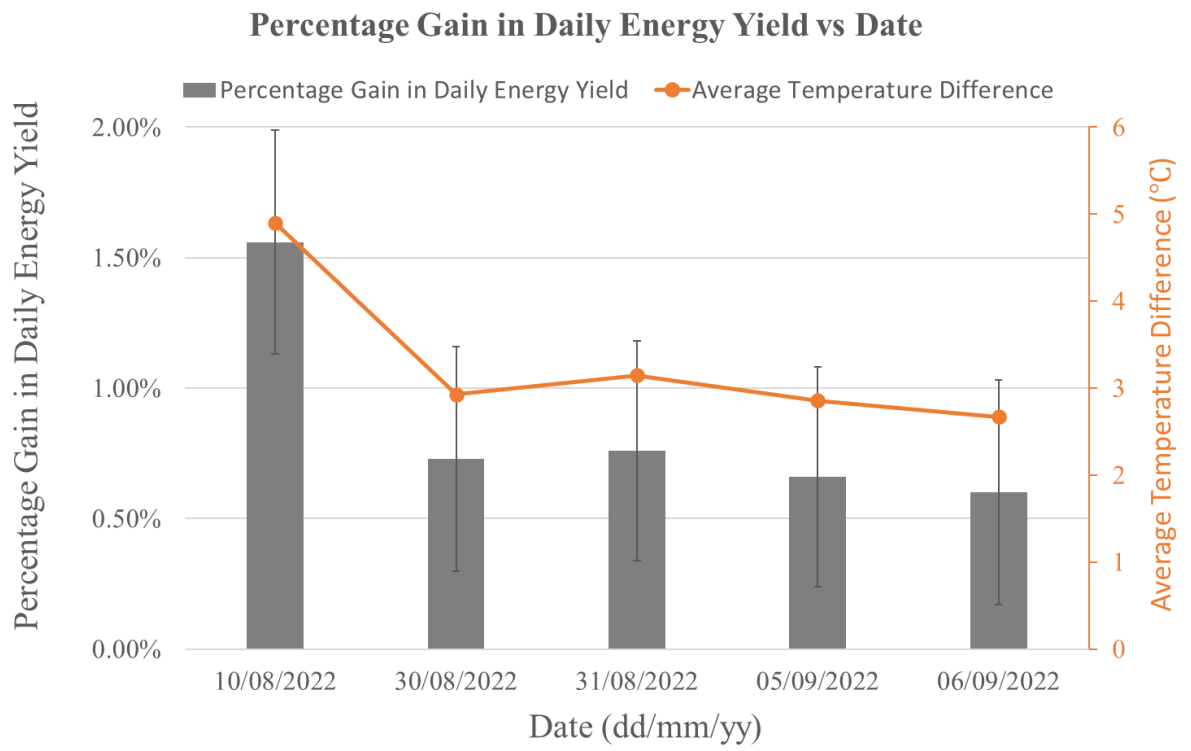

Figure 114: Percentage gain in daily energy yield for IPCoSy 2.2 with no flow when compared to a control PV module.

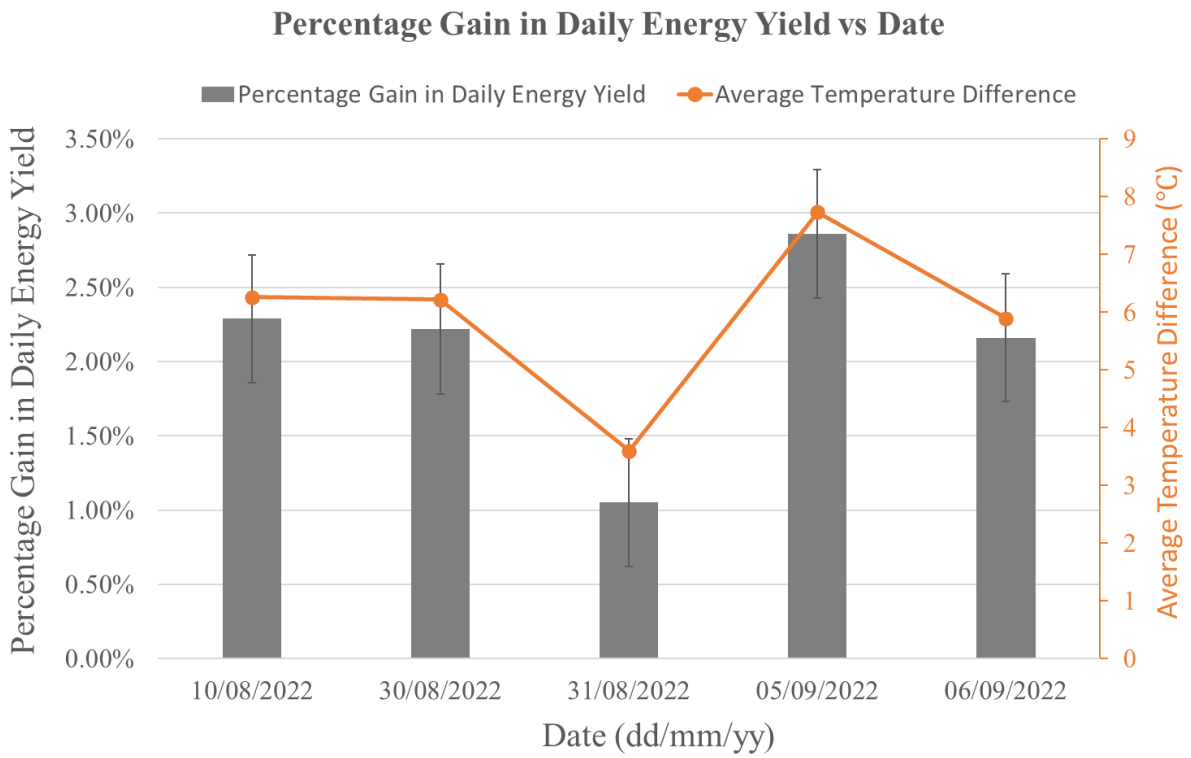

Figure 115: Percentage gain in daily energy yield for IPCoSy 2.2 with no flow when compared to a shielded PV module.

5.5.10 Testing with controlled flow

The results obtained from testing the large-scale prototypes with a controlled active flow are presented in this section. Percentage gross and net energy yield gains were calculated using equations (65) and (66) respectively. Electrical efficiencies of PVs with no controlled flow were calculated using equation (83), while electrical efficiencies of PVs with a controlled flow were calculated using equation (84). In addition, thermal efficiency was calculated using equation (85). Finally, the combined efficiency of the PV module under test was calculated using equation (86).

$$\eta_{\mathrm{E}} = \frac{\text{Electrical Energy Out}}{\text{Energy In}} = \frac{\sum(\mathrm{P_{out}} \times \text{Time})}{\sum(\mathrm{G_{inc}} \times \text{Area} \times \text{Time})} \tag{83}$$

$$\eta_{\mathrm{E}} = \frac{\text{Electrical Energy Out} - \text{Energy consumed by Pump}}{\text{Energy In}} = \frac{\sum(\mathrm{P_{out}} \times \text{Time}) - \sum(\mathrm{P_{pump}} \times \text{Time})}{\sum(\mathrm{G_{inc}} \times \text{Area} \times \text{Time})} \tag{84}$$

$$\eta_{\mathrm{TH}} = \frac{\text{Thermal Energy Out}}{\text{Energy In}} = \frac{\mathrm{Mass_{water}} \times \mathrm{C_{water}} \times (\widehat{\mathrm{T_{out}}} - \widehat{\mathrm{T_{in}}})}{\sum(\mathrm{G_{inc}} \times \text{Area} \times \text{Time})} \tag{85}$$

$$\eta_{\mathrm{Total}} = \eta_{\mathrm{E}} + \eta_{\mathrm{TH}} \tag{86}$$

After some initial testing, it was noted that the chiller was not powerful enough to maintain a constant temperature in the 300L tank when the IPCoSy modules were operated with a controlled flow. This is because the volume of hot water coming out of the IPCoSy modules was increasing the tank temperature quickly, and the chiller could not keep up. Therefore, the output water from the IPCoSy module was discarded for experimentation purposes. The displaced volume in the 300L water tank was manually replaced with cool water from the local water supply.

Throughout most experiments, the control algorithm was not allowed to automatically select temperature thresholds to have a more controlled testing environment. However, Figure 116 shows the automatic control algorithm in operation on the 31st of August, 2022. In this experiment, the hot water coming out of the IPCoSy 1.2 prototype was redirected back into the 300L water tank resulting in an increase in supply water temperature. The control algorithm

was programmed to always allow at least a 10℃ temperature difference between the lower temperature threshold and the temperature of the water supply. Furthermore, the algorithm was programmed to always have a 10℃ difference between the upper and lower temperature thresholds. Moreover, the control system only allowed increments of 5℃ for the lower threshold to allow some hysteresis and not have the pump switching on and off at high frequencies due to continuously changing thresholds in response to changing supply water temperature. Hence, the algorithm started the day with a 30℃ to 40℃ threshold setting. A flowchart of the logic of the automatic threshold cooling control algorithm is shown in Figure 117. Furthermore, the full code is presented in Appendix D – Control algorithms.

As seen in Figure 116, on the second cooling cycle at around 12.30 pm, the algorithm received feedback that the lower temperature threshold was too close to the supply water temperature. This would mean that the pump would keep running and the lower threshold would be difficult to reach. Therefore, the algorithm decided to shift the lower threshold to 35℃ and consequently, the upper threshold became 45℃. Since the water supply temperature never dropped below 20℃, the control algorithm kept the 35-45℃ thresholds for the rest of the day.

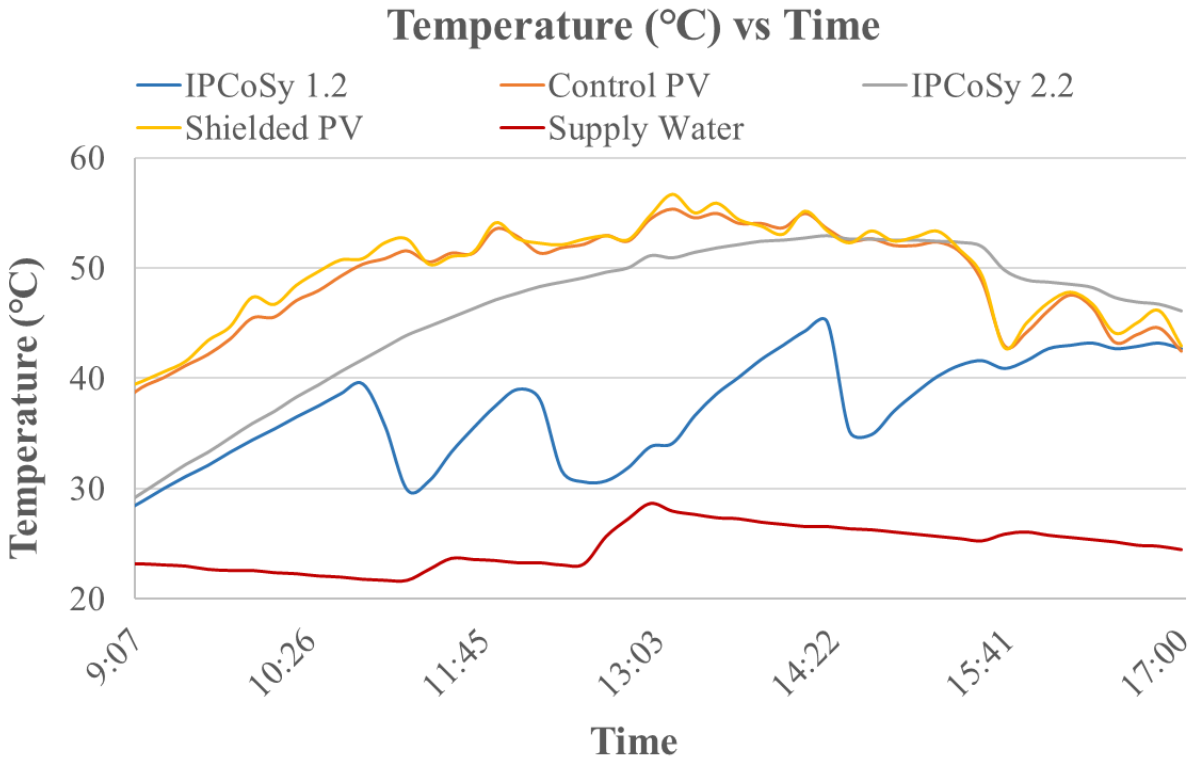

Figure 116: Controlled flow experiment with automatic threshold algorithm activated.

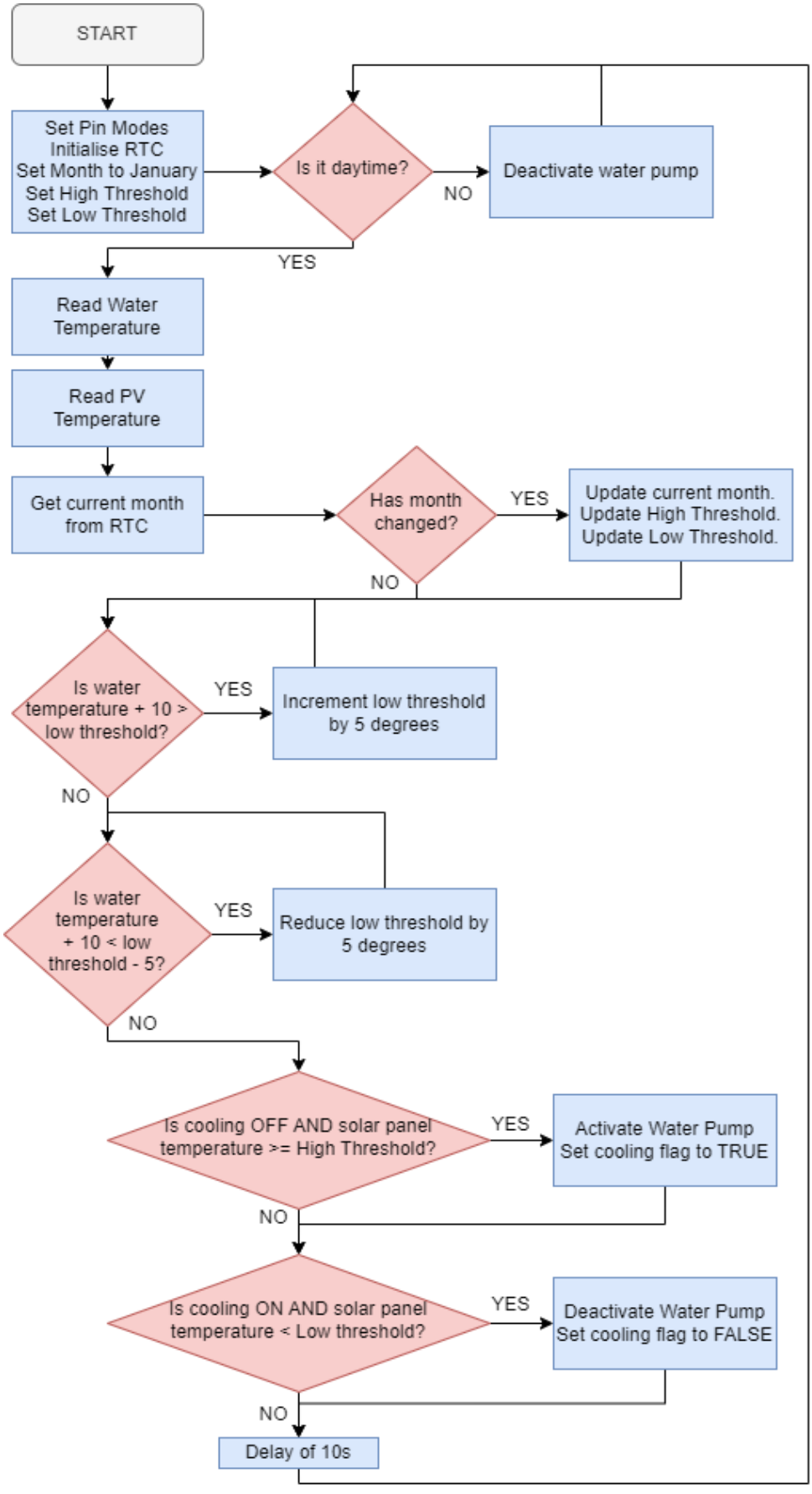

Figure 117: Flowchart of automatic cooling control algorithm.

During this day, the IPCoSy 1.2 prototype yielded 5.96% more gross energy and 4.17% more net energy than the control PV module. Moreover, the IPCoSy 1.2 prototype produced 6.26% more gross energy and 4.46% more net energy than the shielded PV module. In addition, the Control, IPCoSy 1.2, IPCoSy 2.2 and Shielded PVs had overall net electrical efficiencies of 13.84%, 14.42%, 13.95% and 13.80% respectively. Finally, the IPCoSy 1.2 module, with controlled flow using the automatic algorithm, had a thermal efficiency of 35% and a combined module efficiency of 48.7%.

The next set of experiments involved a controlled flow with fixed upper and lower temperature thresholds throughout the day. Only one prototype was tested daily, while the other prototypes were filled with water and left operating with no flow to contribute to the results presented in section 5.5.9 of this chapter. Table 18 shows the results of operating the IPCoSy 1.2 prototype with a controlled flow for nine days. Figure 118 and Figure 119 show the percentage gains in energy yield by the IPCoSy 1.2 prototype compared to the control and shielded PVs respectively. Similar to the results for the small-scale prototypes, it was observed that the difference between the maximum temperature of a standard PV module and the maximum threshold temperature of the cooled PV module directly affects the percentage energy gains. Similarly, the difference between the average temperature of a standard PV module and a cooled PV module directly affects the percentage energy gains. The higher these temperature differences, the more significant the expected energy gains.

Furthermore, these experimentations noted again that the difference between the lower temperature threshold and the average supply water temperature directly impacts the pump power consumption and the resulting net energy gains. The smaller this temperature difference is, the longer it will take for the IPCoSy PV to be cooled to the desired threshold. This causes the pump to work for prolonged periods, thus consuming more energy and consequently decreasing the percentage net energy gains. Another observation was that higher yields were possible when one compares an IPCoSy PV module with a standard PV module installed flat on a roof or a façade, thus blocking wind from reaching the back-side of the PV and eliminating natural and forced heat transfer. This shows that the newly designed modules are ideal for integration in buildings since it is not necessary to allow any space behind the PV modules. The IPCoSy 1.2 prototype resulted in maximum gross and net energy gains of 7.63% and 6.78% respectively, compared to a standard PV module installed in an open rack. Also, maximum gross and net energy gains of 9.02% and 7.64% respectively were recorded

compared to a PV module with a wind-shielded back-side. These results were recorded with an average absolute error of ±0.42%.

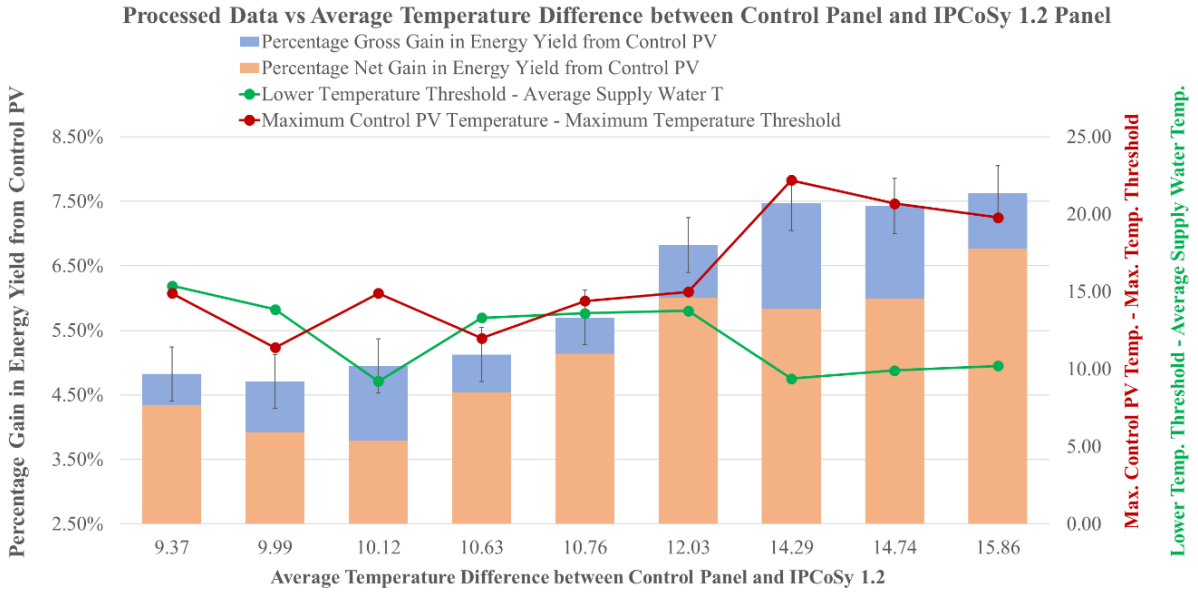

Figure 118: Plot of processed data against average temperature difference between the control PV and the IPCoSy 1.2 prototype.

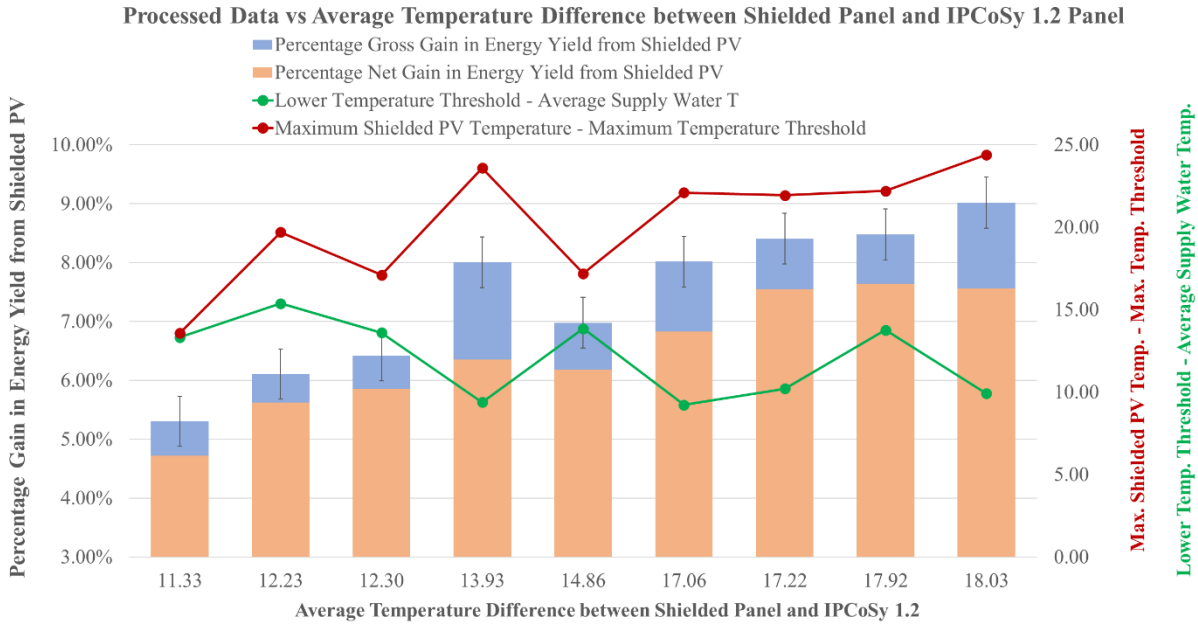

Figure 119: Plot of processed data against average temperature difference between the shielded PV and the IPCoSy 1.2 prototype.

Table 18: Results of controlled flow experiments using IPCoSy 1.2 prototype.

Date	Percentage Gross Gain in Energy Yield from Control PV	Percentage Net Gain in Energy Yield from Control PV	Percentage Gross Gain in Energy Yield from Shielded PV	Percentage Net Gain in Energy Yield from Shielded PV
10/08/2022	7.63%	6.78%	8.41%	7.55%
24/08/2022	4.82%	4.34%	6.11%	5.62%
29/08/2022	7.48%	5.83%	8.01%	6.35%
30/08/2022	7.43%	5.99%	9.02%	7.56%
01/09/2022	5.70%	5.14%	6.42%	5.85%
5/09/2022	4.71%	3.92%	6.98%	6.18%
06/09/2022	6.82%	6.00%	8.48%	7.64%
19/09/2022	5.13%	4.55%	5.31%	4.72%
24/09/2022	4.95%	3.79%	8.02%	6.83%

	Control PV Electrical Efficiency	Shielded PV Electrical Efficiency	IPCoSy 1.2 Electrical Efficiency	IPCoSy 1.2 Thermal Efficiency	IPCoSy 1.2 Combined Efficiency
10/08/2022	13.46%	13.45%	14.58%	25.05%	39.63%
24/08/2022	15.84%	15.66%	16.51%	19.09%	35.60%
29/08/2022	14.60%	14.52%	15.47%	40.75%	56.22%
30/08/2022	14.25%	13.98%	15.03%	36.11%	51.14%
01/09/2022	14.40%	14.30%	15.15%	21.84%	36.99%
5/09/2022	14.15%	13.85%	14.71%	26.16%	40.87%
06/09/2022	14.22%	14.01%	15.07%	27.52%	42.59%
19/09/2022	14.33%	14.30%	14.98%	19.15%	34.13%
24/09/2022	15.13%	14.74%	15.75%	29.40%	45.15%

Buckling of the glass was sometimes noted during control flows on the Type 1.2 prototype. While this did not have any effect in the short testing period, such buckling could result in micro-cracks in the solar cells which in the long term could decrease the efficiency of the PV module and even cause it to fail. Therefore, this design has to be structurally reinforced before exceeding a technology readiness level (TRL) of seven. After the 24th of September, the IPCoSy 1.2 prototype started leaking water due to a manufacturing failure point in the joint

between the PV frame and the aluminium back sheet. Hence, due to limited resources and time and the fact that data had already been recorded, it was decided to focus on the IPCoSy 2.2 prototype for the rest of the experimentation period.

The IPCoSy 2.2 module showed more structural integrity from initial testing, and no buckling was observed during cooling cycles. This robustness was expected since the top and bottom plates were attached to the central aluminium channel supports. Table 19 shows the results of operating the IPCoSy 2.2 prototype with a controlled flow for twenty-seven days. Figure 120 and Figure 121 show the percentage gains in energy yield by the IPCoSy 2.2 prototype compared to the control and shielded PVs respectively. The IPCoSy 2.2 prototype resulted in maximum gross and net energy gains of 6.05% and 4.01% respectively, compared to a standard PV module installed in an open rack. Also, maximum gross and net energy gains of 7.60% and 4.79% respectively were recorded compared to a PV module with a wind-shielded back-side. These results were recorded with an average absolute error of ±0.42%.

Table 19: Results of controlled flow experiments using IPCoSy 2.2 prototype.

Date	Percentage Gross Gain in Energy Yield from Control PV	Percentage Net Gain in Energy Yield from Control PV	Percentage Gross Gain in Energy Yield from Shielded PV	Percentage Net Gain in Energy Yield from Shielded PV
16/08/2022	5.62%	3.79%	5.88%	4.04%
18/08/2022	5.59%	3.75%	6.30%	4.46%
02/09/2022	6.05%	3.47%	7.08%	4.47%
03/09/2022	5.77%	3.60%	5.94%	3.77%
04/09/2022	5.55%	2.96%	6.22%	3.61%
07/09/2022	5.12%	3.34%	5.71%	3.91%
08/09/2022	4.97%	2.76%	5.33%	3.11%
09/09/2022	4.39%	2.47%	4.85%	2.92%
10/09/2022	5.16%	2.81%	5.53%	3.17%
11/09/2022	4.87%	2.34%	7.37%	4.79%
12/09/2022	5.21%	3.01%	7.60%	5.34%
13/09/2022	5.87%	4.01%	6.22%	4.35%
15/09/2022	4.89%	3.24%	5.15%	3.49%
16/09/2022	5.00%	3.05%	5.32%	3.36%
17/09/2022	4.21%	2.45%	4.26%	2.50%
18/09/2022	4.08%	2.33%	6.88%	5.08%
29/09/2022	5.05%	1.51%	5.46%	1.91%
02/10/2022	4.48%	1.87%	6.09%	3.44%

03/10/2022	3.58%	2.10%	5.00%	3.50%
08/10/2022	5.00%	3.67%	5.33%	3.99%
09/10/2022	4.26%	3.11%	4.78%	3.63%
16/11/2022	2.18%	0.72%	2.36%	0.90%
24/11/2022	1.86%	1.32%	2.16%	1.62%
25/11/2022	2.71%	2.19%	4.23%	3.70%
04/12/2022	2.43%	1.95%	3.01%	2.53%
08/12/2022	2.94%	2.42%	3.27%	2.76%
15/12/2022	3.32%	2.76%	3.62%	3.06%

	Control PV Electrical Efficiency	Shielded PV Electrical Efficiency	IPCoSy 2.2 Electrical Efficiency	IPCoSy 2.2 Thermal Efficiency	IPCoSy 2.2 Combined Efficiency
16/08/2022	15.44%	15.42%	16.04%	44.78%	60.82%
18/08/2022	15.45%	15.35%	16.04%	42.54%	58.58%
02/09/2022	14.01%	13.88%	14.50%	58.88%	73.38%
03/09/2022	15.58%	15.56%	16.12%	49.88%	66.00%
04/09/2022	14.56%	14.48%	15.00%	53.78%	68.78%
07/09/2022	14.35%	14.29%	14.81%	43.92%	58.73%
08/09/2022	13.85%	13.77%	14.24%	45.71%	59.95%
09/09/2022	15.92%	15.84%	16.30%	52.34%	68.64%
10/09/2022	15.99%	15.94%	16.44%	56.56%	73.00%
11/09/2022	14.05%	13.72%	14.38%	46.65%	61.03%
12/09/2022	14.79%	14.46%	15.24%	52.92%	68.16%
13/09/2022	14.08%	14.03%	14.64%	43.43%	58.07%
15/09/2022	15.69%	15.61%	16.19%	43.45%	59.64%
16/09/2022	15.14%	15.12%	15.61%	47.73%	63.34%
17/09/2022	16.85%	16.83%	17.23%	48.03%	65.26%
18/09/2022	14.98%	14.59%	15.33%	42.37%	57.70%
29/09/2022	15.47%	15.41%	15.70%	51.57%	67.27%
02/10/2022	14.23%	14.01%	14.48%	40.79%	55.27%
03/10/2022	14.34%	14.14%	14.64%	30.52%	45.16%
08/10/2022	15.11%	15.07%	15.67%	28.32%	43.99%
09/10/2022	14.69%	14.65%	15.20%	26.55%	41.75%
16/11/2022	15.82%	15.81%	15.94%	20.53%	36.47%
24/11/2022	14.63%	14.59%	14.84%	9.86%	24.70%
25/11/2022	16.20%	15.97%	16.55%	12.84%	29.39%
04/12/2022	15.10%	15.01%	15.40%	10.71%	26.11%
08/12/2022	14.72%	14.67%	15.08%	12.22%	27.30%
15/12/2022	16.74%	16.65%	17.13%	11.78%	28.91%

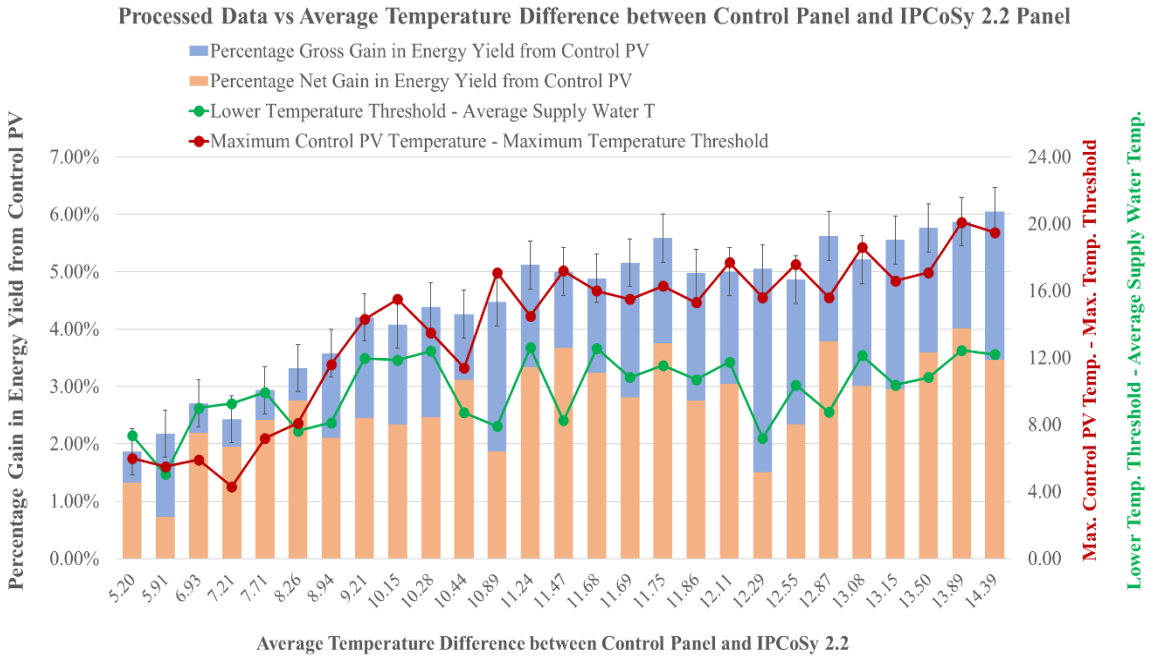

Figure 120: Plot of processed data against the average temperature difference between the control PV and the IPCoSy 2.2 prototype.

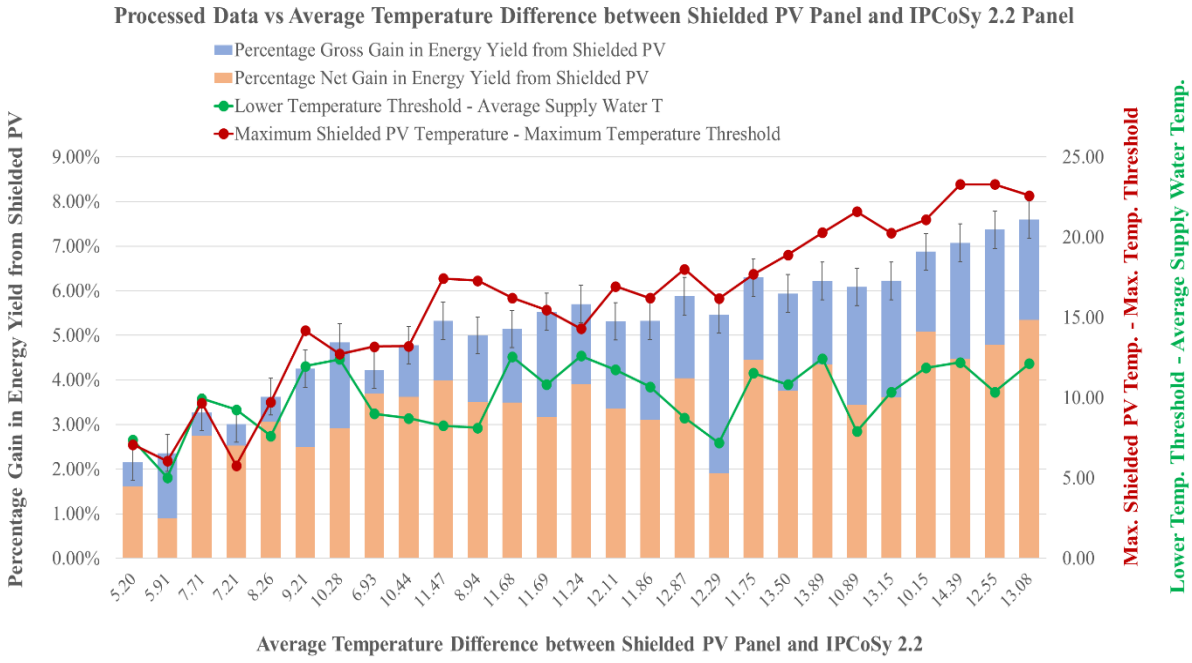

Figure 121: Plot of processed data against the average temperature difference between the shielded PV and the IPCoSy 2.2 prototype.

The results showed that the IPCoSy 2.2 module was performing worse than the IPCoSy 1.2 in terms of percentage gain in energy yield. Therefore, thermal images were captured and analysed to investigate this effect, as shown in Figure 122.

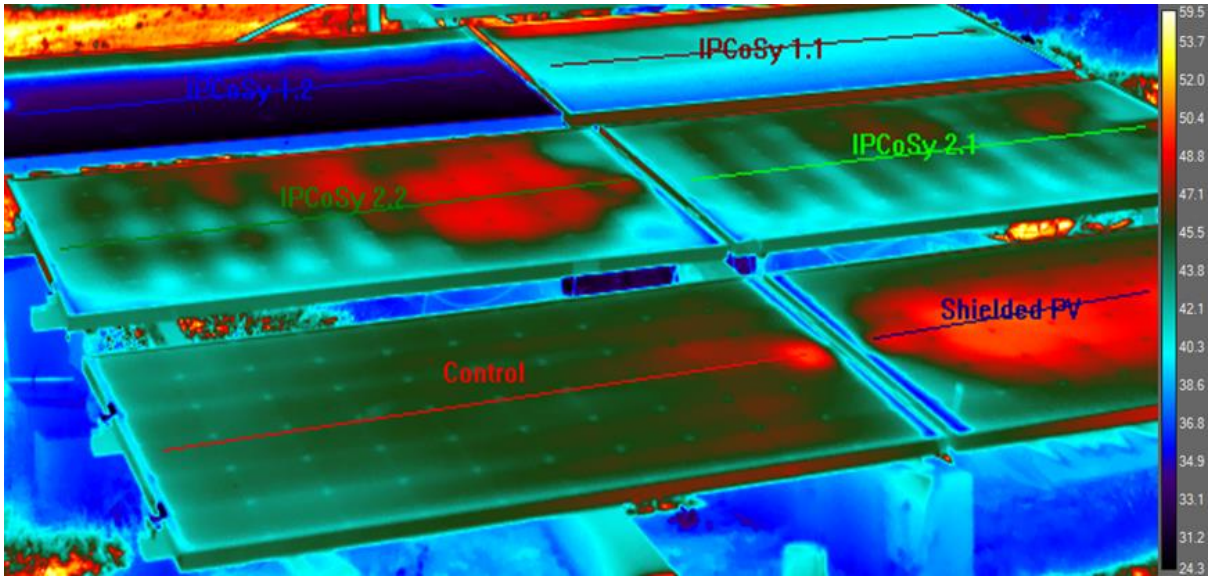

Figure 122: Thermal image analysis of experimental setup.

The thermal image was captured on a day when the controlled flow was applied to the IPCoSy 1.2 prototype while the rest were filled with water and left operating with no flow. Figure 123 shows centrally positioned temperature profiles across the length of the PV modules. All modules showed an increased PV temperature on top of the junction box. This increase in temperature is due to a high power concentration inside the junction box resulting in a high-temperature point. Another observation is that temperature tends to increase towards the central part of the installation compared to the edges. This effect is attributed to the fact that the edges of the installation can cool down by passive or active convection while the central part of the installation is limited by its adjacent PV panel's edges. Therefore, this observation shows that, where possible, PVs should be installed with the junction box situated at the edges of the installation to have the hottest point in the ideal environment for convective cooling.

When comparing the IPCoSy 2.2 and 2.1 prototypes, it is clear that a temperature variation exists between areas with aluminium stiffeners and areas without aluminium stiffeners. This is evident by the eight peaks in temperatures in both profiles, corresponding to the eight aluminium stiffeners in the IPCoSy 2 designs. Furthermore, both prototypes exhibit an increase in temperature in the junction box area because the cooling chamber does not cover this area and, therefore, heat transfer towards the cooling chamber can only occur by conduction. However, it was noted that the IPCoSy 2.2 prototype had higher temperature fluctuations than the 2.1 prototype. This is because the aluminium stiffeners in the 2.1 prototype have holes routed in them, and therefore heat can dissipate efficiently between different areas of the prototype. In contrast, the IPCoSy 2.2 prototype has unmodified aluminium stiffeners and thus,

heat dissipation is much more constrained. This is evidenced by the difference in average temperature levels between the left and right sides of the PV module. Another potential factor affecting the thermal profile across the type 2 prototypes is the presence of air gaps between the top aluminium panel and the back-side of the PV module. This can be improved in future installations by finding a cheap material to act as a filler and thermal interface between the two materials.

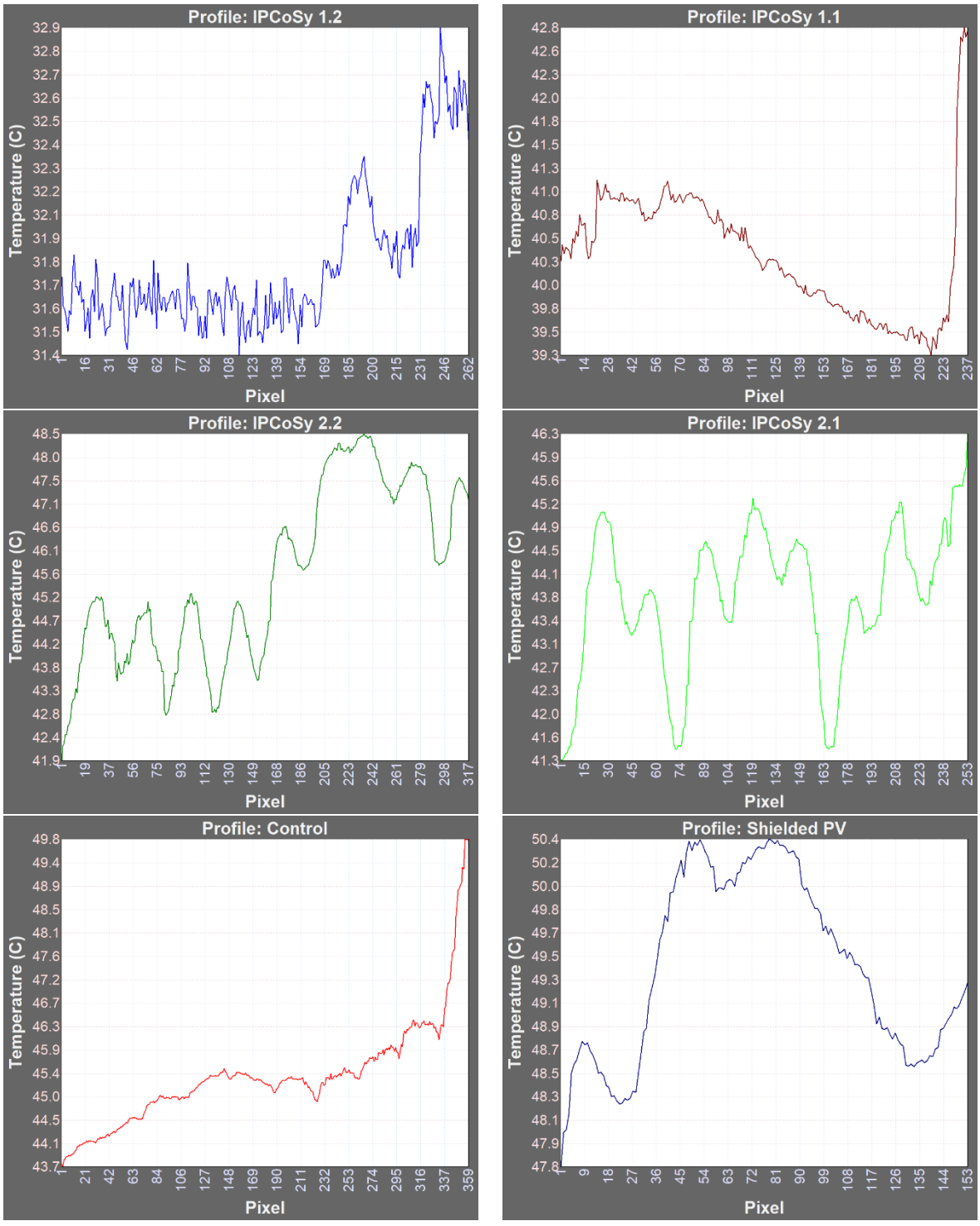

Figure 123: Central temperature profiles across the length of the PV modules.

The IPCoSy Type 1 prototypes show much less fluctuations than the Type 2 prototypes since water is in direct contact with the back-side of the solar cells and no aluminium stiffeners are in contact with the back sheet. A temperature difference of at least 2℃ was also observed across the width of all IPCoSy prototypes. This difference is attributed to the varying density of water as it heats up, resulting in the warmer water rising to the highest area of the prototypes. Therefore, temperature sensors must be positioned on the higher side of the prototypes to ensure that the control algorithm is based on the hottest areas of the PV module. Furthermore, installing IPCoSy in a landscape or a portrait position could potentially have an effect due to the configuration of bypass diodes. However, this hypothesis hasn't been tested in this research. Finally, the temperature profile of the shielded PV shows an increased temperature in the central areas of the PV module since the back-side is covered and therefore, the majority of cooling is only possible through the edges of the PV. The variation of temperature fluctuations between the IPCoSy 1.2 and IPCoSy 2.2 prototypes explains the lower percentage gain in electrical energy yield of the 2.2 prototype.

Besides the benefits of increased energy generation and lower PV maximum temperatures, the IPCoSy modules can be integrated with a water heating system to provide pre-heated water and reduce the energy consumption required. Figure 124 and Figure 125 show a comparison of the electrical, thermal and combined efficiencies of the PV modules under test. The IPCoSy 1.2 prototype exhibited a maximum thermal efficiency of 40.75% and a combined efficiency of 56.22%. In contrast, on the same day, the control PV module produced electrical energy at an average efficiency of 14.60% while the shielded PV performed at an efficiency of 14.52%. In contrast, the IPCoSy 2.2 prototype exhibited a maximum thermal efficiency of 58.88% and a combined efficiency of 73.38%. On the same day, the control PV module produced electrical energy at an average efficiency of 14.01% while the shielded PV performed at an efficiency of 13.88%. This clearly shows that the benefits of IPCoSy can increase in order of magnitude when integrated in buildings or in residential areas as part of the energy production and water heating system. Furthermore, it was noted that on average the IPCoSy 2.2 prototype performed better than the 1.2 prototype in terms of thermal efficiency. This is because:

- IPCoSy 2.2 prototype can dissipate less heat to the environment due to the thicker aluminium sheets and double walls when fitted inside a conventional aluminium PV frame.
- The IPCoSy 1.2 prototype has a certain degree of mixing between the hot and cold water and therefore the desired low threshold temperature is reached faster, resulting in

less hot water output. In contrast, as shown in Figure 87, the IPCoSy 2.2 prototype has little mixing and all the hot water has to be pushed out before the thermocouple, situated at the output of the prototype, detects the lower temperature threshold and signals the control system to stop the cooling flow. While this has a negative effect on the pump energy consumption, it results in a larger volume of water being output at a higher temperature than the input water, resulting in higher thermal efficiencies.

Furthermore, throughout the large-scale experimentation, it was noted that during the summer months, temperature thresholds of 35-40℃ and 35-45℃ result in the highest net percentage gain in electrical energy yields, in agreement with Moharram et al. [74]. In contrast, temperature thresholds of 30-35℃ and 35-40℃ were found to increase the thermal efficiency of the IPCoSy prototype since it strikes a balance between outputting a considerable volume of water and allowing the water time to absorb enough thermal energy. Throughout experimentation, the IPCoSy 1.2 prototype outputted 155.78L of average daily volume of hot water while the IPCoSy 2.2 outputted 260.24L of average daily volume of hot water. The calculations of thermal energy were based on the following assumptions and operating conditions:

- Input water temperatures were controlled by the water chiller and kept at monthly averages shown in Table 20.
- Output water temperatures were taken exactly at the output of the IPCoSy prototypes. Therefore, thermal losses in piping from the prototypes to the storage tank and during prolonged storage were not considered.

Table 20: Average monthly input water temperatures.

Month	Average Input Water Temperature (℃)
August	25.80
September	21.79
October	21.74
November	20.86
December	19.05

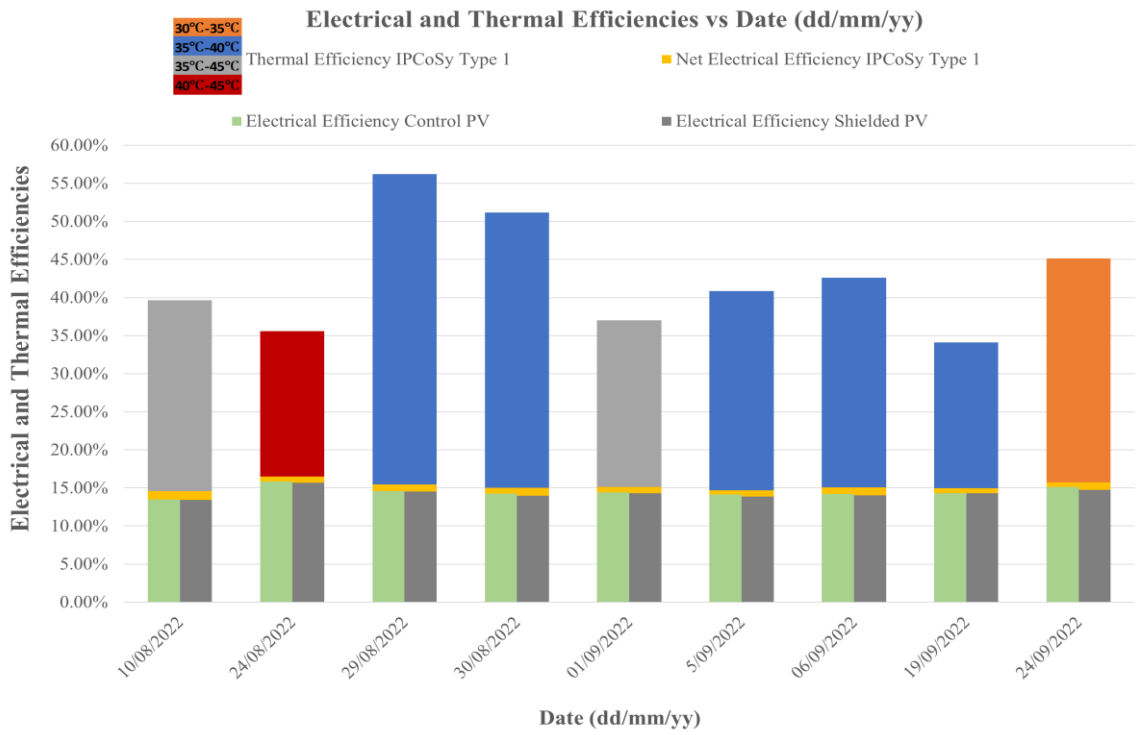

Figure 124: Electrical and thermal efficiencies on different experiment days for IPCoSy 1.2 prototype.

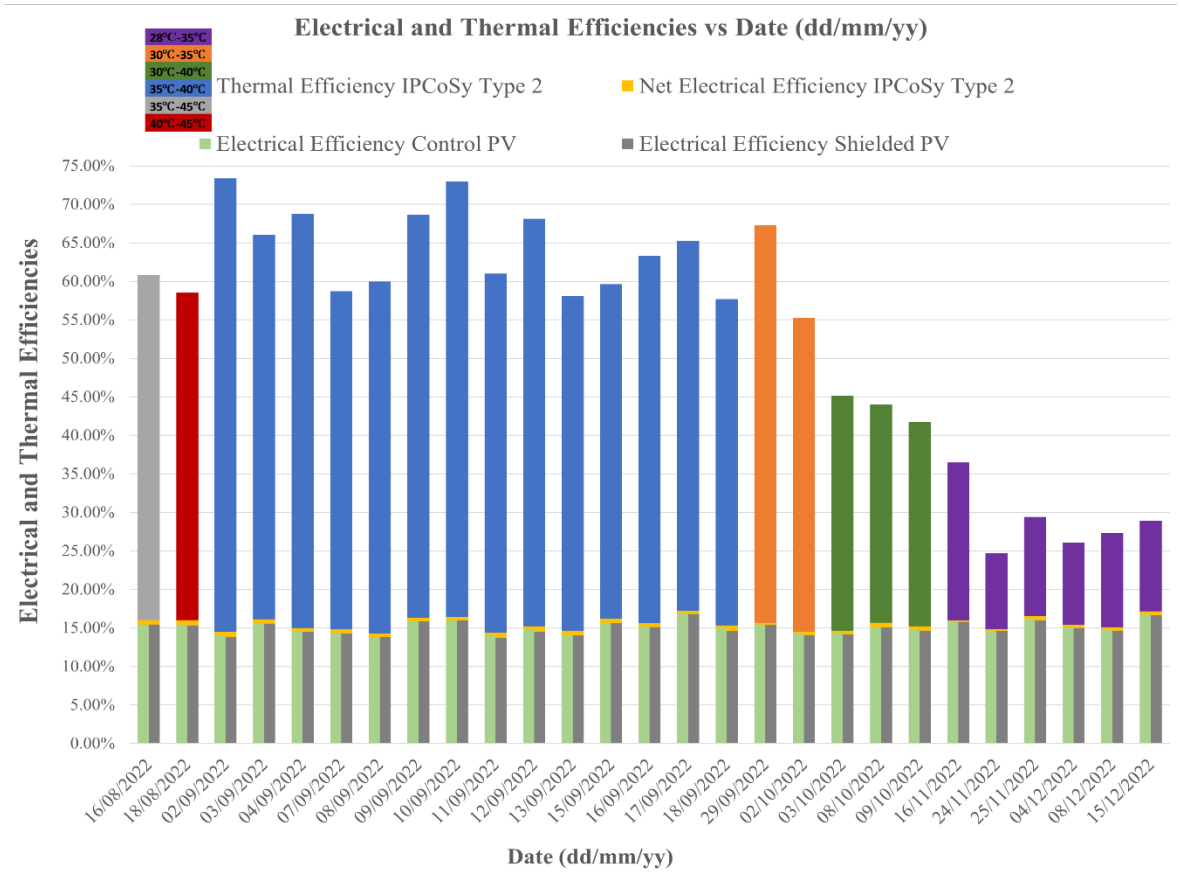

Figure 125: Electrical and thermal efficiencies on different experiment days for IPCoSy 2.2 prototype.

5.5.11 Financial analysis

The IPCoSy concept has been tested throughout this research. It has been proven to provide various benefits, such as an increase in electrical efficiency, lower maximum PV operating temperatures and if integrated with a water heating system, it can act as a water pre-heating stage. However, for this innovation to have practical applications, it has to be developed to a point where it becomes financially viable. This section will analyse the financial viability of the current IPCoSy designs.

Figure 126 from the National Renewable Energy Laboratory (NREL) [132] shows the cost breakdown of all the components and processes involved in assembling 310W, 60 cells PERC modules with dimensions of 1.65x0.992m and an efficiency of 19%. These photovoltaic module parameters are similar to those used for the large-scale IPCoSy experimentation. Table 21 shows the extra material required to produce a Type 1 IPCoSy module: one aluminium sheet, two aluminium angle channels, sealant, and screws or rivets. It was assumed that three times the amount of silicone sealant required for a standard PV module is required for IPCoSy panels. The total added cost to produce an IPCoSy Type 1 panel is €17.54, which equates to €0.059 per Watt. Figure 127 shows a breakdown of a monocrystalline PERC module's total supply-chain costs [132].

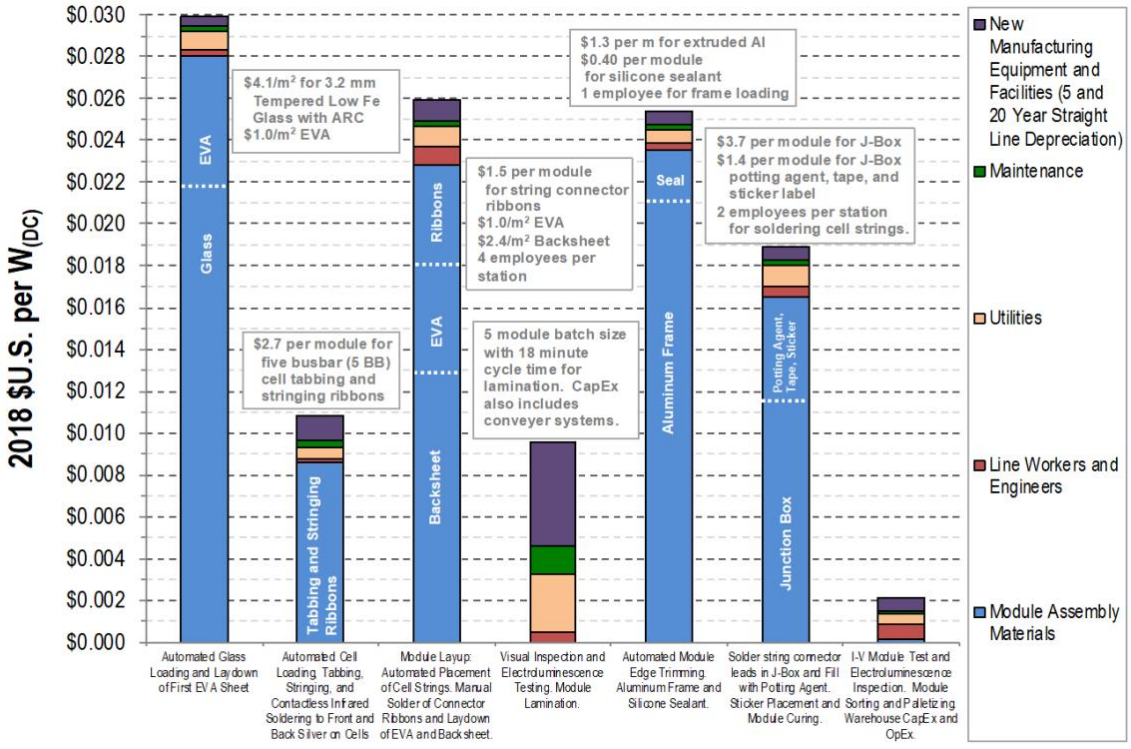

Figure 126: Step-by-step costs for monocrystalline PERC module assembly (module efficiency of 19%, 310 W, 60 cells, 1.650 x 0.992 m^2) [132].

Table 21: Extra material required for IPCoSy type 1 prototype.

IPCoSy 1.2				
Material per PV module	**Information**	**Weight (kg)**	**Price (USD/kg)**	**Total Price (USD)**
2mm Aluminium Sheet	1.65x1	8.94	1.8 [133]	16.10
Aluminium angle channels	2m	0.748	2.3 [134]	1.72
Silicone Sealant	X2	N/A	N/A	0.8
Self-tapping screws	M3	N/A	N/A	0.54
Total added cost per PV module				19.16
IPCoSy 2.2				
2mm Aluminium Sheet	1.65x1	8.94	1.8 [133]	16.10
3mm Aluminium Sheet	1.56x0.91m	11.54	1.8 [133]	20.77
Aluminium U-channels	12.3m	7.80	2.3 [134]	17.94
Silicone Sealant	X2	N/A	N/A	0.8
Self-tapping screws	M3	N/A	N/A	0.54
Total added cost per PV module				56.14

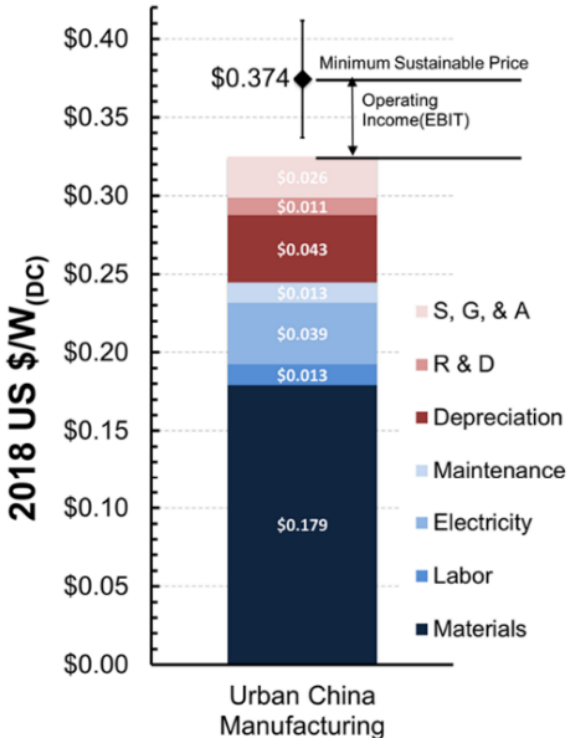

Figure 127: Breakdown of monocrystalline PERC module total supply-chain costs [132].

The added material brings the total material price to produce an IPCoSy Type 1 prototype to a total of 0.243 USD/W_{DC} which brings the Minimum Sustainable Price for a PV module up to €0.401/WDC. This calculation equates to a 17% increase in production costs.

Regarding IPCoSy type 2, one would need to purchase a standard PV module (if not already owned) and also the cooling tank. From Table 21, the material required to construct the IPCoSy 2.2 cooling tank amounts to €51.39. Assuming the exact labour costs incurred during standard solar panel production, outlined in Figure 127 [132], the minimum sustainable price for producing a single IPCoSy 2.2 cooling tank would be €104.94. This calculation equates to a 2.17% increase in production costs when compared to a standard PV module. This value will be used to predict the market price for the IPCoSy 2.2 cooling tank.

Mono facial photovoltaic panels in Malta are sold at an average price of €600/kW_p, and hence, 300W solar panels, similar to those used for this experimentation, cost around €180 each. Therefore, there is an approximate price difference of €77.21 per panel from production to consumer, including shipping and handling costs and profits. Thus, following our previous calculation of a 17% increase in production costs for an IPCoSy module, the new cost of IPCoSy panels would be €197.49 each. Similarly, following the above calculations, the local market price for the IPCoSy 2.2 cooling tank will be assumed to be €182.15. Shipping and handling costs were assumed to remain the same since freight costs using sea transportation are dominated mainly by volume and not by weight. The conversion rate at the time of these calculations was $1 equal to €0.9154.

In the following financial analysis, a residential PV system will be considered, consisting of twelve 300W solar panels connected to a hybrid inverter. A simple payback period will be calculated for standard PV panels, standard PV panels with their back-side shielded from the wind, IPCoSy 1.2 panels and standard PV panels with IPCoSy 2.2 cooling tanks installed at the back. Twelve standard PV panels would cost €2160, IPCoSy 1.2 panels would cost €2369.88 and standard panels with IPCoSy 2.2 installed at the back would cost €4345.8. A Huawei SUN2000-3.68KTL-L1 hybrid inverter is locally sold at €1656. Installation costs for a typical residential photovoltaic system in Malta is around €450/kW_p. If one assumes that the installation labour costs remain the same, one would need to add an extra €15.69 per IPCoSy module to factor in the additional material required for the installation, as outlined in Table *22*. Therefore, the total price for the PV system being considered is €5436 for standard solar panels, €5834.16 for IPCoSy 1.2 panels and €7810.08 for standard solar panels with IPCoSy 2.2

cooling chambers installed at their back-side. In addition, in the following financial analysis, it will be assumed that standard photovoltaic panels have negligible operational and maintenance costs. In contrast, IPCoSy panels will have an annual operating and maintenance cost equal to 0.5% of the initial investment, as per values specified in EN1549-1:2017 for solar collectors. This amounts to €11.85 for the IPCoSy 1.2 panels and €10.93 for the IPCoSy 2.2 cooling chamber.

Table 22: Extra material required for a PV installation using IPCoSy modules.

Fitting	Quantity	Price per item	Total
T-fitting	12	3	36
Plastic Pipe Adaptor	24	1	24
Plastic Elbows	24	1.32	31.68
Water Pipe	50	1.26	63
Pipe Clips	84	0.4	33.6
Total Price			€188.28
Total Price per PV module			€15.69

In Malta, residential PV installations can currently benefit from three government schemes. The first option involves installing a standard PV inverter and benefitting from a grant on the initial investment of up to €2500 and €625/kW_p and hence, benefitting from a feed-in tariff (FIT) of €0.105 for 20 years. The second option involves installing a hybrid PV inverter and benefitting from a grant on the initial investment of up to €3000 and €750/kW_p and hence, benefitting from a feed-in tariff (FIT) of €0.105 for 20 years. The third option involves benefitting from a FIT of €0.15 for 20 years, however, no grant will be conceded on the initial investment [135].

From the PVSYST software weather database, the yearly global incident solar radiation on a photovoltaic system installed in Malta with the same parameters as the IPCoSy experimental setup is 2039.6 kWh/m^2. The average efficiencies of the control PV and the shielded PV were 14.95% and 14.82% respectively. The IPCoSy 1.2 prototype resulted in an average gross increase in electrical efficiency of 6.23% from the control PV modules. In contrast, the IPCoSy 2.2 prototype resulted in an average gross increase in electrical efficiency of 4.45% from the control PV module. Table 23 shows a simple payback period calculation for the standard PV, shielded PV, IPCoSy 1.2 and IPCoSy 2.2 panels. This analysis only considers gross efficiencies since it is assumed that the PV system will be integrated with the building, utilising an existing

water flow. Therefore, no capital and O&M costs are being considered for the water pump. When benefitting from the current government grant, the PV system with standard PVs has a simple payback period of 5.05 years when installed on an open rack and 5.09 years when ventilation is limited at the back-side of the modules. In addition, when IPCoSy 1.2 prototypes are used, a simple payback period of 5.44 years is achieved in contrast with 8.57 years when using standard solar panels with IPCoSy 2.2 cooling chambers installed at the back. When plotting the graphs in Figure 128 to Figure 133, a yearly degradation rate of 0.5% was considered for all PV modules. Figure 128 shows a plot of simple payback on a 20-year time span when benefitting from government grants based only on electrical energy production. This graph shows that the IPCoSy 1.2 system results in a minimal profit increase of €111.62 over twenty years. Furthermore, the IPCoSy 2.2 system results in €2059.38 less profit over a period of twenty years when compared to a similar installation using standard panels with no cooling. This decrease in profit is mainly attributed to the high capital cost of buying both standard solar panels and IPCoSy cooling chambers.

Table 23: Financial analysis of PV system.

	Standard PV	**Shielded PV**	**IPCoSy 1.2**	**IPCoSy 2.2**
Yearly Energy production (kWh)	6012.71	5962.94	6387.30	6280.27
Yearly Income (€) (FIT €0.105)	631.33	626.11	670.67	659.43
Yearly Income (€) (FIT €0.15)	901.90	894.44	958.09	942.04
Initial Investment without grant	5436	5436	5834	7810.08
Initial Investment with grant	2736	2736	3134	5110.08
Yearly O&M cost	0	0	11.85	10.93
Simple payback period (years) (FIT €0.105)	5.05	5.09	5.44	8.57
Simple payback period (years) (FIT €0.15)	6.06	6.11	6.17	8.37
20 year income (FIT €0.105)	9890.69	9786.16	10042.33	7859.89
20 year income (FIT €0.15)	12602.12	12452.81	13090.90	10812.14

Therefore, this shows that the IPCoSy Type 1 concept can be financially viable, especially if installed in an environment having an existing water flow and therefore not requiring extra energy consumption for cooling. In contrast this analysis showed that the IPCoSy Type 2 concept is not financially viable in its current state, and if the only benefit is the increased energy output due to cooling. To make such a system more financially viable, one needs to employ an optimised control algorithm to increase the gains due to cooling and use the hot water produced as a pre-heater to a water heating system.

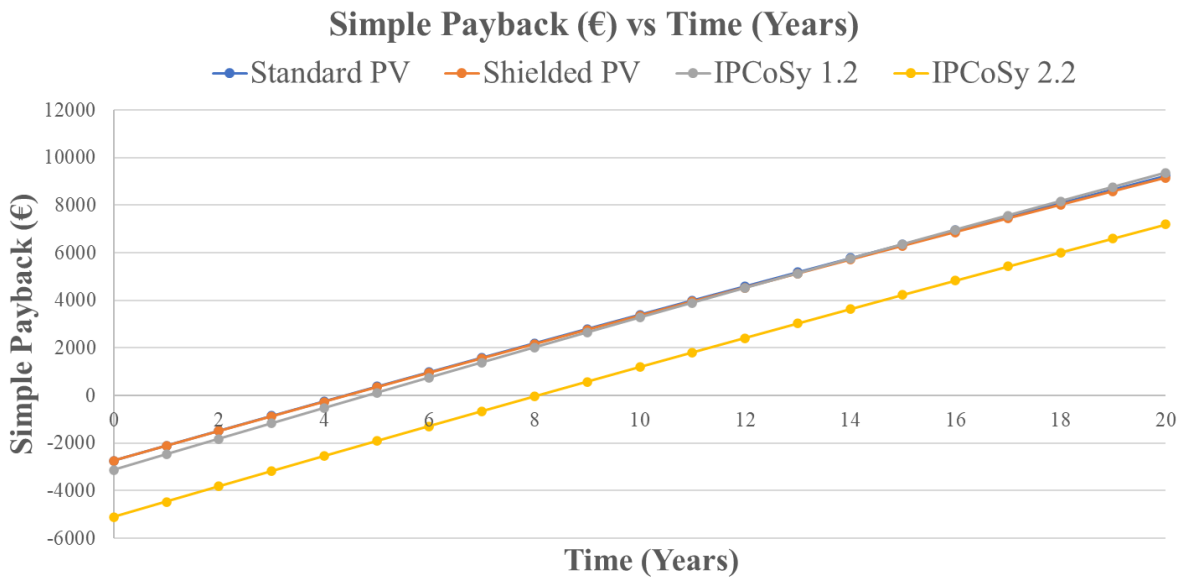

Figure 128: Simple payback on a 20 year time span when benefitting from government grant and neglecting thermal efficiencies.

Figure 129 and Figure 130 shows plots of simple payback on a 20-year time span when benefitting from government grants and utilising the hot water generated as a pre-heater to a water heating system. This analysis is assuming that all the hot water generated by IPCoSy will be used. Furthermore, it is not considering transmission and storage losses of the hot water. To decrease the effect of these assumptions and provide a broad representation, three thermal efficiencies of IPCoSy were chosen. The chosen efficiencies were the minimum, average and maximum thermal efficiencies recorded during experimentation, that is, 19.09%, 27.23% and 40.75% for IPCoSy 1.2 and 9.86%, 38.10% and 58.88% for IPCoSy 2.2. The revenue from the energy saved in water heating was calculated based on a local consumption tariff of €0.1298 [136]. When thermal efficiency is considered, the 20-year profit of the PV system increases from €9248.31 for standard PVs to a range of €29,293.28 to €51,910.16 for IPCoSy 1.2 and €17,484.52 to €68670.09 for IPCoSy 2.2.

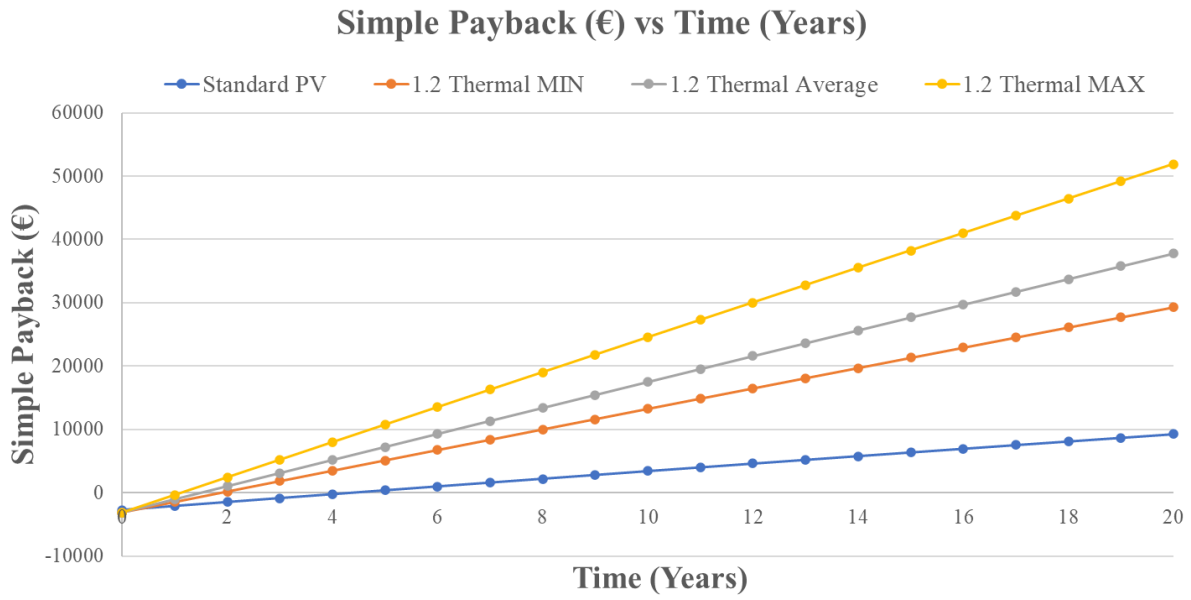

Figure 129: Simple payback on a 20 year time span when benefitting from government grant and considering three thermal efficiencies of IPCoSy 1.2.

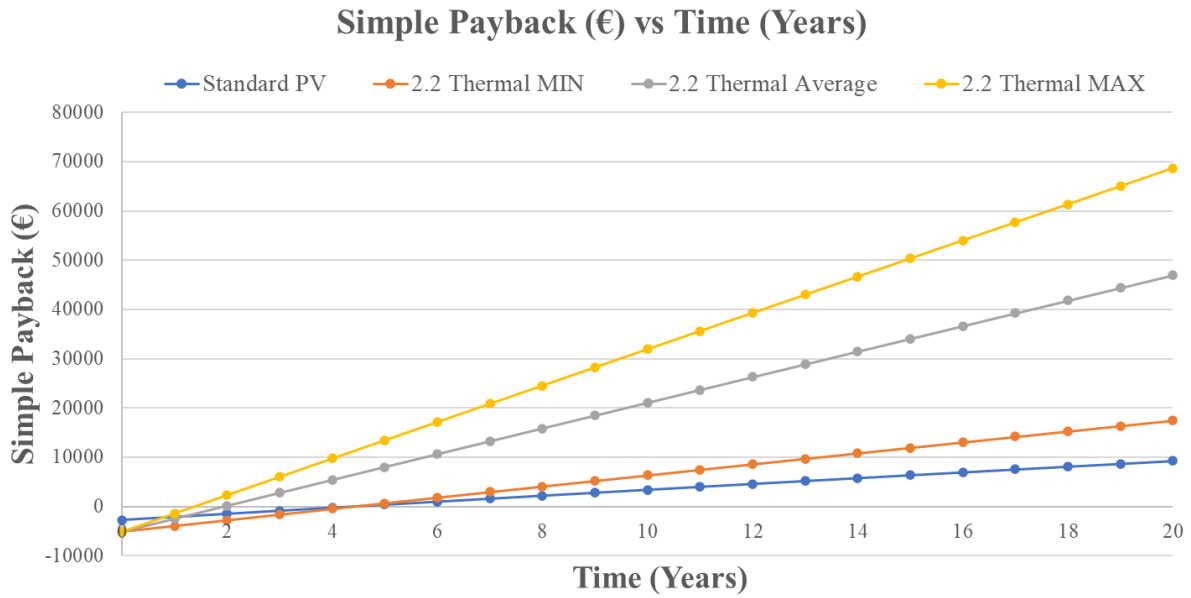

Figure 130: Simple payback on a 20 year time span when benefitting from government grant and considering three thermal efficiencies of IPCoSy 2.2.

Figure 131 shows a plot of simple payback on a 20-year time span without benefitting from any government grant, based only on electrical energy production with a FIT of €0.15. This graph shows that the IPCoSy 1.2 system results in a minimal profit increase of €431.60 over twenty years. Furthermore, the IPCoSy 2.2 system results in €1689.1 less profit over a period of twenty years when compared to a similar installation using standard panels with no cooling.

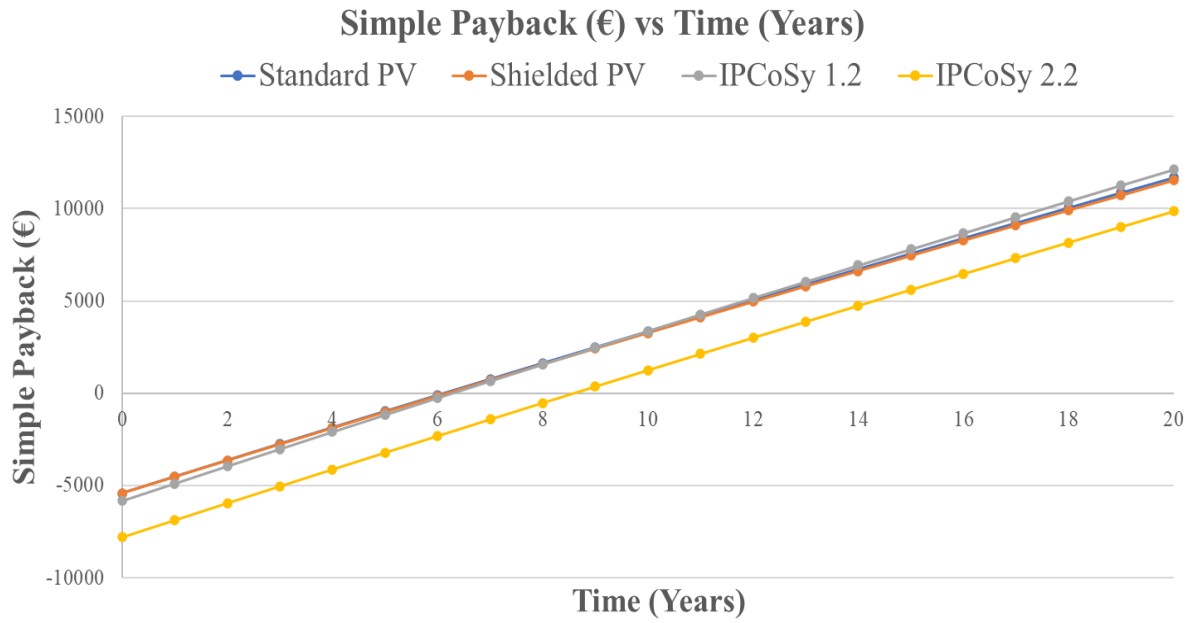

Figure 131: Simple payback on a 20 year time span without benefitting from government grant and neglecting thermal efficiencies.

Figure 132 and Figure 133 shows plots of simple payback on a 20-year time span without benefitting from government grants and utilising the hot water generated as a pre-heater to a water heating system. Similar to the above analysis, the recorded minimum, average, and maximum efficiencies of IPCoSy were chosen. The revenue from the energy saved in water heating was calculated based on a local consumption tariff of €0.1298 [136]. When thermal efficiency is considered, the 20-year profit of the PV system increases from €11,684 for standard PVs to a range of €32,049.39 to €54,666.27 for IPCoSy 1.2 and €20,149.21 to €71,334.78 for IPCoSy 2.2. This analysis shows that considerable profits can be achieved even with the system working at the lowest recorded thermal efficiencies. Therefore, with further research, the IPCoSy concept can reach a technology readiness level where it can be commercialised.

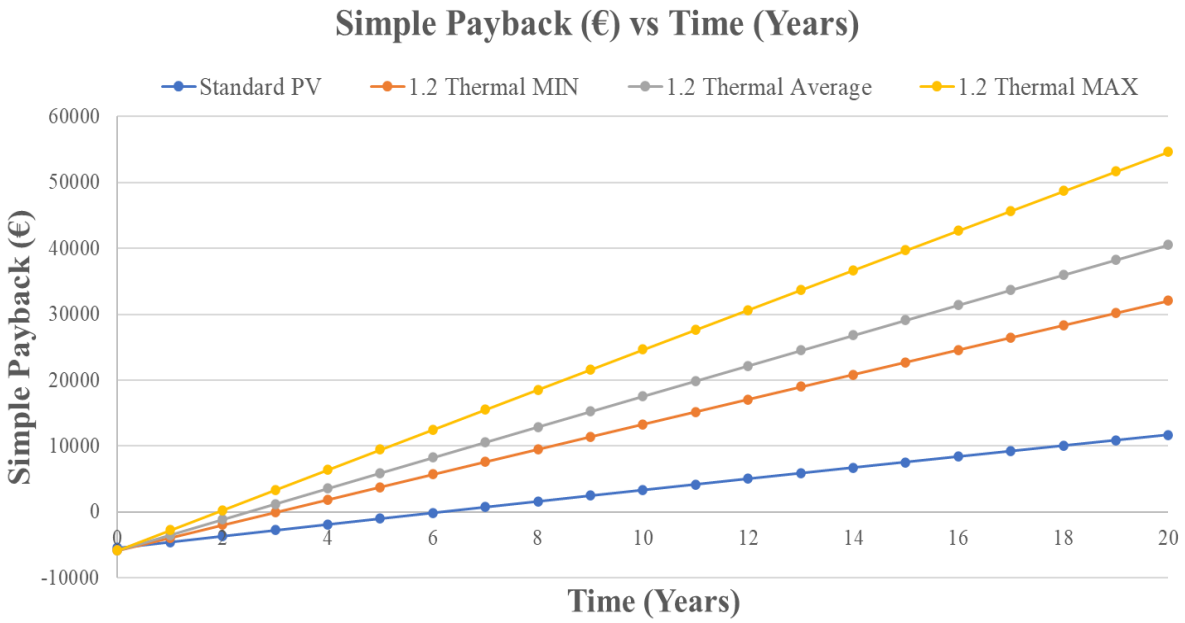

Figure 132: Simple payback on a 20 year time span without benefitting from government grant and considering three thermal efficiencies of IPCoSy 1.2.

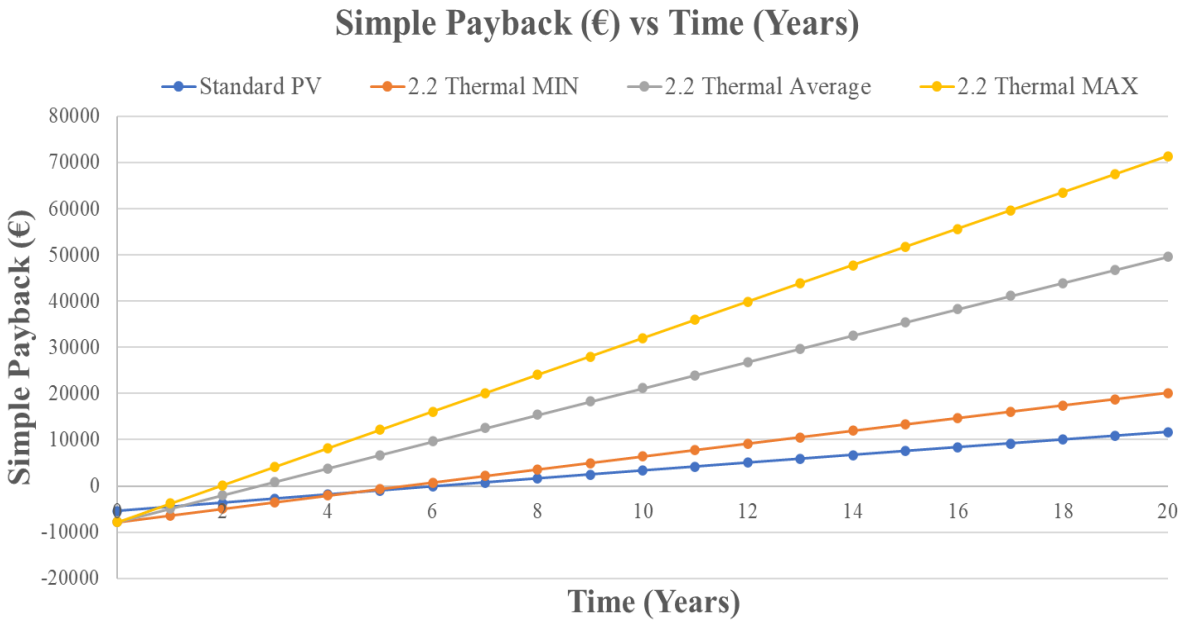

Figure 133: Simple payback on a 20 year time span without benefitting from government grant and considering three thermal efficiencies of IPCoSy 2.2.

5.5.12 Recommendations for future work on IPCoSy

An Innovative Photovoltaic Cooling System termed IPCoSy has been developed and tested throughout this research. The prototype designs have reached a Technology Readiness Level 5. However, further development and optimisation are required before commercialisation.

The IPCoSy Type 1 prototype achieves a good heat transfer between the solar cells and the cooling water. However, the structural instability makes such a prototype difficult to commercialise due to its fragility and potential for failure. Therefore, future work needs to look at ways to increase structural integrity with minimal effect on heat transfer. Another opportunity for improvement exists in the heat transfer between a conventional solar panel and IPCoSy 2.2, which is the after-market design. Researching different materials to act as a thermal interface is essential to achieving a better and more uniform heat transfer. However, a compromise must be found between a material with good thermal conductivity and keeping capital costs at a minimum. Another interesting field to investigate is finding ways to easily maintain the IPCoSy chambers, such as using sponge ball cleaning. Sponge ball cleaning involves introducing small balls with the flow of water with the aim of scrubbing the sides that they come in contact with. These balls are collected again at the end of the maintenance schedule and normal operation of the equipment can be resumed.

An important topic that was not covered by this research is material corrosion. Since the cooling chambers will be in contact with water and even seawater, one must investigate the extent of material deterioration and its effect on the product's lifetime. Furthermore, one can research ways to mitigate this corrosion, such as by introducing changeable sacrificial materials similar to the anode rods in conventional water heaters. Finally, throughout this study, fixed water flow rates were used and the control focused on the switching of such flow rate. Hence, an interesting future study would simulate different flow rates and achieve the optimal flow rate that results in the highest net gains in energy production. Similarly, more in-depth CFD simulations can further improve the IPCoSy design to get an even more efficient cooling. Finally, a potential study would be using different materials to replace the back sheet of the solar cell assembly to get a better heat transfer. Furthermore, in this study, aluminium was used to create the prototypes, however, it would be interesting to investigate the use of other materials, especially recycled plastics, to create the frame of the new photovoltaic module.

In conclusion, Figure 134 shows a cross-section of an idea for a future design following the lessons learnt through this research. The design involves changing the back sheet of the solar

cell assembly from a polymer to a sheet of aluminium, similar to flexible PV panels installed on boats. Hence, this aluminium back sheet is used as the top of an aluminium water chamber underneath the solar cell assembly. The chamber has internal stiffeners joined with both top and bottom surfaces. Therefore, this design would improve the heat transfer from the solar cells to the cooling water and provide the required structural integrity not to deform the solar cells during cooling flows. Furthermore, in areas where hail is not common, the glass on top can be replaced by some type of resin similar to that applied on flexible solar panels. This would decrease the capital cost and the weight of the IPCoSy panel.

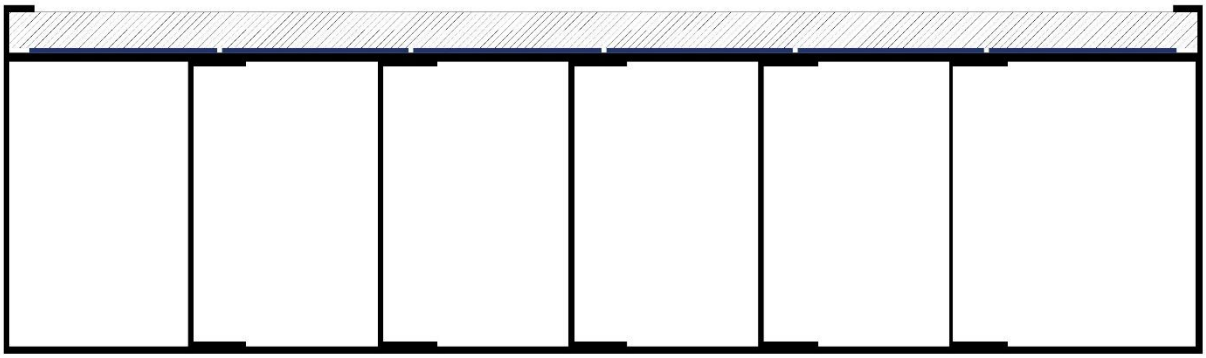

Figure 134: Ideal PV panel incorporating cooling.

5.6 Conclusion

This chapter presented the outcomes of testing a new type of photovoltaic panel that incorporates an innovative back-side cooling technique. The results showed that the IPCoSy photovoltaic module can achieve energy gains of up to 10.82% with a controlled forced flow and up to 3.34% with no flow. The main advantage of the IPCoSy cooling system is its ability to retain a volume of water in contact with the back-side of the PV module, even when the cooling flow is off, resulting in an added specific heat capacity. This added specific heat capacity slows down the temperature increase of the PV, leading to reduced pump switching frequency. IPCoSy also solves the problem of non-uniform solar cell temperatures experienced by current PVT technologies.

Throughout this study, it was observed that the gains that can be achieved with the IPCoSy prototype are considerable. However, these gains can be limited by various factors, including warming the water source and pump energy consumption. Therefore, to increase profits above those reported in this study, one should install the IPCoSy panels in ideal scenarios where the water resource volume is large and a water flow is already present. If the IPCoSy panel is used in floating installations, available water can be used as the cooling fluid. This would mean that

hot water could be discarded without heating the water source or wasting any water. Another ideal application for the IPCoSy panel is in powering reverse osmosis plants. The IPCoSy panel would act as the water transfer medium instead of conventional water pipes. Therefore, the flow generated by the reverse osmosis would keep the IPCoSy panel operating at ideal low temperatures, resulting in an optimised electrical efficiency. In return, the energy produced by the PVs would be used to power the reverse osmosis plant.

Moreover, the IPCoSy panel can also be installed in places that require water heating, such as residences or even in industrial scenarios with large boilers. In such installations, the IPCoSy panel would provide pre-heated water for the boiler while using the water flow to keep the solar panel at a lower temperature. Since water exiting from the IPCoSy panel will be at a higher temperature than the water source, this would significantly increase the efficiency of the building's water heating system. This study showed that maximum thermal efficiencies of 55.88% are possible.

Besides the energy gains, the IPCoSy panel provides other benefits, such as the weight of the water acting as a ballast to increase installation stability and, in hot climates, the lower maximum PV temperature will result in a longer PV lifetime. The design of the Type 1 prototype only involves a slight modification to the current fabrication process of PV panels. Therefore, the capital cost will be primarily limited to the added material for the back plate. Furthermore, IPCoSy does not involve any complex setting up by the user, similar to what is required for spray cooling, since the PV panel already incorporates the cooling chamber and only some basic plumbing is needed to set it up.

6. Research conclusions

This chapter summarises the key findings of this study and the results published in this thesis, in relation to the research aims and objectives. Furthermore, this chapter explains the research limitations and outlines recommendations for future work.

6.1 Achieved aims and objectives

This research aimed to find innovative solutions to optimise offshore photovoltaic installations with a focus on improving power output and increasing economic feasibility. Furthermore, this study aimed to create innovative products that, besides optimising offshore PV installations, can also be implemented for land installations and therefore broaden their market suitability.

The research aims and objectives were successfully met as described below:

O.1 State-of-the-art research was performed on solutions to decrease the effect of various parameters that reduce PV power generation and economic feasibility.

This research started with a background and literature review of the factors contributing to the non-optimal performance of photovoltaic modules. This resulted in identifying the incident solar radiation, efficiency and temperature coefficients of solar cells, and operating temperatures as the main derating factors. Other issues were identified for offshore photovoltaic installations such as an increased probability of potential induced degradation (PID) due to high humidity and an accelerated material degradation due to the corrosive environment. However, the main parameters that were investigated in this study were the incident solar irradiance on offshore photovoltaic panels and their operating temperature.

O.2 A simulation tool that analyses the effect of wave response motion on the incident solar irradiance on offshore PV installations was developed and validated experimentally.

O.3 The effects of pitch, yaw and roll wave response movements on the incident solar radiation on offshore PV installations were analysed separately.

A research gap existed in identifying and quantifying the effect of wave response motion on the insolation on offshore photovoltaic installations. Throughout this study it was noted that no publication had ever addressed the fact that movement due to response to incoming waves would result in varying tilt and orientation angles of an offshore photovoltaic installation.

Furthermore, no available literature had quantified this effect. Thus, the first part of this research focused on addressing this gap. Initially an excel-based simulation software was created that allowed the user to enter wave characteristic equations for pitch, yaw and roll movements. Hence, a NOAA Sun position calculator together with an anisotropic (PEREZ) model were used in order to predict the effect of the three separate movements on the insolation on offshore photovoltaic installations. This simulation model however, required validation. Hence, an experimental setup was created to simulate the wave movements and pyranometers were used to measure the incident solar radiation at every degree of movement. Data showed absolute mean errors between simulation and practice ranging from 0.002% to 0.053%. This showed that the simulation model was valid. Hence, a yearly parametric simulation was performed using a sinusoidal wave movement. Pitch movements resulted in negative effects on the insolation of up to −2.52%. Moreover, pitch movements were identified to have the most predominant effect since these movements directly affect the tilt of the installation. Yaw movements resulted in effects of less than −0.38% on the incident solar radiation. Also, yaw movements resulted in the least negative effects since slight deviations in orientation have minimal effects on photovoltaic systems. Finally, this part of the research showed that roll movements could have a considerable effect on the insolation on an offshore photovoltaic installation. Roll effects are the less intuitive since these movements change both the actual tilt and orientation of the PV modules. These results were published in Elsevier's Solar Energy Advances journal [111].

O.4 The effect of wave response motion on both fixed and tracking offshore PV installations was analysed and results were published.

After the simulation tool received international interest, it was decided to focus on improving and adding other features. Microsoft Excel was already working very slowly, so it was not considered to further increase computations. Hence, a new simulation software was programmed using C language. This software was termed Offshore Solar Irradiance Calculator (OSIC). The new software comprised of a graphical user interface (GUI) that enabled the user to easily navigate through the different options offered by the simulation tool. The new tool included various new features including the option to choose between calculating in radians and degrees, a calendar widget to allow setting the expected date format, and options to choose between moving or fixed for every installation, making the tool suitable for both land and offshore designs. The biggest addition to the simulation tool was the introduction of three solar tracking algorithms, namely Horizontal Single Axis Tracking (HSAT), Vertical Single Axis

Tracking (VSAT) and Dual-Axis Tracking. These new features enabled us to study the effect of wave response motion on offshore tracking system. Results showed that wave response motions can reduce the incident radiation on offshore tracking systems by more than 12%. These findings could have a significant impact on the design of offshore PV installations.

The results were published for the first time in MDPI Energies journal [118]. Furthermore, in 2022, the Solaqua project received a Malta Intellectual Property Award in the scientific initiative category and a World Intellectual Property Organisation (WIPO) medal, and OSIC formed part of the work being done in this project. Discussions are currently underway with the University of Malta's Knowledge transfer office to license and distribute the OSIC simulation tool.

O.5 An innovative PV cooling system that is targeted towards offshore PV installations but can also be applied to land installations was developed. This technology was termed IPCoSy

O.6 Different PV cooling system designs were tested, the most feasible designs were proposed and ideas for future development were suggested.

The second part of this study involved the investigation of the effect of temperature increase on the efficiency of solar cells and finding innovative ways to cool PV panels. From literature it resulted that a research and technology gap existed in having a cooling system that does not impact the front side of the PV module, does not waste resources such as water and does not require a high pump switching frequency. These issues were all addressed with the creation of an Innovative Photovoltaic Cooling System termed (IPCoSy). IPCoSy involved adding a chamber of water in contact with the back-side of PV modules. A cooling flow control algorithm was applied in order to keep the PV temperature within the desired limits. Furthermore, when the cooling flow was switched off, the water remained in contact with the back-side of the PV module resulting in an added specific heat capacity which decreased the rate of temperature increase. Therefore, the pump switching frequency was decreased when compared to conventional cooling systems. This signified a decrease in energy consumption and a longer pump lifetime. The results showed that this innovation increased the energy yield of PV modules by up to 10.82%. IPCoSy was also tested without a forced flow and results showed that the passive cooling can increase the energy yield of PV modules by up to 3.34%. When operated without flow, IPCoSy showed a decreased PV temperature during times of peak solar radiation and a slightly increased PV temperature in the afternoon. Therefore, this resulted

in a net energy gain since at peak solar radiation the PV module is working at a higher efficiency. Furthermore, even with passive cooling, IPCoSy always had a lower maximum temperature when compared to standard PV modules. This effect could prolong the lifetime of the PV module especially in locations where PV operating temperatures exceed maximum allowable levels. Besides increasing the efficiency of PV panels and decreasing their maximum temperature, IPCoSy also outputs warm water that can be used as a pre-heater to water heating systems in order to increase their efficiency. This study showed that maximum thermal efficiencies of 55.88% are possible, assuming no losses in the transmission and storage of the output water. This research proposed two main categories of IPCoSy designs:

- A modification of existing conventional PV modules to incorporate back-side cooling. This design, referred to as Type 1, requires slight modifications in PV module manufacturing.
- An after-market kit that can be attached at the back of existing standard PV modules to add the cooling effect. This design, referred to as Type 2 does not require any modification in PV module manufacturing however, the complete system comes at a higher capital cost.

The results of the small-scale prototype testing were published in Future Publishing LLC Future Energy journal [123]. Furthermore, an abstract to publish the full scale results was accepted for a special edition of MDPI Sustainability and a research paper will be submitted for peer review by October 2023. Moreover, a patent for the IPCoSy designs was granted by the Israeli Patent Office [124]. Finally, in 2022, IPCoSy was given a runner-up Malta Intellectual Property Award (MIPA) under the technology initiative section. Collaborations with international investors are currently underway to increase the technology readiness level of IPCoSy with the aim of manufacturing and distributing the technology worldwide.

6.2 Research limitations

This section describes the limitations of the findings originating from this research.

- Although the OSIC simulation tool allows the user to select different albedo values for the two PV systems being compared, the parametric analyses presented in this thesis always kept the same albedo for a land and an offshore installation. This was done to isolate the effect of wave response motion from other effects such as the reflection of light. Furthermore, albedo values vary for land installations depending on the ground

material, texture and colour. Similarly, the albedo of an offshore installation is not necessarily equal to the albedo of the ocean since photovoltaic panels can be installed on very large rafts which would mean that the raft's albedo value would have an effect on the incident solar radiation. Hence, in order to carry out an accurate analysis, the correct albedo values must be used for both installations, allowing OSIC to output results that are fine-tuned for that particular installation.

- A limitation in the OSIC simulation tool is that it does not consider any variance in PV panel shading. Since, wave response motion changes the tilt and orientation angles of the PV installation, this could result in one row of PVs shading the other, unless the movement is accounted for at the design stage. However, offshore photovoltaic systems will probably be installed at very low installation angles so as to fit a larger number of panels due to lower separation between rows and thus result in a higher energy density.

- The IPCoSy prototypes were not tested in an actual offshore environment which could uncover other challenges such as corrosion and fouling.

- The IPCoSy prototypes were also not tested in combination with other systems such as water heating systems or geothermal systems in order to have a better understanding of maximum system efficiencies.

6.3 Recommendations for future work

Based on the research presented in this thesis and the limitations outlined in the previous section, further research could improve and build upon the findings of this study. Recommendations for future work are already presented separately in other chapters of this thesis however, a summary of the salient points is presented below:

- The OSIC simulation tool can be further improved by allowing the user to enter values for PV module row spacing. Hence, the software would calculate the amount of shading, if any, and also the variance of this shade in response to wave movements.
- The OSIC simulation tool can be integrated with other established PV simulation software, such as PVSYST. This would give users a complete simulation tool capable of predicting the performance of offshore photovoltaic installations in realistic conditions.

- Once, an offshore photovoltaic installation is launched, it would be interesting to acquire real wave, albedo, and irradiance data. Hence, these data are input into OSIC and results are compared.
- The IPCoSy designs can be further optimised in terms of fluid dynamics and heat transfer. This can be done by carrying out a thorough CFD analysis.
- The structural integrity of the final IPCoSy design needs to be optimised using the least materials possible so as to increase financial viability.
- Research should be carried out using different materials other than aluminium that could decrease the manufacturing costs of IPCoSy while improving heat transfer and mechanical stability.
- IPCoSy should be tested in offshore environments and combined with other systems such as boilers and geothermal so as to verify maximum possible system efficiencies and the realistic benefits that can be achieved.

Multiple project applications are currently being submitted to acquire funding to be able to carry out this research. Future projects will possibly see further development of the OSIC simulation tool including integration with other software. Furthermore, funds will allow the development of IPCoSy to above TRL7, making it a commercial product.

6.4 Final remarks

This research contributed new knowledge to the scientific community. The effect of wave response motion on the insolation on offshore photovoltaic installations was studied for the first time. Furthermore, the created simulation tool (OSIC) will allow offshore PV designers to modify their raft designs in order to optimise the incident solar radiation on their PVs and therefore, increase the system efficiency. Furthermore, a patented PV cooling technology (IPCoSy) was designed and tested in this study. This technology could potentially change the current concept of a PV module and revolutionise the integration of renewable energy in buildings and industry. Finally, the findings of this research did not only satisfy the main aim of optimising offshore PV installations but also contributed knowledge to improve the PV industry in general.

Appendix A – Publications by the author

Peer-reviewed publications directly related to this research:

- R. Bugeja, L. Mule' Stagno, and N. Branche, "The effect of wave response motion on the insolation on offshore photovoltaic installations," *Solar Energy Advances*, vol. 1, p. 100008, Jan. 2021, doi: 10.1016/J.SEJA.2021.100008.

- R. Bugeja, L. Mule' Stagno, and L. Dexarcis, "An Offshore Solar Irradiance Calculator (OSIC) Applied to Photovoltaic Tracking Systems," *Energies (Basel)*, vol. 16, no. 9, May 2023, doi: 10.3390/en16093735.

- R. Bugeja, L. Mule' Stagno, and I. Niarchos, "Photovoltaic back-side cooling using the space inside a conventional frame (IPCOSY)," *Future Energy*, vol. 2, no. 3, pp. 20–28, Aug. 2023, doi: 10.55670/fpll.fuen.2.3.3.

- R. Bugeja, L. Mule' Stagno, and I. Niarchos, "Full-Scale Design, Implementation and Testing of an Innovative Photovoltaic Cooling System (IPCoSy)", *Sustainability*, vol. 15, issue 24, doi: https://doi.org/10.3390/su152416900.

Patents resulting from this research:

- R. Bugeja and L. Mule' Stagno, "SYSTEM FOR COOLING A SOLAR PANEL ASSEMBLY," 285827, Aug. 24, 2021 Accessed: Jun. 22, 2023. [Online]. Available: https://israelpatents.justice.gov.il/en/patent-file/details/285827

Conferences:

- Presented the IPCoSy concept in the Malta National Energy Conference 2022.

Awards partly or fully resulting from this research:

- MIPA 2022 award for scientific initiative for Solaqua. L. Mule' Stagno and R. Bugeja.

- WIPO 2022 medal for scientific initiative for Solaqua. L. Mule' Stagno and R. Bugeja.

- MIPA 2022 runner-up award for technological initiative for IPCoSy. R. Bugeja and L. Mule' Stagno.

Appendix B – Funding sources

- Funding of €17,000 was granted by the 2020 Maritime Seed Award through Malta Marittima and TAKEOFF for the IPCoSy project. These finds were utilised to cover expenses related to the patent application.

- Funding of €80,452 was granted by the Energy and Water Agency under the National Strategy for Research and Innovation in Energy and Water (2021-2030). These finds were used to carry out the research on IPCoSy outlined in Chapter 5 of this thesis.

Appendix C – Datasheets

Aleo PV panels used for the IPCoSy experimental setup:

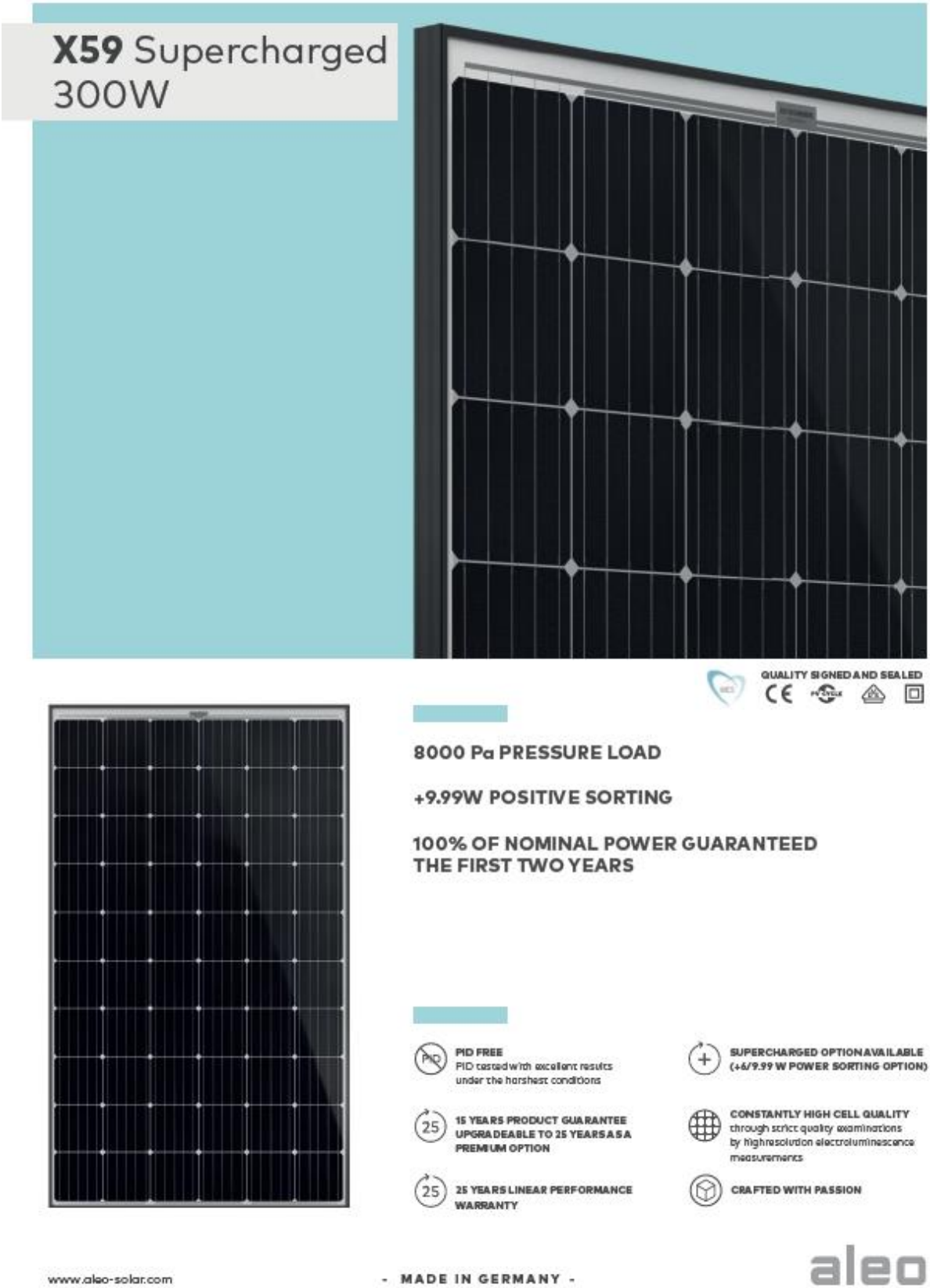

aleo solar module X59 Supercharged

ELECTRICAL DATA (STC)			X59L300
Rated power	P_{MPP}	[W]	300
Rated voltage	V_{MPP}	[V]	32.3
Rated current	I_{MPP}	[A]	9.30
Open-circuit voltage	V_{OC}	[V]	39.5
Short-circuit current	I_{SC}	[A]	9.81
Efficiency	n	[%]	18.3

Electrical values measured under standard test conditions (STC): 1000 W/m²; 25°C; AM 1.5

ELECTRICAL DATA (NMOT)			X59L300
Power	P_{MPP}	[W]	222
Voltage	V_{MPP}	[V]	29,9
Current	I_{MPP}	[A]	7,42
Open-circuit voltage	V_{OC}	[V]	36,9
Short-circuit current	I_{SC}	[A]	7,90
Efficiency	n	[%]	16,9

Electrical values measured under nominal module operating temperature : 800 W/m²; 20°C; AM 1.5; wind 1 m/s; Module temperature NMOT: 44,5°C

ELECTRICAL DATA (LOW IRRADIANCE)			X59L300
Power	P_{MPP}	[W]	58

Electrical values measured under: 200 W/m²; 25°C; AM 1,5

TEMPERATURE COEFFICIENTS			
Temperature coefficient I_{SC}	α (I_{SC})	[%/K]	+0.05
Temperature coefficient U_{OC}	β (V_{OC})	[%/K]	-0.29
Temperature coefficient P_{MPP}	γ (P_{MPP})	[%/K]	-0.40

BASIC DATA JUNCTION BOX		
Length x width x height	[mm]	148 x 123 x 27
IP class		IP67
Cable length	[mm]	1200 (+), 800 (-)
Connectors		MC4
Bypass diodes		3

CLASSIFICATION		
Classification range (positive classification)	[W]	0/+9.99

BASIC MODULE DATA		
Length x width x height	[mm]	1660 x 990 x 42
Weight	[kg]	19
Number of cells		60
Cell size	[mm]	156.75 x 156.75
Cell material		Monocrystalline Si, PERC
Number of bus bars		5
Front sheet		Solar glass (TSG)
Back sheet		Polymer sheet, white
Frame material		Al alloy, black

CERTIFICATIONS AND WARRANTY	
Product Guarantee	15 years, optional 25 years
Power Guarantee	25 years – Linear
Fire Resistance	Class C
Protection Against Electric Shock	II
Certifications	IEC 61215, IEC 61730
	IEC 62716 – Ammonia Resistance
	IEC 61701 – Salt mist Resistance
	IEC 62804 – PID Resistance
	MCS 010; MCS 005

LOADS			
Max. module pressure load (Testload)		[Pa]	8000[1]
Max. module pressure load (Designload)[2]		[Pa]	5333[1]
Max. module suction load (Testload)		[Pa]	2400[1]
Max. module suction load (Designload)[2]		[Pa]	1600[1]
Max. system voltage		[V_{DC}]	1000
Reverse current load	I_R	[A]	20

Mechanical load acc. to IEC/EN 61215:2016
[1] Please observe the mounting conditions in the installation manual
[2] Testload/ Safety factor 1.5 = Designload

Measurement tolerance of P_{MPP} under STC -3/+3% |
Accuracy of other electrical values -10/+10%
Efficiency relating to gross module area

DIMENSIONS [mm]

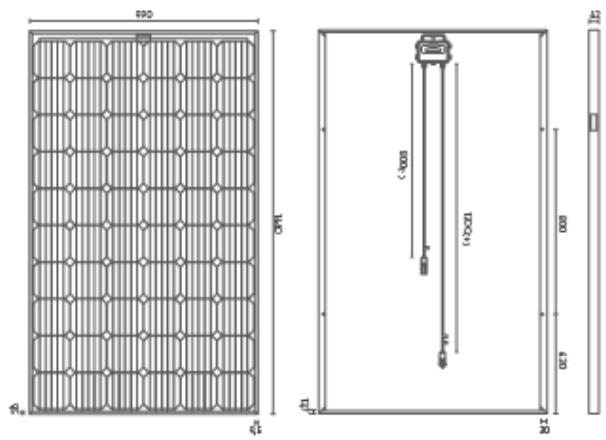

PERFORMANCE GUARANTEE

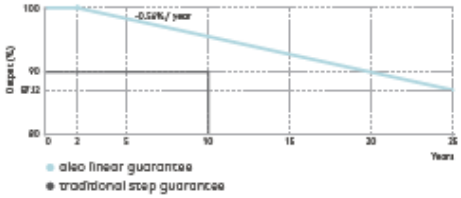

PLEASE CONTACT YOUR AUTHORISED ALEO DEALER

ALEO SOLAR GMBH
Mariusz-Eriksen-Straße 1
17291 PRENZLAU
GERMANY

CONTACT
+49 3984-8328-0
info@aleo-solar.de
www.aleo-solar.com

Enphase IQ7+ inverter used for IPCoSy experimental setup:

ENPHASE.

DATA SHEET
US

IQ7 and IQ7+ Microinverters

The high-powered, smart grid–ready IQ7 and IQ7+ Microinverters dramatically simplify installation while achieving the highest system efficiency.

Part of the Enphase Energy System, the IQ7 Series Microinverters integrate with the IQ Gateway, IQ Battery, and the Enphase Installer App monitoring and analysis software.

Enphase 25 year limited warranty

IQ7 Series Microinverters extend the reliability standards set forth by previous generations and undergo over a million hours of power-on testing, enabling Enphase to provide an industry-leading warranty of up to 25 years.

Connect PV modules quickly and easily to IQ7 Series Microinverters using the included Q-DCC-2 adapter cable with plug-and-play MC4 connectors.

UL CERTIFIED SAFETY

IQ7 Series Microinverters are UL listed as PV Rapid Shutdown Equipment and conform with various regulations when installed according to the manufacturer's instructions.

Easy to install

- Lightweight and simple
- Faster installation with improved, lighter two-wire cabling
- Built-in rapid shutdown compliant (NEC 2014 , 2017, and 2020)

Productive and reliable

- Optimized for high-powered 60-cell/120-half-cell and 72-cell/144-half-cell PV modules
- More than a million hours of testing
- Class II double-insulated enclosure
- UL listed

Smart grid–ready

- Complies with advanced grid support, voltage, and frequency ride-through requirements
- Remotely updates to respond to changing grid requirements
- Configurable for varying grid profiles
- Meets CA Rule 21 (UL 1741-SA) IEEE 1547:2018 (UL 1741-SB, 3rd Ed.)

IQ7-IQ7Plus-DS-02-EN-US-2023-04-14

IQ7 and IQ7+ Microinverters

INPUT DATA (DC)	UNITS	IQ7-60-2-US	IQ7PLUS-72-2-US
Commonly used module pairings[1]	W	235–350	235–440
Module compatibility		60-cell/120 half-cell PV modules only	60-cell/120-half-cell and 72-cell/144-half-cell PV modules
MPPT voltage range	V	27–37	27–45
Operating range	V	16–48	16–60
Min./max. start voltage	V	22/48	22/60
Max. input DC voltage	V	50	60
Max. continuous input DC current	A	10	12
Max. input DC short-circuit current	A	25	
Max. module Isc	A	20	
Overvoltage class DC port		II	
DC port back-feed current	mA	0	
PV array configuration		1 × 1 ungrounded array; No additional DC side protection required; AC side protection requires max 20 A per branch circuit	

OUTPUT DATA (AC)	UNITS	IQ7-60-2-US	IQ7PLUS-72-2-US
Peak output power	VA	250	295
Max. continuous output power	VA	240	290
Nominal (L-L) voltage/range[2]	V	240/211–264, 208/183–229	
Max. continuous output current	A	1.0 (240 V)/1.15 (208 V)	1.21 (240 V)/1.39 (208 V)
Nominal frequency	Hz	60	
Extended frequency range	Hz	49–68	
AC short circuit fault current over three cycles	Arms	5.8	
Max. units per 20 A (L-L) branch circuit[3]		16/13	13/11
Total harmonic distortion	%	<5	
Overvoltage class AC port		III	
AC port back-feed current	mA	18	
Power factor setting		1.0	
Grid-tied power factor (adjustable)		0.85 leading … 0.85 lagging	
Peak efficiency	%	97.6 (240 V)	97.5 (240 V)/97.3 (208 V)
CEC weighted efficiency	%	97	
Nighttime power consumption	mW	60	

MECHANICAL DATA	
Ambient temperature range	-40°C to 65°C (-40°F to 149°F)
Relative humidity range	4% to 100% (condensing)
DC connector type	MC4 (or Amphenol H4 UTX with additional Q-DCC-5 adapter)
Dimensions (H × W × D)	212 mm (8.3") × 175 mm (6.9") × 30.2 mm (1.2") without bracket
Weight	1.08 kg (2.38 lbs)
Cooling	Natural convection—no fans
Approved for wet locations	Yes
Pollution degree	PD3
Enclosure	Class II double-insulated, corrosion-resistant polymeric enclosure
Environ. category/UV exposure rating	NEMA Type 6/outdoor

COMPLIANCE	
Certifications	CA Rule 21 (UL 1741-SA), UL 62109-1, IEEE 1547:2018 (UL 1741-SB 3rd Ed.), HEI Rule 14H SRD 2.0, FCC Part 15 Class B, ICES-0003 Class B, CAN/CSA-C22.2 NO. 107.1-01 This product is UL Listed as PV Rapid Shutdown Equipment and conforms with NEC 2014, NEC 2017, and NEC 2020 section 690.12 and C22.1-2015 Rule 64-218 Rapid Shutdown of PV Systems, for AC and DC conductors, when installed according to the manufacturer's instructions.

(1) Pairing PV modules with wattage above the limit may result in additional clipping losses. See the compatibility calculator at https://link.enphase.com/module-compatibility.
(2) Nominal voltage range can be extended beyond nominal if required by the utility. (3) Limits may vary. Refer to local requirements to define the number of microinverters per branch in your area.

IQ7-IQ7Plus-DS-02-EN-US-2023-04-14

SGT-22 Current Transducers used for IPCoSy experimental setup:

Isolators - RMS transducers

simex

TRG line

SGT-22

- high current and voltage AC/DC signals RMS transducer
- wide range of power supply
- galvanic isolation between input/output/supply circuits
- TS-35 DIN rail mounting
- high accuracy, digital linearization
- standard output signal
- LED indicator on a front panel

SGT-22 transmiter measures AC/DC current or voltage and converts them into standard output signal. Signal processing is performed according to the RMS value algorythm:

$$U(RMS) = \frac{\sqrt{\int f^2(t)dt}}{T}$$

Max. current in steady state is up to 5A. For measuring greater currents external shunt is required. Max. instantaneous overload is 25A (for 1 s.). By analogy - for voltage bigger than 750 V AC, transformer is necessary. All the circuits (input/output/supply) are galvanically isolated.
For advanced users the calibrations procedure is also available.

PIN ASSIGNMENT

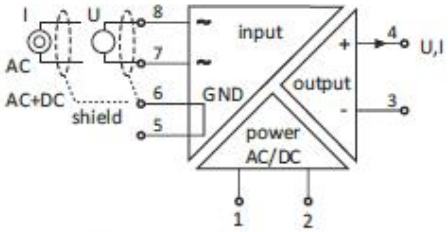

PRINCIPLE OF OPERATION

The transmitter measures the input signal and converts according to preset parameters then calculates the output signal. Green LED informs that transducer is supplied and processor works properly. There are two potentiometers on the housing, which can be used for calibrating "Zero" and „Range". It is advised to use auto-calibration button for reference voltage, if input signal is AC.

TECHNICAL DATA

Power supply **Power consumption**	18 V ÷ 350 VDC; 18 V ÷ 230 VAC for DC supply: 1.5 W, for AC supply 1.5 VA
Input signal	voltage RMS: max. range 0 ÷ 750 V; resistance ≥2 MΩ / 230V current RMS: max. range 0 ÷ 5A; resistance ~ 0,02Ω / 5A instantaneous overload for internal shunt: max 25 A for 1s peak ratio: twice of measuring range
Signal shape	free (DC+AC)
Signal sampling	100 kHz
Frequency	range: 3 Hz ÷ 10 kHz
Output signal	voltage: 0 ÷ 10V / max. load 2kΩ current: 0/4 ÷ 20 mA / max. load 750Ω or any other
Accuracy	0.2%
Nonlinearity	0.025%
Load error	0,05% / FS
Temperature drift	0.006% / °C
Digital filter time constant	standard 1s, other on request
Operating temperature	0°C ÷ +55°C
IP protection	IP 20
Dimensions (WxHxD)	22.5 x 99 x 114.5 mm
Mounting	TS-35 DIN rail

TRANSMITTER CALIBRATION

WARNING: The transmitter is preset.
Incorrect calibration may cause malfunction.

For RMS AC signals, the calibration should start with setting the reference voltage:
- short the input contacts and push „Uodn" button for 6 s. till the green LED starts flashing. For a further 4 s. the transmitter is calibrated.

Calibration can be improved using „0%" and "100%" potentiometers. Provided that the signal fed to the input is accurately measured.

CASE DIMENSIONS

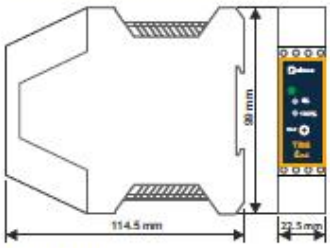

ORDERING

SGT-22-Y-X-2-3-001

input signal range:
0 - 5 A
0 - 750 V

output:
1 : 0 - 5 mA
2 : 0 - 20 mA
3 : 4 - 20 mA
4 : 0 - 5 V
5 : 0 - 10 V
6 : 1 - 5 V

Ordering examples:
SGT-22-0.3A-5-2-3-001
Isolator, in.: 0-3A, out.: 0-10V

KKATAEN_v1.14.071

80-556 Gdańsk, ul. Wielopole 11, Poland, tel. (+48) 58 762-07-77, fax 58 762-07-70, www.simex.pl

SlAi-8 used to transmit current measurements to datalogger through RS-485:

simex

SIAi-8

- analogue inputs module
- 8 independent analogue inputs (voltage or current)
- RS-485 / Modbus RTU
- galvanic separation of the inputs from the module supply voltages
- LEDs for module operation and Modbus transmission signalling
- input signals connected by means of the socket-plug connectors

Module **SIAi-8** allows to measure analog values from 8 current (or voltage) inputs via the RS-485 connection, with speed rate about 10 Hz (every channel). Measurement results can be internally recalculated due to one of available characteristics: linear, square or user definable multipoint (max. 20 points length). It finds application in distributed control and visualization systems.
Standard functions of Modbus transmission allow to changing of device address or detect its type. All **SIAi-8** operating functions, available via the RS-485, can be implemented from any typical visualization software or, for instance, with a suitably **MultiCon** controller.

TECHNICAL DATA

Power supply **Current consumption**	10V ÷ 30V DC; external fuse (required): T - type, max. 1 A 55 mA typical
Inputs	8 independent analogue inputs: current 0-20 mA; 4-20 mA or voltage 0-10 V; 2-10 V; 0-5 V; 1-5 V
Measurement accuracy	± 0.25% ± one digit
Galvanic separation	all 8 inputs are galvanically isolated from module supply and RS-485 interface
Communication interface	RS-485, 1200 ÷ 115200 bit/s, 8N1, Modbus RTU
Number of modules	max. 128 in a single network
Data memory	non-volatile memory, EEPROM type
Operating temperature	0°C ÷ +50°C (standard), -20°C ÷ +50°C (option)
Storage temperature	-10°C ÷ +70°C (standard), -20°C ÷ +70°C (with option **08**)
Humidity	max. 90%, non-condensing
Protection class	IP 20 (housing and connection clips)
Case	on the 35 mm strip; material: ABS
Dimensions	101 x 22,5 x 80 mm
Weight	120 g max.

TERMINALS CONNECTION

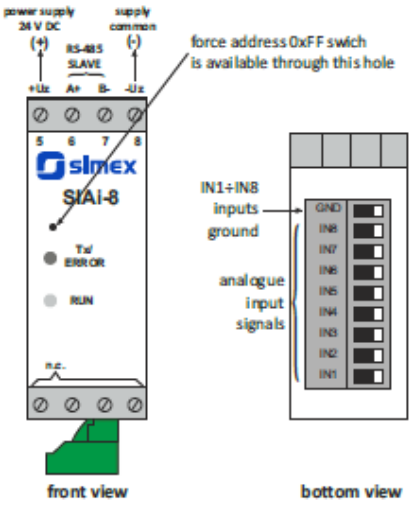

CONNECTION AND PRINCIPLE OF OPERATION

Connect the supply voltage to the module (+Uz, -Uz, typically 24V DC) and two wires RS-485 (A+, B-) communication interface. Module inputs are located on the lower edge of the case (look: bottom view).
Directly after power on the device is signalling its normal operation flashing green LED, marked „RUN" (about 2 times/sec.). Short flashes of LED marked "TX/ERROR" signalize activity of RS-485 interface, and permanent light of this LED means malfunction of the device.
Module makes the measurements from eight inputs in cycles.

ORDERING

SIAi-8X-XX1

options:
00 : no options
08 : operating temp. -20°C ÷ +50°C

type of inputs:
N : voltage inputs
P : current inputs

KKATAEN_v1.21101

Appendix D – Control algorithms

Control Algorithm for sinusoidal wave movements:

```
#include <Servo.h>

// Define servo pins
#define SERVO_PIN_1 9
#define SERVO_PIN_2 10

// Define servo objects
Servo servo1;
Servo servo2;

// Initial angles for solar panel tilt and orientation
int tiltAngle = 0;
int orientationAngle = 0;

// Current amplitude selector (0 to 3)
int amplitudeSelector = 0;

// Amplitude values corresponding to amplitude selector
int amplitudeValues[] = {20, 15, 10, 5};

// Data logger control pin
const int dataLoggerControlPin = 11;

// Oscillation mode
enum OscillationMode {
  TILT_ONLY,
  ORIENTATION_ONLY,
  BOTH_TILT_AND_ORIENTATION
};

OscillationMode oscillationMode = BOTH_TILT_AND_ORIENTATION;
// Default mode: Both tilt and orientation

void setup() {
  // Initialize serial communication
  Serial.begin(9600);

  // Set data logger control pin as output
  pinMode(dataLoggerControlPin, OUTPUT);

  // Attach servo objects to pins
  servo1.attach(SERVO_PIN_1);
  servo2.attach(SERVO_PIN_2);
```

```
  // Prompt user for initial angles
  Serial.println("Enter initial tilt angle:");
  while (!Serial.available()) {}
  tiltAngle = Serial.parseInt();

  Serial.println("Enter initial orientation angle:");
  while (!Serial.available()) {}
  orientationAngle = Serial.parseInt();

  // Move servos to initial positions
  servo1.write(tiltAngle);
  servo2.write(orientationAngle);

  // Prompt user for amplitude selector
  Serial.println("Enter amplitude selector:");
  Serial.println("0. 20 degrees");
  Serial.println("1. 15 degrees");
  Serial.println("2. 10 degrees");
  Serial.println("3. 5 degrees");
  while (!Serial.available()) {}
  amplitudeSelector = Serial.parseInt();

  // Prompt user for oscillation mode
  Serial.println("Select oscillation mode:");
  Serial.println("1. Tilt Only");
  Serial.println("2. Orientation Only");
  Serial.println("3. Both Tilt and Orientation");
  while (!Serial.available()) {}
  int selectedMode = Serial.parseInt();

  // Validate and set the oscillation mode
  if (selectedMode == 1) {
    oscillationMode = TILT_ONLY;
  } else if (selectedMode == 2) {
    oscillationMode = ORIENTATION_ONLY;
  } else if (selectedMode == 3) {
    oscillationMode = BOTH_TILT_AND_ORIENTATION;
  } else {
    Serial.println("Invalid oscillation mode. Using default mode: Both tilt
and orientation.");
  }
}

void loop() {
  // Start data logging
  startDataLogging();
```

```
  // Perform sinusoidal oscillations based on the selected oscillation mode
  switch (oscillationMode) {
    case TILT_ONLY:
      performOscillations(amplitudeValues[amplitudeSelector], true, false);
      break;
    case ORIENTATION_ONLY:
      performOscillations(amplitudeValues[amplitudeSelector], false, true);
      break;
    case BOTH_TILT_AND_ORIENTATION:
      performOscillations(amplitudeValues[amplitudeSelector], true, true);
      break;
    default:
      // Invalid mode, perform both tilt and orientation oscillations as
default
      performOscillations(amplitudeValues[amplitudeSelector], true, true);
      break;
  }

  // Stop data logging
  stopDataLogging();

  // Increment amplitude selector
  amplitudeSelector++;

  // Check if the last amplitude is reached
  if (amplitudeSelector > 3) {
    // Exit loop
    break;
  }
}

void startDataLogging() {
  digitalWrite(dataLoggerControlPin, HIGH); // Set data logger control pin to
logic high
}

void stopDataLogging() {
  digitalWrite(dataLoggerControlPin, LOW); // Set data logger control pin to
logic low
}

void performOscillations(int amplitude, bool tiltEnabled, bool
orientationEnabled) {

  int steps = 360; // 360 degrees for a complete cycle

  // Calculate the increment value for each step
  float increment = 2 * PI / steps;
```

```
  // Move the servos in a sinusoidal pattern
  for (int i = 0; i <= steps; i++) {
    if (tiltEnabled) {
      int tiltAngle = amplitude * sin(i * increment) + tiltAngle;
      servo1.write(tiltAngle);
    }

    if (orientationEnabled) {
     int orientationAngle = amplitude * sin(i * increment) + orientationAngle;
      servo2.write(orientationAngle);
    }

    delay(20);
  }
}
```

Control Algorithm for the automatic threshold cooling:

```
// Include the required libraries
#include <RTClib.h>
#include <Adafruit_MAX31855.h>

// Thermocouple connections
#define WATER_THERMOCOUPLE_CLK 13
#define WATER_THERMOCOUPLE_CS 12
#define WATER_THERMOCOUPLE_DO 11

#define SOLAR_PANEL_THERMOCOUPLE_CLK 10
#define SOLAR_PANEL_THERMOCOUPLE_CS 9
#define SOLAR_PANEL_THERMOCOUPLE_DO 8

// Relay pin
#define RELAY_PIN 7

// Constants
const int MONTHS = 12;
const int TEMPERATURE_DIFFERENCE = 10;
const int TEMPERATURE_INCREMENT = 5;

// Array of temperature thresholds for each month (in degrees Celsius)
const int temperatureThresholds[MONTHS] = {32, 35, 35, 40, 40, 45, 45, 45, 40,
35, 35, 32};

// Variables
int currentMonth = 0;
int highThreshold = temperatureThresholds[currentMonth];
int lowThreshold = highThreshold - TEMPERATURE_DIFFERENCE;
```

```
bool coolingOn = false;

// Create instances of the RTC and MAX31855 classes
RTC_DS1307 rtc;
Adafruit_MAX31855 waterThermocouple(WATER_THERMOCOUPLE_CLK,
WATER_THERMOCOUPLE_CS, WATER_THERMOCOUPLE_DO);
Adafruit_MAX31855 solarPanelThermocouple(SOLAR_PANEL_THERMOCOUPLE_CLK,
SOLAR_PANEL_THERMOCOUPLE_CS, SOLAR_PANEL_THERMOCOUPLE_DO);

void setup() {
  pinMode(RELAY_PIN, OUTPUT);
  digitalWrite(RELAY_PIN, LOW);  // Relay is initially off

  // Initialize the RTC
  rtc.begin();

  // Check if the RTC is running. If not, set it to the current date and time
  if (!rtc.isrunning()) {
    rtc.adjust(DateTime(F(__DATE__), F(__TIME__)));
  }
}

void loop() {
  DateTime now = rtc.now();

  // Check if the current time is between 7 AM and 7 PM
  if (now.hour() >= 7 && now.hour() < 19) {
    // Read temperatures
    float waterTemperature = readWaterTemperature();
    float solarPanelTemperature = readSolarPanelTemperature();

    // Get the current month from the RTC
    if (now.month() != currentMonth) {
      currentMonth = now.month();
      highThreshold = temperatureThresholds[currentMonth - 1];
      lowThreshold = highThreshold - TEMPERATURE_DIFFERENCE;
    }

    if (waterTemperature + 10 > lowThreshold) {
    // Increase lowThreshold in steps of 5 degrees until the condition is met
      while (waterTemperature + 10 > lowThreshold) {
        lowThreshold += TEMPERATURE_INCREMENT;
      }
    } else {
// Decrease lowThreshold in steps of 5 degrees, maintaining the 10-degree
difference
      while (waterTemperature + 10 < lowThreshold - TEMPERATURE_INCREMENT) {
```

```
        lowThreshold -= TEMPERATURE_INCREMENT;
      }
    }

    highThreshold = lowThreshold + TEMPERATURE_DIFFERENCE;

    if (!coolingOn && solarPanelTemperature >= highThreshold) {
      // Activate water pump and cooling
      digitalWrite(RELAY_PIN, HIGH);
      coolingOn = true;
    } else if (coolingOn && solarPanelTemperature < lowThreshold) {
      // Deactivate water pump and stop cooling
      digitalWrite(RELAY_PIN, LOW);
      coolingOn = false;
    }

  } else {
    // If outside the time range, turn off the water pump and cooling
    digitalWrite(RELAY_PIN, LOW);
    coolingOn = false;
  }

  delay(10000);
}

float readWaterTemperature() {
  // Code to read water temperature from the water thermocouple
  float temperature = waterThermocouple.readCelsius();
  return temperature;
}

float readSolarPanelTemperature() {
  // Code to read temperature from the solar panel thermocouple
  float temperature = solarPanelThermocouple.readCelsius();
  return temperature;
}
```

Appendix E – Patent certificates

Copy of Patent Certificate:

State of Israel
Patent Office

מדינת ישראל
רשות הפטנטים

חוק הפטנטים, התשכ"ז- 1967
Patents Law, 5727 - 1967

תעודת פטנט

CERTIFICATE OF PATENT

This is to certify that the following particulars have been recorded in the Register of Patents:

זאת לתעודה כי הפרטים דלהלן נרשמו בפנקס הפטנטים

Patent No:	285827	**מס' הפטנט:**
Date of Application:	24/08/2021	תאריך הבקשה:
Title of Invention:		שם האמצאה:
SYSTEM FOR COOLING A SOLAR PANEL ASSEMBLY		מערכת לקירור מכלול לוח סולרי

Patentee(s): **בעלי הפטנט:**

University of Malta
Customer No: 961907
TAL-QROQQ MSD 2080
MSD
MALTA

Inventor(s): **ממציא(ים):**

Luciano MULE STAGNO
Customer No: 961909

Ryan BUGEJA
Customer No: 961911

Date of Publication:	01/10/2022	תאריך פרסום קיבול הבקשה:
Date of Grant:	02/01/2023	תאריך מתן פטנט:

Ofir Alon אופיר אלון
רשם הפטנטים
המדגמים וסימני המסחר
Commissioner of Patents
Designs and Trademarks

תעודה זו הינה אישור כי דבר מתן הפטנט* נרשם בפנקס הפטנטים

This Certificate certifies that the grant of the Patent* has been recorded in the Register of Patents.

Copy of Patent Renewal Certificate:

תאריך : ט"ו אדר תשפ"ג

08/03/2023
מספרכם :

לכבוד
ריינהולד כהן ושותפיו
רחוב הברזל 26א'
תל אביב - יפו 69710

רצ"ב תעודת חידוש פטנט מס'

תעודת חידוש פטנט
CERTIFICATE OF PATENT RENEWAL

Patent No. **285827** פטנט מס'

in the name of — על שם

University of Malta

This is to certify that the prescribed fee has been paid and that the patent been renewed until the expiry

מאושר בזה כי האגרה הקבועה שולמה והפטנט חודש עד לתום

of 6 Years from 24/08/2021 — 6 שנים מיום

בשם רשם הפטנטים
For Registrar of Patents

טופס פר' 55 (3) 14.02.2021

רחוב אגודת ספורט הפועל מס' 1, הגן הטכנולוגי מלחה,
בניין מס' 5, ירושלים, מיקוד 96951.
טל' : 972-73-3927100 פקס : 972-2-6467774
www.patents.gov.il

Appendix F – IPCoSy manufacturing designs

Type 1.1:

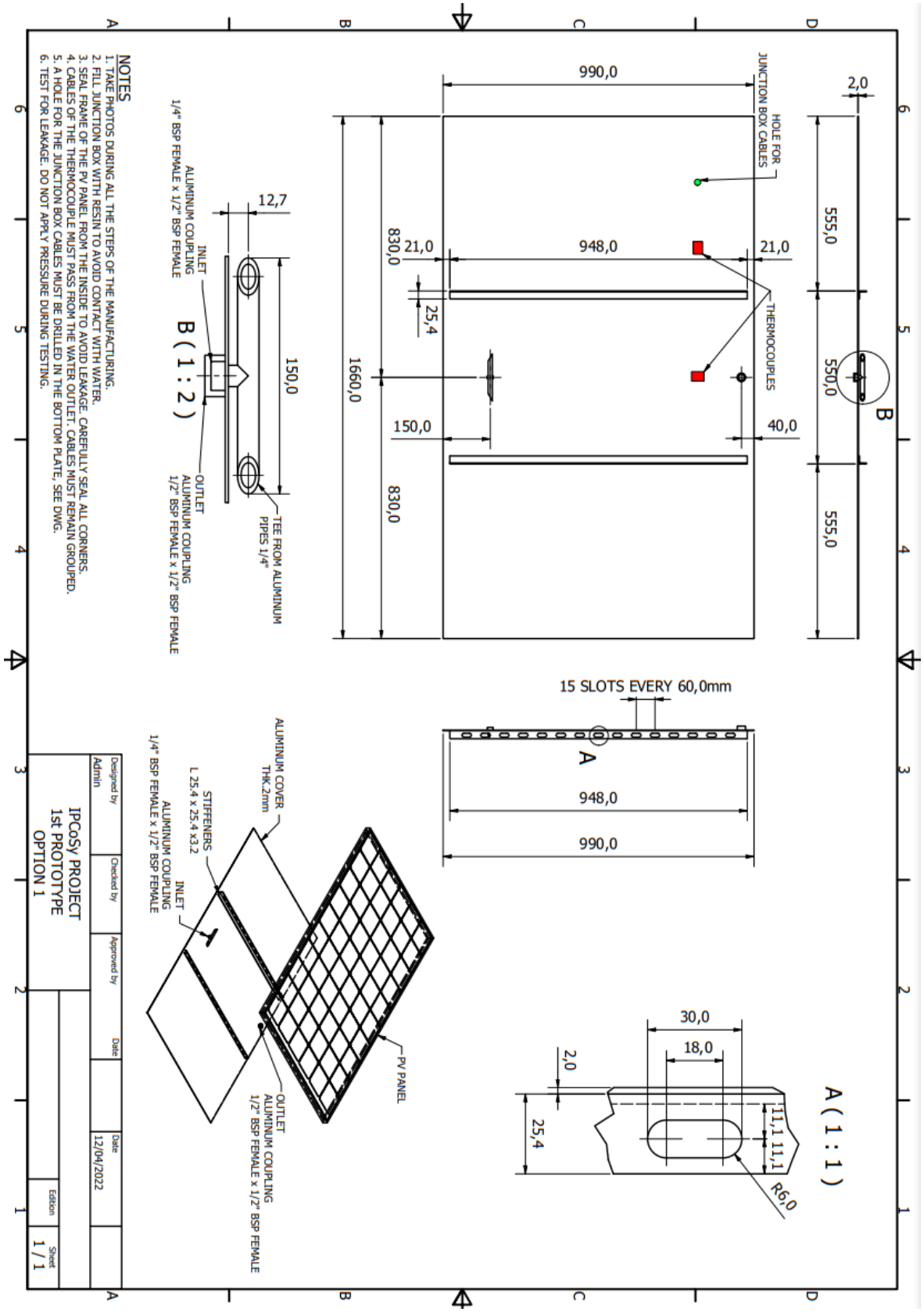

Type 1.2:

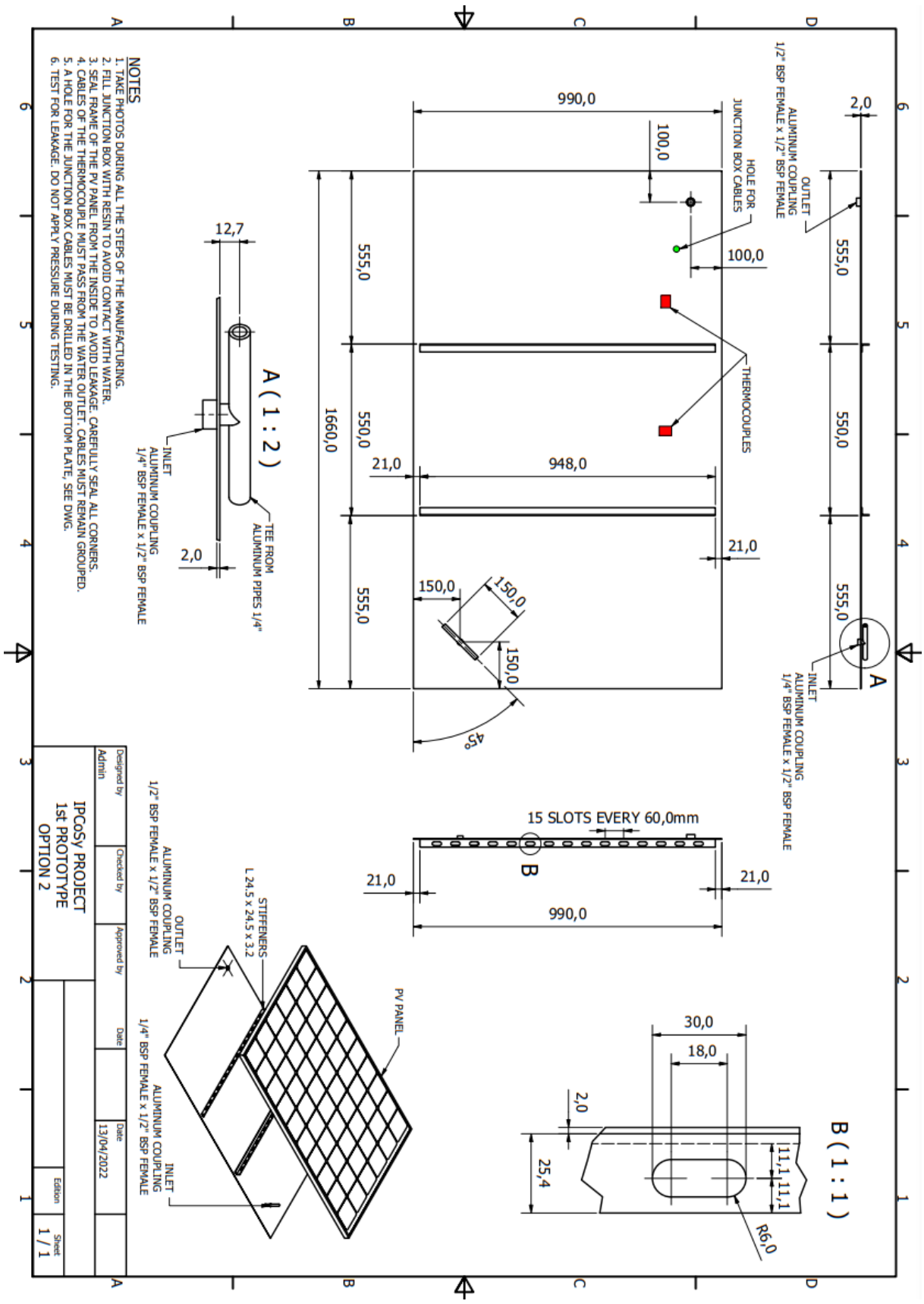
NOTES
1. TAKE PHOTOS DURING ALL THE STEPS OF THE MANUFACTURING.
2. FILL JUNCTION BOX WITH RESIN TO AVOID CONTACT WITH WATER.
3. SEAL FRAME OF THE PV PANEL FROM THE INSIDE TO AVOID LEAKAGE. CAREFULLY SEAL ALL CORNERS.
4. CABLES OF THE THERMOCOUPLE MUST PASS FROM THE WATER OUTLET. CABLES MUST REMAIN GROUPED.
5. A HOLE FOR THE JUNCTION BOX CABLES MUST BE DRILLED IN THE BOTTOM PLATE, SEE DWG.
6. TEST FOR LEAKAGE. DO NOT APPLY PRESSURE DURING TESTING.
990,0
100,0
555,0
550,0
1660,0
21,0
948,0
150,0
45°
HOLE FOR JUNCTION BOX CABLES
THERMOCOUPLES
OUTLET ALUMINUM COUPLING 1/2" BSP FEMALE x 1/2" BSP FEMALE
INLET ALUMINUM COUPLING 1/4" BSP FEMALE x 1/2" BSP FEMALE
A (1 : 2)
12,7
2,0
TEE FROM ALUMINUM PIPES 1/4"
B (1 : 1)
15 SLOTS EVERY 60,0mm
30,0
18,0
25,4
11,1
R6,0
STIFFENERS L 24.5 x 24.5 x 3.2
PV PANEL
IPCoSy PROJECT
1st PROTOTYPE
OPTION 2
Designed by
Admin
Checked by
Approved by
Date
13/04/2022
Edition
Sheet
1 / 1

Type 2.1:

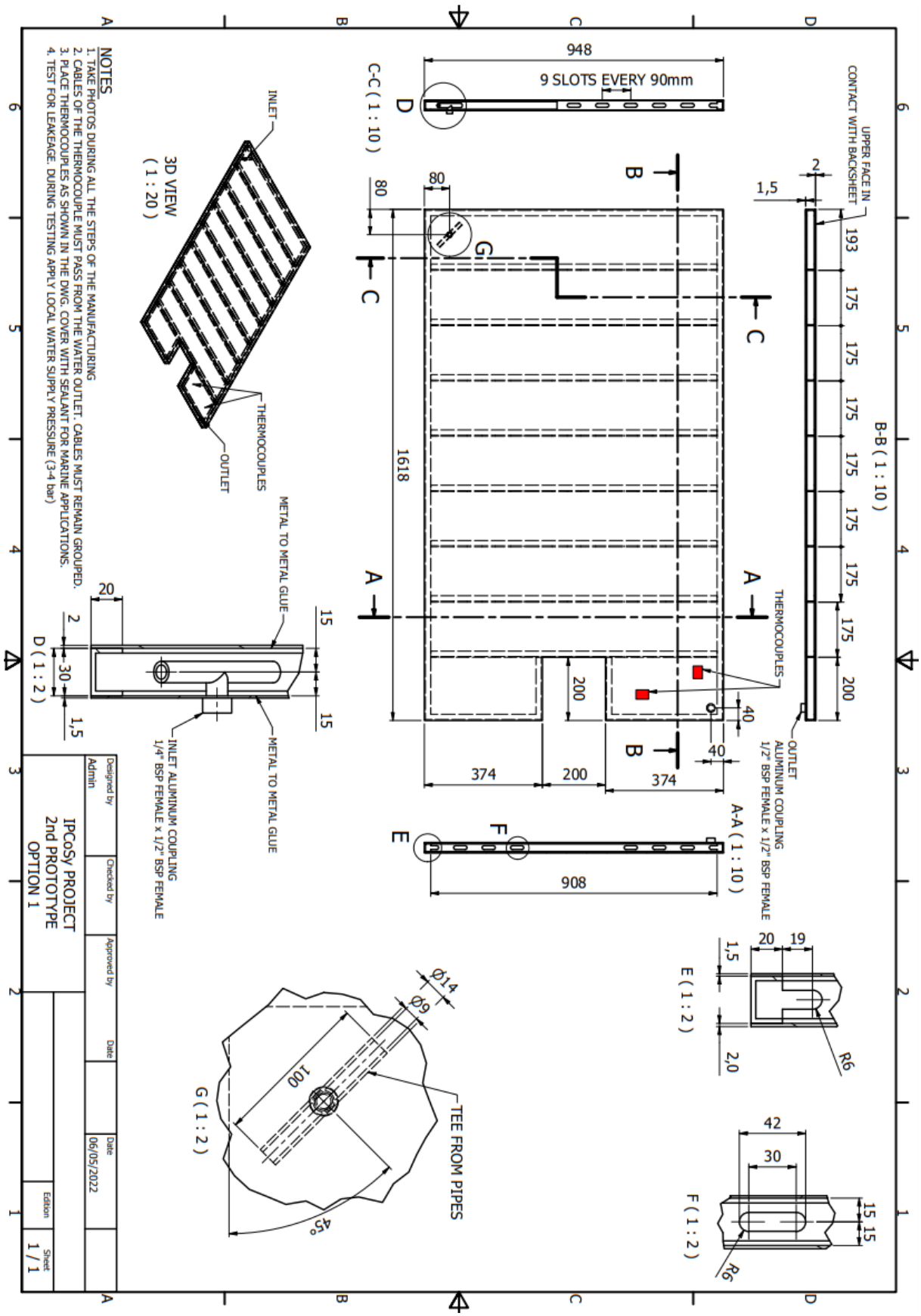
948
9 SLOTS EVERY 90mm
C-C (1 : 10)
B-B (1 : 10)
UPPER FACE IN CONTACT WITH BACKSHEET
1618
374
200
908
THERMOCOUPLES
OUTLET ALUMINUM COUPLING 1/2" BSP FEMALE x 1/2" BSP FEMALE
A-A (1 : 10)
3D VIEW (1 : 20)
INLET
OUTLET
METAL TO METAL GLUE
D (1 : 2)
INLET ALUMINUM COUPLING 1/4" BSP FEMALE x 1/2" BSP FEMALE
E (1 : 2)
F (1 : 2)
G (1 : 2)
TEE FROM PIPES
NOTES
1. TAKE PHOTOS DURING ALL THE STEPS OF THE MANUFACTURING
2. CABLES OF THE THERMOCOUPLE MUST PASS FROM THE WATER OUTLET. CABLES MUST REMAIN GROUPED.
3. PLACE THERMOCOUPLES AS SHOWN IN THE DWG. COVER WITH SEALANT FOR MARINE APPLICATIONS.
4. TEST FOR LEAKEAGE. DURING TESTING APPLY LOCAL WATER SUPPLY PRESSURE (3-4 bar)
IPCoSy PROJECT
2nd PROTOTYPE
OPTION 1
Designed by
Admin
Checked by
Approved by
Date
Date
06/05/2022
Edition
Sheet
1 / 1

Type 2.2:

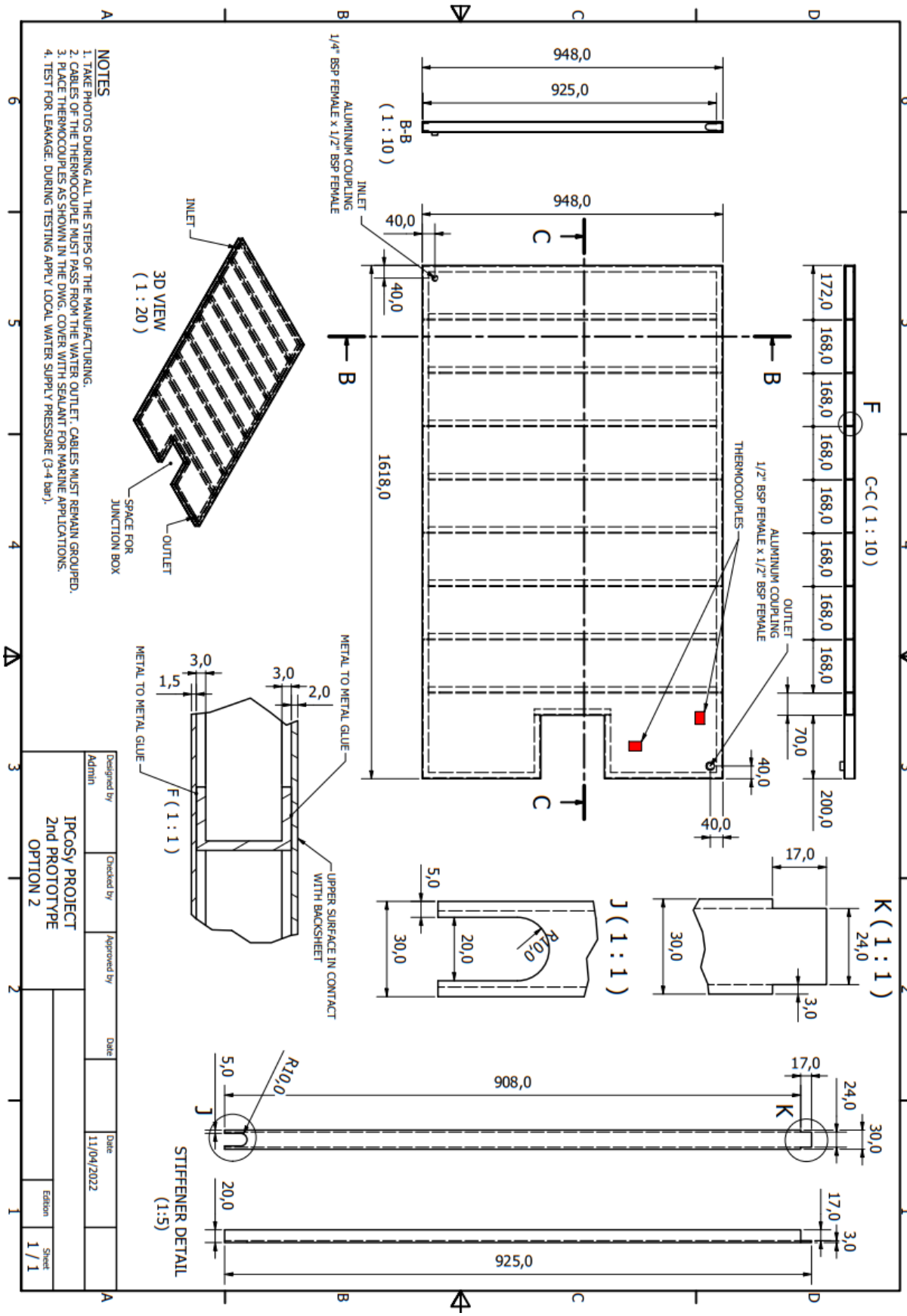
NOTES
1. TAKE PHOTOS DURING ALL THE STEPS OF THE MANUFACTURING.
2. CABLES OF THE THERMOCOUPLE MUST PASS FROM THE WATER OUTLET. CABLES MUST REMAIN GROUPED.
3. PLACE THERMOCOUPLES AS SHOWN IN THE DWG. COVER WITH SEALANT FOR MARINE APPLICATIONS.
4. TEST FOR LEAKAGE. DURING TESTING APPLY LOCAL WATER SUPPLY PRESSURE (3-4 bar).
3D VIEW (1 : 20)
INLET
OUTLET
SPACE FOR JUNCTION BOX
B-B (1 : 10)
948,0
925,0
ALUMINUM COUPLING 1/4" BSP FEMALE x 1/2" BSP FEMALE
INLET
40,0
40,0
948,0
1618,0
C-C (1 : 10)
172,0
168,0
168,0
168,0
168,0
168,0
168,0
168,0
70,0
200,0
ALUMINUM COUPLING 1/2" BSP FEMALE x 1/2" BSP FEMALE
OUTLET
THERMOCOUPLES
40,0
40,0
F (1 : 1)
3,0
1,5
3,0
2,0
METAL TO METAL GLUE
METAL TO METAL GLUE
UPPER SURFACE IN CONTACT WITH BACKSHEET
J (1 : 1)
5,0
30,0
20,0
R10,0
K (1 : 1)
17,0
24,0
30,0
3,0
STIFFENER DETAIL (1:5)
5,0
R10,0
908,0
17,0
24,0
30,0
20,0
925,0
17,0
3,0
IPCoSy PROJECT
2nd PROTOTYPE
OPTION 2
Designed by
Admin
Checked by
Approved by
Date
11/04/2022
Edition
Sheet
1 / 1

References

[1] M. Hasanuzzaman, A. B. M. A. Malek, M. M. Islam, A. K. Pandey, and N. A. Rahim, “Global advancement of cooling technologies for PV systems: A review,” *Solar Energy*, vol. 137. pp. 25–45, 2016. doi: 10.1016/j.solener.2016.07.010.

[2] European Commission, “Renewable Energy Directive.” Accessed: Jun. 28, 2023. [Online]. Available: https://energy.ec.europa.eu/topics/renewable-energy/renewable-energy-directive-targets-and-rules/renewable-energy-directive_en#:~:text=On%2030%20March%202023%2C%20a,adopted%20and%20enter%20into%20force.

[3] Energy and Water Agency, “Malta’s 2030 National Energy and Climate Plan,” 2019. Accessed: Jun. 28, 2023. [Online]. Available: https://energywateragency.gov.mt/wp-content/uploads/2022/04/MT-NECP-FINAL-2020-10-05_Corrigendum.pdf

[4] M. National Statistics Office, “Census of Population and Housing 2011,” 2012. [Online]. Available: https://nso.gov.mt/en/publicatons/Publications_by_Unit/Documents/01_Methodology_and_Research/Census2011_PreliminaryReport.pdf

[5] M. MacDonald, “Feasibility Study for Increasing Renewable Energy Credentials,” 2009.

[6] K. Trapani and D. L. Millar, “Proposing offshore photovoltaic (PV) technology to the energy mix of the Maltese islands,” *Energy Convers Manag*, vol. 67, pp. 18–26, 2013, doi: 10.1016/j.enconman.2012.10.022.

[7] M. Suri, T. A. Huld, E. D. Dunlop, and H. A. Ossenbrink, “Potential of solar electricity generation in the European Union member states and candidate countries,” *Solar Energy*, vol. 81, pp. 1295–1305, 2007, doi: 10.1016/j.solener.2006.12.007.

[8] Malta National Statistics Office, “Renewable Energy from Photovoltaic Panels (PVs): 2022,” NR107/2023. Accessed: Jun. 28, 2023. [Online]. Available: https://nso.gov.mt/renewable-energy-from-photovoltaic-panels-pvs-2022/#:~:text=In%202022%2C%20the%20stock%20of,the%20Gozo%20and%20Comino%20region.

[9] M. Camilleri, M. Dimech, and A. Drago, “Spatial distribution of demersal fishery resources, environmental factors and fishing activities in GSA 15 (Malta Island),” *MedSudMed Technical Document*, vol. 15, no. 13, p. 97, 2008, [Online]. Available: http://scholar.google.com/scholar?hl=en&btnG=Search&q=intitle:Spatial+distribution+of+demersal+fishery+resources,+enviromental+factors+and+fishing+activities+in+GSA+15+(Malta+Island)#0

[10] M. Grech, L. M. Stagno, M. Aquilina, M. Cadamuro, and U. Witzke, “Floating Photovoltaic Installations in Maltese Sea Waters,” 2016.

[11] A. Sahu, N. Yadav, and K. Sudhakar, “Floating photovoltaic power plant: A review,” *Renewable and Sustainable Energy Reviews*, vol. 66. pp. 815–824, 2016. doi: 10.1016/j.rser.2016.08.051.

[12] M. Djordjevic, “40 MW floating PV plant in China connected with Sungrow’s inverters,” 2017. [Online]. Available: https://www.pv-magazine.com/2017/05/19/floating-pv-plant-in-china-connected-with-sungrows-inverters/

[13] Amir Garanovic, “China commissions 320MW floating solar power plant,” Business Developments & Projects. Accessed: Jul. 19, 2023. [Online]. Available: https://www.offshore-energy.biz/china-commissions-320mw-floating-solar-power-plant/

[14] PV Tech, “Masdar and Indonesian power giant to build world’s largest floating solar plant.” Accessed: Jul. 21, 2020. [Online]. Available: https://www.pv-tech.org/news/masdar-and-indonesian-power-giant-to-build-worlds-largest-floating-solar-pl

[15] L. M. Stagno, “Sustainable Energy 2014 : The ISE Annual Conference,” in *Floating Photovoltaics – Technological Issues, Cost and Practical Implications.*, 2014.

[16] Y. Sahu, P. Agrawal, and M. D. Shahabuddin, “Floating Solar Photovoltaic System: An Emerging Technology,” in *National Seminar on Prospects and Challenges of Electrical Power Industry in India - NSPCEPII*, 2015, pp. 219–226. [Online]. Available: http://docslide.net/documents/floating-solar-photovoltaic-system-an-emerging-technology.html

[17] K. Trapani, D. L. Millar, and H. C. M. Smith, “Novel offshore application of photovoltaics in comparison to conventional marine renewable energy technologies,” *Renew Energy*, vol. 50, pp. 879–888, 2013, doi: 10.1016/j.renene.2012.08.043.

[18] T. Cai, S. Duan, and C. Chen, “Forecasting power output for grid-connected photovoltaic power system without using solar radiation measurement,” in *2nd International Symposium on Power Electronics for Distributed Generation Systems, PEDG 2010*, 2010. doi: 10.1109/PEDG.2010.5545754.

[19] J. A. Duffie and W. A. Beckman, *Solar Engineering of Thermal Processes: Fourth Edition*. 2013. doi: 10.1002/9781118671603.

[20] J. D. Mondol, Y. G. Yohanis, and B. Norton, “The impact of array inclination and orientation on the performance of a grid-connected photovoltaic system,” *Renew Energy*, vol. 32, no. 1, pp. 118–140, 2007, doi: 10.1016/j.renene.2006.05.006.

[21] L. M. Stagno, C. Yousif, and M. G. Rebé, “Optimising Photovoltaic Power Generation and Useable Area By Varying the,” no. June, pp. 4102–4108, 2013.

[22] S. Beringer, H. Schilke, I. Lohse, and G. Seckmeyer, “Case study showing that the tilt angle of photovoltaic plants is nearly irrelevant,” *Solar Energy*, 2011, doi: 10.1016/j.solener.2010.12.014.

[23] E. D. Mehleri, P. L. Zervas, H. Sarimveis, J. A. Palyvos, and N. C. Markatos, “Determination of the optimal tilt angle and orientation for solar photovoltaic arrays,” *Renew Energy*, 2010, doi: 10.1016/j.renene.2010.03.006.

[24] A. B. Rao and G. R. Padmanabhan, “Effect of angle of incidence on the performance of a silicon solar cell,” *physica status solidi (a)*, vol. 1, no. 1, pp. K29–K32, 1970, doi: 10.1002/pssa.19700010130.

[25] P. Gevorkian, *Alternative Energy Systems in Building Design*, vol. 23. 2012.

[26] N. AL-Rousan, N. A. M. Isa, and M. K. M. Desa, “Advances in solar photovoltaic tracking systems: A review,” *Renewable and Sustainable Energy Reviews*, vol. 82. 2018. doi: 10.1016/j.rser.2017.09.077.

[27] H. J. Loschi, Y. Iano, J. León, A. Moretti, F. D. Conte, and H. Braga, “A Review on Photovoltaic Systems: Mechanisms and Methods for Irradiation Tracking and Prediction,” *Smart Grid and Renewable Energy*, vol. 06, no. 07, 2015, doi: 10.4236/sgre.2015.67017.

[28] A. J. Narendrasinh Parmar, A. N. Parmar, and V. S. Gautam, “Passive Solar Tracking System,” *International Journal of Emerging Technology and Advanced Engineering Website: www.ijetae.com ISO Certified Journal*, vol. 5, no. 1, pp. 67–88, 2015.

[29] M. J. Clifford and D. Eastwood, “Design of a novel passive solar tracker,” *Solar Energy*, vol. 77, no. 3, pp. 269–280, Sep. 2004, doi: 10.1016/J.SOLENER.2004.06.009.

[30] C. Alexandru and C. Pozna, “Different tracking strategies for optimizing the energetic efficiency of a photovoltaic system,” in *2008 IEEE International Conference on Automation, Quality and Testing, Robotics, AQTR 2008 - THETA 16th Edition - Proceedings*, 2008. doi: 10.1109/AQTR.2008.4588958.

[31] Karen Barbosa de Melo *et al.*, “A study on the influence of locality in the viability of solar tracker systems.,” in *Proceedings XXII Congresso Brasileiro de Automática*, 2018. doi: 10.20906/cps/cba2018-0622.

[32] G. Li, R. Tang, and H. Zhong, “Optical performance of horizontal single-axis tracked solar panels,” in *Energy Procedia*, 2012. doi: 10.1016/j.egypro.2012.01.270.

[33] Z. Li, X. Liu, and R. Tang, “Optical performance of vertical single-axis tracked solar panels,” *Renew Energy*, vol. 36, no. 1, 2011, doi: 10.1016/j.renene.2010.05.020.

[34] R. Chandel and S. S. Chandel, “Performance analysis outcome of a 19-MWp commercial solar photovoltaic plant with fixed-tilt, adjustable-tilt, and solar tracking configurations,” *Progress in Photovoltaics: Research and Applications*, vol. 30, no. 1, 2022, doi: 10.1002/pip.3458.

[35] S. Seme *et al.*, “Dual-axis photovoltaic tracking system – Design and experimental investigation,” *Energy*, vol. 139, 2017, doi: 10.1016/j.energy.2017.05.153.

[36] M. Rahimi, M. Banybayat, Y. Tagheie, and P. Valeh-E-Sheyda, “An insight on advantage of hybrid sun-wind-tracking over sun-tracking PV system,” *Energy Convers Manag*, vol. 105, 2015, doi: 10.1016/j.enconman.2015.07.086.

[37] Y. Ueda, T. Sakurai, S. Tatebe, A. Itoh, and K. Kurokawa, “Performance Analysis of Pv Systems on the Water,” in *23rd European Photovoltaic Solar Energy Conference and Exhibition*, 2008. doi: 10.4229/23rdEUPVSEC2008-4EP.1.3.

[38] K. Trapani and M. Red??n Santaf??, “A review of floating photovoltaic installations: 2007-2013,” *Progress in Photovoltaics: Research and Applications*, vol. 23, no. 4. pp. 524–532, 2015. doi: 10.1002/pip.2466.

[39] C. Ferrer-Gisbert, J. J. Ferrán-Gozálvez, M. Redón-Santafé, P. Ferrer-Gisbert, F. J. Sánchez-Romero, and J. B. Torregrosa-Soler, “A new photovoltaic floating cover system for water reservoirs,” *Renew Energy*, vol. 60, 2013, doi: 10.1016/j.renene.2013.04.007.

[40] R. Cazzaniga, M. Rosa-Clot, P. Rosa-Clot, and G. M. Tina, “Floating tracking cooling concentrating (FTCC) systems,” in *Conference Record of the IEEE Photovoltaic Specialists Conference*, 2012, pp. 514–519. doi: 10.1109/PVSC.2012.6317668.

[41] R. Xu, C. Liu, H. Liu, Z. Sun, T. L. Lam, and H. Qian, “Design and optimization of a wave driven solar tracker for floating photovoltaic plants,” in *IEEE/ASME International Conference on Advanced Intelligent Mechatronics, AIM*, 2019. doi: 10.1109/AIM.2019.8868847.

[42] G. M. Tina and F. Bontempo Scavo, “Energy performance analysis of tracking floating photovoltaic systems,” *Heliyon*, vol. 8, no. 8, Aug. 2022, doi: 10.1016/j.heliyon.2022.e10088.

[43] A. D. C. Pronk, D. Dizdar, and W. A. Schuurmans, “Sun-Spotter: gravity point displacement as solar-tracking principle,” in *Proceedings of the International Association for Shell and Spatial Structures (IASS) Symposium 2015, Amsterdam*, 2015.

[44] S. S. Shinde, “Implementation of Efficient Liquid Solar Array System Using GSM and Launchpad,” *International Journal of Computer Sciences and Engineering*, vol. 7, no. 6, 2019, doi: 10.26438/ijcse/v7i6.873876.

[45] P. E. Campana, L. Wästhage, W. Nookuea, Y. Tan, and J. Yan, “Optimization and assessment of floating and floating-tracking PV systems integrated in on- and off-grid hybrid energy systems,” *Solar Energy*, vol. 177, 2019, doi: 10.1016/j.solener.2018.11.045.

[46] H. Bahaidarah, A. Subhan, P. Gandhidasan, and S. Rehman, “Performance evaluation of a PV (photovoltaic) module by back surface water cooling for hot climatic conditions,” *Energy*, vol. 59, 2013, doi: 10.1016/j.energy.2013.07.050.

[47] A. Shukla, K. Kant, A. Sharma, and P. H. Biwole, “Cooling methodologies of photovoltaic module for enhancing electrical efficiency: A review,” *Solar Energy Materials and Solar Cells*, vol. 160, pp. 275–286, 2017, doi: 10.1016/j.solmat.2016.10.047.

[48] J. Siecker, K. Kusakana, and B. P. Numbi, “A review of solar photovoltaic systems cooling technologies,” *Renewable and Sustainable Energy Reviews*, vol. 79. pp. 192–203, 2017. doi: 10.1016/j.rser.2017.05.053.

[49] E. Radziemska, “The effect of temperature on the power drop in crystalline silicon solar cells,” *Renew Energy*, 2003, doi: 10.1016/S0960-1481(02)00015-0.

[50] S. Chander, A. Purohit, A. Sharma, Arvind, S. P. Nehra, and M. S. Dhaka, “A study on photovoltaic parameters of mono-crystalline silicon solar cell with cell temperature,” *Energy Reports*, 2015, doi: 10.1016/j.egyr.2015.03.004.

[51] C. Wen, C. Fu, J. L. Tang, D. X. Liu, S. F. Hu, and Z. G. Xing, “The influence of environment temperatures on single crystalline and polycrystalline silicon solar cell performance,” *Sci China Phys Mech Astron*, 2012, doi: 10.1007/s11433-011-4619-z.

[52] M. Boussaid, A. Belghachi, K. Agroui, M. Abdelaoui, and M. Otmani, “Solar cell degradation under open circuit condition in out-doors-in desert region,” *Results Phys*, 2016, doi: 10.1016/j.rinp.2016.09.013.

[53] T. A. Olukan and M. Emziane, “A comparative analysis of PV module temperature models,” in *Energy Procedia*, 2014. doi: 10.1016/j.egypro.2014.12.433.

[54] D. L. King, W. E. Boyson, and J. A. Kratochvil, “Photovoltaic array performance model,” *Sandia Report No. 2004-3535*, 2004, doi: 10.2172/919131.

[55] O. Dupré, R. Vaillon, and M. A. Green, *Thermal Behavior of Photovoltaic Devices*. 2017. doi: 10.1007/978-3-319-49457-9.

[56] A. Royne, C. J. Dey, and D. R. Mills, “Cooling of photovoltaic cells under concentrated illumination: A critical review,” *Solar Energy Materials and Solar Cells*, 2005, doi: 10.1016/j.solmat.2004.09.003.

[57] H. G. Teo, P. S. Lee, and M. N. A. Hawlader, “An active cooling system for photovoltaic modules,” *Appl Energy*, 2012, doi: 10.1016/j.apenergy.2011.01.017.

[58] N. Arcuri, F. Reda, and M. De Simone, “Energy and thermo-fluid-dynamics evaluations of photovoltaic panels cooled by water and air,” *Solar Energy*, 2014, doi: 10.1016/j.solener.2014.03.034.

[59] R. Mazón-Hernández, J. R. García-Cascales, F. Vera-García, A. S. Káiser, and B. Zamora, “Improving the electrical parameters of a photovoltaic panel by means of an induced or forced air stream,” *International Journal of Photoenergy*, 2013, doi: 10.1155/2013/830968.

[60] P. Valeh-E-Sheyda, M. Rahimi, A. Parsamoghadam, and M. M. Masahi, “Using a wind-driven ventilator to enhance a photovoltaic cell power generation,” *Energy Build*, 2014, doi: 10.1016/j.enbuild.2013.12.052.

[61] A. R. Amelia *et al.*, “Cooling on photovoltaic panel using forced air convection induced by DC fan,” *International Journal of Electrical and Computer Engineering*, 2016, doi: 10.11591/ijece.v6i1.9118.

[62] E. Touti, M. Masmali, M. Fterich, and H. Chouikhi, “Experimental and numerical study of the PVT design impact on the electrical and thermal performances,” *Case Studies in Thermal Engineering*, vol. 43, 2023, doi: 10.1016/j.csite.2023.102732.

[63] M. J. Huang, P. C. Eames, and B. Norton, “Thermal regulation of building-integrated photovoltaics using phase change materials,” *Int J Heat Mass Transf*, 2004, doi: 10.1016/j.ijheatmasstransfer.2003.11.015.

[64] M. M. Farid, A. M. Khudhair, S. A. K. Razack, and S. Al-Hallaj, “A review on phase change energy storage: Materials and applications,” *Energy Conversion and Management*. 2004. doi: 10.1016/j.enconman.2003.09.015.

[65] R. Stropnik and U. Stritih, “Increasing the efficiency of PV panel with the use of PCM,” *Renew Energy*, 2016, doi: 10.1016/j.renene.2016.06.011.

[66] C. J. Smith, P. M. Forster, and R. Crook, “Global analysis of photovoltaic energy output enhanced by phase change material cooling,” *Appl Energy*, 2014, doi: 10.1016/j.apenergy.2014.03.083.

[67] A. H. A. Al-Waeli *et al.*, “Evaluation of the nanofluid and nano-PCM based photovoltaic thermal (PVT) system: An experimental study,” *Energy Convers Manag*, vol. 151, 2017, doi: 10.1016/j.enconman.2017.09.032.

[68] W. Pang, Y. Liu, S. Shao, and X. Gao, “Empirical study on thermal performance through separating impacts from a hybrid PV/TE system design integrating heat sink,” *International*

Communications in Heat and Mass Transfer, 2015, doi: 10.1016/j.icheatmasstransfer.2014.11.004.

[69] M. Benghanem, A. A. Al-Mashraqi, and K. O. Daffallah, "Performance of solar cells using thermoelectric module in hot sites," *Renew Energy*, 2016, doi: 10.1016/j.renene.2015.12.011.

[70] A. Kane, V. Verma, and B. Singh, "Optimization of thermoelectric cooling technology for an active cooling of photovoltaic panel," *Renewable and Sustainable Energy Reviews*. 2017. doi: 10.1016/j.rser.2016.11.114.

[71] M. Rajvikram and G. Sivasankar, "Experimental study conducted for the identification of best heat absorption and dissipation methodology in solar photovoltaic panel," *Solar Energy*, 2019, doi: 10.1016/j.solener.2019.09.053.

[72] T. C. Cheng, C. H. Cheng, Z. Z. Huang, and G. C. Liao, "Development of an energy-saving module via combination of solar cells and thermoelectric coolers for green building applications," *Energy*, 2011, doi: 10.1016/j.energy.2010.10.061.

[73] F. Schiro, A. Benato, A. Stoppato, and N. Destro, "Improving photovoltaics efficiency by water cooling: Modelling and experimental approach," *Energy*, 2017, doi: 10.1016/j.energy.2017.04.164.

[74] K. A. Moharram, M. S. Abd-Elhady, H. A. Kandil, and H. El-Sherif, "Enhancing the performance of photovoltaic panels by water cooling," *Ain Shams Engineering Journal*, 2013, doi: 10.1016/j.asej.2013.03.005.

[75] S. Nižetić, D. Čoko, A. Yadav, and F. Grubišić-Čabo, "Water spray cooling technique applied on a photovoltaic panel: The performance response," *Energy Convers Manag*, vol. 108, pp. 287–296, 2016, doi: 10.1016/j.enconman.2015.10.079.

[76] M. Abdolzadeh and M. Ameri, "Improving the effectiveness of a photovoltaic water pumping system by spraying water over the front of photovoltaic cells," *Renew Energy*, 2009, doi: 10.1016/j.renene.2008.03.024.

[77] M. K. Smith *et al.*, "Water Cooling Method to Improve the Performance of Field-Mounted, Insulated, and Concentrating Photovoltaic Modules," *J Sol Energy Eng*, 2014, doi: 10.1115/1.4026466.

[78] A. Saxena, S. Deshmukh, S. Nirali, and S. Wani, "Laboratory based Experimental Investigation of Photovoltaic (PV) Thermo-control with Water and its Proposed Real-time Implementation," *Renew Energy*, 2018, doi: 10.1016/j.renene.2017.08.029.

[79] S. Krauter, "Increased electrical yield via water flow over the front of photovoltaic panels," in *Solar Energy Materials and Solar Cells*, 2004. doi: 10.1016/j.solmat.2004.01.011.

[80] A. Hadipour, M. Rajabi Zargarabadi, and S. Rashidi, "An efficient pulsed- spray water cooling system for photovoltaic panels: Experimental study and cost analysis," *Renew Energy*, vol. 164, pp. 867–875, Feb. 2021, doi: 10.1016/j.renene.2020.09.021.

[81] A. Farrugia, "Design and analysis of different cooling effects on photovoltaic panels," University of Malta, 2014.

[82] S. Dubey and G. N. Tiwari, "Analysis of PV/T flat plate water collectors connected in series," *Solar Energy*, 2009, doi: 10.1016/j.solener.2009.04.002.

[83] S. A. Kalogirou, Y. Tripanagnostopoulos, and A. Athienitis, *Modeling and simulation of passive and active solar thermal systems*. 2012. doi: 10.1016/B978-0-08-087872-0.00308-5.

[84] H. Arias, J. Cabrera, and J. Hernandez, "Performance evaluation of a mono-crystalline PV module cooled by a flat plate solar collector in thermosyphon mode," in *2015 IEEE 42nd Photovoltaic Specialist Conference, PVSC 2015*, 2015. doi: 10.1109/PVSC.2015.7355825.

[85] H. A. Zondag, D. W. de Vries, W. G. J. van Helden, R. J. C. van Zolingen, and A. A. van Steenhoven, "The yield of different combined PV-thermal collector designs," *Solar Energy*, 2003, doi: 10.1016/S0038-092X(03)00121-X.

[86] E. Rebollo, F. R. Blanquez, I. Lopez, C. A. Platero, and C. Carrero, "Overall feasibility of low cost conversion from PV to PVTw," in *Proceedings of 2013 International Conference on Renewable Energy Research and Applications, ICRERA 2013*, 2013. doi: 10.1109/ICRERA.2013.6749833.

[87] B. Sandnes and J. Rekstad, "A photovoltaic/thermal (PV/T) collector with a polymer absorber plate. Experimental study and analytical model," *Solar Energy*, 2002, doi: 10.1016/S0038-092X(01)00091-3.

[88] Z. Peng, M. R. Herfatmanesh, and Y. Liu, "Cooled solar PV panels for output energy efficiency optimisation," *Energy Convers Manag*, 2017, doi: 10.1016/j.enconman.2017.07.007.

[89] S. Fakouriyan, Y. Saboohi, and A. Fathi, "Experimental analysis of a cooling system effect on photovoltaic panels' efficiency and its preheating water production," *Renew Energy*, 2019, doi: 10.1016/j.renene.2018.09.054.

[90] S. M. Shalaby, M. K. Elfakharany, B. M. Moharram, and H. F. Abosheiasha, "Experimental study on the performance of PV with water cooling," *Energy Reports*, vol. 8, 2022, doi: 10.1016/j.egyr.2021.11.155.

[91] B. Du, E. Hu, and M. Kolhe, "Performance analysis of water cooled concentrated photovoltaic (CPV) system," *Renewable and Sustainable Energy Reviews*. 2012. doi: 10.1016/j.rser.2012.09.007.

[92] G. M. Tina, M. Rosa-Clot, P. Rosa-Clot, and P. F. Scandura, "Optical and thermal behavior of submerged photovoltaic solar panel: SP2," *Energy*, 2012, doi: 10.1016/j.energy.2011.08.053.

[93] R. Lanzafame *et al.*, "Field experience with performances evaluation of a single-crystalline photovoltaic panel in an underwater environment," *IEEE Transactions on Industrial Electronics*, 2010, doi: 10.1109/TIE.2009.2035489.

[94] M. Rosa-Clot, P. Rosa-Clot, G. M. Tina, and P. F. Scandura, "Submerged photovoltaic solar panel: SP2," *Renew Energy*, vol. 35, no. 8, pp. 1862–1865, 2010, doi: 10.1016/j.renene.2009.10.023.

[95] S. A. Abdulgafar, O. S. Omar, and K. M. Yousif, "Improving The Efficiency Of Polycrystalline Solar Panel Via Water Immersion Method," *International Journal of Innovative Research in Science, Engineering and Technology (An ISO Certified Organization)*, vol. 3297, no. 1, pp. 8127–8132, 2007, doi: 10.4172/20904541.1000166.

[96] MIRARCO Energy, "MIRARCO.org." Accessed: Jan. 14, 2020. [Online]. Available: https://www.mirarco.org/wp-content/uploads/mirarco_ERCM_Projects/Floating_PV-InformationSheet.pdf

[97] Ocean Sun, *Ocean Sun Benefits*. Accessed: Jun. 30, 2023. [Online]. Available: https://oceansun.no/benefits/

[98] Z. A. A. Majid, M. H. Ruslan, K. Sopian, M. Y. Othman, and M. S. M. Azmi, "Study on performance of 80 watt floating photovoltaic panel," *Journal of Mechanical Engineering and Sciences*, 2014, doi: 10.15282/jmes.7.2014.14.0112.

[99] S. Oliveira-Pinto and J. Stokkermans, "Assessment of the potential of different floating solar technologies – Overview and analysis of different case studies," *Energy Convers Manag*, vol. 211, 2020, doi: 10.1016/j.enconman.2020.112747.

[100] W. T. Beauchamp, T. T. Hart, and M. L. Sanders, "Blue/red reflecting solar cell covers for GaAs cells," in *Conference Record of the IEEE Photovoltaic Specialists Conference*, 1993. doi: 10.1109/pvsc.1993.346896.

[101] C. M. Maghanga, G. A. Niklasson, C. G. Granqvist, and M. Mwamburi, "Spectrally selective reflector surfaces for heat reduction in concentrator solar cells: Modeling and applications of TiO2:Nb-based thin films," *Appl Opt*, 2011, doi: 10.1364/AO.50.003296.

[102] S. Krauter and R. Hanitsch, "Actual optical and thermal performance of PV-modules," *Solar Energy Materials and Solar Cells*, 1996, doi: 10.1016/0927-0248(95)00143-3.

[103] S. Suryanto and F. Firman, "The Vacuum Technique for Cooling PV Cell," 2022, doi: 10.2991/978-94-6463-078-7_13.

[104] Advanced Energy Industries, "Understanding Potential Induced Degradation," *White Paper - AE*, 2013.

[105] G. R. Mon, J. Orehotsky, R. G. Ross, and G. Whitla, "Predicting Electrochemical Breakdown in Terrestrial Photovoltaic Modules.," in *Conference Record of the IEEE Photovoltaic Specialists Conference*, 1984.

[106] S. Pingel *et al.*, "Potential induced degradation of solar cells and panels," in *Conference Record of the IEEE Photovoltaic Specialists Conference*, 2010. doi: 10.1109/PVSC.2010.5616823.

[107] V. Naumann *et al.*, "Explanation of potential-induced degradation of the shunting type by Na decoration of stacking faults in Si solar cells," *Solar Energy Materials and Solar Cells*, 2014, doi: 10.1016/j.solmat.2013.06.015.

[108] R. Swanson *et al.*, "The surface polarization effect in high-efficiency silicon solar cells," in *15th PVSEC*, Shanghai, China, 2005.

[109] R. G. Ross, G. R. Mon, L. C. Wen, and R. S. Sugimura, "Measurement and characterization of voltage- and current-induced degradation of thin-film photovoltaic modules," *Solar Cells*, 1989, doi: 10.1016/0379-6787(89)90037-9.

[110] P. A. Schweitzer, *Mechanical and Corrosion-Resistant Properties of Plastics and Elastomers*. 2000. doi: 10.1201/9781482270280.

[111] R. Bugeja, L. Mule' Stagno, and N. Branche, "The effect of wave response motion on the insolation on offshore photovoltaic installations," *Solar Energy Advances*, vol. 1, p. 100008, Jan. 2021, doi: 10.1016/J.SEJA.2021.100008.

[112] A. Luque and S. Hegedus, *Handbook of Photovoltaic Science and Engineering*. 2011. doi: 10.1002/9780470974704.

[113] S. A. Kalogirou, *Solar Energy Engineering: Processes and Systems*. 2009. doi: 10.1016/B978-0-12-374501-9.00014-5.

[114] B. Y. H. Liu and R. C. Jordan, "The long-term average performance of flat-plate solar-energy collectors," *Solar Energy*, 1963, doi: 10.1016/0038-092x(63)90006-9.

[115] R. Perez, P. Ineichen, R. Seals, J. Michalsky, and R. Stewart, "Modeling daylight availability and irradiance components from direct and global irradiance," *Solar Energy*, 1990, doi: 10.1016/0038-092X(90)90055-H.

[116] R. Perez, R. Stewart, C. Arbogast, R. Seals, and J. Scott, "An anisotropic hourly diffuse radiation model for sloping surfaces: Description, performance validation, site dependency evaluation," *Solar Energy*, 1986, doi: 10.1016/0038-092X(86)90013-7.

[117] U.S Department of Commerce and NOAA Research, "NOAA Earth System Research Laboratory." Accessed: May 08, 2020. [Online]. Available: https://www.esrl.noaa.gov/gmd/grad/solcalc/calcdetails.html

[118] R. Bugeja, L. Mule' Stagno, and L. Dexarcis, "An Offshore Solar Irradiance Calculator (OSIC) Applied to Photovoltaic Tracking Systems," *Energies (Basel)*, vol. 16, no. 9, May 2023, doi: 10.3390/en16093735.

[119] The GTK Team, "The GTK project - a free and open-source cross-platform Widget Toolkit." Accessed: Jan. 17, 2023. [Online]. Available: https://www.gtk.org/

[120] The Glade project, "Glade - A User Interface Designer," https://glade.gnome.org/.

[121] Martin F Johansen, "InductiveComputerScience/pbPlots: A plotting library available in many programming languages.," https://github.com/InductiveComputerScience/pbPlots.

[122] misja.com, "Epoch Converter." Accessed: Jan. 17, 2023. [Online]. Available: https://www.epochconverter.com/

[123] R. Bugeja, L. Mule' Stagno, and I. Niarchos, "Photovoltaic backside cooling using the space inside a conventional frame (IPCOSY)," *Future Energy*, vol. 2, no. 3, pp. 20–28, Aug. 2023, doi: 10.55670/fpll.fuen.2.3.3.

[124] R. Bugeja and L. Mule' Stagno, "System for Cooling a Solar Panel Assembly.," 285827, Aug. 24, 2021 Accessed: Jun. 22, 2023. [Online]. Available: https://israelpatents.justice.gov.il/en/patent-file/details/285827

[125] Omega Engineering Inc., "Thermocouple types." Accessed: May 22, 2023. [Online]. Available: https://www.omega.com/en-us/resources/thermocouple-types#:~:text=Accuracy%3A%20Type%20T%20thermocouples%20have,per%20ANSI%2FASTM%20E230).

[126] British Standards Institute, "BS 7671 Requirements for Electrical Installations. IET Wiring Regulations | BSI Group," British Stadards IET Wiring Regulations.

[127] D. Faiman, "Assessing the outdoor operating temperature of photovoltaic modules," *Progress in Photovoltaics: Research and Applications*, 2008, doi: 10.1002/pip.813.

[128] H. C. Hottel and B. B. Woertz, “Evaluation of flat-plate solar heat collector,” *ASME (Am. Soc. Mech. Eng.); (United States)*, vol. 64, no. 1. 1942.

[129] R. W. Bliss, “The derivations of several ‘Plate-efficiency factors’ useful in the design of flat-plate solar heat collectors,” *Solar Energy*, vol. 3, no. 4, 1959, doi: 10.1016/0038-092X(59)90006-4.

[130] M. R. Elkinton, A. L. Rogers, and J. G. McGowan, “An investigation of wind-shear models and experimental data trends for different terrains,” *Wind Engineering*, vol. 30, no. 4, 2006, doi: 10.1260/030952406779295417.

[131] R. N. Farrugia, “The wind shear exponent in a Mediterranean island climate,” *Renew Energy*, vol. 28, no. 4, 2003, doi: 10.1016/S0960-1481(02)00066-6.

[132] M. Woodhouse, B. Smith, A. Ramdas, and Robert Margolis, “Crystalline Silicon Photovoltaic Module Manufacturing Costs and Sustainable Pricing: 1H 2018 Benchmark and Cost Reduction Roadmap,” 2019.

[133] Alibaba, “High quality professional aluminum sheet factory 1-8 series aluminum plain sheet plate.” Accessed: Jun. 16, 2023. [Online]. Available: https://www.alibaba.com/product-detail/High-Quality-Professional-Aluminum-Sheet-Factory_1600614324143.html?spm=a2700.7724857.0.0.7c422a9bHLVF2m&s=p

[134] Alibaba, “Chinese manufacturers 6063 aluminium alloy Extrusion aluminum Profile/Pipe/Tube/Angle/Bar/Channel.” Accessed: Jun. 16, 2023. [Online]. Available: https://www.alibaba.com/product-detail/Chinese-manufacturers-6063-aluminium-alloy-Extrusion_1600366239820.html?spm=a2700.galleryofferlist.normal_offer.d_image.24da49d8obTh1u

[135] Regulator for Energy and Water Services, “2021 Renewable Energy Sources Scheme (Active).” Accessed: Jun. 17, 2023. [Online]. Available: https://www.rews.org.mt/#/en/sdgr/463-2021-renewable-energy-sources-scheme

[136] Regulator for Energy and Water Services, “Regulated Electricity Tariffs,” Approved Electricity Tariffs applicable as from 31st March, 2014 Residential. Accessed: Jun. 21, 2023. [Online]. Available: https://www.rews.org.mt/#/en/fa/31